Design considerations for a high temperature image sensor in 4H-SiC

ERASMUS EXCHANGE WITH UNIVERSITY OF NAPLES "FEDERICO II", ITALY

MARCO CRISTIANO

"Man meets God behind every door science can open."

(A. Einstein)

Abstract

This thesis is part of a project, Working on Venus, funded by the Knut and Alice Wallenberg Foundation (one of the largest Swedish funders of research) and developed by KTH in collaboration with Linköping University. The goal of this project is to create a lander able to investigate the planet Venus and to work under extreme conditions, i.e. it has to be able to withstand at high levels of radiation and high temperatures such as that of Venus surface (that is about 460 °C) without integrating a dedicated bulky cooling system to reduce the overall weight and volume of the system.

In this thesis it will be investigated in detail the 4H-SiC performances to realize a CMOS image sensor for UV photography that operates at high temperature.

This work will include discussions and proposals on possible future applications, such as the realization of 4H-SiC phototransistors.

Acknowledgements

This work is the result of hard work and a lot of times spent alone to achieve the goal. After this work I really understand what it means to work completely alone and to obtain a result relying by my own.

First of all, I want to thank my supervisor Professor Carl-Mikael Zetterling and my examiner Professor Mikael Östling for accepting me at the KTH, giving me the opportunity to do my Master's Thesis in Sweden, in one of the most important institutes of Microelectronics and Applied Physics in Europe.

I would like to thank my Italian supervisor Professor Niccolò Rinaldi for the opportunity to be an Erasmus student at KTH.

Thanks to Shuoben Hou that has helped me often during this work.

Thanks to my dear friend Aniello Falco that, from Germany, has spent a lot of time to help me on some problems, despite its hard work. I will never forget the long discussions on WhatsApp!

Obviously, at the moment I would not be here to write these acknowledgements if I had not had behind an extraordinary family that with their financial and moral support has gave me the opportunity to complete my university studies, in order to fulfill the dream that I had as a child. For this reason, I do not know if now or in the future I will never be able to properly thank you for all the sacrifices that you have made for me until this day. Today, if I look back and I see the progress made so far, I really realize that without your help I would have been only a small raft in the middle of a storm. Thank to you all the difficult moments are appeared easy and free of hostility. So, thank you, thank you and thank you again!

In particular, thanks mom for putting up with me for five years, while I was studying like a crazy man and the blasphemies had not boundary. You with your calm, also suffering my ire, you have always given me inner calm and a smile on my lips. Besides, who can be more skilled than a mother to keep calm her son and restore its happiness! So, Thank you mom.

A big thank goes to the most special family that I have ever met in my life, the Daniele and Conte family. I thank the members of this family from the first to the last one, for giving me moral support and to have always believed in me. Also, I cannot ever forget the happiness shown from you after the result of my university exam. You have not treated me as an acquaintance or a friend, but as a real son. In your life you will meet many people, but few of them will leave something inside you for all your life. Today, I can tell you that your actions and your support shown towards me will always indelibly remain in my heart. I will never forget all the life and moral discussions made with Mr. Giovanni Daniele on the sofa in front of the TV. To you I have especially to say thank you to have done to note me and to change parts of my character that I would have never been able to find alone. Furthermore, I say thank you for all the personal life suggestions that you have gave me. Today, I can be really happy to have met you! Thanks again!

But the biggest thanks that I have to do to this family is thank you for having given birth to a daughter so unique and special that I can now have by my side as my woman. In life not everyone is so privileged to meet a wonderful woman to talk of the personal problems, fears, difficulties and life choices. In the darkest and difficult moments of my life, as also the difficulties encountered during this experience abroad, even at a distance greater than 2000 km, I felt your closeness, also with a simple smile or a funny discussion. It is really impressive how my life can be become so clear and rosy in any grim and hostile situation, simply shaking your hand or looking in your eyes. In fact, this makes you different from all the other people that I know, thanks to your ability to understand and to be close to me in all the moments, both good and bad moments. In fact, for this, today, I can consider me one of the happiest men on Earth. Whatever choices I will take in the future, I am sure that having a shield and a support so hard by my side, nothing will fear me. Thank you Francesca!

A final thanks goes to myself! This experience abroad has improved me as a person, and also so much! The first thing that I learned is that in your life there are few persons that will help you. Therefore, find the force in yourself and learn to fight alone. The life is a fight. You can obtain the best things only with the sacrifice, and after you have to fight to keep them. In your life do not pray to have an easy life, but you have to pray to have the force to fight for a hard life, because who fights can lose, but who does not fight has already lost! The life puts you in front of a lot of difficult tests, and it is not important that you are able to overcome all of them, but it is important that you are able to deal with them! In your life you have to learn that the word "I cannot do" is forbidden! A stupid expression like "I cannot do" has the power to prevent to the people to realize their dreams. In reality, with the commitment and the constancy the things that you are not able to do are very few. "I cannot do" is only a stupid block that we use to convince ourselves and surrender.

In fact, as we learn from *Steve Jobs*: "*Sometimes life hits you in the head with a brick. Don't lose faith […].You've got to find what you love. And that is as true for your work as it is for your lovers. Your work is going to fill a large part of your life, and the only way to be truly satisfied is to do what you believe is great work. And the only way to do great work is to love what you do. If you haven't found it yet, keep looking. Don't settle. As with all matters of the heart, you'll know when you find it. And, like any great relationship, it just gets better and better as the years roll on. So keep looking until you find it. Don't settle. Stay hungry. Stay foolish.*"

Contents

Introduction

Silicon carbide (SiC) is nowadays the material of choice, compared to other semiconductor materials, because of its important features due to the large bandgap, such as high temperature operation, optical advantages, high critical electric fields, high thermal conductivity.

Up to this date, many studies show the realization of SiC Integrated circuits (ICs) in both digital and analog [1].

The Knut and Alice Wallenberg Foundation granted the project **WOV - Working on Venus** almost 23 MSEK for 5 years. Venus has fascinated mankind since ancient times [2] for various reasons, such as its proximity to Earth, its similarity to our planet in terms of size and its diversity in terms of atmosphere. Although many things could be investigated by far, some of the properties of interest require the use of an orbiter or a lander. The first is a spacecraft that orbits around a planet or a moon without landing on it, at a certain distance from the surface of the celestial body. The second is a type of spacecraft that descents and stops on the surface of the celestial body. It is equipped with sophisticated scientific instrumentation and appropriate electronic systems to perform specific tasks [3,4]. A surface temperature of 460 °C with an atmospheric pressure of around 92 bar (the same pressure is possible to measure at a depth of 1 km in the terrestrial ocean) is an extremely challenging environment. For these reasons the electronics of earlier landers, sent from the Soviet Union (*Venera* probes [5]) on Venus in the '70s, failed after a few hours. Venus atmosphere consists mainly of CO_2. Furthermore, there are few images of the surface due to the presence of atmospheric cloud covering [4]. Basic scientific investigation of the atmosphere of Venus and its seismic activities over time would be useful for climate modeling and planetary understanding. Imaging could answer the question of whether there is or there was life on Venus [6].

KTH will demonstrate, for the first time, all the electronics needed to work on Venus building the entire lander system without bulky or heavy cooling system with the aim to investigate the planet surface for one year.

As previously mentioned a few images of the surface of Venus are currently available, derived mainly from the *Venera* landers, which used panoramic tv cameras that sent images back until the electronics failed [5]. Some of the collected images rose the suspect of the possible presence of actual or previous life on Venus. Obviously, the only way to get more information and eventually solve this issue is a long time surface's monitoring program. It is clear that in order to do this the lander needs an image sensor which can operate at high temperatures, with all the associated electronics.

The block diagram of the proposed system is shown in the following figure.
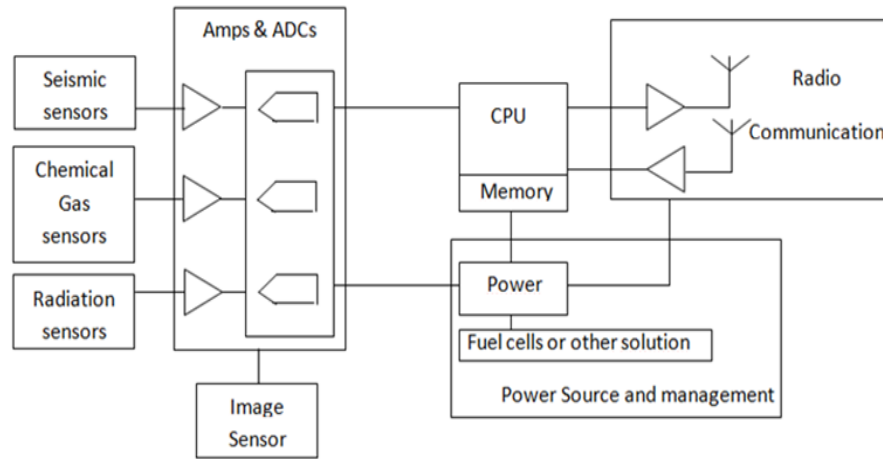
Figure 1. Block diagram of Venus lander system

As shown in Figure 1 the system consists of various parts ranging from the entire network of sensors to the RF transmission.

In this thesis the possibility of realization of an image sensor in SiC for UV imaging will be investigated, starting from a detailed analysis of the behavior of the photodetector when the temperature changes and focusing the attention on a particular temperature, i.e. 460 °C. In particular, several photodetectors will be simulated and designed, one of which will also be experimentally tested under UV light. In addition, since the CMOS technology is one of two baseline for the imaging (the other is the CCD technology), even the possibility to use this technique, to the case, will be theoretically investigated, observing if it can operate at higher temperatures if made of SiC.

The thesis is divided into five chapters. **Chapter 1** provides a general description of the electrical and optical properties of silicon carbide including the advantage of its use at high temperature and in UV imaging. **Chapter 2** describes the operating principle of an image sensor in CMOS technology (showing also the advantage of UV imaging) by focusing on the theoretical analysis of a *pin* diode in 4H-SiC to obtain its main parameters and its performances in light detection. **Chapter 3** describes some photodiodes simulations varying the temperature and other technological parameters. The same chapter also lists the simulations and the SPICE parameters extraction of a NMOS in 4H-SiC, belonging to an investigated CMOS technology, to find out whether or not it is suitable for high-temperature operations. The chapter includes, also, simulations of some phototransistors used as sensing elements, followed by an example of spice simulation of the entire circuit of a pixel. **Chapter 4** shows the experimental results obtained on a photodiode provided by KTH, and a comparison of them with those obtained from simulations. **Chapter 5** lists the conclusions of the analysis carried out and suggests possible future developments.

Chapter 1

Material, electrical and optical properties of SiC

1.1   Crystal properties of SiC

A crystal is a solid object composed of atoms having a geometrically regular arrangement repeated in the three spatial dimensions indefinitely. Most of the crystal structures can be described through the use of a basic unit cell repeated in the space, that allows to describe the position of all atoms in the entire crystal. For example, the silicon carbide is presented as a crystal composed of two elements of the IV group, namely silicon (Si) and carbon (C). Normally, SiC crystallizes in the structure of *zinc-blende* (Figure 1.1a [7]), which means that the atoms are arranged within the unit cell forming a tetrahedron composed of a silicon atom at the center and four carbon atoms to the vertices, covalently bonded to the same (Figure 1.1b [8]) with a bond length of about 1.89 Å between a silicon atom and a carbon atom, and of about 3.08 Å between two silicon atoms and two carbon atoms.
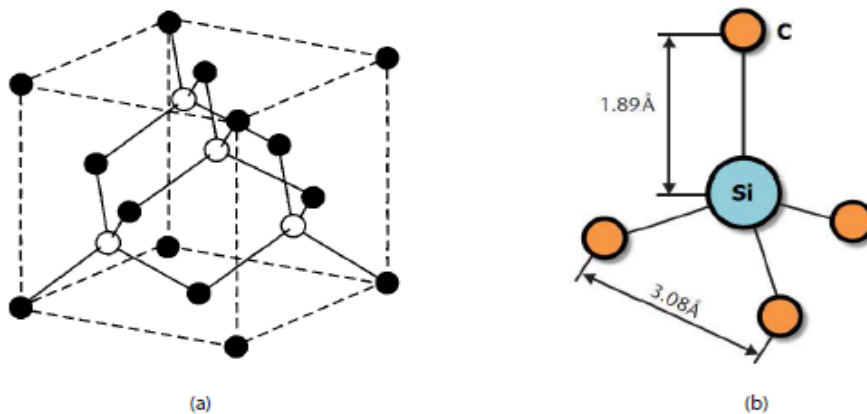
Figure 1.1. Zinc-blend crystal structure (a). Tetrahedron building block of all SiC crystals (b).

The silicon carbide can exhibit different crystal structures which differ according to how the atoms of silicon and carbon are connected to form the basic cell. This feature goes under the name of *polytypism* and each crystal obtainable takes the name of *polytype*. Instead of analyzing each polytype referring to the basic unit cell, it is possible to consider that each polytype has a hexagonal structure, and it consists of many SiC bilayers

overlapping one another packed according to a hexagonal pattern. In fact, when perfect spheres of constant radius are packed close together, within a plan, they organize themselves creating a hexagonal pattern. The cause of this type of packaging is due to the covalent bond of the atoms that make up the basic cell, which means that each silicon atom is surrounded by exactly four carbon neighbors atoms. Then, if one imagines to have a layer of silicon atoms packed according to a hexagonal pattern with a layer of smaller atoms of carbon superimposed (the two layers form a SiC bilayer, see Figure 1.2a [7]), the subsequent SiC bilayer will necessarily be positioned so such that the atoms are exactly centered between three atoms of the underlying layer. Proceeding in this way, for each two overlapping layers, one obtains the resulting crystalline structure. If the third double layer is placed directly on the first double layer and this structure is repeated in this order, the resulting crystal takes the name of *wurtzite*, even if the third layer could also be packed in a different position both from the first and the second double layer. In fact, indicating with A the position of the first double layer of atoms, the next layer could occupy both the position B and the position C (Figure 1.2b [7]). In Figure 1.2b is shown the wurtzite structure, which is a repetition of the sequences of layers AB. The name of each polytype is composed by a number and a letter, where the number represents how many the double layers of silicon and carbon atoms that make up the basic sequence are, and the letter represents the resulting structure of the crystal (C for cubic, H for hexagonal, and R for rhombohedral).
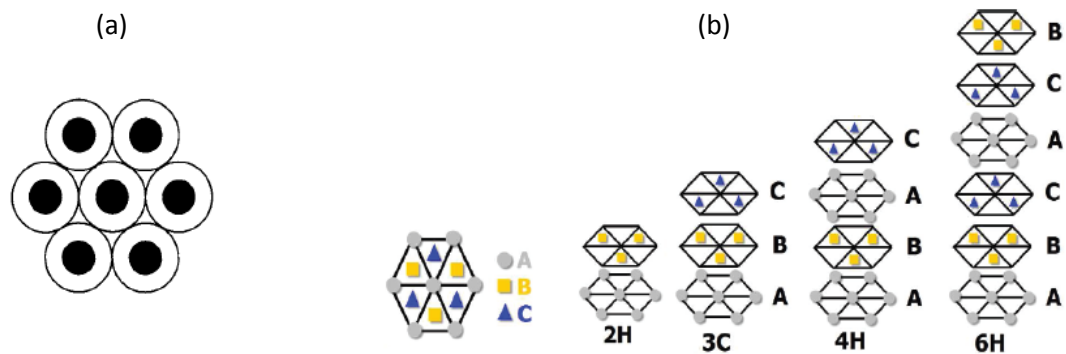
Figure 1.2. (a) One double layer of hexagonally close packed atoms where the white atoms are Si and black atoms are C. (b) Crystal structure of different SiC polytypes: 2H, 3C, 4H, 6H. Top view.

It is very interesting to note that, despite the fact that the different polytypes have the same proportion of silicon and carbon atoms, both electrical and optical properties differ from one polytype to another, as a direct consequence of the different packing sequence. Moreover, even the unit cell varies between the different polytypes, as well as also the number of atoms per cell.

1.2 Electrical properties of SiC

Table 1.1 summarizes both electrical and optical properties for different SiC polytypes.

Property	Unity	Si	3C-SiC	6H-SiC	4H-SiC
Bandagap, E_g (at room temperature)	(eV)	1.12	2.4	3	3.2
Critical Field, E_C	(MV/cm)	0.25	2	2.5	2.2
Thermal Conductivity, λ (at room temperature)	(W/cm K)	1.5	5	5	5
Satured electron drift velocity, v_{sat} (at room temperature)	(10^7 cm/s)	1	2.5	2	2
Electron mobility, μ_n (at room temperature)	(cm^2/V s)	1350	1000	500	950
Hole mobility, μ_p (at room temperature)	(cm^2/V s)	480	40	80	120
Relative dielectric constant, ε_r	(adim)	11.9	9.7	10	10

Table 1.1. Electrical properties of Si and SiC [7].

As can be seen from Table 1.1, the high sustainable electric field, the high thermal conductivity, the high carriers' saturated velocity and the high bandgap, it causes the silicon carbide to be a suitable material for high power, high temperature and high frequency applications, and for the realization of a visible blind photodetector.

1.2.1 Wide bandgap: many advantages

The energy bandgap is the minimum energy required to excite an electron from the valence band to the conduction band. The SiC wide bandgap gives it many fundamental properties that make it more suitable for certain applications. One of the typical semiconductors' problem is the intrinsic temperature. This temperature is very important because if it is exceeded, the semiconductor becomes intrinsic again and the device fails, since no longer exists a PN junction exists anymore. Furthermore, the thermal energy, due to lattice vibrations, can create electron-hole pairs also at room temperature. Therefore, if the temperature becomes very high, the number of generated may exceed the number of the carriers obtained from the doping process, and lead the device to become intrinsic again. For example, silicon has an intrinsic temperature of about 300 °C, while, for 4H-SiC, since its bandgap is about three times the silicon one, the intrinsic temperature raises to about 1000 °C (the exact value of the instrinsic temperature depends on the polytype and the doping). This gives to the silicon carbide an advantage in terms of high temperature operations.
Another advantage related to the wide bandgap is the high performance in the UV optical detection. Obviously, it is obtained that, for its bandgap, the SiC is completely "blind" and cannot detect the low energy light, i.e. photons having high wavelengths (that is to say,

e.g., the visible range). However, it should be remembered that the SiC is an indirect gap material such as silicon (i.e., the wave vector of the minimum of the conduction band does not coincide with the maximum of the valence band one), which makes it inefficient in terms of optical emission [7].

A third advantage descending from the wide bandgap is the ability to withstand at high electric fields without triggering the avalanche multiplication (i.e the breakdown operation). In fact, by defining ε_i as the threshold ionization energy (the minimum energy required to trigger the impact ionization), in the simple case of parabolic valence and conduction bands described by the equation $\varepsilon = \hbar^2 k^2 / 2m^*$, it can be shown that [9,10]:

$$\varepsilon_{ie} + \varepsilon_{ih} = 3\varepsilon_g \tag{1.1}$$

where ε_{ie} and ε_{ih} are respectively electrons and holes threshold ionization energies, and ε_g is the bandgap energy. In accordance with the eq. (1.1) it is obtained that, unlike the silicon, where a field of about 0.25 MV/cm is necessary to accelerate the carriers and to trigger the impact ionization phenomenon, in SiC this happens at a value at least ten times greater than the previous (typical value of breakdown electrical field is about 2 MV/cm). This makes SiC well suited for power applications that require to sustain high breakdown voltages. The critical electric field plays a fundamental role in the determination of the breakdown voltage. In fact, considering a P^+/N^- junction and the case of a NPT structure (non-punch-through) where an electric field's triangular profile is assumed, recalling that the depletion region extends primarily within the little doped region, where an uniform doping is assumed, it is obtained that:

$$V_{BR} = \frac{E_C W}{2} \tag{1.2}$$

where V_{BR} is the breakdown voltage, E_c is the critical electric field and W is the depletion width. The Eq. (1.2) suggests that, if the same V_{BR} is considered, it is possible obtain the same breakdown voltage with a N^- region ten times smaller, or it is possible to obtain a breakdown voltage ten times greater with the same W. Furthermore, given that the same breakdown voltage is obtained with a ten times thinner depletion region, this is translated into a lower specific on-state resistance and, therefore, in a lower static power dissipation in this low doped region. In fact, it is possible to state that:

$$W \approx \sqrt{\frac{2\varepsilon V_{BR}}{qN_D}} \qquad \rightarrow \qquad N_D = \frac{2\varepsilon V_{BR}}{qW^2} = \frac{\varepsilon E_C^2}{2qV_{BR}} \tag{1.3}$$

while the specific on-resistance $R_{on\text{-}sp}$ into this low doped region is:

$$R_{on-sp} = \frac{W}{q\mu_n N_D} = \frac{4V_{BR}^2}{\varepsilon \mu_n E_C^3} \tag{1.4}$$

Therefore, reasoning for a fixed breakdown voltage, comparing SiC with Si, the N⁻ region doping can be increased one hundred times and the thickness can be reduced ten times, also obtaining an on-resistance one thousand lower.

Obviously, it has to be taken into account that the electrons mobility μ_n and the relative dielectric constant ε_r of the SiC are lower than Si, which translates in an effective reduction of the on-resistance (compared to silicon) between 200 and 400 times, depending on the polytype.

Another important SiC's property is the thermal conductivity, 2-3 times higher than the silicon one. The high thermal conductivity gives it a high capacity to carry and transfer the heat. This is a fundamental property in power and high-frequency electronics, where large heat amounts are produced on the chip (because of the large power density involved in the process). Of course, the heat has to be effectively disposed, both to avoid the device performances degradation, and the device failure [8]. In fact, according to Eq. (1.5):

$$\Delta T = \theta \frac{t}{\lambda} \tag{1.5}$$

ΔT is the temperature increase at the junction, θ is the thermal flow, t is the device thickness and λ is the thermal conductivity. Setting a certain thickness, and assuming the same temperature increase at the junction, given that the SiC thermal conductivity is three times larger than in silicon, a thermal flow three times larger is obtainable.

One last important SiC's property is the ability to work in high-frequency applications. This property descends from the fact that, for the same breakdown voltage of a Si device, the SiC device can be made smaller. Obviously, this results in the advantage of having a faster device, since the signal must travel a shorter distance. Also, since the SiC relative dielectric constant is lower than Si one, the parasitic capacitances will be smaller, since the capacitance is directly proportional to it.

1.2.2 Models of electrical parameters of SiC

In this section the electrical models of SiC will be presented. This models will be also included in the next simulations.

1.2.2.1 Intrinsic carrier concentration

For any intrinsic semiconductor the electrons concentration is equal to the holes concentration, and this is called *intrinsic concentration*. Through the mass-action law $np = ni^2$, and taking into account the temperature dependence, it is possible to demonstrate that the intrinsic concentration is:

$$ni = \sqrt{N_C N_V} \left(\frac{T}{300}\right)^{\frac{3}{2}} \exp\left(-\frac{E_g}{k_B T}\right) \tag{1.6}$$

where E_g is the bandgap energy in eV, T is the temperature in K, N_c and N_V are, respectively, the effective density of states in the conduction and in the valence band in cm^{-3}, and k_B is the Boltzmann constant (8.6173324×10^{-5} eV K^{-1}). In particular, for the 4H-SiC, it is possible to calculate the N_C, N_V and E_g, as the temperature changes, by the following formulas [11]:

$$N_C = 3.25 \ 10^{15} \ T^{\frac{3}{2}} \qquad (1.7)$$

$$N_V = 4.8 \ 10^{15} \ T^{\frac{3}{2}} \qquad (1.8)$$

$$E_g = E_g(0) - 6.5 \ 10^{-4} \ \frac{T^2}{T + 1300} \qquad (1.9)$$

where $E_g(0)$ is the energy bandgap at $T = 0$ K (about 3.26 eV) [11]. Using Eq. (1.7), (1.8) and (1.9) the SiC intrinsic concentration at different temperatures was obtained (see Figure 1.3). It is compared with the Si intrinsic concentration [76].
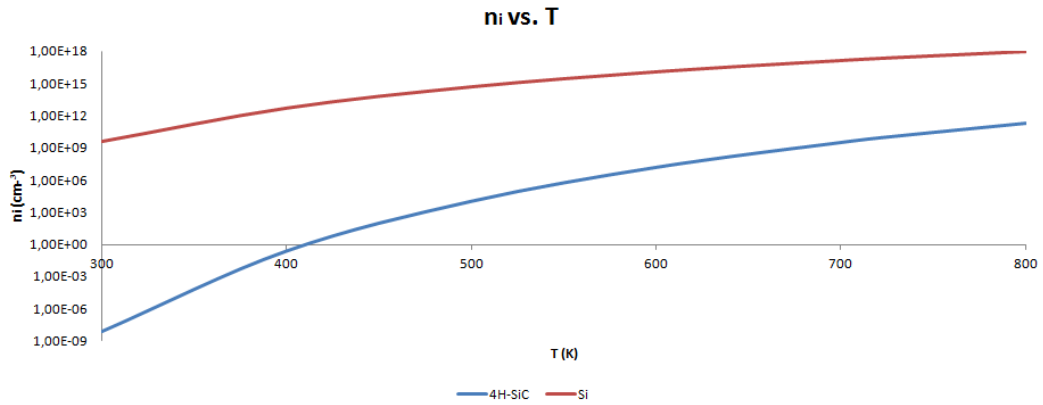
Figure 1.3. Intrinsic carrier concentration at different temperatures.

As can be seen from Figure 1.3, the SiC intrinsic concentration is much lower than Si intrinsic concentration at room temperature, also showing an exponential with negative exponent. This property, as will be subsequently shown, is of considerable importance if the SiC must be used in "sensing" applications, since the reverse current (also known as dark current) is directly proportional to the intrinsic concentration. SiC's devices have less sensitivity to the temperature increases if compared with silicon devices.

1.2.2.2   Mobility model

The carriers mobility (both electrons and holes) is defined as the modulus of the drift velocity divided for the drift electric field to which they are subject:

$$\mu_{n,p} = \frac{|v_{n,p}|}{E} \qquad (1.10)$$

where *n* and *p* subscripts are, respectively, for electrons and holes. Eq. (1.10) is used to simply describe as the free carriers moving within the lattice when an electric field is applied from the outside. In fact, there are several scattering mechanisms that act reducing the mean free path of the carriers. They are optical and acoustic scattering, scattering by neutral and ionized impurities, scattering with vacancies or dislocations in the lattice, and scattering with the surface [8].

Assuming that a single isotropic scattering process takes place, the mobility can be derived as follows:

$$\mu_{n,p} = \frac{q \, \tau_{n,p}}{m^*_{n,p}} \tag{1.11}$$

where *q* is the carrier charge (1.6×10^{-19} C), $\tau_{n,p}$ is the relaxation time (it describes the average time between two successive scattering events), and $m^*_{n,p}$ is the effective carriers mass, that is different from the mass m_0 (mass in vacuum) subject only to external stresses. In the effective mass the potential effects associated to the lattice are also included, and, therefore, this parameter depends on the band in which the carrier is located.

Obviously, since the scattering mechanisms can act all simultaneously, the total mobility will be determined from a combination of the various mobilities relative to each scattering mechanisms. Through the use of the Matthiessen rule for the collision times, it is possible to calculate the mobility associated to different independent causes in the following way:

$$\frac{1}{\mu_{n,p}} = \sum_i \frac{1}{\mu^i_{n,p}} \tag{1.12}$$

where $\mu_{n,p}$ is the actual mobility and the index *i* identifies the mobility due to the *i*-th independent cause of scattering.

In fact, since $\mu \propto \tau$ and $\tau \propto 1 / (\textit{probability of scattering})$, it is possible to write the above rule or in terms of mobility or of collision times (the formula expression does not change [12]). To understand just why the total mobility is calculated using this empirical law, just keep in mind that this law follows a law in which the bigger parameter is the dominant one in the process. In fact, if there are only two causes of scattering we obtain $1/\tau = 1/\tau_A + 1/\tau_B$, or $1/\mu = 1/\mu_A + 1/\mu_B$, where μ_A is the mobility that the material would have if there is only the A scattering cause, and no other source scattering, and μ_B is the mobility that the material would have if there is only the B scattering cause, and no other source scattering. In fact, if both causes act, the total mobility is reduced. Instead, if the cause A does not acts, the mobility for this scattering cause becomes theoretically infinite, and, therefore, the total mobility will depend only on the B cause. Vice versa if B cause is not present.

The low-field mobility of the 4H-SiC can be modeled using the Lindefelt's model, based in turn on the Arora's model [13], which allows to describe the mobility dependence on the temperature and doping, without taking into account the electron-hole scattering, as follows [14]:

$$\mu_{n,p}(T,N) = \mu_{n,p}{}^{min} + \frac{\mu_{n,p}{}^{delta} \left(\frac{T^*}{T_0}\right)^{\alpha_{n,p}}}{\left(1 + \frac{N_D + N_A}{N_{n,p}{}^\mu}\right)^{\gamma_{n,p}}}$$

(1.13)

where the parameters in Eq. (1.13) are summarized in the Table 1.2.

Parameter	Unity	Value
$\mu_n{}^{min}$	(cm²/V s)	0
$\mu_p{}^{min}$	(cm²/V s)	15.9
$\mu_n{}^{delta}$	(cm²/V s)	1141
$\mu_p{}^{delta}$	(cm²/V s)	108.1
$N_n{}^\mu$	(cm⁻³)	1.94×10^{17}
$N_p{}^\mu$	(cm⁻³)	1.76×10^{19}
γ_n	(adim)	0.61
γ_p	(adim)	0.34
α_n	(adim)	-2.15
α_p	(adim)	-2.15

Table 1.2. Lindefelt's model parameters.

When high electric fields are present, the mobility does not grow linearly with the applied electric field (because $v_{drift} = \mu E$), due to the high phonon scattering. In fact, in this case the carriers drift velocity tends to saturate at the v_{sat} value (2×10^7 cm/s in 4H-SiC), involving a mobility saturation.
The high-field mobility follows the Caughey-Thomas model [15]:

$$\mu_{n,p}(E) = \frac{\mu_{n,p}{}^{low}}{\left[1 + \left(\frac{\mu_{n,p}{}^{low} E}{v_{sat}}\right)^\beta\right]^{\frac{1}{\beta}}}$$

(1.14)

where both β and v_{sat} are temperature dependent:

$$\beta = \beta_0 \left(\frac{T}{T_0}\right)^{\beta_{exp}}$$

(1.15)

$$v_{sat} = v_{sat0} \left(\frac{T}{T_0}\right)^{-v_{sat-exp}}$$

(1.16)

where $\beta_0 = 2$, $\beta_{exp} = 0$, $v_{sat0} = 2.5{\times}10^7$ cm/s and $v_{sat-exp} = 0.5$ both for electrons and holes (for more details see Appendix).

Figure 1.4 shows the high-field mobility trends as a function of doping, both for electrons and for holes [8,15].
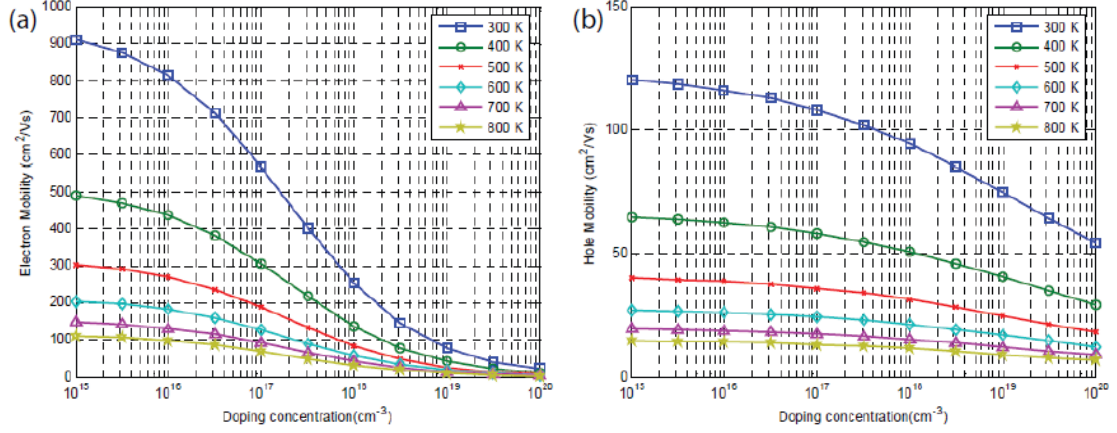
Figure 1.4. High-field mobility trends for 4H-SiC as a function of doping, for electrons (a) and holes (b) [15].

1.2.2.3 Mechanisms of generation and recombination

Generation and recombination phenomena occur when the semiconductor is not at the thermodynamic equilibrium (in this condition the mass action law $np = n_i^2$). In particular, when the carriers concentration is much greater than the equilibrium one (i.e. $np > n_i^2$), the system tends to return to the equilibrium condition through a recombination mechanism. Vice versa, when the carriers concentration is much lower than that of equilibrium (i.e. $np < n_i^2$), the system tends to return to the equilibrium condition through a generation mechanism.

In SiC, as for any indirect bandgap semiconductor (where both the direct generation and direct recombination processes, i.e. band-to-band processes, are highly unlikely), the recombination process is mainly due to the *Shockley-Read-Hall* (SRH) recombination (both in the bulk and at the surface) and the *Auger recombination*. The SRH process takes place via intermediate centers, called *recombination centers* or *traps*, whose energy level are located inside the bandgap. These traps, due to the presence of impurities or defects, in the crystal lattice, can capture an electron (or a hole) temporarily from the conduction band (or valence band), ensuring its recombination with hole (or an electron) from the valence band (or conduction band), as represented in Figure 1.5a [8].
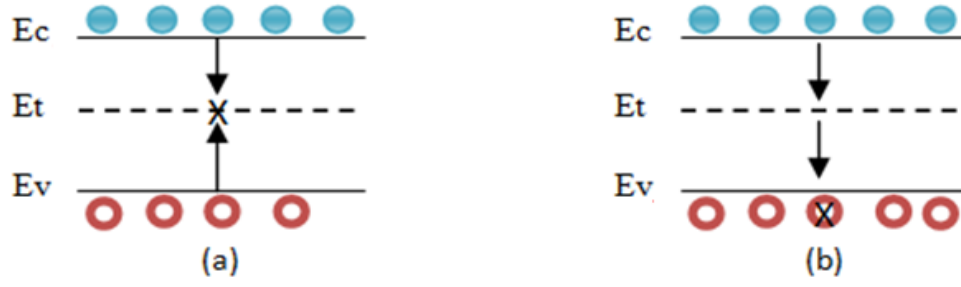
Figure 1.5. SRH recombination processes. (a) An electron that falls from the conduction band is captured by a trap, where it recombines with a hole coming from the valence band. (b) An electron that falls from the conduction band is captured by a trap, and then it decays in the valence band where it recombines with a hole.

Obviously, recombination can also occur when an electron falls from the conduction band and it is captured by a trap. It then decays in the valence band where it recombines with a hole (see Figure 1.5b).

The bulk net recombination rate U ($U=R-G$, where R and G are respectively the recombination and the generation rates) is given by:

$$U_{SRH} = \frac{np - n_i{}^2}{\tau_p(n + n_1) + \tau_n(p + p_1)} \tag{1.17}$$

where $\tau_{n,p}$ are the electrons and holes lifetime respectively. The lifetime are fundamental parameters in the recombination process, since it represents the average time after which the carrier disappears undergoing recombination. They also depend from temperature, defects concentrations, doping type and concentration, and material [8]. Instead, n_1 and p_1 are given by:

$$n_1 = n_i \exp\left(\frac{E_T - E_i}{k_B T}\right) \tag{1.18}$$

$$p_1 = n_i \exp\left(\frac{E_i - E_t}{k_B T}\right) \tag{1.19}$$

If $E_t = E_i$, i.e. it is considered that the capture probability of a hole is the same of the capture of an electron, it is possible to say that the maximum U is equal to:

$$U_{SRH} = \frac{np - n_i{}^2}{\tau_p(n + n_i) + \tau_n(p + n_i)} \tag{1.20}$$

The value of U can tell if a recombination or generation process is going on. In fact, if $pn > n_i^2$, $U > 0$, and then recombination prevails. Vice versa, if $pn < n_i^2$, $U < 0$, and then generation prevails. Obviously, what has been said for the recombination, it is also applicable to the generation process. If energy is provided to the system, a trap can capture an electron that moves from the valence band to the trap, leaving a hole in the valence band; or, providing energy to an electron trapped, making it leaves the trap level and

12

passes in the conduction band, thus generating an electron in the conduction band (see Figure 1.6).
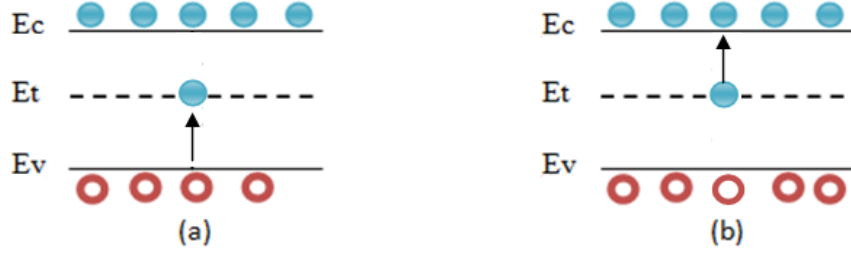
Figure 1.6. SRH generation processes. (a) An electron is trapped at Et level with the generation of a hole in the valence band. (b) An electron trapped at Et level, passes from Et to Ec, generating an electron in the conduction band.

In a similar way it is possible to describe the generation-recombination surface process. The only difference regards U, defined in Eq. (1.17), where the recombination rates $s_{n,p}$ depending on doping appear, instead of the electrons and holes average life time [8]:

$$U_{SRH,surf} = \frac{np - n_i{}^2}{\frac{1}{s_p}(n + n_1) + \frac{1}{s_n}(p + p_1)} \tag{1.21}$$

The Auger generation-recombination occurs when the resulting energy from the recombination of an electron and a hole, following a band-to-band transition, is provided to another electron (or hole), which will be excited to a higher energy level (or lower) within the conduction band (or valence band). This means that this mechanism is a process that involves three carriers. The *net recombination velocity* is described by the following equation [8]:

$$U_{Auger} = (C_n n + C_p p)(np - n_i{}^2) \tag{1.22}$$

where $C_n = 5 \times 10^{-31}$ cm^{6}s^{-1} and $C_p = 2 \times 10^{-31}$ cm^{6}s^{-1} in 4H-SiC.

After the interaction, the third carrier, normally, loses the acquired energy transferring it to the lattice in the form of thermal vibration. If this energy is high enough, it can generate another electron-hole pair due to ionizing collision with the lattice. For example, when the energy carriers are due to the acceleration produced by a high-intensity electric field in the semiconductor, Auger generation mechanism is called *impact ionization mechanism* (since the excess in energy of the third carrier can trigger an impact ionization mechanism inside the semiconductor). In the Figure 1.7 are represented the Auger generation-recombination processes.
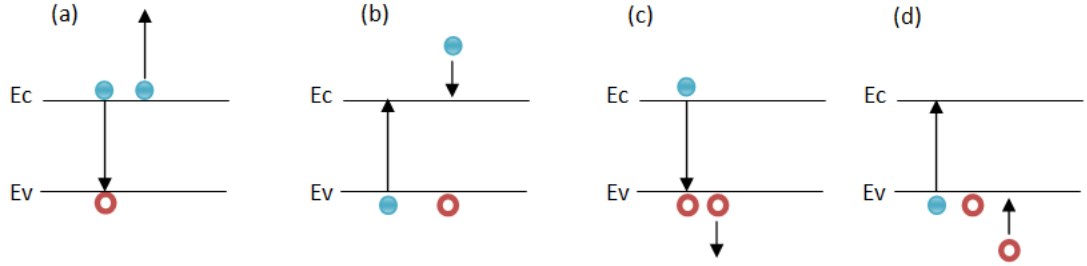
Figure 1.7. Auger Processes. (a) eeh recombination. (b) eeh generation. (c) ehh recombination. (d) ehh generation.

Finally, the electrons and holes generation rate G_i due to impact ionization, is given by the following expression [16]:

$$G_i = \alpha_{A-n}\, n\, v_n + \alpha_{A-p}\, p\, v_p \tag{1.23}$$

where $\alpha_{A\text{-}n}$ and $\alpha_{A\text{-}p}$ are, respectively, the electron and hole ionization coefficients (they represent the reciprocal of the mean free path of the carriers), v_n and v_p are the electron and hole drift velocity respectively, and n and p are the concentrations of electrons and hole respectively (it is important remembers that $(n,p)\, v_{n,p} = |J_{n,p}|/q$, where $J_{n,p}$ are, respectively, the electrons and holes current densities). When the impact ionization phenomenon takes place it is possible, to obtain G_i, to use the *Okuto-Crowell's model* [17], which allows to derive the electrons and holes ionizations coefficients, taking into account both the dependences on the electric field F and on the temperature T, as shown in the following equation:

$$\alpha_A = A\left(1 + B(T - 300)\right) F \exp\left(-\left[\frac{C(1 + DT - D300)}{F}\right]^2 \right) \tag{1.24}$$

where A, B, C, and D are the fitting parameters shown in the Table 1.3.

Parameter	Unity	Value for electrons	Value for holes
A	V^{-1}	3.25×10^5	3.25×10^5
B	K^{-1}	-3.29×10^{-2}	-3.29×10^{-2}
C	V/cm	1.71×10^7	1.71×10^7
D	K^{-1}	0	0

Table 1.3. Okuto-Crowell parameters for 4H-SiC [18].

1.2.2.4   Incomplete ionization

When a semiconductor is doped, at room temperature the dopant atoms will be totally or partially ionized according to the relationship between impurities levels (remembering that E_A and E_D depend on dopant type, acceptor or donor) ant the thermal energy ($k_B T$) [8]. If the impurities levels are not superficial (they are also known as *Shallow impurities,*

because they require little energy to ionize, typically around the thermal energy or even less), but are *deeper* (they are also known as *Deep impurities*, because they are impurities that require energies larger than the thermal energy to ionize and, therefore, only a fraction of the impurities present in the semiconductor contribute to the number of free carriers), one has to take into account the incomplete ionization of the dopant. Typically, it is assumed that an impurities level is *deep* if it is far from the valence, or conduction, band for an energy ≥ 150 meV. To model the incomplete ionization of dopants, such as boron, aluminum, nitrogen and phosphorus, are used the following expressions [16]:

$$N_D{}^+ = \frac{N_D}{1 + g_D \exp\left(\frac{E_C - E_D}{k_B T}\right) \exp\left(\frac{E_F - E_C}{k_B T}\right)} \tag{1.25}$$

$$N_A{}^- = \frac{N_A}{1 + g_A \exp\left(\frac{E_A - E_V}{k_B T}\right) \exp\left(-\frac{E_F - E_V}{k_B T}\right)} \tag{1.26}$$

where $N_D{}^+$ and $N_A{}^-$ are the ionized donor and acceptor impurity concentrations (i.e. the electrons and holes impurity concentrations, respectively), N_D and N_A are the donor and acceptor impurity concentrations, g_D and g_A are the degeneracy factor of donors and acceptors, respectively, that are assumed equal to 2 and 4, E_A and E_D are the acceptor and donor energy levels, respectively, E_C and E_V are the low conduction band and the high valence band energy level, E_F is the Fermi energy level, k_B is the Boltzmann's constant, and T is the temperature in K. Furthermore, E_C-E_D and E_A-E_V represent the ionization energies of the donor and acceptor atoms, respectively. The incomplete ionization (that is a big problem in SiC) seriously afflicts the device behavior, bacause it also strongly depends both from the temperature and the doping (for example, a problem can be the strong increase of the bulk resistance).

1.2.2.5   Bandgap narrowing

Although in the simulations that will be shown later, the bandgap narrowing effect will not be included, for completeness it is right to include it within the SiC electrical properties. The bandgap narrowing phenomenon consists in a reduction of the bandgap, and it occurs when the doping levels are very high ($> 10^{19}\, cm^{-3}$). In fact, in this case, due to the large number of donor levels just below the conduction band edge (if one refers to the case of n-type doping), it is like there is a lowering of the E_c level, with a consequent E_g reduction. It must be observed that, if the bandgap reduces, the intrinsic concentration grows a lot compared to the usual value (for a fixed temperature), because it is inversely proportional to E_g, through an exponential dependence. The high doping effect can be modeled, in the energy bands diagram, with the occurrence of an occupied energy band that partially overlaps the conduction band, in the case of a high n-type doping (see Figure 1.8b), or the valence band, in the case of a high p-type doping.
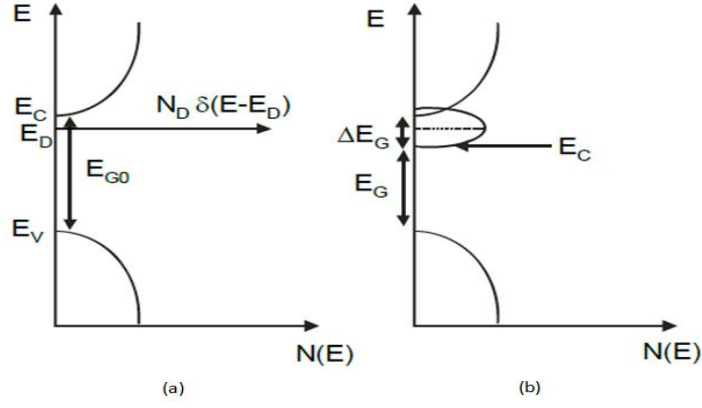
Figure 1.8. (a) Density of states of a non-degenerate doped semiconductor, i.e. where the bandgap narrowing does not take place. (b) Density of states of a degenerate doped semiconductor, i.e. where the bandgap narrowing occurs.

The bandgap narrowing, as well as on the doping, also depends on the temperature, and can be modeled through the displacement of the lower limit of the conduction band and the upper limit of the valence band with the following equations [8,19]:

$$\Delta E_c = A_{nc} \left(\frac{N_D^+}{10^{18}} \right)^{1/3} + B_{nc} \left(\frac{N_D^+}{10^{18}} \right)^{1/2} \tag{1.27}$$

$$\Delta E_v = A_{nv} \left(\frac{N_D^+}{10^{18}} \right)^{1/4} + B_{nv} \left(\frac{N_D^+}{10^{18}} \right)^{1/2} \tag{1.28}$$

for a n-type semiconductor, and from the following expressions for a p-type semiconductor [8,19]:

$$\Delta E_c = A_{pc} \left(\frac{N_A^-}{10^{18}} \right)^{1/3} + B_{pc} \left(\frac{N_A^-}{10^{18}} \right)^{1/2} \tag{1.29}$$

$$\Delta E_v = A_{pv} \left(\frac{N_A^+}{10^{18}} \right)^{1/4} + B_{pv} \left(\frac{N_A^+}{10^{18}} \right)^{1/2} \tag{1.30}$$

In the Table 1.4 the parameters values of the Eq. (1.27) - (1.30) required for the band edges displacements (in eV) for n-type and p-type 4H-SiC semiconductor are summarized.

Parameter	Unity	Value
A_{nc}	eV cm	-1.5×10^{-2}
B_{nc}	eV cm$^{3/2}$	-2.93×10^{-3}
A_{nv}	eV cm$^{3/4}$	1.9×10^{-2}
B_{nv}	eV cm$^{3/2}$	8.74×10^{-3}
A_{pc}	eV cm	-1.57×10^{-2}
B_{pc}	eV cm$^{3/2}$	-3.87×10^{-4}
A_{pv}	eV cm$^{3/4}$	1.3×10^{-2}
B_{pv}	eV cm$^{3/2}$	1.15×10^{-3}

Table 1.4. Parameters to calculate the band edge diplacements in n-type (the values with subscript *n*) and p-type (the values with subscript *p*) 4H-SiC [19].

1.3   Optical properties of 4H-SiC

The optical properties of a material are crucial to understand how it behaves when it interacts with light, and to understand what are the effects that light produces in the semiconductor after the interaction. To this end, in this paragraph some 4H-SiC basic optical parameters, such as complex refractive index, absorption coefficient and penetration depth will be shown.

1.3.1   Light absorption

As known from quantum mechanics, the light energy is emitted from the bodies in the form of discrete quantities of energy, known as "*quantum*" (thanks to Max Planck). In particular, with the introduction of the quantum of light, proposed by Albert Einstein with the study of the photoelectric effect (i.e. the electron emission from the surface of a metal when struck from an electromagnetic radiation), the idea that the same electromagnetic radiation, as well as the light, was made up of quantum, called *photons*, introduced assumptions that becomes necessary to describe the energy exchange between light and matter. As known, the energy E associated at a quantum of frequency v is equal to:

$$E = h\,v = h\,\frac{c}{\lambda} \tag{1.31}$$

where h is the Planck constant (6.626×10^{-34} J s $= 4.135\times10^{-15}$ eV s, remembering that 1eV $= 1.602\times10^{-19}$ C), c is the light speed (3×10^{8} m/s) and λ is the wavelength in *m*. The Eq. (1.31) encloses the dual nature of light. In fact, from the interaction with the material the corpuscular nature of light emerges. It consists of a set of photons each of which has quantized energy E. Instead, in the propagation, the wave nature emerges, characterized from a wavelength λ and a frequency v.

But, what happens when a photon interacts with a semiconductor? To understand this, one must take into account the energy band diagram of the semiconductor.

The photon absorption by a semiconductor causes the generation of an electron-hole pair. According to the theory of particle nature of light, a photon is not always absorbed by the

semiconductor, but this happens if and only if the photon impacts on the semiconductor with a certain energy (or wavelength, as noted by. Eq. 1.31). All depends upon a fundamental parameter value, namely the bandgap E_g. There are three distinct situations according to the relationship between the photon energy E_{ph} and the amplitude of the bandgap E_g: $E_{ph} < E_g$, $E_{ph} = E_g$ and $E_{ph} > E_g$. In the first case, the photon's energy is not enough to excite an electron from the valence band to the conduction band, and thus the light is not absorbed and passes through the semiconductor without interacting with it (see Figure 1.9a). Instead, both in the second and in the third case, the photon is absorbed by the semiconductor, creating an electron-hole pair (see Figure 1.9b and Figure 1.9c).
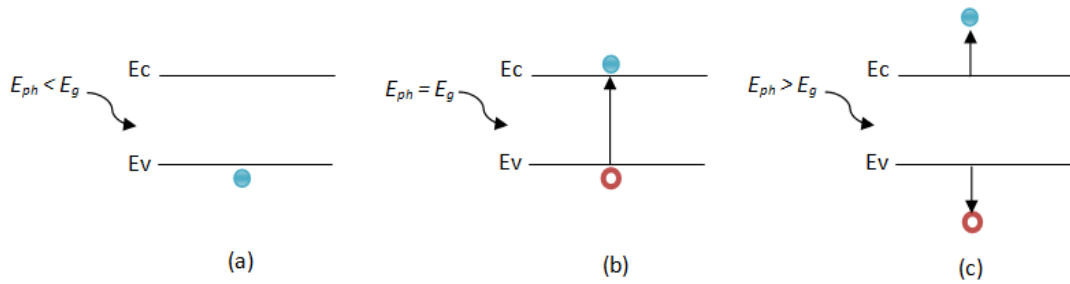
Figure 1.9. Possible cases of light absorption. (a) The photon with energy lower than the bandgap is not absorbed from the semiconductor. (b) The photon with energy equal to the bandgap is efficiently absorbed. (c) The photon with an energy higher than the bandgap is not efficiently absorbed.

It is important to stress that the absorption, which takes place when the photon energy is equal or greater than the bandgap energy, not always occurs in an efficient way. In fact, if a photon is absorbed with an energy equal to E_g, it generates an electron-hole in an efficient way, since it will transfer to the electron an energy exactly equal to the bandgap potential energy to make the jump from the valence band to the conduction band. On the other hand, if the photon comes with an energy greater than the bandgap (i.e. $E_{ph} = E_g + \Delta E$), it will be absorbed but it will transfer the excess in kinetic energy $\Delta E = E_{ph} - E_g$. This excess tends to lead the electron to higher levels within the conduction band. This excess in energy is not useful for photo-conversion (since that the maximum output power is related to the bandgap energy), and it is lost as heat, i.e. it is dissipated via *Joule effect* (this phenomenon goes under the name of *Thermalization*). Then, in the first case, the incident power is completely lost. In the second case, the incident power will be absorbed as efficiently as possible, assuming that each useful photon generates an electron-hole pair, because all the incident power is actually converted into electrical power output. In the third case, part of the incident power will be converted into electrical power output, and part will be converted into heat.

Obviously, the dissipated heat has to be monitored and, if it is possible, drained because when the temperature rises it strongly degrades the performances of the device. This effect in the case of the SiC is however quite limited, due to its excellent thermal capacity, compared to a silicon device. In fact, in the short wavelength absorption (with the absorption of photon with high energy), this problem can be serious. The SiC, instead, is able to solve this problems.

The 4H-SiC (like any other semiconductor), cannot absorb all the wavelengths of the electromagnetic spectrum, but only a portion of it. To estimate which is the critical wavelength λ_c, beyond which the 4H-SiC does not absorb, one must refer to Eq. (1.31), considering the photon energy expressed in eV:

$$E = \frac{1.24}{\lambda}$$

(1.32)

where E is the photon energy expressed in eV and λ is the wavelength in μm.
From Eq. (1.32) follows that, considering that the 4H-SiC bandgap is 3.22 eV (using Eq. 1.9), at room temperature, the critical wavelength is:

$$\lambda_c = \frac{1.24}{3.22} = 0.3846 \ \mu m = 384.6 \ nm$$

(1.33)

In fact, this justifies why the silicon carbide, and in particular the 4H-SiC (with its wide bandgap), is one of the most suitable semiconductor to work in UV detection (remembering that the ultraviolet occupies the portion of the electromagnetic spectrum that extends from 10 - 400 nm), resulting, also, completely "blind" to the visible spectrum (see Figure 1.10).
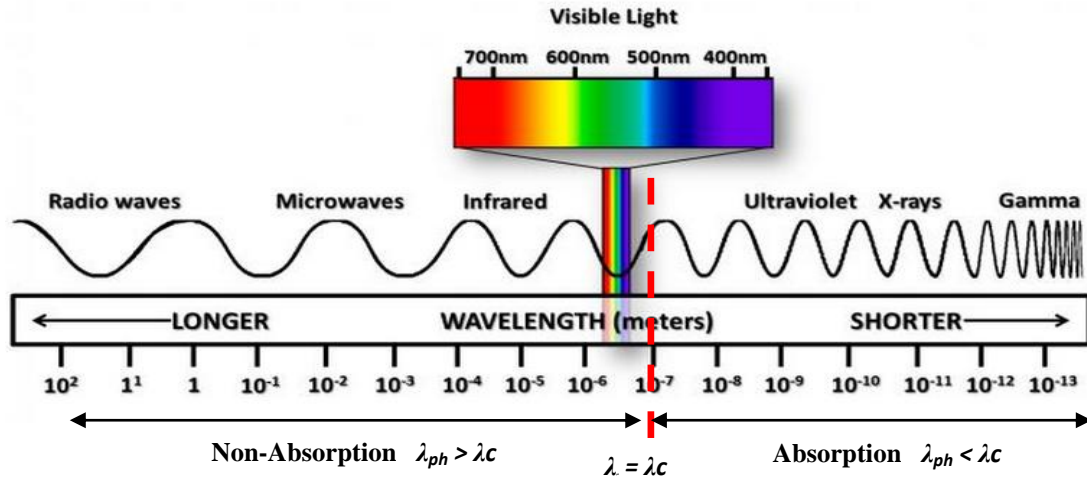
Figure 1.10. Portion of the electromagnetic spectrum absorbed from 4H-SiC.

1.3.2   Complex refractive index

When an electromagnetic radiation travels in the vacuum, it travels at maximum speed, namely the speed of light c. Instead, when the light penetrates in a different material than the vacuum, the radiation continues its propagation with a lower speed related to the speed in the vacuum by the refractive index n. The refractive index of a material is a dimensionless quantity that allows to quantify the propagation speed reduction of an electromagnetic radiation passing through a material. Furthermore, in addition to the

reduction of the propagation speed, one should take into account how the electromagnetic wave varies its propagation direction due to the refraction phenomenon.

The refractive index *n* is defined in the following way:

$$n = \frac{c}{v} \tag{1.34}$$

where *c* is the light speed (3×10^8 m/s) and *v* is the electromagnetic wave speed in the material. Approximating, it is possible to assume a constant refractive index, equal to the value that it assumes at a certain wavelength. For example, for the 4H-SiC, it is typically assumed equal to 2.68461 at a wavelength of 0.5 μm [20].

But, in general, the refractive index is a function of the light frequency (being $c = \lambda f$) because it is dependent on the wavelength. Furthermore, a medium is dispersive if the permittivity depends from the frequency.

The material dispersion is a physical phenomenon that causes the separation of a wave in different spectral components with different wavelengths, due to the dependence of the wave phase velocity by the wavelength in the medium (remember that the phase velocity, for a material without losses, is equal to $\frac{\omega}{\beta} = \frac{\omega}{\omega \sqrt{\varepsilon \mu}} = \frac{1}{\sqrt{\varepsilon \mu}}$). For this reason, in general, the materials do not exhibit a refractive index equal for all monochromatic waves which constitute a generic polychromatic incident beam. Consequently, the deviation of the radiation crossing the material, with a certain wavelength, can be measured evaluating the refractive index of that material for the given wavelength.

The wavelength dependence of the refractive index is usually quantified using empirical formulas, as the *Cauchy's equation* (the relation between the refractive index and the wavelength is also known as *Dispersion Formula*).

This equation is used to determine the light dispersion in the medium and has the following formulation:

$$n(\lambda) = A + \frac{B}{\lambda^2} \tag{1.35}$$

where *A* and *B* are coefficients that can be determined fitting the above equation to the measured refractive indices for known wavelengths.

For 4H-SiC the *Cauchy's equation* becomes [11]:

$$n(\lambda) \cong 2.5610 + \frac{3.4 \ 10^{-2}}{\lambda^2} \tag{1.36}$$

where $A = 2.5610$, $B = 3.4 \times 10^{-2} \ \mu m^2$ e λ is the wavelength in μm.

Moreover, for most of the transparent materials, the refractive index regularly decreases increasing the wavelength, i.e. $\partial n / d\lambda < 0$.

In fact, starting from Eq. (1.36) and differentiating it with respect to λ, it is possible to obtain:

$$\frac{\partial n}{\partial \lambda} \cong -\frac{6.8\ 10^{-2}}{\lambda^3} \tag{1.37}$$

For the 4H-SiC this value is -0.546 μm^{-1} (this trend is also known as *Chromatic dispersion*; see Figure 1.11 [20]).
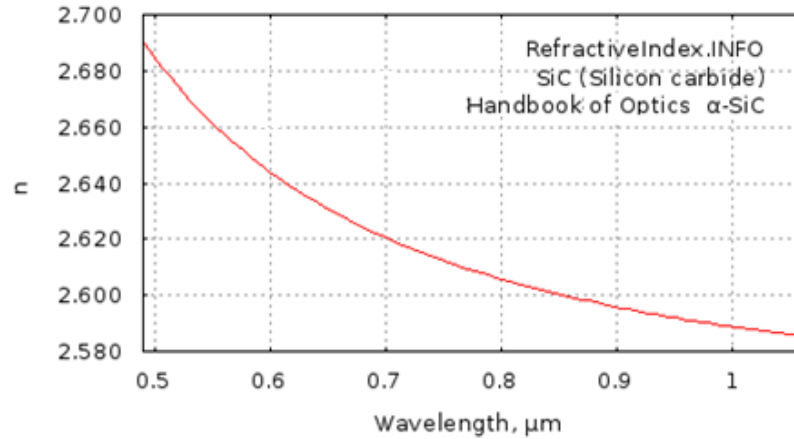
Figure 1.11. Refractive index of α-SiC versus wavelength [20].

The refractive index defined up to now only allows to study how an electromagnetic wave deflects its trajectory passing from one medium to another thanks to *Snell's law* applied at the interface between the two materials with different refractive index. *Refraction* is the phenomenon that occurs when light, or in general an electromagnetic wave, passes through the separation surface between two transparent substances to the considered wavelength. In fact, in this case, the incident ray undergoes a deviation from its original direction. This study requires the *Snell's law* use, where the refraction index is used.

However, when a material presents *absorption*, it is no longer possible to describe the refractive index with a real number. Now, it is necessary to define a *complex refractive index*, defined as follows:

$$\tilde{n} = n + i\,k \tag{1.38}$$

where the real part *n* is still called *refractive index*, while the imaginary part *k* is called *extinction coefficient*, and both vary with the wavelength. As will be shown later, the imaginary part of the complex refractive index will quantify the *light absorption* inside the material.

Through the *Ellipsometry* it is possible to derive both the real part (see Figure 1.12) and the imaginary part (see Figure 1.13) of the complex refractive index of 4H-SiC [21]. The *Ellipsometry* is an optical technique that allows to investigate the optical properties of a thin-film material, such as the complex refractive index, through the analysis of the reflected light polarization arising from the material. With this technique it is also possible

to obtain other useful properties of the material under test, such as crystalline nature, doping concentration and electrical conductivity.
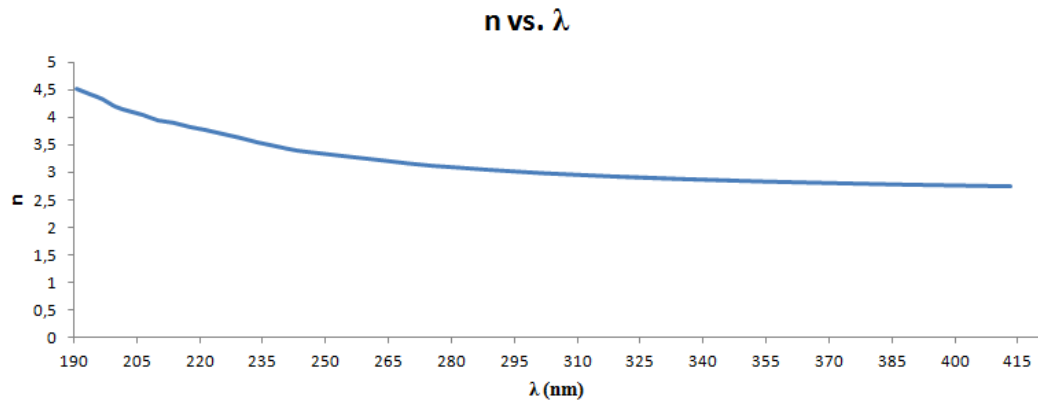
Figure 1.12. Real part of 4H-SiC complex refractive index.
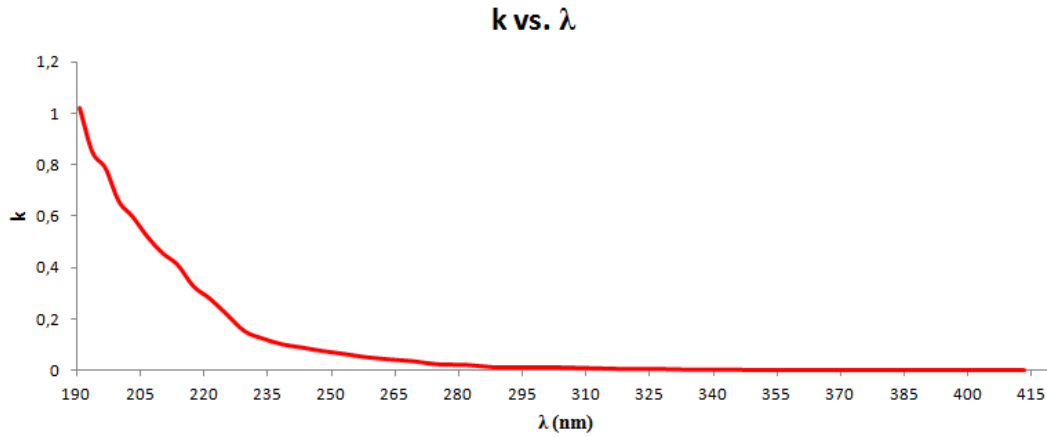
Figure 1.13. Imaginary part of 4H-SiC complex refractive index.

1.3.3   Absorption coefficient

The *absorption* is the ability of a material to absorb the energy associated to the electromagnetic radiation that propagates within it [22]. When a medium is *perfectly transparent* to the passage of light (or a generic electromagnetic wave), it allows the passage of radiation through it without changing the intensity of the incident radiation (i.e. the radiant energy that enters is equal to the leaving one). When a material is instead *absorbent*, the energy emerging from the medium is lower than that which enters, or, in the case of an *opaque* material, is reduced to be practically zero.

Through an empirical relationship, known as the *Lambert-Beer's law*, it is possible to evaluate the light amount absorbed by a medium, based on the nature and the thickness of the medium. In fact, when a monochromatic light beam of intensity I_0 passes through a medium of thickness d, a part of it is absorbed by the medium itself, and the other part is transmitted, with residual intensity equal to I_1.

The Lambert-Beer's law states that:

$$I_1 = I_0 e^{-\alpha d}$$

(1.39)

where α is the *absorption coefficient* of the material in cm^{-1}, and d is its thickness in cm. Starting from the light beam intensity, that equal to the number of photons of a given wavelengths (or photons flux Φ/cm^2) which passes through a unit cross section of a sample in time unit, it is possible to evaluate the luminous power density associated to that particular wavelength as follows:

$$P = \Phi \frac{h\,c}{\lambda}$$

(1.40)

where Φ is the photons flux in *photons/s*, P is the luminous power density associated at a particular wavelength in W/cm^2, and $\frac{h\,c}{\lambda}$ is the photon energy in J.

This relation is useful because, starting from the Eq. (1.39), multiplying both terms for the photon's energy, a relation similar to the Eq. (1.39) is obtained. Now, the relation between the optical incident power on the upper surface of the material and the light power that leaves the lower surface of the material, with a thickness d, is considered [9]:

$$P(d) = P_{inc}\, e^{-\alpha d}$$

(1.41)

where P_{inc} is the optical incident power density on the top surface and $P(d)$ is the light power density that leaves the lower surface. Hence, to quantify the material ability to absorb photons of energy equal to hv (and, therefore, to generate carriers, as shown later), one has to evaluate the absorption coefficient α.

It is possible to demonstrate that the absorption coefficient is related to the imaginary part of the complex refractive index using the following equation [9]:

$$\alpha = \frac{4\,\pi\,k}{\lambda}$$

(1.42)

where k is the imaginary part of the complex refractive index and λ is the wavelength in cm. In Figure 1.14 the absorption coefficient α in cm^{-1} obtained for 4H-SiC is shown. It was calculated starting from k values shown in Figure 1.13.
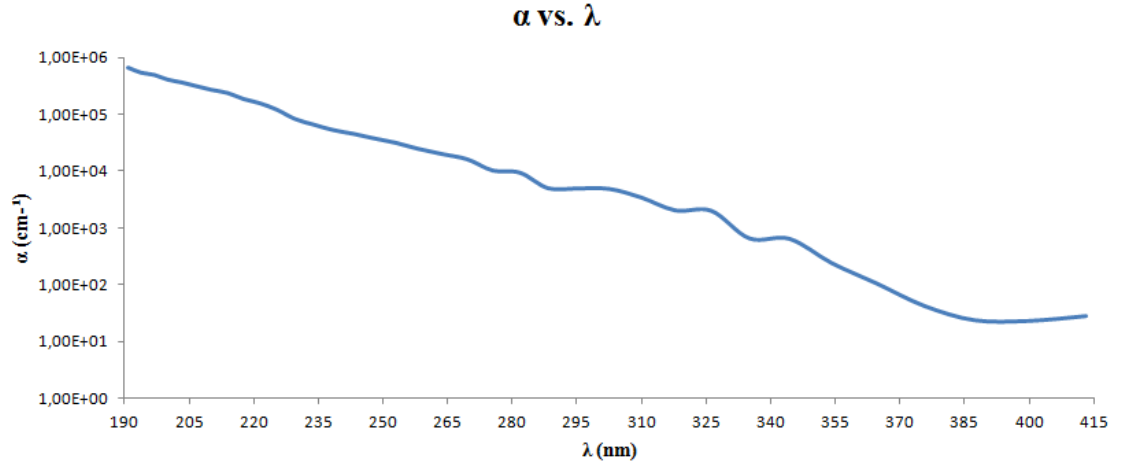
Figure 1.14. Absorption coefficient of 4H-SiC in log-scale.

1.3.4   Absorption depth

When an electromagnetic radiation strikes the material surface, a part of it can be reflected, while the other part is transmitted through the material. For the transmitted light, according to the nature of the material, and the wavelength of the radiation, the electromagnetic field can travel very deep within the material itself, or it can drop very quickly to zero near the surface. To obtain a measure of how deep the light can penetrate a parameter known as *absorption depth* is used.

The absorption depth is defined as the distance from the surface (or depth) for which the incident power (or radiation intensity), and then the number of photons, at a certain wavelength, is reduced by *1/e* (or, approximately, of 37 %) compared to the its initial value at the surface.

Therefore, in accordance with the Beer-Lambert's law of the Eq. (1.39), generalizing for a distance z from the surface, the electromagnetic wave intensity, within a material, decays exponentially starting from the initial value at the top of the surface. If the penetration depth is indicated with δ, according to its definition, it is obtained that:

$$I(z) = I_0 e^{-\alpha z} \qquad \rightarrow \qquad I(\delta) = I_0 e^{-\alpha \delta} = \frac{I_0}{e} \qquad \rightarrow \qquad \delta = \frac{1}{\alpha} \qquad (1.43)$$

where I_0 is the light intensity on the top surface, α is the absorption coefficient and δ is absorption depth in μm.

Then, from the α values in Figure 1.14, it was obtained the 4H-SiC absorption depth with the wavelength variation, as shown in Figure 1.15.
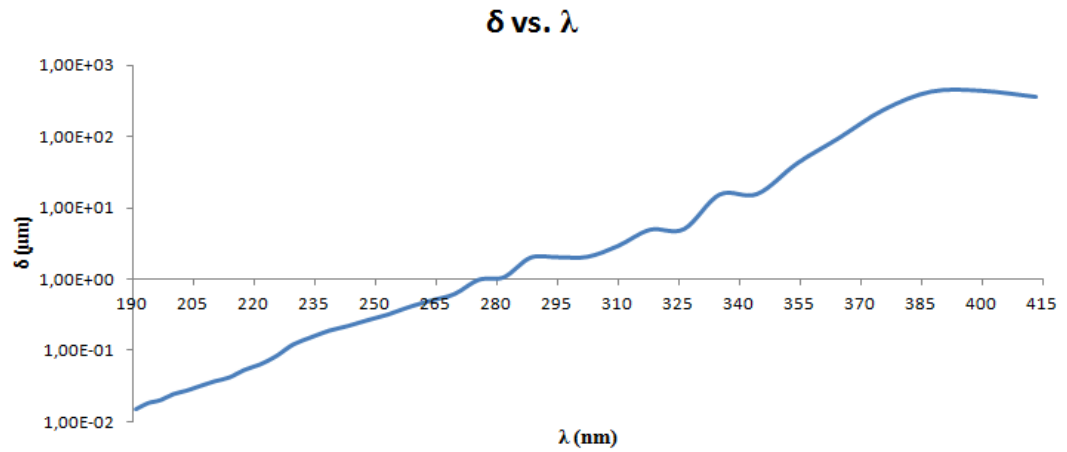
Figure 1.15. 4H-SiC absorption depth in log-scale.

Figure 1.15 suggests, therefore, that in 1 µm of 4H-SiC material, it is possible to absorb almost all the portion of the spectrum of interest.

Chapter 2

Image sensor: 4H-SiC implementation

2.1   Ultraviolet photography for Venus investigation

The human eye visible range belongs to the portion of the electromagnetic spectrum between 400 and 700 nanometers. In the typical photography, in fact, this is the spectrum of the radiation that is used. However, there is a large light amount in the electromagnetic spectrum that the human eye cannot see, despite this it brings a considerable amount of interesting information. There is another band of the electromagnetic spectrum, the UV band, which extends from 10 to 400 nm. The ultraviolet band is divided into four sub-bands: UVA, which extends from 400 to 320 nm (also called long-wave UV or black light), UVB, which extends from 320 to 280 nm (also known as medium wave), UVC, which extends from 280 to 100 nm (also called short-wave), and VUV, that extends from 100 to 10 nm (also called vacuum ultraviolet).

The ultraviolet light, tends to interact with the materials in an unique way due to its short wavelength, because it tends to be reflected by many materials, making possible to display the surface topology of an object, without that light penetrates it. This reflected UV light can be absorbed (or detected) from some materials, like the 4H-SiC. In fact, because of its short wavelength, it is easily scattered by surface features (e.g. surface scratches) that cannot be detected with long wavelengths. This allows the possibility to solve even smaller features of an object surface. For this property the UV light is used, especially, when one is not able to obtain detailed information regarding an object, that cannot be obtained with the classical photography methods. For example, one of the major fields of application for the ultraviolet radiation is the archaeological photography, where is of great interest the revelation of colors, images, signs that have survived despite the passage of time, the degradation level of an ancient object because of the humidity, the detection of hidden cracks, the verifying the authenticity of an artifact, etc.

In fact, there are two ways to use ultraviolet radiation to take pictures: *reflected ultraviolet* and *ultraviolet fluorescence photography*. The first technique is used in medical or criminological field or to detect scratches on a surface, that are not easily detectable in the visible or IR range, because shorter wavelengths tend to undergo a stronger scattering due to the surface compared with longer wavelengths. This technique relies on the use of two UV lamps (these act as radiation sources) that directly illuminate the object, and through the use of a sensitive camera in the UV band, the UV light reflected from the surface of the object is recovered (obviously, the sun is an UV source to do UV photo). Furthermore, in this case, necessary filters are applied to filter the possible visible light, and to allow the passage of the only UV light. It is important to underline that, during the process, the wavelength does not change.

The second technique is applied in the archeological field, and it consists in the illumination of the object surface with UV light. This time, the signal is not detected in the UV band, but in the infrared (IR) or in the visible band. In fact, the fluorescent material absorbs UV radiation and re-radiates at a longer wavelength, for example in the visible. In this case, however, it is important to note that, unlike the first technique, the presence of reflected light is not taken into account. Diffused light will be considered instead.

The solar radiation is the first UV source that can be used to do an UV photo for planet investigation. Obviously, if the quantity of UV radiation is reduced (for atmosphere absorption), the lander can be provided of lamps integrated inside it, using the techniques above shown.

This considerations suggests that ultraviolet photography can be of great help for the detailed investigation of a planet's surface, such as Venus. In fact, it is not surprising that one of the first detailed Venus' surface images, captured by the NASA's Pioneer Venus Orbiter, launched in 1978, are false color images implemented using ultraviolet images of the planet Venus (even if in this photo the clouds were investigated via UV light, and not the surface). It is shown in Figure 2.1. This technique consists in elaborated images taken originally in black and white or filtered on specific wavelengths, and recombine them to simulate the effective coloring.
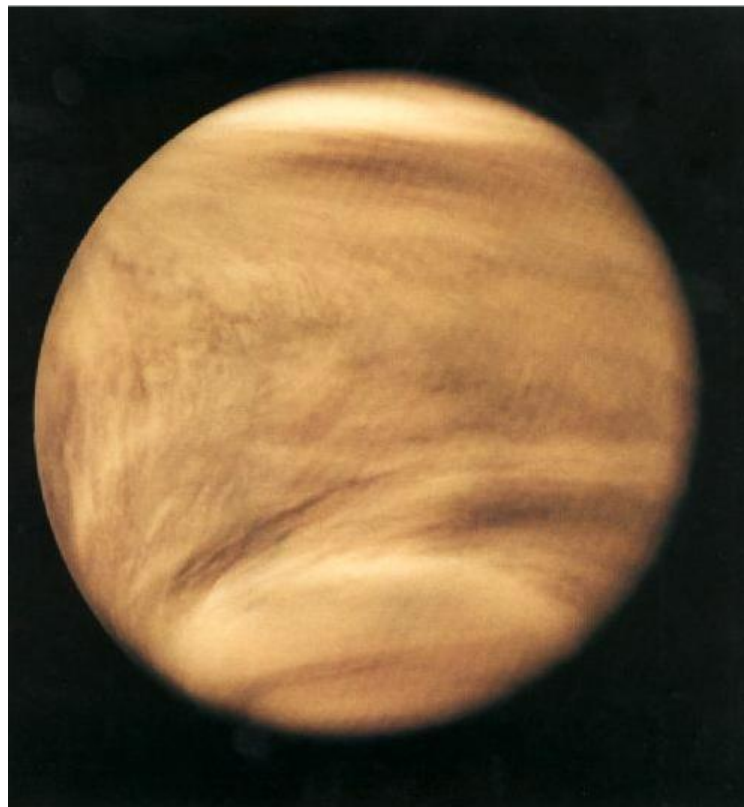
Figure 2.1. One of the first ever close up photograph of Venus, captured by NASA's Pioneer Venus spacecraft. It's actually a false color image made from ultraviolet images of the planet [73,74].

Moreover, one must remember that the sun is the best source of free UV radiation (employable for UV photography), but the quantity and the quality of the UV radiation that

reaches the planet depends on the weather's conditions. For example, a bright and dry day is preferable to one cloudy and rainy day, because in the first case there is, theoretically, a greater amount of UV radiation available. The Venus' atmosphere, formed mainly of carbon dioxide, it is much more dense than Earth's one. In addition, the density and the composition of the atmosphere creates a massive greenhouse effect on the surface which makes it the hottest planet in the solar system .

Venus is shrouded by a thick layer (about 20 km) of highly reflective clouds, composed primarily of sulfuric acid. This high amount of water vapor also prevents the passage of visible light, but allows the passage of the ultraviolet radiation only and in particular of UVB and UVA (that are however attenuated because of the thick layer of clouds [28]). This is why the best way to investigate the Venus' surface is through the use of UV photography. It has to be considered, also, that the pressure on Venus is extremely high (about 90 atmospheres, i.e. 90000 hPa) and it could also lead to doubts on the sensor being able or not to resist to it. Another problem is related to the corrosive Venus' atmosphere. However if the sensor will be integrated inside the lander, and, therefore, with a proper protection, this should not be a serious problem.

2.2 CMOS image sensor: basic operation and pixel characterization

In this section the basic concepts of the operation of a CMOS sensor will be presented, focusing on the *pixel* structure and operation. The *pixel* is the smallest element of the *image*, characterized by a certain position, color and intensity on the sensor. The attention will be focused on the possible implementation in 4H-SiC, in order to answer to requests made in the previous chapter. For the implementation process the same realization process of current silicon CMOS image sensors will be considered.

2.2.1 CMOS image sensor: overview

The CMOS image sensors are integrated electronic semiconductor devices, capable of capturing an image when they are exposed to light (photons), and then to manipulate and convert the voltage signal produced into a digital signal that will be processed downstream by other devices (for example a monitor, TV, etc.). CMOS technology is a relatively new technology, developed as an alternative to CCD (Charge Coupled Devices) that is already present from many years. The main difference that exists between the two technologies is about how the stored charge in the pixel itself is read, once the sensor has been exposed to light.

For the CCD technology the charge to be read is shifted pixel by pixel, after being collected in the pixels. The charge is finally collected at the output, where it will be actually converted into an analog voltage. Therefore, to read an entire row, in a certain position, first you need to discharge all the lines under it, and then read the one of interest.

In this operation a shift register is also present, shown in black in Figure 2.2, which can contain an entire row at a time.

Instead, for CMOS sensors the charge-voltage conversion immediately occurs within the pixel, and, thereafter, this voltage is transferred to the output using a suitable column bus, to be suitably amplified and converted into digital output (see Figure 2.2).
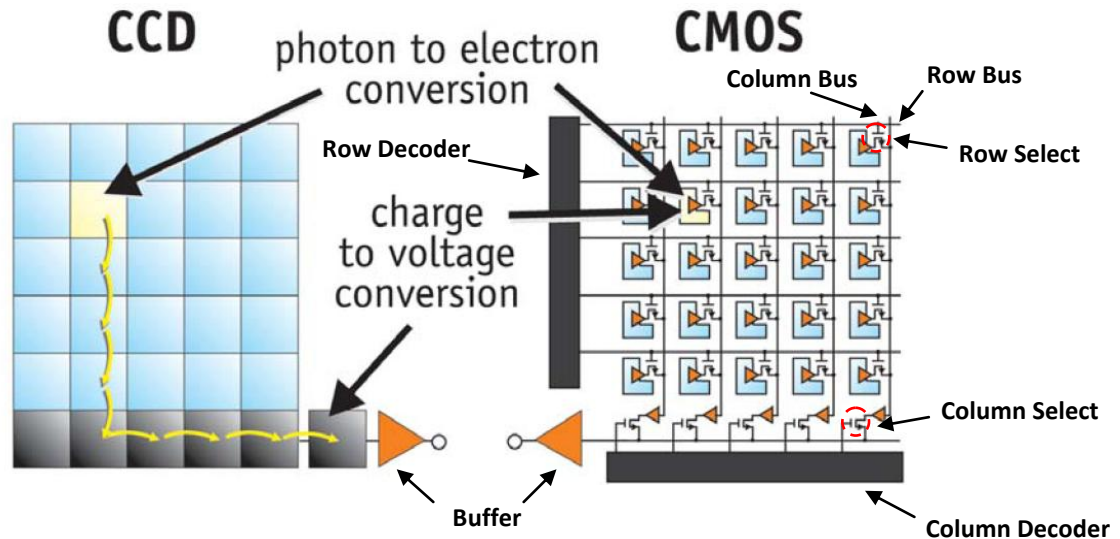
Figure 2.2. CCD Technology versus CMOS Technology.

The main differences, between the two technologies, are collected in Table 2.1.

CMOS	CCD
Low cost of manufacture	*Mature technology and optimized*
High integration capacity	*Low dark current*
Low power consumption	*Low complexity of the sensor*
Random access	*Photodiode output: Charge domain operation*
High complexity of the sensor	*Chip Output: Voltage (Analog)*
Single external clock and single external power supply	*Low Presence of noise*
High velocity	*High uniformity*
Photodiode output: Voltage	*High color accuracy*
Chip Output: Bit (Digital)	
Moderate presence of noise	
Low / Moderate uniformity	
Medium color accuracy	

Table 2.1. Main differences between the CMOS and CCD silicon technology.

Despite CCD technology is a mature technology on the market, for astronomical and space applications, nowadays a lot of companies are moving on the CMOS technology for space applications, for the low cost of manufacture. Moreover, the pixel structure and the pixel operation of a CMOS image sensor are easier than CCD technology. In fact, in the CCD

technology potential wells to collect the photogenerated carriers and a gate electrodes series are required. For this, in the following, the CMOS structure will be taken into account. Furthermore, this will be the first 4H-SiC CMOS image sensor proposed for UV photo at high temperature that will be investigated for space applications.

Figure 2.3 shows a block diagram of a CMOS sensor.
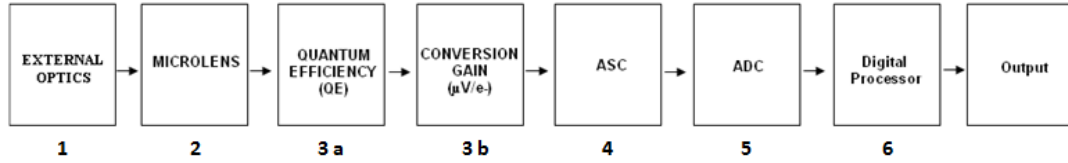
Figure 2.3. CMOS Imager Block diagram.

The following is a brief description of each block of the block diagram presented in Figure 2.3:

1- An external converging biconvex lens produces a flip image of the real object. Every object's point in the scene has an image that can be obtained as the intersection of three optical rays, one passing through the centre of the lens, and therefore not deviated from the lens itself, one parallel to the optical axis, which will pass through the fire "f" of the lens (or the "focal plane"), and a third ray that crosses the other fire, closer to the object, that will be diverted along the optical axis (see Figure 2.4).
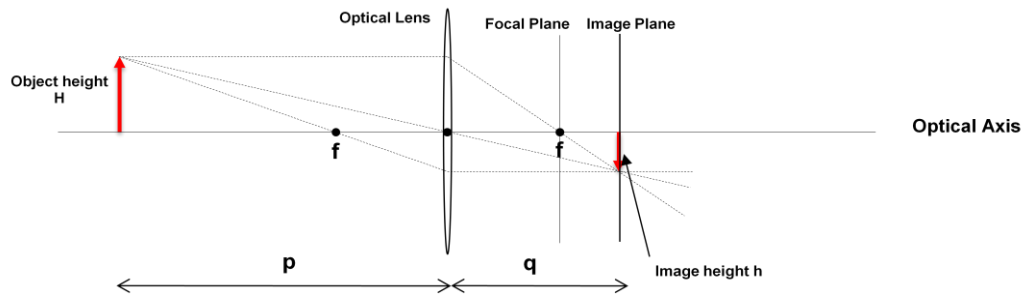
Figure 2.4 Image capture.

Calling p, the distance between the object and the lens, q the distance between the lens and the image, h the image height and H the object height, the focus f and the enlargement I can be calculated with the following formulas:

$$\frac{1}{f} = \frac{1}{p} + \frac{1}{q} \qquad\qquad I = \frac{h}{H} = \frac{q}{p} \qquad\qquad (2.1)$$

Of course, in Figure 2.4, it is possible to note that if the sensor is out of the *image plane* (that is the plan that contains all the image points of the object), then each image point on the sensor will not be a point, but a halo of diameter d, and in this case it will referred to as *blurred object* (see Figure 2.5). In fact, the so called focusing process is realized moving the lens to bring the object image to coincide with the sensor position,

whose relative position related to the object is fixed. In this way, each object point, as expected, will be seen as a point by the sensor.
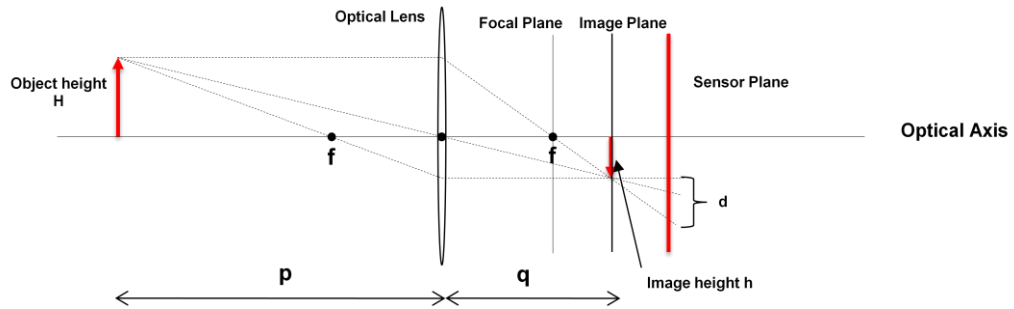
Figure 2.5 Image capture with blurred object.

Then, for the property of converging lenses, it is possible to get a *real* image on the sensor plane. However the image is flipped upside-down, both horizontally than vertically. In fact, for the correct representation on a monitor, the sensor must be read with a readout circuit that is able to read starting from the last row, in the lower right and then read one line at a time from the bottom, moving from right to the left for increasing columns indices, since the monitor reconstructs the image from the top left to the bottom right.

2- When light strikes the pixel, to convert this signal into an electrical signal, via the photo conversion phenomenon, one must take into account that a part of the light could not be used, with a consequent loss of the useful signal and the image quality. In fact, in the sensor the light sensitive area is only a part of the total area of the pixel. There is a parameter, the *Fill Factor*, which describes the ratio between the actual light sensitive area and the pixel total area. This happens because a part of the area of each pixel is used by transistors, electrodes, or registers, that belong to the pixel structure itself. For this reason *microlenses* are used having the same size of a single pixel, to maximize the photons amount that arrives on each individual photodiode, by making the rays, that otherwise would be lost, converging on the same. This technique allows a large increase in the *Quantum Efficiency* of the photodiode, which will be responsible for the photo-conversion, at parity of Fill Factor (see Figure 2.6).
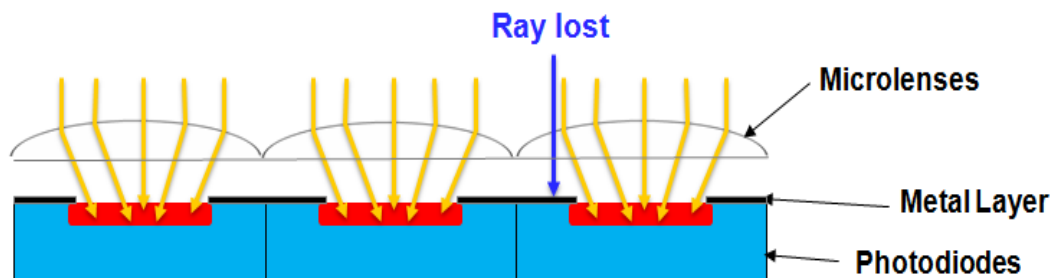
Figure 2.6 Microlenses system. The blue ray would be lost without the presence of microlenses.

In fact, in a typical CMOS imager, the microlenses system, presented above, works correctly only if the rays are normally incident (i.e. perpendicular) on the sensor's surface. Indeed, for the property of converging lenses, the rays that are parallel to the lens' optical axis converge at a point of the axis that is the "focus" f. However, when the rays come from the edges of the scene, they will not be parallel to the optical axis, but they are oblique incident on the pixels at the edge of the sensor. Instead the rays that arrive on the central part of the sensor are normally incident. This means that the alignment is not optimal to the photodiodes. They will be however focused, by the lens, in a non-optimal position, and this means moving from the center to the edges of the sensor the output signal will always be weaker. This cause a not uniform brightness of the scene, with a quality loss of the image at the edges. This problem becomes more significant when the lenses have a very small focus and, therefore, are not far away from the sensor plane. This phenomenon goes under the name of *vignetting*. In this case, the microlenses should be slightly moved from the initial position (i.e. that of perfect overlap with the pixel below), making sure that also the oblique rays can correctly arrive on the area of pixels (see Figure 2.7).
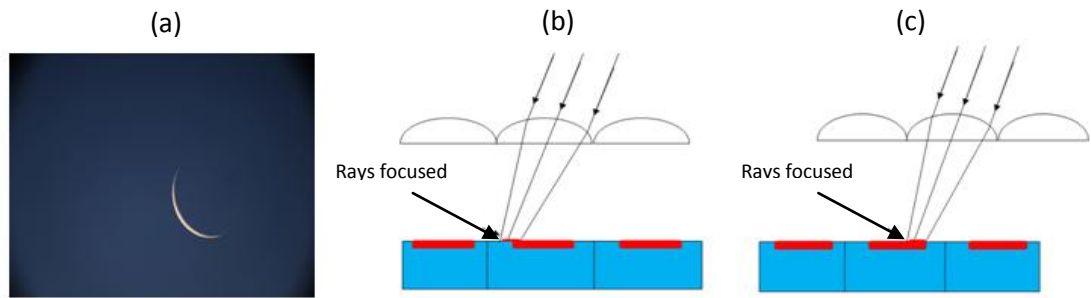
Figure 2.7. (a) Photo of the moon suffering from Vignetting. (b) Vignetting cause. (c) Vignetting problem solution.

3- The photoconversion, i.e. the conversion of light energy (absorbed in the form of photons) into electrical energy, occurs through the use of the pixel itself, and in particular of the photosensitive part, the *photodetector*. The photodetector will be described in detail in the next paragraph. The pixel is schematically shown, in the block diagram in Figure 2.3 (blocks 3a and 3b). Nevertheless these are represented with two separate blocks, it is the same pixel that performs all and two operations at the same time.

4- This part of the description of the operation of the CMOS sensor goes far beyond the scope of this thesis, but for completeness at least an outline is provided on how the downstream of the pixel is treated.
Once exposed to light, at the output of the pixel will be present a certain analog voltage proportional to the amount of collected light. Via the Row Select (see Figure 2.2), the output of the pixel is connected to a vertical *bus*, common to all the pixels of a same column. The column goes to end up inside a *Readout* circuit (it is also known as *ASC*, which stands for *Analog Signal Chain*, see Figure 2.8), where the pixel output voltage is

compared with a reference voltage, typically the same *Reset Voltage* (which will be discussed later in the detailed analysis of the operation of a pixel), and amplified by a certain gain *K* that depends on how has been designed the amplifier, as shown in Figure 2.8.
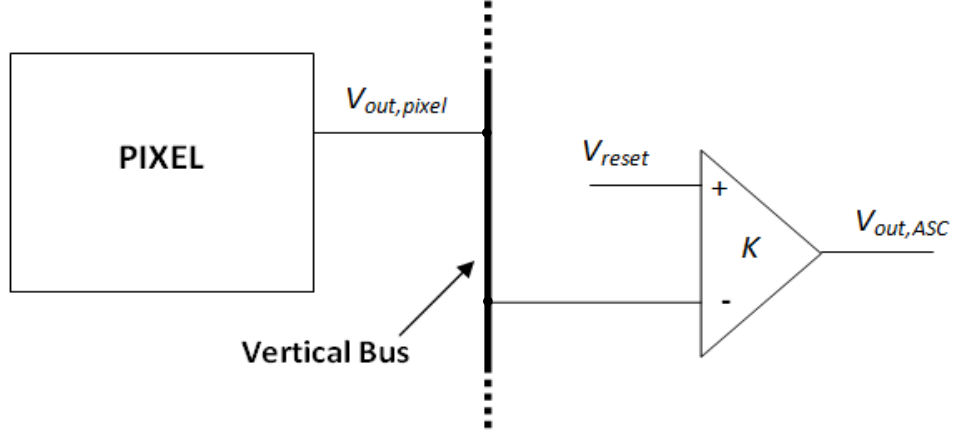
Figure 2.8. Readout circuit.

If everything works correctly, at the output of the amplifier should be measured a voltage equal to:

$$V_{out,ASC} = K\left[V_{reset} - (V_{reset} - \Delta V)\right] = K\,\Delta V \qquad (2.2)$$

where ΔV is the video signal of interest and V_{reset} is the reset voltage. In real applications, the presence of a noise, which goes under the name of *reset noise*, causes a change in the pixel voltage read out. This source of noise is caused either by the reset voltage being it not stable over time, and by the channel resistance of NMOS (inside the structure of pixels) that suffers the presence of *thermal noise*, also known as *Johnson noise*. The thermal noise is produced in any real dissipative system (like a resistance) which is at a different temperature from absolute zero, and it is due to the fluctuation of carriers within the conductor element. This noise manifests with a small voltage over the resistor that randomly varies over time. This is a problem because this voltage could be interpreted in a wrong way (in terms of color) since it is seen as an output signal produced by the pixel itself. Hence, after the reset operation, the voltage across the photodiode will not be exactly equal to the reset voltage supply, but it will be a random value equal to $V_{reset} + V_{noise}$ (where V_{noise} is the voltage that models the reset noise). Therefore, after light exposure, the pixel output cannot have a value of $V_{reset} - \Delta V$, but of $V_{reset} + V_{noise} - \Delta V$, and following the same analysis reported in Eq. (2.2), it is possible to state that:

$$V_{out,ASC} = K\left[V_{reset} - (V_{reset} + V_{noise} - \Delta V)\right] = K\left(\Delta V - V_{noise}\right) \qquad (2.3)$$

From Eq. (2.3) it is clear that the video signal of interest is highly corrupted. For this reason, it is introduced a double *Sample & Hold* circuit (S&H). It samples in two instants immediately following one another across the photodiode. First it samples the voltage across the photodiode with superimposed the reset noise, before light exposure. Second it samples the voltage across the photodiode, always with superimposed the noise but, this time, after the light exposure, in a way that the voltage is reduced of an amount equal to ΔV (equal to the discharge of the junction capacitance of the photodiode).
In this way it is possible to obtain:

$$V_{out,ASC} = K \left[(V_{reset} + V_{noise}) - (V_{reset} + V_{noise} - \Delta V) \right] = K \, (\Delta V) \qquad (2.4)$$

In particular, the two sampled voltages, by S&H circuit, are applied to the comparator and amplifier input, via the Column Select (CS), controlled by the Column Decoder (see Figure 2.2). Figure 2.9 shows a full schematic of a *Readout circuit*.
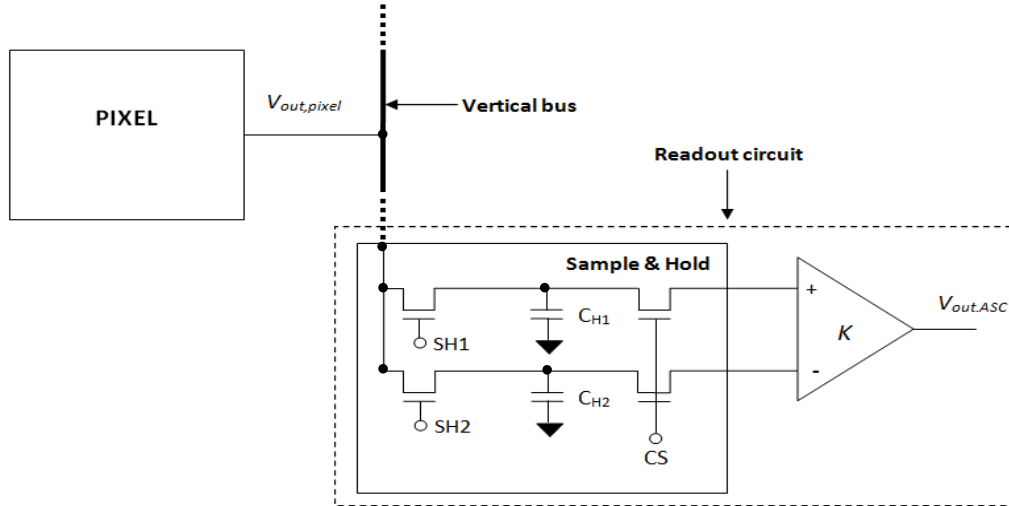
Figure 2.9. Readout circuit with double S&H and comparator and amplifier.

Referring to Figure 2.9, when the signal *SH1* is high and *SH2* is low, a voltage equal to $V_{out, pixel} = V_{reset} + V_{noise}$ will be read and stored across the capacitor *CH1*. Instead, when the signal *SH2* is high and *SH1* is low, a voltage equal to $V_{out, pixel} = V_{reset} + V_{noise} + \Delta V$ will be read and stored across the capacitor voltage *CH2* (assuming that in that moment the photodiode was illuminated, and then an electrical signal in output has been produced). At this point, when the *CS* signal (Column Select) becomes high, the voltages stored on the capacitors are applied at the amplifier input, which calculates the difference and amplifies it of a *K* factor. This voltage available at the amplifier output is sent to the Analog/Digital converter downstream.
Finally, it is important to emphasize that all the internal control signals are managed by an appropriate *control/processing unit* in the sensor, the implementation of which goes beyond the scope of this thesis.

5- The ADC (*Analog to Digital Converter*) is needed to transform an analog signal such as that received as input from the readout circuit, into a digital output of N bits. For example, let us consider a N bits ADC, which receives an analog signal in input, with a maximum excursion equal to V_{max}. Then, this analog input range, which extends from 0 to V_{max}, will be divided into 2^N zones, each of amplitude equal to $q = V_{max}/2^N$, where each of them will be associated at a certain digital word. Therefore, each analog voltage that falls into one of these areas, will be transformed into a specific word of N bits. There are different types of converters commonly used, including the *Flash converter* (also called *direct-converter*), *successive approximation*, *pipeline*, *tracking* converter and even more, whose detailed operation, in addition to the analysis of the classic errors committed by the same (*non-linearity error*, *gain error*, *offset error*, *quantization error*, etc.), are not the object of this thesis.

Figure 2.10 shows a description of the operation of an ADC.
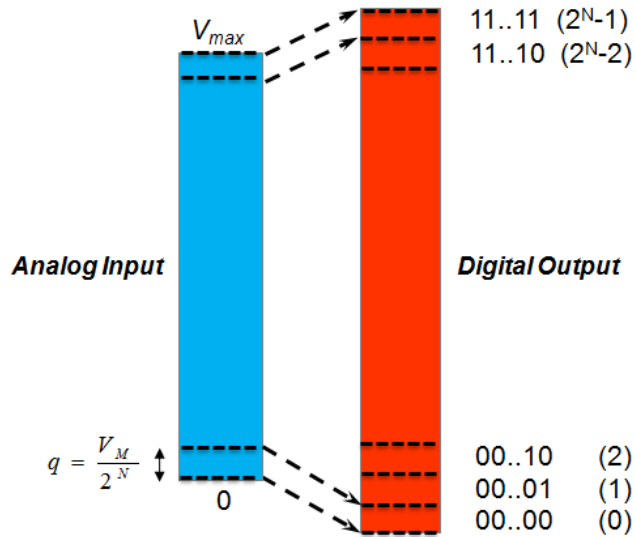
Figure 2.10. ADC conversion scheme.

6- The last block, present in Figure 2.3, represents the part of the digital logic of the sensor needed to perform the *Digital Signal Processing* (i.e. the so-called *Digital Manipulation*), including the *Color Processing* and *Image Enhancement*. All the digital logic of the sensor is a *SOC* type (*System on Chip*), which is an integrated circuit on a single chip containing an entire system (i.e., in addition to the central microprocessor, necessary for the whole part of processing and control, it integrates also the RAM memory, a clock generator, various peripheral circuits, power management circuitry, etc.).

For example, one of the fundamental operations of the digital circuit is the *Recognition of color* phase. In this case, where the realization of an UV image is treated, the image can be easily reproduced, for example, in *Grayscale*. Now, to each digital voltage value (produced by the ADC) corresponding to a certain analog voltage value, a certain gray gradually increasing in intensity will be associated. For example, reasoning with 4 bits, the value 0000 corresponds to black while the value 1111 corresponds to white, and all intermediate values are different levels of intensity of gray. In fact, for example, the

value 0001 will be a very dark gray level, the value 0010 will be a slightly less dark gray, and so on forward. Obviously, increasing the number of bits available for the conversion, greater the number of gray shades that it is possible to get, improving the image's quality (see Figure 2.11).
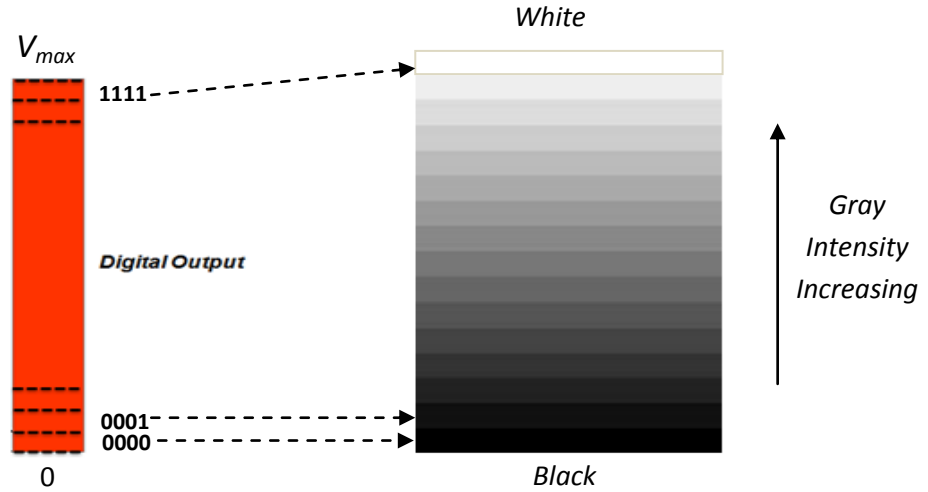
Figure 2.11. Correspondence between each digital word of the ADC output and different gray scale values.

Referring to the previous analysis, attention must be paid to one thing. Between the second and third block, in Figure 2.3, for a typical CMOS image sensor, that depicts a scene in the visible colors to the human eye, a filter, which goes under the name of *CFA* (*Color Filter Array*), is present. Therefore, in Figure 2.3 has been omitted on purpose, because in an UV image, that uses a 4H-SiC photodiode for the photoconversion, it is not possible to use the same principle of operation. Of course, the problem is to understand how to work in such a case.

In fact, for a sensor operating in the visible range, once the electrons are created in the photodiode, due to incident photons at different wavelengths, all the electrons have the same energy and the information about the photons' frequency that have generated them is lost. Hence, if the photodiode is directly illuminated, it will not be able to reconstruct the scene colors, but it could get only the light intensity (proportional to the total number of incident photons). This would be the way to proceed if it wants to create a black and white or grayscale image, but not a color image. To solve this problem it is necessary to know before which is the frequency of incident photons on the photodiode to be sure about which photons have generated those electrons. That's why the CFA is used. The CFA is a filter capable of permitting the passage of only a certain frequency when crossed by a ray of light coming from a certain point in the shooting scene. Only after filtering, the light beam will be directed onto the photodiode, to ensure that the electrons have been created by a certain group of photons at a certain frequency. Obviously, since a large number of CFA cannot be used on a same pixel to filter all colors at the same time, particular filters are used, as the *Bayer Filter*, which is made of only three types of CFA, i.e. green (550 nm), red (650 nm) and blue (450 nm). In fact, every color of the visible band (400-700 nm), can be represented by a linear combination (i.e. overlapping) of the three primary colors, which are green, red and blue. The problem that arises now is that every

single CFA covers a single pixel, which implies that, in this case, it can reproduce only one of the three components of the real color of the shooting scene point. For example, if it is shooting the orange color, passing through a red CFA, it will be filtered, and in output it will only get the red component, while the blue and green components are lost. However, to reproduce the color orange, the sensor must provide an electrical signal to the monitor that contains all three components that make up the orange color. To solve the problem, it is possible to exploit the human eye property according to which it is not able to distinguish differences in color if the points are very close one another (situation even more true in the sensors in which the pixels are distant between them of a few microns). Therefore, it is not make a big mistake to consider the two missing components from adjacent pixels to reconstruct the color of the considered point. This approximation is called *color interpolation*, and it is an operation carried out by a dedicated algorithm, directly implemented on the digital circuit (called SOC, as previously anticipated).

Figure 2.12a shows the Bayer Filter, where it is noted that in order to do a correct approximation, we have to make sure that adjacent pixels have the CFA of the two missing components.
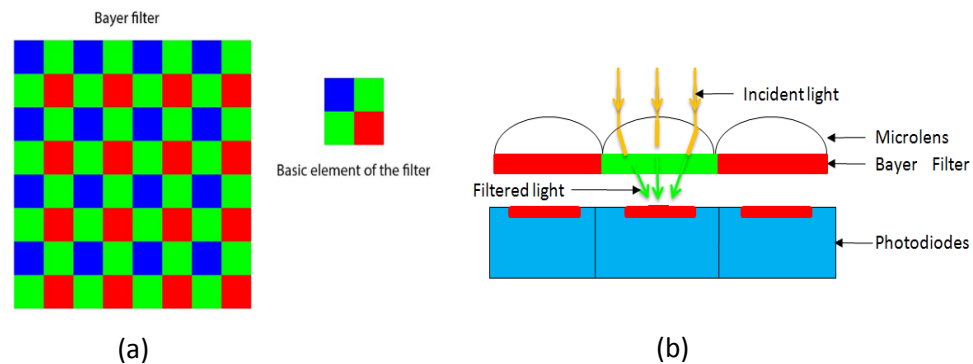
Figure 2.12. (a) Bayer Filter. (b) Typical CMOS structure (Not adapted for UV imaging with 4H-SiC photodiodes).

Now, if the photodiode is made in 4H-SiC, this route cannot be followed because when the radiation arrives at the photodiode, no matter if it is red, blue or green or filtered by the CFA, it will not be absorbed, since the material absorbs only in the UV range. Therefore, it must be removed completely to do not block the passage of the UV radiation that now is the one of interest. For this reason, the only way, to reconstruct the UV image, is only to expose the sensor directly to the light (i.e. the sensor is put at "bare"), and treat the wavelengths in the UV band all in the same way, reasoning then on the radiation intensity to convert it in an appropriate gray intensity (as seen above in Figure 2.11). In practice there are also particular techniques, such as the *false color* and *pseudo-color*, that are applied for the elaboration of gray scale images. The first technique allows to accentuate some particular color differences in images taken outside the visible electromagnetic spectrum using colors belonging to the visible spectrum (for example, infrared, ultraviolet or X-rays, which reveal information or pictures that normally are not perceptible to the human eye but can be detected only by special instruments), as happens for images captured by remote sensing satellites, space telescopes or space probes. In fact the captured

images are in black and white, or filtered on specific wavelengths, and then the actual color is simulated. The second technique, however, very applied in the case of images detected in grayscale, allows to map each intensity value of gray with a color, based on particular tables or functions.

Another possible solution would be to build a new type of filter that covers the photosensitive part and behaves in a manner similar to the Bayer filter, but with some modifications. If instead of the CFA filters green, red and blue, ultraviolet radiation filters are used, able to filter only one wavelength for each UV sub-band (i.e., one for UV long-wave band, one for the UV medium-wave band and one for UV short-wave band), interpreting, by means of appropriate algorithms, the filtered radiation in the long-wave UV band (also called UVA band) as the red color of the visible spectrum, the filtered radiation in the medium-wave UV band (also called UVB band) as the green color of the visible spectrum and the filtered radiation in the short-wave UV band (also called UVC band) as the blue color of the visible spectrum, at this point, the color interpolation algorithm should treat the UV radiations as if they were the RGB colors of the visible spectrum, providing a color image.

This is only a personal suggestion, which does not currently find any practical feedback. In Figure 2.13 is shown a possible implementation of this solution. The implementation would require, of course, the investigation of suitable materials to this task, to ensure that they can withstand at high investigation temperatures.
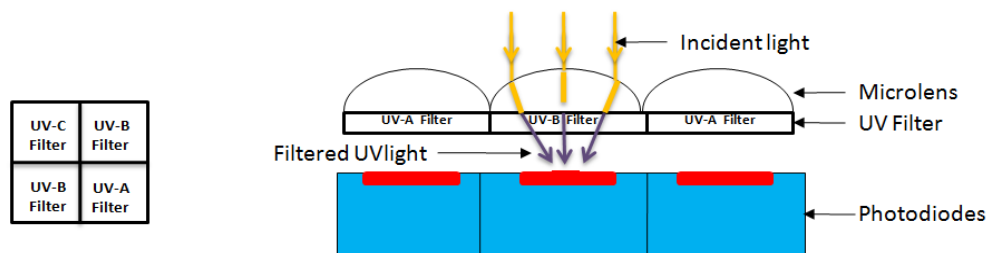
Figure 2.13. (a) Basic element of proposed UV Filter. (b) CMOS structure modified with the insertion of the proposed UV Filter.

To complete the description of the basic operation of an image sensor, one last thing must be emphasized, regarding the lenses type that are commonly used by typical CMOS sensors.

The typical lenses, used for visible photography, have a high *transmittance* (i.e. the ratio between the intensity of light passing through the material and the intensity of light incident on the material itself) that, in the best case, starts from 360 nm (see Figure 2.14), if one refers to a generic *glass* lens.
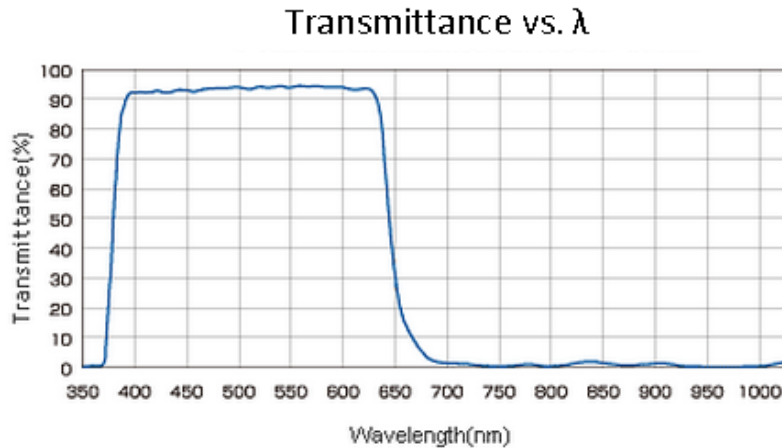
Figure 2.14. Typical spectral response of a glass lens.

The response type, such as the one presented in Figure 2.14, is mainly due to the mix of different elements in the lenses itself, such as Lanthanum, Barium, Tantalum, Boron, Thorium and Uranium (also called activated glass). These elements are specifically used to block infrared and ultraviolet radiation, in order to obtain a better graphic yield. Furthermore, the typical lenses undergo special antireflection treatments to completely cut the UV band, making sure that the spectral response of the common lens extends, typically, from 400 nm to 700 nm. Obviously, this is a serious obstacle to the realization of a photo in the UV band. Hence, an appropriate glass, that allows to capture even the ultraviolet radiation, is required (an objective specifically designed for ultraviolet photos, the UV-Nikkor 55 mm, was used in the Apollo mission).

The best solution is the use of different minerals to be included in the lens. The most common materials are the *fused quartz* and the *fused silica*, which have an excellent transmittance in the UV band. It is right to point out that the fused quartz and the fused silica are both silicon compounds. This compound is the *silica*, with a chemical formula SiO_2. From an engineering point of view the two compounds represent the same thing, but often are differentiated because the first has a crystalline structure and the second presents an amorphous structure, and because the first has a degree of purity different from the second. The reason that typically leads to choose between the two materials is related to the degree of purity: the fused silica is a silica glass (SiO_2) with a purity of 99.9999%, compared to the typical purity of the melted quartz glass that is 99.9%. This gives, to the fused silica, light transmission characteristics significantly better than the fused quartz in the UV range, maintaining these transmission levels up to wavelengths of the order of 1900 nm (i.e. up to the infrared band). Also, both materials besides of having excellent optical transmission properties, are extremely suitable for high temperature applications, due to their excellent thermal properties: *thermal conductivity* of 1.4 W/mK, the *maximum operating temperature* of 950-1300 °C, and a *linear thermal expansion coefficient* of about $0.55 \times 10^{-6}/°C$ [23].

Figure 2.15 shows the typical transmittance of a glass made of fused silica, commercially available (Spectrosil 2000 [24]), for UV applications.
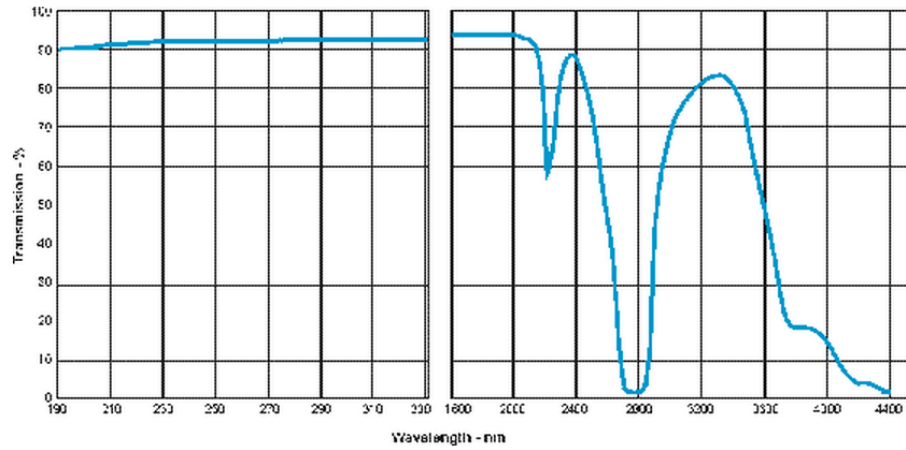
Figure 2.15. UV Fused Silica Glass transmission [24].

2.2.2 Pixel characterization: architecture and operation

The digital images are composed of millions of elementary points. This elementary points are called *pixel*.

The number of output pixels defines the resolution of the sensor, and therefore the image resolution. This parameter is directly related to the definition of the reproduced image. Therefore, to improve the image quality the resolution has to be increased.

Returning to the basic diagram of a CMOS image sensor, Figure 2.16 shows the typical architecture of a 3T pixel circuit (3T stands for "three transistors", as can be seen in the scheme).
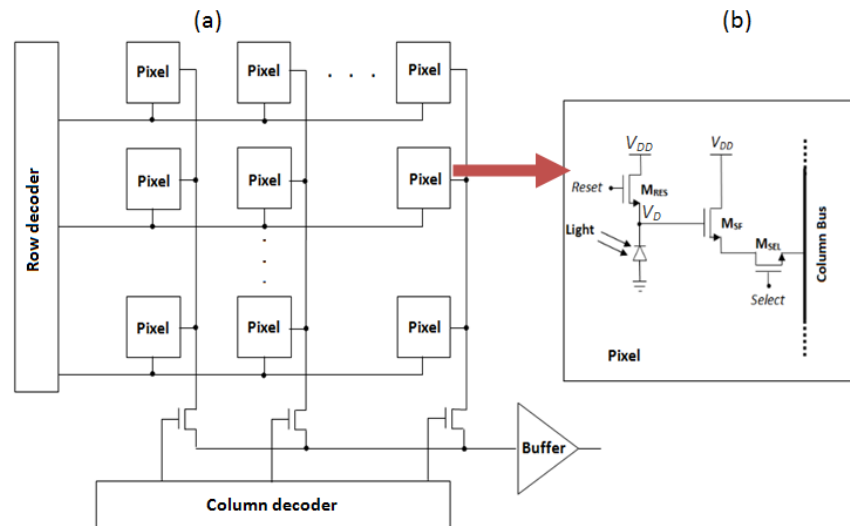
Figure 2.16. (a) Schematic diagram of a CMOS image sensor. (b) 3T pixel architecture.

As can be seen from Figure 2.16, a pixel is made up of three NMOS transistors, which make up all the necessary electronics to manage the operation of the pixel, and a photodetector that runs the photoconversion, and, in this case, is represented by a diode.

The pixel operation is managed by two signals, the *Reset* (that will be indicated with V_{Reset} in what follows), which is common to all the pixels of the array and it simultaneously resets all the pixels of the sensor if activated, and the *Select* (that will be indicated with V_{Select} in what follows) that, supplied by the external processing circuitry, allows to transfer the analog signal, produced by pixel, on the column bus, for the next amplification phase and the encoding of the digital word.

Each of the three transistors has a particular task in the operation of the pixel itself:

- M_{RES} is the *reset transistor*. It has the task to reverse bias the photodiode.
- M_{SF} is a transistor in the *common-drain* configuration (the subscript *SF* stands for *source follower*). It allows to transfer the voltage in input on the output, with an unity gain.
- M_{SEL} is the *select transistor*. It allows to transfer the voltage present on the source of the source follower on the column bus, when activated.

The operation of the pixel can be seen composed by three phases:

1- *Photodiode reset*: this phase is used to "*reset*" the photodiode to a known value, which, in this case, is equal to V_{Reset} - V_{th}, where V_{th} is the threshold voltage of M_{RES}. In this way the diode is reverse biased (in fact, the cathode voltage is $V_D = V_{Reset}$ - V_{th}). This is necessary to extend the depletion region and obtain a high electric field over the same to separate the photogenerated carriers due to the light absorption.

2- *Photodiode light exposure*: during this phase the photogenerated carriers are collected due to the photons absorption. The time during which the photodiode is exposed to light is called *integration time* (T_{int}). During this time, the electron-hole pairs, which are created in the depletion region, will be separated by the electric field present in the region itself, respectively, in the N region and in the P region. Not only these carriers will be collected, since even the superficial and deep photogenerated carriers, according to the value of the incident wavelength, will be separated from the field and they will contribute to the photogenerated current, if they have a sufficient diffusion length to reach the depletion region. If, in a first approximation, the diode behavior is analyzed as a planes and parallels plates capacitor, equal to the junction capacitance, since the electrons are accumulated in the N region and the holes are accumulated in the P region it is possible to see a potential difference across the diode, which tends to directly bias the junction. This voltage opposes the initial reverse bias voltage (V_{Reset} - V_{th}), causing a voltage reduction of ΔV across the diode, compared to the initially value, which depends on how long the diode has been exposed to light. Obviously, it will maximum balance V_{Reset} - V_{th}, stopping the photogeneration process. This happens if the integration time is too high. To avoid that the voltage across the diode is reduced a lot, a minimum value below which it is not possible to go is imposed. This means that there will be a maximum of carriers (electrons and holes) that can be collected, and if this condition is reached, *pixel saturation* condition is reached.

The parameter that represents the maximum electrons value (or holes) that can be collected is known as *Full-well*.

In fact, the phenomenon analyzed can also be treated in terms of space-charge region narrowing, because the electrons sent in N and the holes sent in P will neutralize, respectively, positive ions in the N region and negative ions in the P region, reducing the depletion region width. Being the space-charge region proportional to the reverse voltage applied, its reduction means a reduction of the reverse voltage itself with a direct proportionality.

It is interesting to underline that, during the light exposure phase, the photodiode is left floating. This means that the light energy into electrical energy conversion occurs without power consumption.

3- *Pixel reading*: through the source follower M_{SF} (also known as *voltage buffer*), the voltage across the diode is transferred to the drain of the transistor M_{SEL} which, once turned on, via the SELECT signal on the gate, it will transfer the voltage over the diode on the output. The voltage transfer from the gate to the source of M_{SF} occurs with unity gain, being a source follower. Thanks to its high input impedance and its low output resistance, the voltage transfer will occur with an almost null input absorption, decoupling the photodiode from the bus reading.

This step is repeated two times, before and after the light absorption phase, in agreement with what it was previously said about the Readout circuit operation. A first reading step is performed to read the reverse voltage imposed on the photodiode, before that it is exposed to light, storing this value on the capacitor CH1 through the S&H circuit. A second reading step is performed to read the voltage on the photodiode, after light exposure, sampling, on the capacitor CH2, the effective voltage on the photodiode reduced by the useful video signal ΔV. This phase is necessary to remove any noise source that could possibly destabilized the reset reverse voltage on the photodiode.

At this point, through the Readout circuit, the two available voltages in the S&H circuit will be compared between them in the ASC block. This is done to pick up and amplify the net video signal ΔV, recovering, thus, only the useful information coming from collected photons. With the ADC block, this signal will be converted into a digital signal, and subsequently analyzed by appropriate algorithms to reconstruct the color associated with it.

It is useful to point that in Figure 2.16 a *Buffer* was also represented (with a triangle) at the output of the array of pixels. This buffer has not any role in the functioning of the pixels. It only serves to connect the sensor with the outside (decoupling the pixel matrix from the outside).

In Table 2.2 and in Figure 2.17 [25] are shown, respectively, a summary of the operation stages of a pixel, and the trend of voltages under an appropriate timing.

Phase	M_{RES}	M_{SEL}	Operation performed
Reset	ON	OFF	The photodiode is inversely polarized with a tension on the cathode equal to $V_D = V_{DD}\text{-}V_{th}$
Integration	OFF	OFF	The photodiode, left in floating mode, is discharged by an amount equal to ΔV, or effect of the reverse *saturation current* (also known as *dark current*) if light does not affect, or effect of the *photogenerated current*, proportional to the intensity of incident radiation.
Reading	OFF	ON	The pixel is connected to its column bus to make available, in output, the value of the analog voltage created, proportional to the amount of photons collected.

Table 2.2. Pixel operation phases.
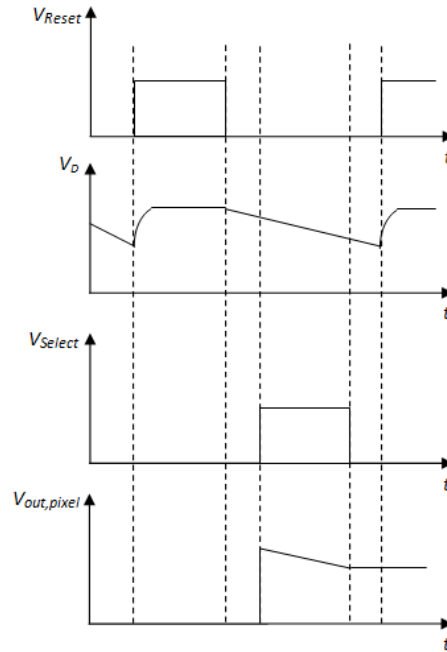
Figure 2.17. Trend of voltages in the pixel operation under an appropriate timing [25].

Before concluding the discussion about the pixel operation, one last thing has to be added, about the possible reset transistor M_{RES} operation mode.

In practice, there are two possible operation modes of this transistor that are *soft reset* and *hard reset*.

In the first case, the reset voltage (i.e., the transistor gate voltage) and the drain voltage of the transistor M_{RES} are both assumed equal to the supply voltage V_{DD}, which means that the source voltage at most will rise to the value of V_{Reset} - V_{th} = V_{DD} - V_{th}. In fact, if the source voltage rises above this value, M_{RES} will go OFF because V_{gs} becomes lower than V_{th}.

In the second case, instead, V_{Reset} is assumed greater than the supply voltage V_{DD}, which allows to reset the diode to the V_{DD} voltage. The source, that will always under the M_{RES} gate voltage for a quantity equal to V_{th} (else it goes in OFF state), can rise up to the V_{DD} value, but not further because, after this value, the V_{DS} becomes zero, i.e. the transistor would theoretically be in ON, working with a zero current (i.e., it is practically OFF) [26]. In the above discussion made and in what follows, it is assumed that the pixel operates in *soft reset* mode.

2.2.3   4H-SiC PIN diode photodetector

In this paragraph the operation of a photodetector will be treated, since it will be the device that will realize the photoconversion, i.e. the conversion of light energy into electrical energy.
In fact, to understand if a pixel, or the whole sensor, is able to efficiently work with increasing temperatures, the first step is to understand if the photoconversion occurs in the most efficient way possible. This inevitably requires a detailed analysis of the photodetector.
The study will begin with the presentation of the main performance parameters that characterize a photodetector (which will be subsequently investigated in detail whit the temperature variations). Subsequently, a theoretical analysis of a 4H-SiC *pin* photodetector will be treated, and, finally, the process flow of a 4H-SiC pin diode developed at KTH will be presented. Furthermore, this device will be also simulated and experimentally tested, in next chapters.

2.2.3.1   Efficiency parameters

For the photodiode characterization two efficiency parameters, which are useful to evaluate and compare the performance of different photodiodes, are examined: *quantum efficiency* and *responsivity*.
The quantum efficiency η is a dimensionless quantity defined as follows [9]:

$$\eta = \frac{I_{ph}}{q} \frac{hv}{P_{inc}} \qquad (2.5)$$

where I_{ph} is the generated photocurrent in *A*, q is the electron charge, h is the Planck constant in *J s*, v is the photon frequency in *Hz* and P_{inc} is the incident optical power in *W*.
Remembering the definition of the electric current (i.e., $I = qnvA$, where n is the carriers number density, of charge q, which move with a common drift velocity v, under the action of an electric field, and A is the section crossed by the carriers themselves in the unit of time), the amount I_{ph}/q represents the carriers number per second (i.e., the number of photogenerated electron-hole pairs), which contribute to the photocurrent I_{ph}. However,

from Eq. (1.40), it is observed that the amount *Pin/hv* represents the number of incident photons per second.

Therefore, the ratio presented in the Eq. (2.5) tells that the quantum efficiency is the number of carriers that contribute to the photogenerated current compared to the total number of incident photons.

This parameter is very important because it allows to quantify which is the exact fraction of photogenerated carriers that is able to reach the junction and it is transformed into useful current for each wavelength.

In fact, when a photon is absorbed, and it generates an electron-hole pair, it is not certain that this pair will be useful to the photocurrent. If a carrier is photogenerated very close to the surface or in depth, it can have a diffusion length that is not sufficient to reach the depletion region where they will be pushed in the N region under the action of the field, if it is an electron generated in P (or in the P region if it is a hole generated in N). Furthermore, when the carriers are generated close to the surface, they can also spread to the contact, instead of spreading towards the space-charge region. These carriers recombine at the contact without giving any contribution to the photogenerated current with a recombination velocity theoretically infinite. Besides this, one must also take into account the high density of surface defects arising from the processing of the device. For example, when the crystal is cut during manufacturing, surface defects are inevitably introduced, due to the presence of incomplete covalent bonds due to the interruption of the material. Indeed, in practice, to reduce these surface defects, a silicon dioxide layer is deposited, to achieve passivation and to complete part of the dangling bonds.

This means that, inside the device, gradient concentrations are established. The concentration is high in the center of the P or N region, and it is very low both in the proximity of the space-charge region (in fact is zero, being the depletion region a region free of mobile carriers), and near the contacts (due to the high contact recombination velocity and the high surface recombination). Because of these gradient concentrations, a carriers diffusion process is established, from the higher concentration to the lower concentration, where the lowest concentration is not present only towards the depletion region but also towards the surface. This means that if a carrier is created close to the surface, it will probably spread towards the contact and not towards the depletion region, thus not contributing to the photogenerated current. Vice versa, if it is generated near the depletion region, or beyond the point where the concentration is maximum, it will probably spread towards the depletion region and it will contribute to the photogenerated current.

To evaluate this minority carriers trend (electrons in P and holes in N), one should solve the fundamental equations of semiconductors (continuity equations and current equations) assuming the steady state conditions (i.e., it is neglected the terms that depend on time) and of quasi-neutrality (i.e., it is supposed to be in low injection levels), taking also into account the actual generation rate G of electrons and holes (charges generated due to the incident light radiation in the unit of time and volume) and the recombination velocity of the same (tendency of the charges to return to the concentration value in thermodynamic equilibrium conditions), both within the device (by using the recombination velocity U_{SRH}) and at the surface (by introducing the so called surface recombination speed, typically denoted by $U_{SRH,surf}$, different for electrons and holes).

At state of the art, there are not carrier concentrations analysis within of a 4H-SiC photodetector, but to get an idea of what is happening it is possible to examine Figure 2.18, where the carriers concentration in a silicon $N^+ P^-$ diode, with a N^+ region of 1 μm implanted in a P^- region of 300 μm is considered.
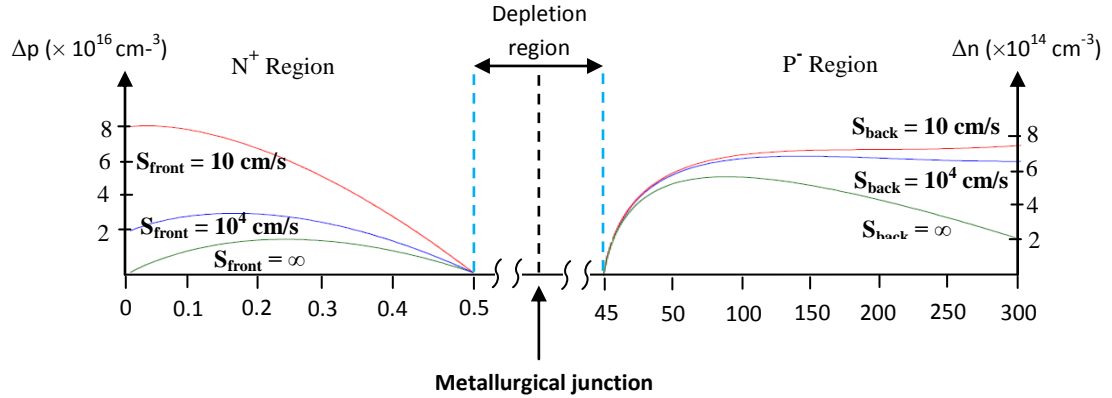
Figure 2.18. Minority carriers gradients in P and N regions versus different surface recombination velocity.

Then, this causes an inevitable reduction of the quantum efficiency (see Figure 2.19) both when the wavelengths are very small, because they are absorbed in surface, and when the wavelengths are very long, because they are absorbed deeper, which involves that the carriers are not able to reach the space charge region, and therefore they do not contribute to the photocurrent.

For this reason, the quantum efficiency is a fundamental parameter of the photodetector.

The quantum efficiency defined in Eq. (2.5) is also called *external quantum efficiency*, often also indicated with η_{ext}, because it refers to photons impacting on the outer surface of the device (in the following it will be used either η or η_{ext}).

However, when the photons reach the device, they are not all absorbed, but a part of them is reflected (because of a not zero reflectance at the air/material separation surface). This means that the photons that are actually absorbed and generate electron-hole pairs are only an amount of the total incident photon (the study of the reflectance of a 4H-SiC photodiode will be analyzed in greater detail in the following paragraph).

Instead, referring to the photons that actually penetrate into the material the quantum efficiency is called *internal quantum efficiency η_i*, defined as the ratio between the number of created pairs divided by the number of actually absorbed photons in the material. Of course, if the photons are not reflected, but penetrate into the material, considering an ideal material (i.e. it is free of defects), each absorbed photon exactly generates a pair of free carriers, which means that η_i is typically a value very close or even equal to unity [9].

Being interested in the number of photogenerated carriers that contributes to the photocurrent, given the total number of incident photons, only the device external quantum efficiency will be taken into consideration, in the following discussion.

Then, ideally, for all the incident wavelengths smaller than *1.24/E$_g$* (the critical wavelength), one should have an unitary quantum efficiency, i.e. all the photons are absorbed, whatever the frequency (or wavelength), generating carriers useful for the

photocurrent. Unfortunately, in reality, for all causes presented above, and because the photons are not all absorbed, the quantum efficiency of a real device will be lower than the ideal, and the real trend is shown in Figure 2.19.
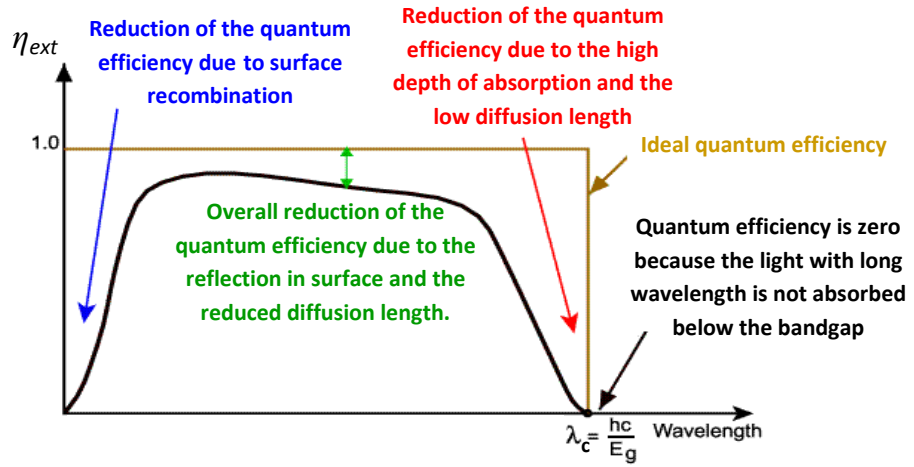
Figure 2.19. Ideal and real external quantum efficiency versus wavelength.

The second efficiency parameter of a photodetector is the *responsivity R*, defined as follows[9]:

$$R = \frac{I_{ph}}{P_{inc}} \tag{2.6}$$

It is measured in *A/W*, and represents the device ability to convert the incident optical power in photocurrent.
From Eq. (2.5) it is observed that:

$$\frac{I_{ph}}{P_{inc}} = \frac{\eta\, q}{h\, v} \tag{2.7}$$

and replacing the Eq. (2.7) in Eq. (2.6) one obtains [9]:

$$R = \frac{I_{ph}}{P_{inc}} = \frac{\eta\, q}{h\, v} = \frac{\eta\, \lambda(\mu m)}{1.24} \tag{2.8}$$

obtained by replacing *v* with the quantity *c/λ*, and replacing the quantities *h*, *c* and *q* with the corresponding values.
By Eq. (2.8) it is possible to observe that, setting the quantum efficiency value equal to the ideal one, the responsivity should grow linearly with the considered wavelength. In reality, given that it is related, in a direct proportionality, to the quantum efficiency, since the latter varies according to what is shown in Figure 2.19, also the responsivity varies in a similar way, growing linearly with the incident wavelength, but only in a particular wavelengths range (see Figure 2.20).
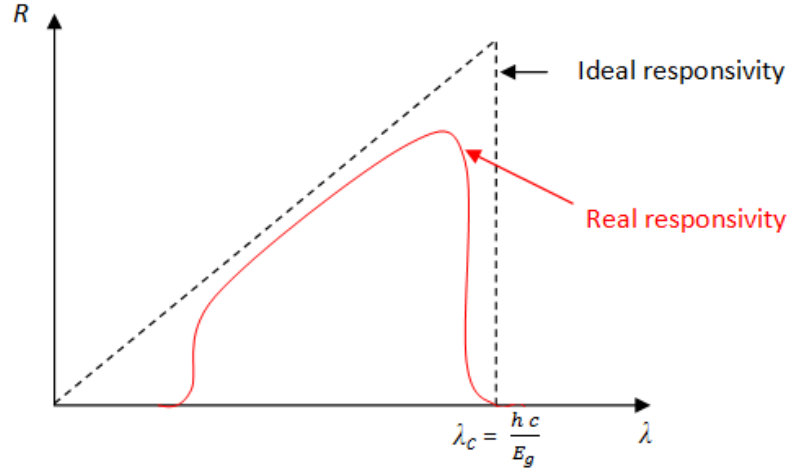
Figure 2.20. Ideal and real responsivity versus wavelength.

The relationship between responsivity and quantum efficiency is very important because to calculate the quantum efficiency it is necessary to exactly know the number of photogenerated carriers by the incident photons, which is quite difficult to assess. To calculate the responsivity it is necessary to estimate the ratio between the photogenerated current, that can be evaluated through a simple current measurement, or from simulations, and the incident power, which is known since it is sent from the outside. At this point, using the relationship (2.8), once the responsivity is known, the quantum efficiency is obtained.

In the analysis that will be done after, recombination to the contact and surface recombination will be neglected, taking only into account the carriers ability to reach the space charge region if they have the right diffusion length. In this region they will be separated to contribute to the photocurrent. Furthermore, the reflectance at the separation air/device surface will be taken into account. This implies that both the responsivity and the quantum efficiency, will never be zero for small wavelengths, as shown in Figure 2.19 and 2.20, since if the carriers, have a diffusion length sufficient to reach the space charge region, they will give a contribution to the photogenerated current as predicted by the Eq. (2.8).

2.2.3.2   4H-SiC reflectance: before and after SiO$_2$ passivation

When light strikes on a discontinuity surface between two different media it suffers, in general, both a refraction and a reflection, in accordance with what is expected by the *Fresnel equations*. These equations describe the light behavior when it is incident on a discontinuity surface between two media with different refractive indices, giving the fraction of reflected light and the fraction of transmitted one (see Figure 2.21). Furthermore, in these equations it is assumed that the interface is flat and homogeneous, and the light is a plane wave.

The reflection of light, as predicted by the Fresnel equations, is known as *Fresnel reflection*.

Figure 2.21 shows the representation of the reflection and refraction which an incident ray undergoes. In the figure θ_i indicates the angle between the incident ray and the normal to the discontinuity surface, θ_r indicates the angle formed between the reflected ray and the normal to the discontinuity surface, θ_t indicates the angle formed between the transmitted ray and the normal to the discontinuity surface, n_0 is the refractive index of the medium containing the incident ray and the reflected ray and n is the refractive index of the medium containing the refracted ray.
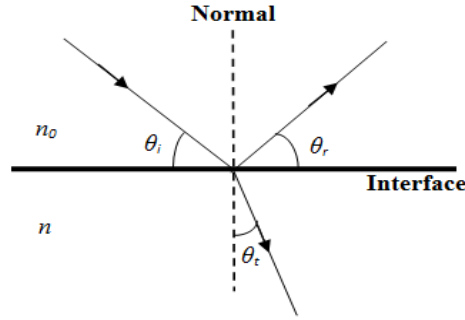
Figure 2.21. Representation of the reflection and refraction of the incident beam.

The relationships between these angles are two, the *reflection law* and the *Snell's law* (also known as the *refraction second law*). The first allows to relate the angle formed by the incident ray with the normal to the discontinuity surface to the angle formed by the reflected ray with the normal to the discontinuity surface, and the second allows to relate the incidence angle with the refraction angle, formed between the incident ray and refracted ray with the normal to the discontinuity surface.

The reflection law is:

$$\theta_i = \theta_r \qquad (2.9)$$

and the Snell's law is:

$$n_0 \sin(\theta_i) = n \sin(\theta_t) \qquad (2.10)$$

To calculate the amount of incident power that is reflected from the interface, the *reflectance R* is used.

The calculation of *R* varies depending on the polarization of the incident light. Indicating the *plane of incidence* as the plane formed by the propagation vector of the incident wave and the normal to the discontinuity surface, it is possible to distinguish two cases. The first case is that the incident light is polarized with its electric field perpendicular to the incidence plane (in which, for the first refraction law, are contained the incident ray, the reflected ray and the refracted ray), and it is referred to as *s-polarized* light (where "*s*" stands, from the German "*senkrecht*", for perpendicular). The second case is that of incident light polarized with the electric field parallel to the incidence plane, and it is

referred to as *p-polarized light* (where *"p"* stands for parallel). Since these two types of polarization are orthogonal to each other, an incident plane wave, of any polarization, can be decomposed into a s-polarized wave and p-polarized wave (i.e. it can be decomposed in two components, TE and TM respectively), which can be separately treated.

In the case of s-polarized light, and generic incidence, it is possible to demonstrate that the reflectance R (or R_s) is equal to:

$$R = \left| \frac{n_0 \cos(\theta_i) - n \cos(\theta_t)}{n_0 \cos(\theta_i) + n \cos(\theta_t)} \right|^2 \qquad (2.11)$$

and in the case of p-polarized light, and generic incidence, it is possible to demonstrate that the reflectance R (or R_p) is equal to:

$$R = \left| \frac{n_0 \cos(\theta_t) - n \cos(\theta_i)}{n_0 \cos(\theta_t) + n \cos(\theta_i)} \right|^2 \qquad (2.12)$$

In general, as noted in the first chapter, the refractive index n is a complex quantity and depends on the incident wavelength. This implies that also the reflectance is, in general, a complex quantity and it depends on the incident wavelength.

If the absorption is neglected (not taking into account the imaginary part of n, i.e. k) and the case of s-polarized light (with normal incidence the s-polarization and the p-polarization are indistinguishable, since with $\theta_i = \theta_t = 0 \rightarrow R_p = R_s$) and normal incidence is considered (i.e. $\theta_i = \theta_t = 0$ from the Snell's law), it is obtained that:

$$R(\lambda) = \left(\frac{n_0 - n}{n_0 + n} \right)^2 \qquad (2.13)$$

If one considers that the medium with refractive index n_0 is air (i.e. n_0 is equal to 1 for each wavelength, because the air behaves, in practice, as the vacuum), and the medium with refractive index n is 4H-SiC (see Figure 1.12), it is possible calculate, using the Eq. (2.13), the reflectance air/4H-SiC versus the wavelength variation, which is shown in the Figure 2.22.
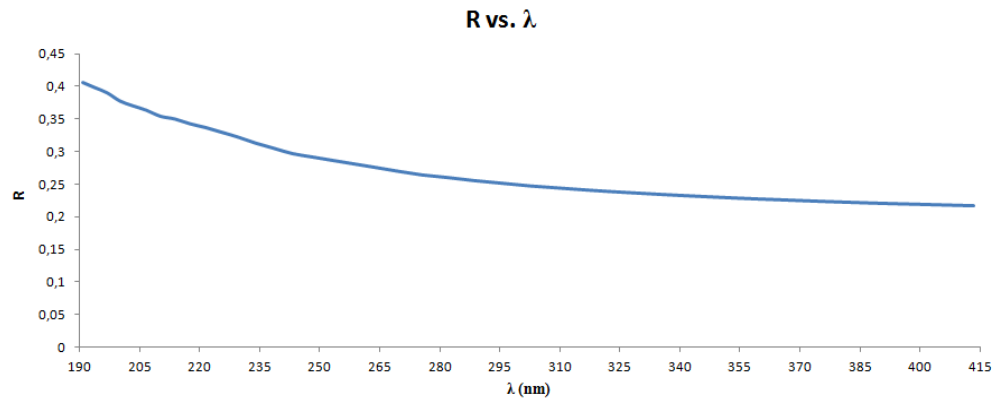
Figure 2.22. Reflectance at discontinuity air/4H-SiC.

50

Figure 2.22 shows that, at the air/4H-SiC surface discontinuity, the light undergoes a high reflection over a large wavelengths range inside the UV band, with a peak of about 40% at 190 nm.

By the deposition of an *antireflective coatings* (*ARC*), deposited above the device itself, it is possible to greatly reduce the light reflectance.

In particular, the silicon dioxide is one of the materials of first choice for the antireflective coating. Indeed, the silicon dioxide is used as a *passivation* material for the semiconductor devices for various reasons, including the protection of the device from external contamination due to the surrounding environment that can irretrievably alter its electrical characteristics, the reduction of the incomplete bonds at the surface to reduce the surface recombination, the protection of the side areas of the PN junctions from excessive leakage currents in reverse bias, etc. Instead, now, it will be shown how the silicon dioxide deposition on a 4H-SiC device can also reduce the light reflectance, in order to ensure that a greater amount of light energy can penetrate inside the material and to be converted into electrical energy.

In fact, now, a structure like that presented in Figure 2.23 is considered, where, above a medium, supposed of 4H-SiC, is deposited a silicon dioxide layer with a thickness d = 50 nm (the choice of this thickness is justified by the next analysis), considering always the normal incidence case.
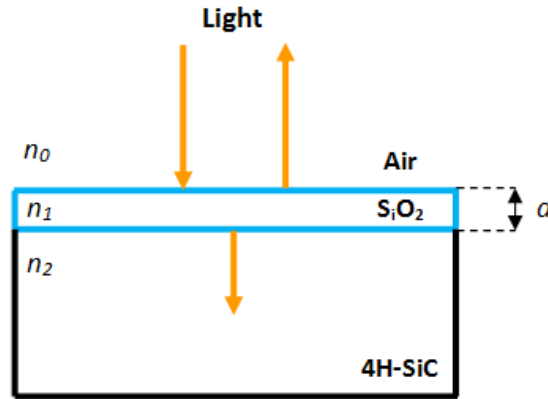
Figure 2.23. SiO$_2$ deposition on a 4H-SiC medium.

Through a matrix approach, it can be shown that, in this case, the reflectance is equal to:

$$R = \frac{r_1{}^2 + r_2{}^2 + 2\,r_1\,r_2 \cos{(2\theta)}}{1 + r_1{}^2 r_2{}^2 + 2\,r_1\,r_2 \cos{(2\theta)}} \tag{2.14}$$

with:

$$r_1 = \frac{n_0 - n_1}{n_0 + n_1} \tag{2.15}$$

$$r_2 = \frac{n_1 - n_2}{n_1 + n_2} \tag{2.16}$$

$$\theta = \frac{2 \pi n_1 d}{\lambda} \qquad (2.17)$$

where n_0, n_1, n_2 are, respectively, the refractive index of air, SiO$_2$ and 4H-SiC, r_1 and r_2 are, respectively, the reflection coefficients at the discontinuity air/SiO$_2$ and SiO$_2$/4H-SiC, and θ is phase shift, suffered by the wave in the antireflective layer.

As shown in the Eq. (2.14), now, it must also take into account of the silicon dioxide refractive index with the wavelength variation. In literature the trend of the silicon dioxide refractive index versus the wavelength is known, and this trend is shown in Figure 2.24 [27]. It has to be noted that the imaginary part of the complex refractive index, k, has not been reported, because it is zero for all the wavelengths of interest, confirming that the silicon dioxide does not absorb light, but the light completely crosses it, if it is not reflected.
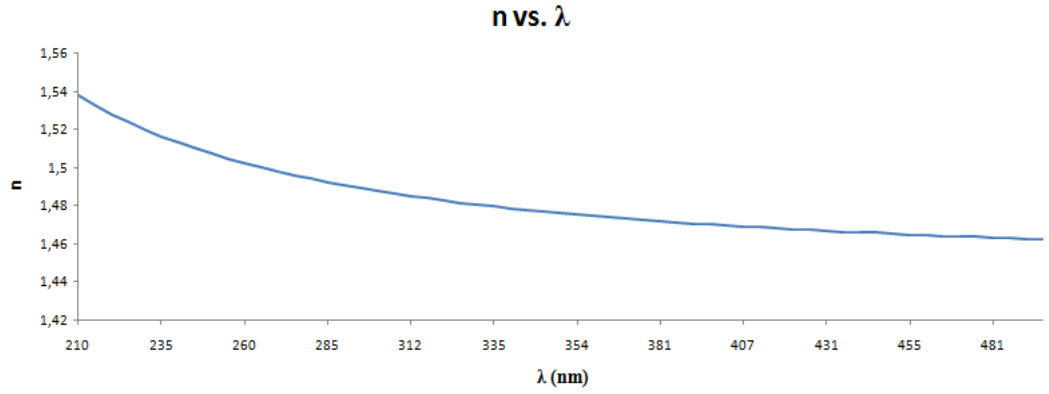
Figure 2.24. SiO$_2$ refractive index versus wavelength.

The available values of the silicon dioxide refractive index are contained in the range of wavelengths 210 nm - 2500 μm, but, given that the available values of the 4H-SiC refractive index are in the range 190 nm - 415 nm, to make a reflectance comparison, with and without oxide deposition, the range of analysis for wavelengths has been limited to the range 210 nm - 400 nm (pointing out that the analysis of interest is, principally, in the UV band).

Using equations (2.14), (2.15), (2.16) and (2.17), the reflectance trend, as a wavelength function, is obtained with the deposition of a silicon dioxide layer, for example, of 200 nm on a 4H-SiC medium, as shown in Figure 2.25.
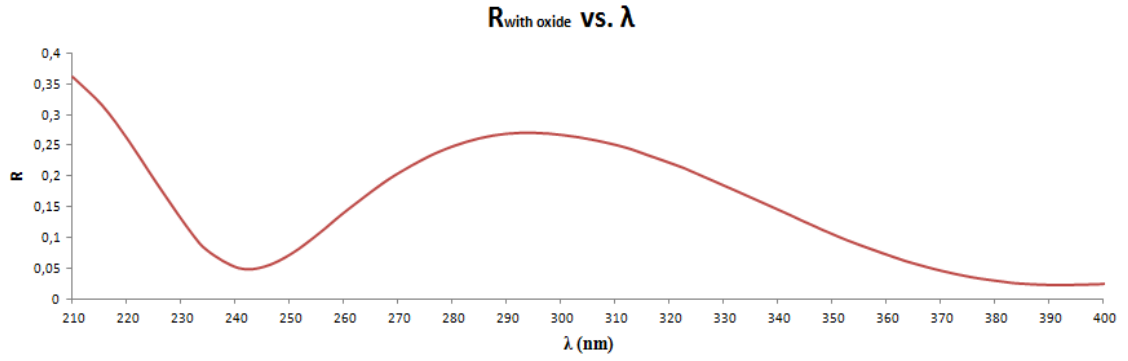
Figure 2.25. Reflectance after silicon dioxide deposition.

At this point, it is possible to compare the reflectance before and after the silicon dioxide layer deposition, as shown in Figure 2.26.
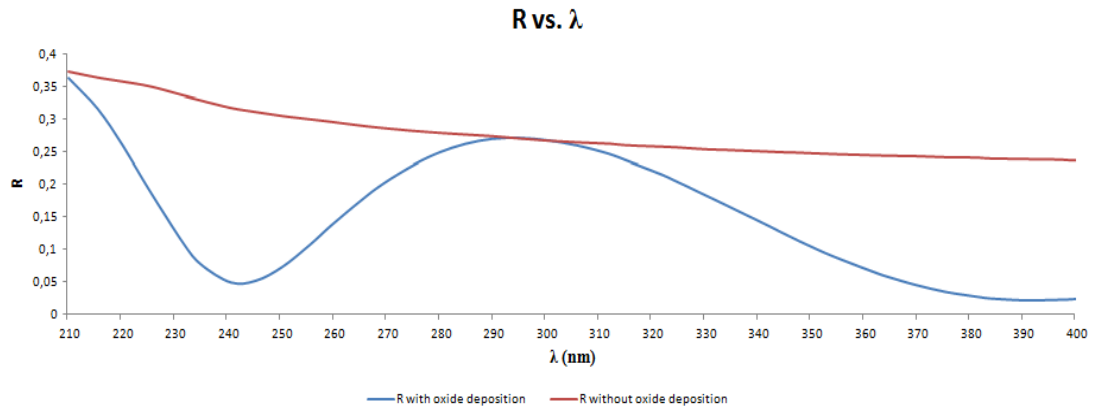
Figure 2.26. Reflectance before and after SiO$_2$ passivation layer deposition.

From Figure 2.26 the clear reflectance reduction is observed, due to passivation with a silicon dioxide antireflective coating of 200 nm.

Obviously, the advantage to have a very low reflectance, on the range of frequencies of interest, results in an improvement both in terms of quantum efficiency and of responsivity. In fact, reducing the amount of reflected light, it is obvious that the number of collected photons is increased and, therefore, for the same incident power, a greater generation of electron-hole pairs is possible, that will contribute to the overall photocurrent.

Finally, it is interesting to clarify why it was chosen a silicon dioxide thickness of 50 nm. To understand this, various analysis have been done (following the procedure shown before), but varying the antireflective coating thickness, limiting the analysis only to the portion of UV band analyzable (210 - 400 nm). The results obtained are shown in Figure 2.27.
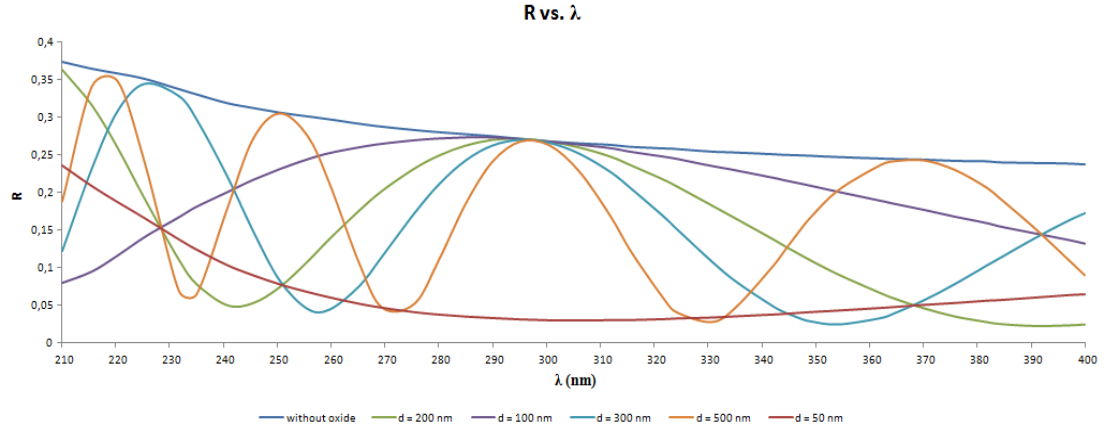
Figure 2.27. Reflectance versus wavelength with different silicon dioxide thicknesses.

Then, as confirmed by Figure 2.27, the choice of a thickness of 50 nm is the best choice in terms of reflectance, because it represents the best compromise in terms of wavelength, especially if it works with wavelengths between 280 - 330 nm. Instead, for example, working between 210 - 270 nm, or between 330 and 400 nm, changing the layer thickness would be better. Obviously, this design choice depends on the use in the UV band of the photodetector.

2.2.3.3 Theoretical analysis of a 4H-SiC PIN photodetector

In Figure 2.28 the P^+N^- junction photodiode is shown.
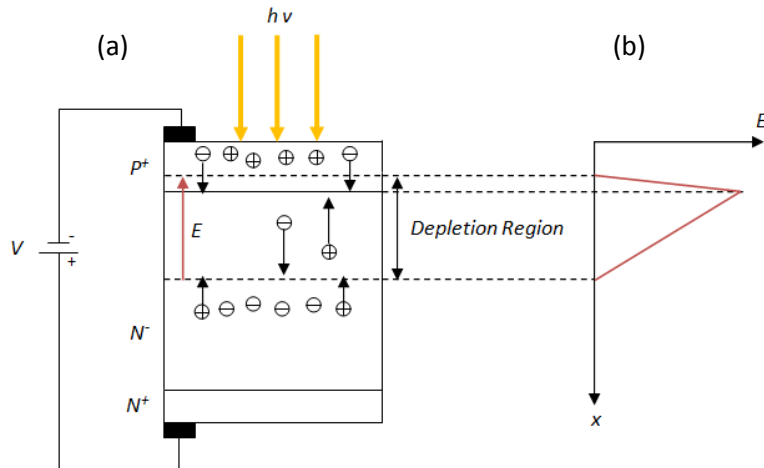
Figure 2.28. (a) Junction photodiode structure. (b) Field profile.

The first thing to point out is that the silicon carbide is an indirect bandgap semiconductor. This means that to absorb efficiently the light, the SHR generation-recombination through intermediate traps levels has to be exploited. Obviously, this also means that the opposite process (if the silicon carbide has to be used, for example, to create a LED), is very inefficient, because when the electron when recombines with a hole in the valence band,

54

the decay is not direct, and the photon emission of a given wavelength (or energy equal to the bandgap) is not possible (provided that there is an interaction with a phonon that varies the amount of motion of the electron, but this process has a very low probability of occurrence).

The basic principle of operation of a junction photodiode is very simple [9]. When the diode is reverse biased, thanks to the wide extension of the space charge region, and therefore in the presence of a high electric field in the space charge zone, which opposes to the diffusion of the majority carriers, only the passage of a small current through the device is permitted, also known as *dark current* (which would be nothing more than the reverse saturation current of the diode). If, at this point, the diode is illuminated, the photons absorption, both in the neutral P$^+$ and N$^-$ regions (obviously the greater absorption of photons occurs at the surface, since it is directly exposed to the incident radiation), and in the depletion region, will cause the electron-hole pairs generation. The photogenerated carriers, if generated in the space charge region, under the action of the electric field applied from the outside, will be accelerated in opposite directions and sent, respectively, to the P$^+$ region, if it is a hole, and to the N$^-$ region if it is an electron. Of course, as observed from Figure 2.28, pairs generated close to the surface or deep will be collected in the respective regions, but, in this case, the hole generated in N$^-$ region has first to diffuse through the N$^-$ region and, then, under the action of the field, to be shipped in the P$^+$ region. Instead an electron generated in the P$^+$ region has first to diffuse through the P$^+$ region and, after, under the action of the field, be delivered in the N$^-$ region.

Once separated the photogenerated carriers will give rise to a photocurrent, the value of which depends, obviously, on the quantum efficiency [9].

This photogenerated current will go to superimpose to the reverse current of the P$^+$N$^-$ junction, causing an increase in the reverse current of the diode itself, in reverse bias conditions.

It is interesting to note that this photogenerated current is a current made up of minority carriers.

Indeed, it is remembered that the current in a diode, in thermodynamic equilibrium conditions, is zero, since the diffusion current of the majority carriers (electrons that diffuse from N$^-$ to P$^+$, and holes that diffuse from P$^+$ to N$^-$) is exactly balanced by a drift current as the majority carriers progressively diffuse, i.e. a current of minority carriers that are rejected in the corresponding regions by the electric field that is created within the depletion region. If a forward bias voltage is applied to the junction, the effect is a reduction of the *potential barrier* seen by the majority carriers, from the initial value of qV_{bi}, to a value equal to $q(V_{bi} - V)$, where V is the voltage applied from the outside and V_{bi} is the *built-in potential*. This will trigger a greater majority carriers diffusion which leads to an exponential increase in the current value (which is precisely due to the majority carriers that crossing the junction), remembering that the current I of a diode, in function of the external bias V, is given by:

$$I = I_0 \left(e^{\frac{V}{V_T}} - 1 \right)$$

(2.18)

where I_0 is the reverse saturation current (i.e. the minority current) and V_T is the thermal voltage.

However, if a diode is reverse biased, the diffusion of the majority carriers is reduced, or even it becomes zero (since, now, the potential barrier is not reduced of -V, but it is increased of +V). This is due to the fact that the extension of the emptied region and, therefore, the presence of a high electric field, opposes to the passage of the majority carriers. In this case, from equation (2.18), it is observed that the current flowing in the diode is only the minority current, i.e. the reverse saturation current I_0. In fact, from the Eq. (2.18), it is possible to obtain that the current I is equal at -I_0, because it is a current that flows in the opposite direction to the conventional direction of the current in direct polarization, that is positive from P to N.

Then, when the light invests the device, its effect is to generate electron-hole pairs, which are separated from the field and sent in the corresponding N and P regions. These carriers (which give life to the photogenerated current I_{ph}) are minority carriers that are added to the initial minority current (I_0 in reverse bias), causing an increase of the reverse current itself. Obviously, the light does not act on the potential barrier, causing an increase or decrease of the same (this variation is related only to the value of the outside bias voltage), but the only thing that the light can do is to increase the reverse current flowing through the diode, generating a current that is precisely equal to the photogenerated current.

Figure 2.29 shows a graphical representation of the photodiode operation mode. The following representation shows only what happens to the holes but, of course, the same applies to the electrons.

$$I = I_0\left(e^{\frac{V}{V_T}} - 1\right) = I_0\,e^{\frac{V}{V_T}} - I_0 = I_{diff} - I_{drift} = 0$$

where $I_{diff} = I_{drift}$

(a)

(b)

Holes that pass the barrier by diffusion from P to N region → I_{diff}

I_{drift}

Holes driven in the P region from the electric field E

Holes that don't pass the barrier by diffusion from P to N region

$|U|$

E

qV

qV_{bi}

$q(V_{bi} - V)$

P⁺

N⁻

x

Depletion Region

$$I = I_0\left(e^{\frac{V}{V_T}} - 1\right) = I_0\, e^{\frac{V}{V_T}} - I_0 = I_{diff} - I_{drift}$$

with $I_{diff} > I_{drift}$, and I_{drift} that doesn't change respect the thermodynamic equilibrium

(b)

(c)

Holes that pass the barrier by diffusion from P to N region

I_{diff}

$|U|$

E

I_{drift}

Holes driven in the P region from the electric field E

Holes that don't pass the barrier by diffusion from P to N region

qV

$q(V_{bi} + V)$

qV_{bi}

P⁺

N⁻

x

Depletion Region

$$I = I_0\left(e^{\frac{V}{V_T}} - 1\right) = I_0\, e^{\frac{V}{V_T}} - I_0 = I_{diff} - I_{drift}$$

$$\cong -I_0$$

with $I_{diff} < I_{drift}$, and I_{drift} that doesn't change respect the thermodynamic equilibrium

(c)

(d)

Light

Holes that pass the barrier by diffusion from P to N region

I_{diff}

$|U|$

E

I_{ph} I_{drift}

Holes driven in the P region from the electric field E

Holes that don't pass the barrier by diffusion from P to N region

qV

$q(V_{bi} + V)$

qV_{bi}

P⁺

N⁻

x

Depletion Region

$$I = I_0\left(e^{\frac{V}{V_T}} - 1\right) = I_0\, e^{\frac{V}{V_T}} - I_0 - I_{ph}$$

$$= I_{diff} - I_{drift}$$

$$\cong -I_0 - I_{ph}$$

with $I_{diff} < I_{drift}$, and I_{drift} that change respect the thermodynamic equilibrium due to the addition of I_{ph}

(d)

Figure 2.29. (a) Thermodynamic equilibrium. (b) Direct bias of PN junction. (c) Reverse bias of PN junction without light absorption. (d) Reverse bias of PN junction with light absorption. (e) I-V characteristics in dark and light conditions.

From what has been said so far, it immediately follows that the best solution to optimize the photons collection is to extend the space charge region as far as possible, because only if the photons are directly absorbed in the space charge region electron-hole pairs, that will be automatically separated from the electric field present therein, will be created and delivered to the corresponding regions. Of course, the pairs also generated within the neutral regions will contribute to the photocurrent but, in this case, care must be taken regarding the diffusion length, which if it is not enough, makes that the carriers recombine before they reach the depletion region. Thus they will not be useful for the overall photocurrent.

Furthermore, the carriers diffusion length should be checked when the temperature changes, as well as at the doping variations. Luckily, experimental results show high diffusion length values for the carriers even with high doping concentrations. For example, at 300K, in a N-type 4H-SiC layer, with a doping concentrations greater than 10^{18} cm^{-3}, the holes diffusion length is of about 2 μm [29] (other experimental results show a very slow reduction of the ambipolar diffusion length, even at high temperatures [30]). This suggests that the diffusion length temperature and doping dependence should not be a big problem in the photogeneration, provided that the thickness of the epitaxial layers is chosen in accordance with the previsions of the light penetration depth (see Figure 1.15).

In practice, to obtain high quantum efficiencies, and therefore high photogenerated currents, if low brightness levels have to be detected, it is possible to use *avalanche photodiodes*. In this case, the photocurrent is amplified by avalanche multiplication. In the following the response of the photodiode in avalanche conditions will be shown. In any case, if the photodetector has to be used as the basic element of an image sensor, working in avalanche conditions it is certainly not the best choice. In this case, it is true that the photogenerated current will be amplified, but it is also true that the dark current of the photodiode will be amplified too (the dark current is seen as a noise source in the sensing). This would lead the sensor to detect the presence of light when no light is present.

The structure of a pin junction diode is not different from the one presented in Figure 2.28. The only difference that exists between the diode presented in Figure 2.28 and a pin diode

resides in the N⁻ region doping, inserted between the P⁺ region and the N⁺ region. The N⁻ region is called, in fact, the *intrinsic region*, because its doping is reduced at least of two or three orders of magnitude, compared to that of the P⁺ and N⁺ regions. In fact, appropriately varying the thickness of the region, thanks to the low free carrier concentration and high resistivity present in it [9], applying outside low reverse bias voltages, it is possible to have a completely (or almost) emptied N⁻ region, in which region the applied voltage falls almost entirely. Instead, the P⁺ and N⁺ regions have only two tasks: to generate and sustain the field inside the structure, and to collect the photogenerated carriers. In fact, in this case, the P⁺ and N⁺ regions are not typically made very thick (above all the P⁺ region), to ensure that the light can easily penetrate the material and reach the depletion region. Instead, if the depletion region is made wider than the P⁺ region, and it is completely depleted, this allows to obtain a good absorption of photons that will be then converted into electron-hole pairs (see Figure 2.30).

Moreover, in many practical applications, the light is made to hit (through the use of lenses that focus the radiation) on the upper part of the device, realizing, through an etch, also openings (or windows) within the top contact.
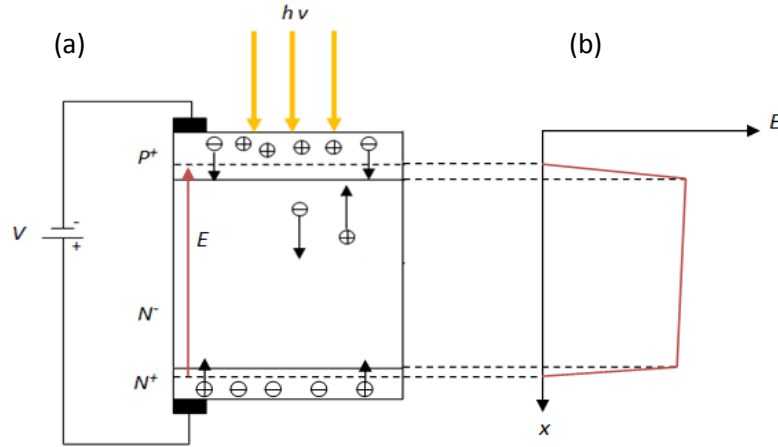
Figure 2.30. (a) *Pin* junction photodiode structure. (b) Field profile in the case of intrinsic completely depleted region.

Assuming that for every incident photon exactly one electron-hole pair is generated, this implies that the internal quantum efficiency of a pin photodiode can reach the maximum value of 100%, without presenting internal optical gains. In fact, the optical gain, often denoted by Γ_G, is defined as the ratio between the output current, collected at the electrodes, and the primary photocurrent generated by light absorption. It is obvious that, if particular internal amplification mechanisms like the avalanche multiplication are not triggered, the output current is exactly the primary photogenerated current, and the optical gain is 1 (or 100%).

At this point, it is interesting to better understand which is the dark current of a pin photodetector, since this is the major disturb source in an image sensor (in particular if it has to work at high temperatures).

Starting from the continuity equations of electrons and holes, and from the Poisson's equation, considering the N⁻ region that is not completely depleted, it is possible to treat

the device as a typical P$^+$N$^-$ junction. The continuity equations of electrons and holes and the Poisson's equation are useful to determine the current density evolution and the electric field evolution inside the device, obtaining, in particular, that the diffusion current density J_{diff} is given by:

$$J_{diff} = J_0 \left(e^{\frac{qV}{KT}} - 1 \right)$$
(2.19)

where J_0 is the reverse saturation current density in of a *short diode*, and it is equal to:

$$J_0 = \left(\frac{q\, n_i{}^2 D_p}{N_d\, L_p\, \tanh\left(d_n/L_p\right)} + \frac{q\, n_i{}^2 D_n}{N_a\, L_n\, \tanh\left(d_p/L_n\right)} \right)$$
(2.20)

where n_i is the intrinsic carrier density in cm^{-3}, D_n e D_p are, respectively, the electron and hole diffusion coefficient in cm^2/s, N_d and N_a are, respectively, the electron and hole carrier concentration in cm^{-3}, L_n and L_p are the carrier diffusion lengths in cm, d_n and d_p are the doped-region depths in cm, V is the external voltage applied in V, and J_0 is the reverse saturation current density in A/cm^2. When the diode is reverse biased, and it is not light exposed, the J$_0$ would be the only current flowing in the diode, also known as *dark current density*.

From the Eq. (2.20) it is possible to note that the reverse saturation current density is related to the doping level and the thicknesses of the P$^+$ and N$^-$ regions, and the diffusion lengths. The most important thing to note is the direct proportionality with the square of the intrinsic carrier concentration, which grows exponentially with the temperature, as shown in to paragraph 1.2.2.1.

Obviously, this can be a serious problem, especially when the diode has to work as a photodetector for an image sensor. In fact, in reverse bias conditions, being it the only current present inside the diode, if this grows too much with temperature, even when the photodiode is not light exposed, the sensor would detect a current significantly different from zero, only because of the increase in temperature having so a mistake in the device's behavior.

Fortunately, this is not a significant problem for the 4H-SiC which, thanks to its high bandgap, has a low intrinsic concentration, both at room temperature, where n_i is about 8.6×10^{-9} cm^{-3} (compared to silicon that at room temperature has a n_i of about 10^{10} cm^{-3}), and at very high temperatures such as, for example, 800 K, where the intrinsic concentration is 1.92×10^{11} cm^{-3}.

In fact, analytically results show that realizing a P$^+$N$^-$ diode in 4H-SiC with a P$^+$ region with a doping level of 10^{19} cm^{-3} and a thickness of 0.3 µm, and a N$^-$ region doped to 10^{15} cm^{-3} with a thickness of 10 µm, the diffusion current density, at 0 V, is equal to only 10^{-49} A/cm^2.

The significant advantage to use a photodiode in 4H-SiC in the realization of an image sensor is that it can work at high temperature (in addition to all the other thermal and electrical properties of the silicon carbide itself).

But, before going on, it is important to focus the attention on one thing. At low temperature, such as room temperature, the thermal agitation and the presence of trap centers in semiconductors, cause the presence of a generation and recombination current density, J_{gr}, that must be taken into account in the calculation of the total current density, since it especially dominates at low temperatures.

In fact, when the photodiode is in reverse bias conditions, given the low carriers concentration of the entire depletion region ($pn << ni^2$), the dominant generation processes are those of generation-recombination. The generation and recombination of electrons and holes within the semiconductor, arises when there are recombination centers, or traps, which can be surface defects, crystal lattice dislocations, substitutional or interstitial impurity atoms, etc. This causes the creation of a current due to the carriers generation within the depletion region, causing that the total reverse current, that running through the PN junction, is given by the sum of the diffusive component of the neutral regions (J_0 previously analyzed, i.e., J in reverse bias conditions), and the generation current in the depletion region. The analysis of the generation-recombination current can be carried on using the Shockley-Read-Hall theory for generation-recombination processes.

It is possible to demonstrate that this generation-recombination current density, J_{GR}, which arises from indirect mechanisms in the the space charge region, is given by the following equation:

$$J_{gr} = \frac{q \, n_i}{2 \, \tau_m} \left(\frac{2 \, \varepsilon_0 \, \varepsilon_{SC} \, (N_a + N_d)}{q \, (N_a \, N_d)} \right)^{1/2} \sqrt{V_{bi} - V} \qquad (2.21)$$

where τ_m is the avarage value of the carrier lifetime in s, V_{bi} is the built-in voltage in V (that, for the silicon carbide, is about 3 V at room temperature), V is the external voltage applied in V, ε_0 is the vacuum dielectric constant, ε_{SC} is the silicon carbide dielectric constant in F/cm, N_a is the acceptor doping and N_d is the donor doping in cm^{-3}.

Considering the same diode above decribed, it is analytically observed that, at room temperature and with a voltage of 0 V, the generation and recombination current is almost 10^{-25} A/cm^2 [16]. This evidences that this current cannot be neglected at low temperatures. Thus, the total current density is given, as previously mentioned, by the sum of the diffusion current density, in reverse bias, and the generation-recombination current density:

$$J_{total} = -J_0 - J_{gr} \qquad (2.22)$$

Comparing the equations (2.20) and (2.21) it is possible to observe that J_0 is proportional to ni^2, while the J_{gr} is proportional to n_i. Both exponentially depend on the temperature but, for temperatures between 300 and 400 K, since the negative sign of the exponent, n_i is much greater than ni^2, which implies that the dominant term in Eq. (2.22) is J_{gr}. Instead, when the temperature grows beyond 400 K, the exponent becomes positive, and J_0 grows much faster of J_{gr}, implying that the dominant term in Eq. (2.22) is J_0.

Therefore, neglecting J_0 at low temperatures, and considering that J_{total} is approximately equal to $-J_{gr}$, if a P^+N^- junction is considered, Eq. (2.21) can be approximated as follows:

$$J_{gr} = \frac{q \, n_i}{2 \, \tau_m} \left(\frac{2 \, \varepsilon_0 \, \varepsilon_{SC}}{q \, N_d} \right)^{1/2} \sqrt{V_{bi} - V}$$

(2.23)

and placing:

$$W = \left(\frac{2 \, \varepsilon_0 \, \varepsilon_{SC}}{q \, N_d} \right)^{1/2} \sqrt{V_{bi} - V}$$

(2.24)

where W is the depletion region width, it is possible to emphasize the dependence of $J_{total} \approx - J_{gr}$ from the depletion region width, as it is shown in the following equation:

$$J_{gr} = \frac{q \, n_i \, W}{2 \, \tau_m}$$

(2.25)

Hence, the Eq. (2.25) shows that, at low temperatures, the total current is directly proportional to the extension of the space-charge region which, in turn, is directly proportional to the reverse voltage applied, in addition to being a generation-recombination current.

Since the purpose of this thesis is to investigate what happens at high temperatures, it is not a great mistake to assume negligible this thermal generation current, and consider only the diffusive component. In any case, both from the simulations (including in the simulations the generation-recombination mechanisms [44]) and from the experimental measurements, the sum of both currents will be shown, regardless of whether it is a generation-recombination current or a diffusion current.

At this point, if the diode is reverse biased and light exposed, in steady-state conditions, in addition to the diffusion current J_{diff} (which, in reverse bias, would be simply the reverse saturation current J_0), there will be also the presence of a current that is generated within the space charge region, which would be a *drift current*, since, in this region, the carriers generated by light absorption will move under the effect of a high electric field due to the same outside voltage applied [31]:

$$J_{tot} = J_{dr} + J_{diff}$$

(2.26)

where J_{dr} is the drift current due to the generated carriers within the space charge region, and J_{diff} is the diffusion current due to the carriers generated outside the depletion layer (i.e. in the neutral regions), and that spread to the space charge region to be separated and collected in the corresponding regions.

Besides that, neglecting the thermal generation current, the assumption that the thickness of the P^+ region is smaller than the absorption depth $1/\alpha$ is added [31].

In order to calculate the drift current, we must first evaluate the electron-hole generation rate $G(x)$, defined as the number of pairs generated per unit volume and unit time, and it is equal to:

$$G(x) = \Phi_0 \, \alpha \exp(-\alpha \, x) \qquad (2.27)$$

where Φ_0 is the incident photon flux per unit area and unit time, that is possible to derive from Eq. (1.40), remembering that the effective optical power that enters the device, and that what will actually be converted into electron-hole pairs is only an amount of the power incident on the outside, because of the reflection at the surface. In fact, if the incident optical power outside the device is defined with P_{inc}, and with RP_{inc} is defined the optical power that is reflected on top surface, the power that will enter in the device will be $P_{inc}(1-R)$, and the incident photon flux will be:

$$\Phi_0 = \frac{P_{inc}(1-R)}{A \, h \, v} \qquad (2.28)$$

where R is the reflectance and A is the diode area. Then, it is possible to write the Eq. (2.27) as follows:

$$G(x) = \frac{P_{inc}(1-R)}{A \, h \, v} \, \alpha \exp(-\alpha \, x) \qquad (2.29)$$

As discussed before, both the reflectance and the absorption coefficients are wavelength dependent. Therefore, theoretically, to know how the photons are absorbed when the incident radiation penetrates, and decays exponentially within the device, this analysis should be repeated for each wavelength.

Starting from Figures 1.14 and 2.25, in Figure 2.31 is shown the generation rate for a wavelength λ equal to 270 nm, at which α is equal to 7.65×10^4 cm^{-1} and R is equal to 0.2. Furthermore, an incident optical power P_{inc} of 10 μW, a device with an area A of 975x875 μm^2 and an intrinsic region with a thickness of 1 μm, have been considered (this dimension is equal to that of one device that will be subsequently simulated).
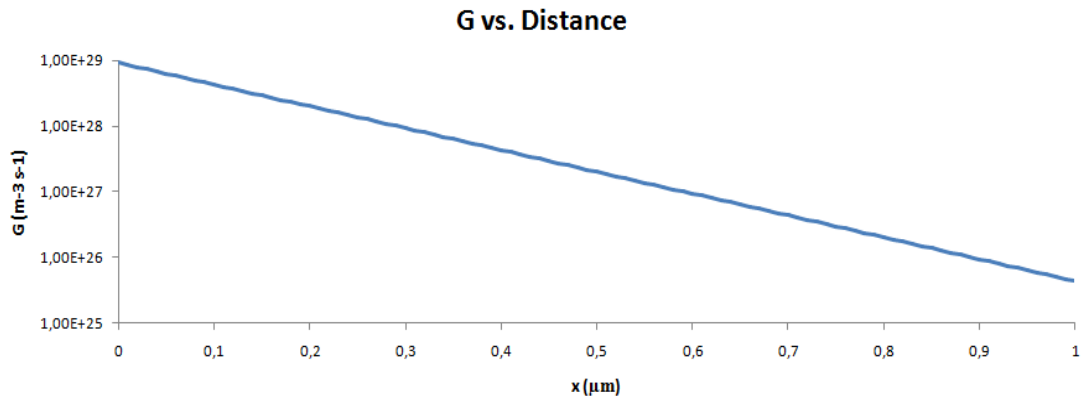
Figure 2.31. Carrier generation vs. distance from the top in 4H-SiC at 270 nm in log-scale.

From Figure 2.31 it is possible to observe that the radiation at 270 nm is efficiently absorbed within the device, since there is an uniform carriers generation within the same. Of course, the device thickness, the depletion of the intrinsic region, etc., are important parameters to evaluate because a wrong sizing of the device can result in an inefficient photoconversion, as shown in Figure 2.32.
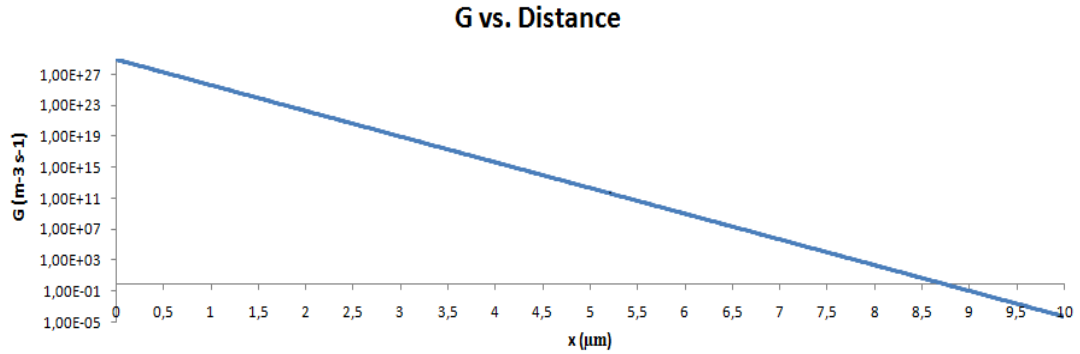
Figure 2.32. Carrier generation vs. distance from the top in 4H-SiC at 270 nm in a log-scale plot.

In this figure it is possible to see that assuming that the thickness of the P^+ and N^+ regions are very small (tenths of a micron, to greatly reduce the absorption both at the surface and in depth), the best choice is to choose an intrinsic region with a thickness of 4-5 µm at most to avoid an inefficient photoconversion, setting an external reverse voltage able to completely empty the intrinsic region itself.

Obviously, this reasoning can be repeated for different wavelengths, for the same incident optical power, to properly size the intrinsic region thickness, to optimize the carriers generation within the device, as can be observed from Figure 2.33 (note that it is useless to calculate it for thickness values greater than 1 µm, because, for small wavelengths, such as 190 nm, G is already zero after 0.6 µm).
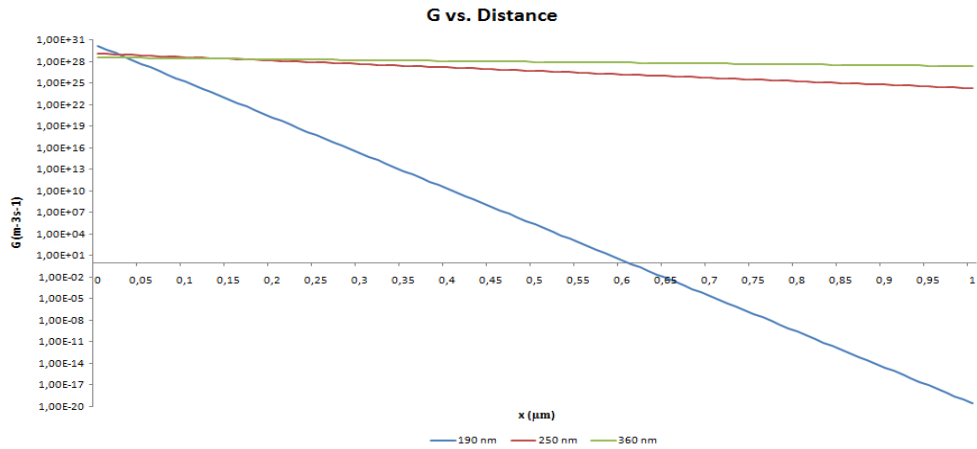
Figure 2.33. Carrier generation vs. distance from the top, in 4H-SiC, at 190 nm, 250 nm and 360 nm in log-scale.

Given the carriers generation rate, it is possible to calculate the drift current in the following way [31]:

$$J_{dr} = q \int_0^{W_D} G(x)\,dx = q\Phi_0[1 - \exp(-\alpha W_D)] \qquad (2.30)$$

where W_D is the depletion layer width. It is noted that in the space-charge region a quantum efficiency of 100% has been assumed to consider that each incident photon exactly generates one electron-hole pair useful for the drift current. Otherwise, the optical power that actually penetrates into the device also has to be multiplied for the quantum efficiency itself [31].

Therefore, from Eq. (2.30) it is noted that if the depletion region is extended as much as possible, there will be a higher absorption of photons inside the region, and thus a greater drift current.

Before proceeding in the calculation of diffusive component of the photocurrent, two assumptions will be done. The first assumption is that the intrinsic region is completely depleted, to assume the intrinsic region width exactly equal to W_D (crucial for the functioning of the pin diode itself). The second assumption is that the surface absorption is neglected, to do not consider the production of the carriers in the P^+ layer, in order to focus the attention only on the diffusion towards the intrinsic region of the minority carriers generated in the N^+ layer, i.e. the holes.

For $x>W_D$, it is possible to obtain the minority carriers density in the N^+ region using the one-dimensional diffusion equation (also known as one-dimensional continuity equation) for the holes in the N^+ region, supposing to be in steady state conditions (in order to cancel the time-dependent term dp/dt) and including the generation terms and the recombination terms considering the recombination velocity in a N-type semiconductor. In low injection conditions, and using the SRH theory, it is possible to derive that $U = p_n\text{-}p_{n0}/\tau_p$ (where $p_n\text{-}p_{no}$ would be the holes excess in N^+).

Therefore, it gets [31]:

$$D_p \frac{\partial^2 p_n}{\partial x^2} - \frac{p_n - p_{n0}}{\tau_p} + G(x) = 0 \qquad (2.31)$$

where D_p is the holes diffusion coefficient, τ_p is the carriers lifetime, and p_{n0} is the equilibrium holes density ($p_{n0} \approx ni^2/N_D$).

Imposing the following boundary conditions:

$$p_n = p_{n0} \quad for\ x = \infty \qquad (2.32)$$

$$p_n = 0 \quad for\ x = W_D \qquad (2.33)$$

the solution of Eq. (2.31) is given by [31]:

$$p_n = p_{n0} - [p_{n0} + C_1 \exp(-\alpha W_D)] exp\left(\frac{W_D - x}{L_p}\right) + C_1 \exp(-\alpha x) \qquad (2.34)$$

where $L_p = \sqrt{D_p \tau_p}$ is the hole diffusion length, and the constant $C_1 \equiv \left(\frac{\Phi_0}{D_p}\right)\frac{\alpha L_p^2}{1 - \alpha^2 L_p^2}$. The Eq. (2.33) is not surprising because the minority carriers density goes to zero at the edge of the depletion region, in a reverse biased diode [9].

At this point, it is possible to derive the diffusion current, as follows [31]:

$$J_{diff} = -q D_p \left.\frac{\partial p_n}{\partial x}\right|_{x=W_D} = -q \Phi_0 \frac{\alpha L_p}{1 + \alpha L_p} \exp(-\alpha W_D) - \frac{q p_{n0} D_p}{L_p} \qquad (2.35)$$

Doing the sum of the diffusive component external to the depletion region, i.e. Eq. (2.35), and the drift component within the depletion region, i.e. Eq. (2.30), the total current density in the device is obtained:

$$J_{tot} = -q \Phi_0 \left[1 - \frac{\exp(-\alpha W_D)}{1 + \alpha L_p}\right] - \frac{q p_{n0} D_p}{L_p} \qquad (2.36)$$

Thus, as can be seen from Eq. (2.36), the total current density is given by the sum of a first component related to the flow of incident photons, when the device is illuminated, and a second constant component (when the temperature is fixed), which does not vary with the incident photon flux. This result is not surprising, since, if the device works in dark conditions, i.e. Φ_0 is zero, the first term vanishes, and only the constant term remains, representing nothing more than the reverse saturation current of a typical reverse biased diode, as predicted by the equations (2.19) and (2.20).

Under illumination conditions being the second term negligible compared to the first the reverse current of the diode is in direct proportion with the incident photon flux.

Obviously, the second term of the Eq. (2.36) exponentially depends from the temperature (through ni^2 in p_{n0}). This means that, if a Φ_0 value is fixed, when the temperature increases, the second term can (in absolute value) increase the J_{tot}. To understand if J_{tot} changes, or not, due to the second term variations, it is possible to follow two paths: $\partial J_{tot}/\partial T$ is analytically calculated, or the trend is automatically observed by simulations and experimental results. Since in the Eq. (2.36) a lot of terms depend from the temperature (and for the 4H-SiC, in literature, these data are not present), the second path will be followed.

Furthermore, the external quantum efficiency, previously defined in the Eq. (2.5), should also be recalculated. Using the equations (2.35) and (2.36), one obtains [9]:

$$\eta = \frac{|J_{tot}/q|}{P_{inc}/A\,h\,v} = (1 - R)\left(1 - \frac{\exp(-\alpha W_D)}{1 + \alpha L_p}\right) \qquad (2.37)$$

Therefore, from the Eq. (2.37), it is observed that the quantum efficiency is reduced from the value of 100%, due to the reflection R and the light absorbed outside the depletion region [31]. To achieve high quantum efficiencies, therefore, the upper part of the photodiode must be varied, to appropriately reduce the reflectance R, and to make sure that αW_D is much greater than 1. If the absorption coefficient is small (which means that the device is not effectively skillful to absorb certain wavelengths), to increase the collection efficiency, it is necessary to extend the depletion region as much as possible. Vice versa, if the absorption coefficient is high (which means that the device is effectively skillful to absorb certain wavelengths), then it is possible to safely reduce the depletion region.

Obviously, choosing the depletion region thickness one must take into account also an important trade-off. When the depletion region extends, the extension increases the time that the carriers employ to cross the depletion region itself, before being collected. This implies that the device, from a speed response point of view, becomes very slow. Therefore, it is always preferable a device with a high absorption coefficient and a reduced W_D. Unfortunately, the absorption coefficient is not something that the designer can decide, because it depends on the material type and, therefore, it cannot be changed without changing the material itself.

In many applications and where low light levels should be detected, it is desirable to have a photodetector that is as sensitive as possible, possibly using an internal current gain. To do this, the so-called *avalanche photodiodes* (*APD*) are used. These diodes can be simple pin diodes, where the only difference, compared to those shown above, is that the diode, when reverse biased, is led to operate near the *breakdown voltage*. In this case, the photogenerated carriers, within the depletion region, travel at their saturation velocity, and if they gain sufficient energy, thanks to the field present within the depletion region, they can trigger, via collisions with the lattice atoms, an *impact ionization* process. Typically, the field required to produce the impact ionization is in the order of 10^4 - 10^5 V/cm and it can be sustained by the silicon carbide without any problem. Then, the primary carriers, for impact ionization, give rise to secondary electron-hole pairs which, in turn, traveling in opposite directions, under the field action, and impacting with the lattice, can generate other carriers, and so on. This process, known as *impact ionization* or *avalanche multiplication*, leads to a carriers multiplication and, hence, to an internal gain.

The impact ionization process is a three-carrier collision process [9], because, thanks to the high energy acquired by the primary carriers (i.e. kinetic energy, since, in the depletion region, the high field causes that the carrier has a very high drift velocity, and in particular the saturation velocity, which leads to an increase of the kinetic energy of the carrier itself), one can get a new electron-hole pair for collision with a lattice atom. Typically, the impact ionization energy of the primary carriers must be greater than the bandgap energy, if, bumping with an atom in the lattice, it wants to generate a new carriers pair (that is also valid for the secondary carriers, to create new electron-hole pairs).

The avalanche process is a random phenomenon and it is an asymmetric process. It is a random phenomenon because even if the breakdown voltage is applied, one cannot be sure that the carriers accelerated by the field, are actually able to trigger the impact ionization phenomenon. To achieve this, they must acquire an energy greater than the bandgap, and this must happen in a space less than their mean free path, because if they bump before

acquiring sufficient energy they do not generate any carrier for impact ionization. Furthermore, this process is asymmetric because the probability of starting the avalanche is typically higher for a type of carrier rather than another (for example, in silicon, the ionizing collisions are 30-50 times more frequent for electrons than for holes [9]).

Therefore, to study the avalanche process, a very important parameter has to be considered, which is the *impact ionization coefficients* α_A, particularized both for electrons and for holes, as already discussed in section 1.2.2.3. They are of crucial importance because they represent the reciprocal of the average distance covered by the electrons and holes, in the direction of the electric field, to create electron-holes pairs. Furthermore, these coefficients are also defined as the average number of ionizing collisions per unit length and, therefore, represent nothing more than the number of secondary carriers generated per unit length [9]. If W_D is the region width in which the avalanche phenomenon is triggered (that generally coincides with the depletion region width), the amount $\alpha_A W_D$ represents the probability to obtain an ionizing collisions. This, being a probability, cannot become greater than 1, because it would mean that it can generate carriers, for avalanche, within the W_D region also without injecting any carriers inside.

Therefore, due to the triggering of the impact multiplication phenomenon for photogenerated carriers, the device output current appears to be amplified of a quantity M_{ph}, called *multiplication factor* due to impact ionization (or *avalanche gain*), that can be described by an empirical relationship as follows [31]:

$$M_{ph} = \frac{I - I_{MD}}{I_P - I_D} \tag{2.38}$$

where I is the total multiplied current in A, I_P is the primary (non multiplied) photocurrent in A, and I_D and I_{MD} are, respectively, the primary and multiplied dark currents in A [31]. Starting from this empirical relationship, it can be shown that the avalanche gain, is given by [31]:

$$M = \left\{ 1 - \int_0^{W_D} \alpha_n \exp\left[-\int_x^{W_D} (\alpha_n - \alpha_p)\, dx' \right] dx \right\}^{-1} \tag{2.39}$$

where W_D is the depletion-layer width, and α_n and α_p are, respectively, the electron and hole ionization rates [31].

Typically, as shown also by Eq. (1.24), the ionization coefficients α depend on the electric field, which is not generally uniform along the depleted region, i.e. α is an $\alpha(E(x))$ function. But, if it is assumed, like in the case of a pin diode, given the low intrinsic region doping, a practically constant field (see Figure 2.30) in the intrinsic region itself can be assumed (the intrinsic region is now assumed coincident with the emptied region W_D). This means that is possible to consider the ionization coefficients as position-independent (i.e. independent from x).

Assuming that the ionization coefficients for electrons and holes are equal, and equal at α, it is obtained that the avalanche gain, at $x = 0$, is equal, simply, to [31]:

$$M = \frac{1}{1 - \alpha W_D} \tag{2.40}$$

As can be seen from Eq. (2.40) the breakdown is reached when the current goes to infinity, as described in Eq. (2.38), i.e. when αW_D becomes 1, which means that the probability of ionizing collisions is maximum, or that each carrier has an ionizing collision.

The breakdown analysis has been reported just for completeness but, as can be seen from Eq. (2.38), in the amplification phase of the total output current, when the avalanche process starts, not only the photogenerated current is amplified, but the dark current too. Obviously, this is a serious problem, especially when the photodetector has to be used as the basic element in an image sensor. In fact, if the diode is reverse biased close to the breakdown voltage, but it is not hit by photons, the high amplification of the dark current would be interpreted, by downstream circuitry, as if the diode works under light exposure, when it is not so, leading to misinterpretations. Therefore, from this point of view, when the diode works as a basic element in an image sensor, the dark current amplification is seen as a noise source (or disorder) in the photography, and it must be kept under control. In other words, this means that the breakdown should never be reached. In the subsequent simulations the breakdown voltage as the temperature varies will be derived, just to have an idea of which are the reverse voltages values that are possible to use, before reaching the onset of breakdown.

2.2.3.4 Equivalent circuit of a PIN diode

For the analysis that will follow it is important to introduce a pin photodiode's equivalent circuit, as shown below [9].
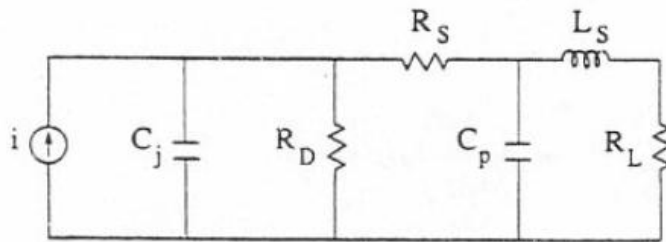
Figure 2.34. Equivalent circuit of a pin photodiode [9].

In the equivalent circuit shown in Figure 2.34, the pin diode has been modeled as the parallel of a constant current generator i, which represents the photogenerated current (for a certain wavelength value) and a capacitor C_j, which represents the photodiode junction capacitance and arises because of the presence of the depletion region itself and it is

69

therefore related to its extension and thus to the reverse voltage applied. In fact, being the diode reverse biased, it is possible to have a significant increase in the depletion region extension and, consequently, an increase of the parasitic capacitance effect, related to the space charge region itself.

As already anticipated in section 2.2.2, the diode can be treated, substantially, as a capacitor (i.e. the junction capacitance) that is charged to a voltage exactly equal to the reverse voltage set from the outside. When the light arrives (and then generates the constant photogenerated current), the photogenerated current, that passes through the photodiode (from the cathode to the anode), causes a discharge, at constant current, of the same capacitor, of a certain amount proportional to the intensity of the photogenerated current (and, thus, at the intensity of the incident radiation).

The junction capacitance can be calculated, approximately, as follows:

$$C_j = \varepsilon_0 \varepsilon_{rSiC} \frac{A}{W_D} \tag{2.41}$$

where A is the surface of the P^+ and N^+ regions (i.e. the junction area), and W_D is the depletion region width.

In Figure 2.34 other important parameters for the representation of an equivalent circuit of a pin diode are also reported. C_p is a parasitic capacitance, external to the wafer, and it represents the sum of the coupling capacitance between the contacts, the various interconnections and the wafer (also known as *fringing capacitance*) and the coupling capacitance between the package (or encapsulation) and the wafer (or, also, coupling capacitance between contacts and the power supply or the ground). L_S is the total series inductance, mainly due to the length of the interconnections and contacts. R_D, also known as *shunt resistance*, or *junction resistance*, is mainly due to carriers that cross the space charge region, which has a high value at zero voltage and in reverse bias condition. In fact, thanks to the space charge region extension, because of the low doping and of the low conductivity in this region, this is a region devoid of free carriers, which makes this region as an insulating layer inside a doped semiconductor. Furthermore, this resistance is very small in direct polarization (given the limited extension of the space charge region itself). R_S, also known as *series resistance* of the diode, represents the sum of the resistances of the contacts (also known as *spreading resistance*), and the resistances of the neutral regions of the diode (these contributions are low given the high doping of the neutral regions). R_L, instead, is a load resistance, which represents all that is downstream of the diode itself.

Of course, given that the diode works in reverse bias, the so-called *diffusion capacitances* associated at the neutral regions have been neglected. They can be calculated, simply, as the charge variation injected in the neutral regions at the variation of the applied voltage. In fact, now, the diode does not work in forward bias, and therefore there are not diffusive mechanisms [9].

Given the typical values of these parameters [9], if an infinite resistance R_D is considered (typical values are hundreds of MΩ), a zero resistance R_S (typical values are tens of Ω), and capacitive and inductive effects are neglected (typical values of C_p are of fF, and L_S are

of pH), considering that the diode works connected to a load theoretically infinite (which is possible if the diode works without any load, or if it is connected to a load resistance theoretically infinite, as a *MOSFET* gate resistance), the ideal equivalent circuit of the pin diode becomes equal to the circuit shown in Figure 2.35.
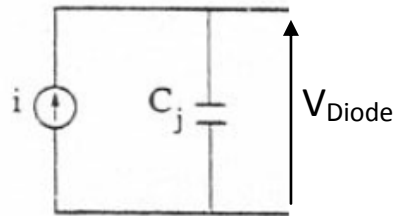
Figure 2.35. Ideal equivalent circuit of a pin photodiode.

2.2.4   Fabrication for 4H-SiC PIN diode

One of the pin diodes that will be simulated later was produced on a wafer (EB12rw) processed at KTH.

But, before showing the detailed description of the manufacturing process, it is interesting to introduce an overview on the technology used to fabricate silicon carbide devices.

To realize SiC devices it is possible to use the same technology used for the Si, except of some differences due to the high thermal stability and chemical properties of SiC [8].

For example, the *wet chemical etching* (etching process that use etchants in liquid phase), in SiC technology, is possible only at high temperatures because of strong chemical bonds between silicon and carbon. In fact, a *plasma etching* is preferable. In this case the etch process is assisted by the use of a *plasma* (it is an ionized gas, consisting of a set of electrons and ions and globally neutral, i.e. the total electric charge is null). The plasma is produced ionizing a gas in a vacuum system through the use of a radio frequency source (the RF operation frequency, of the power source, is frequently 13.56 MHz). The plasma etching allows to obtain an etch at lower temperatures because the plasma is an ionized highly reactive gas, and it is different than other etching processes requiring temperatures higher than 350 °C. Moreover, the dopant diffusion velocity within the silicon carbide is quite slow [7]. It forces, to obtain a certain doping profiles, to use *epitaxial growth* and *ion implantation* techniques [8]. Finally, all the thermal processes used for silicon, such as thermal oxidation, contact annealing, activation of implanted impurities, etc., require much higher temperatures when applied to the SiC.

In particular, the manufacturing process of the photodiode will be the same to that used for the realization of bipolar integrated circuits (IC), used at KTH, with only a few modifications.

In what follows an outline of the main manufacturing steps used to produce SiC devices is reported.

2.2.4.1   Wafer cleaning

To reduce the process uncertainty and to obtain better results in the next process steps, a cleaning of the surface of the SiC wafer is of fundamental importance. It consists, in the removal of organic contaminations (a compound in which one or more carbon atoms are joined via covalent bonds to atoms of other elements, mainly hydrogen, oxygen, and nitrogen) and inorganic contaminations (any chemical compound that does not contain carbon atoms), native oxides or previous process steps residues. This step is crucial, especially before the oxide deposition and metallization. There are several techniques for cleaning, *wet* or *dry*. Regarding the *dry cleaning* techniques, typically they use hydrogen or oxygen plasma to remove residues of the previous process steps, such as the hardened photoresist (after a lithography step).

Regarding the technique of *wet cleaning*, several recipes are used. They are shown in Table 2.3.

Description	Chemicals	Ratio	Temperature (°C)	Time	Removals
RCA SC1	$H_2O : NH_4OH : H_2O_2$	5:1:1	80-90	10 min	Organic
RCA SC2	$H_2O : HCl : H_2O_2$	5:1:1	80-90	10 min	Ionic/Metal
Seven up	$H_2SO_4 : H_2O_2$	3:1	90-110	5 min	Organic/Metal
IMEC	$H_2O : HF: C_3CH(OH)CH_3H$	100:1:1	25	100 sec	Oxide
Aqua regia	$HCl : HNO_3$	3:1	50	5min	Metal
Dilute HF	$HF : H_2O$	1:10	25		Oxide
BHF	$HF : NH_4F$	1:7	25		Oxide

Table 2.3 Standard recipes used for wet cleaning of SiC wafers [8].

For the manufacture of integrated circuits in SiC, before thermal oxidation or lithography for SiC etching, standard chemical products are used. They are Seven-Up and IMEC. At the same time BHF is used to remove native oxides before metallization. RCA SC1 and RCA SC2 ("SC" stands for *standard clean*) are used, if necessary, after the SiC etching.

2.2.4.2   Epitaxial growth

Epitaxial growth is a process to deposit a thin layer of single-crystal material on single-crystal substrate. Epitaxial growth occurs in such way that the crystallographic structure of the substrate is reproduced in the growing material (also crystalline defects of the substrate are reproduced in the growing material [33]). This is a fundamental step for the SiC devices realization, since it allows to obtain layers with a purity level much higher than those that are typically exhibited by the substrate. This is very important because the electrical properties of a device do not depend only on their design but also on the amount of defects in the same. For this reason, a process, to realize SiC devices, starts from a SiC substrate above which epitaxial layers are grown. The growth of these layers is done

through the use of techniques of *chemical vapor deposition* (CVD), if the growth rate required is fairly low. Instead, if a higher growth rate is required, other techniques have to be used, like *liquid-phase epitaxy* (LPE, that is a method to grow semiconductor crystal layers from the melt on solid substrates) or *sublimation epitaxy technique* (the sublimation of a substance is the transition phase from solid to gaseous state, without passing through the liquid state) [8]. Typically there is a trade-off between growth rate and quality of the layer increased. In particular, if a high growth rate is required, i.e. below 1 mm/h, the quality has to worsen, and vice versa [7].

2.2.4.3   SiC etching

The Etching is an important step to achieve mesa structures that define the photodiode regions. *Dry etching techniques* (anisotropic and selective techniques, due to the high difference between vertical and lateral attack speed), such as *reactive ion etching* (RIE) or *inductively coupled plasma* (ICP) [7], are typically used for silicon carbide etching, since *wet chemical etch* are difficult to control because of its isotropic properties (i.e. the attack speed is the same both in the vertical direction than in the horizontal direction). Wet etching does not allow to obtain net the trenches necessary for the SiC structure that it must obtain, besides that require high temperatures (> 350 °C), because of the strong bonds between the atoms of silicon and carbon [8]. In the photodiode that has been realized, HBr and Cl_2 etching have been used, with photoresist masks, to realize the mesa structures (which would be nothing more than the emitter, base and collector regions in the bipolar process used). The oxide masks are preferred to the metal masks (the masks are necessary to suitably impress the photoresist in specific regions), since the first permits a better protection of the SiC regions that must not undergo the etching process than the second and, furthermore it allows to avoid the so-called *trench effect* along the side walls. This effect essentially consists in a consumption of the SiC at the edges of the mask, which becomes increasingly greater moving from the top to the bottom of the layer subjected to the process of selective etching, because the metal tends to reflect the ions sent for the etch to the lower region of the layer, causing a greater etching in the lower part than in the upper one. Furthermore, avoiding the use of metal masks is better, if possible, because they can contaminate the furnace, causing serious problems, especially during thermal oxidation [8].

2.2.4.4   Lithography

Seven lithography steps are required to realize the BJT and the photodiode. The lithography process is the same used for silicon. First of all, the process starts with a coverage of the device with photoresist, which is a substance sensitive to UV radiation. The photoresist can be positive or negative. In the first case the substance of which it is composed inhibits the dissolution where the material has not been impressed by the light. In the same time, the UV light dissolves the bonds only in the areas that have been light

exposed. Then, the exposed areas are removed. In the second case the photoresist contains a small percentage of photosensitive agent that promotes the formation of bonds between the molecules of base when exposed to UV light. Therefore, under the action of UV radiation, the film hardens, allowing the removal, through solvents, only of the parts not exposed to light [32]. Then, a glass (quartz) mask, on which the design with the windows to be opened on the wafer is reproduced, is overlapped to the wafer itself. Subsequently, the not useful resist dissolves and can be easily removed with suitable substances, such as sodium hydroxide.

For the manufacturing process of the photodiode a *stepper* has been used. The *stepper* is a machine that allows to impress the photoresist, aligning the masks and focusing the UV radiation through an appropriate system of lenses on the wafer covered with the resist, even from a distance of several centimeters from the same wafer. This is useful to reduce the image printed on the resist and create structures for hundreds of dies, moving continuously the wafer under the lens of the stepper itself. The *stepper* that is used is the g-line DSW 8500/2035 5:1, with a resolution of 1 μm, due to the large features of the components designed for this work. A 2-inch SiC substrate was placed on a 4-inch Si substrate wafer, since the machine is calibrated for a technological process for silicon wafers of 4 inches. Obviously, this requires further steps to achieve an adequate alignment accuracy during the lithography [8].

2.2.4.5   Ion implantation

The only available technique to perform a selective doping in silicon carbide is the ion implantation. In fact, as previously mentioned, if the thermal diffusion is used in SiC, the dopant will have a low diffusion velocity within the lattice itself [7]. Moreover, ion implantation is the technique most widely used when high dopant concentrations are required, such as, for example, highly doped ohmic contacts or devices isolations have to be realized. The ion implantation is done at high temperatures (typically between 300-800 °C), to minimize the possible crystallographic damages. Furthermore, the ion implantation is followed by an *annealing* step, always at high temperature (1500-1700 °C). This step is necessary to activate the dopant implanted and to reduce the damages suffered by the crystalline lattice following the ionic bombardment. In this way a SiC's re-crystallization is achieved, preserving, thus, the surface morphology and avoiding the presence of dopant *outdiffusion*. This undesired effect occurs at high temperature, where dopant atoms diffuse from the material with high doping level to the material with low doping level. This is common in high temperature epitaxial deposition where it does not allow to have a sharp change in dopant concentration between epi-layer and the substrate. Obviously, the temperature of epitaxial deposition must be reduced to control the outdiffusion [33]. Furthermore, during the annealing step, several important factors must be taken into account, to achieve the desired results in the process (time, temperature, ambient gases, etc. [8]).

2.2.4.6 Oxidation and oxide deposition

The thermal oxidation is an usually process performed at temperatures between 800-1200 °C, and it is a technique that forces an oxidizing agent to diffuse into the wafer at high temperatures and to react with it.

The manufacturing process of the SiC provides the possibility of thermally grow silicon dioxide, as well as the possibility to deposit it on the wafer surface, which is very interesting given that other materials with a high bandgap does not allow the formation of native SiO_2 oxides. In fact, the SiC is the only semiconductor compound, with wide bandgap, which allows the growth of native SiO_2 oxide, as the silicon, while other wide bandgap compounds, such as GaN (a direct bandgap semiconductor that generally crystallizes under the form of wurtzite with E_g = 3.510 eV at 0 K) and AlGaN (a direct wide bandgap semiconductor realized with an alloy of GaN, that has a wurtzite structure, and AlN, that has a zinc-blende structure, and whose bandgap amplitude depends on the molar fraction of GaN and AlN present in the compound that forms the AlGaN [34]), have high breakdown fields and high carrier mobilities, but, however, these III-V nitride compounds do not possess a native oxide similar to SiO_2 [35].

The thermal growth of the silicon dioxide is typically used as a sacrificial layer, to remove impurities or surface damage, or as a passivation layer for devices made in silicon carbide. Furthermore, it is used as mask, during the plasma etching and ion implantation, where the deposition of SiO_2 is preferred, thanks to the thicker oxide layers, on the order of *microns*, which can be realized. Comparing the process to the oxide deposition on silicon, it is necessary to take into account three main differences. The first is that the oxidation rate is much lower compared to the silicon. The second is the need to remove all the carbon atoms resulting from the oxidation process, since their presence at the interface SiC/SiO_2 can negatively affect the electrical properties. The third is the high consumption of SiC due to causes related to the first two points. Furthermore, the oxidation rate on a surface of carbon atoms is different from the oxidation rate on a silicon surface, since in the first case, the oxidation speed is faster than in the second (remember how is formed a SiC crystal as shown in Chapter 1).

To grow thick SiO_2 layers, PECVD technique is used. The *plasma enhanced chemical vapor deposition* is a deposition process that takes place inside vacuum chambers where the precursors (reagents starting to get a certain molecule or compound, vaporized and activated by the plasma) condense on the substrate surface forming coatings such as oxides, nitrides, carbides, metals, etc.

In the process realized at KTH, three etch attacks are required to make the N^+ emitter (this is for a BJT, while in the case of the photodiode, whit an etching of the emitter, the emitter is completely removed), base (P^+ region) and the collector plus (N^+ region). But, each attack is performed after a sacrificial oxidation in N_2O ambient, to reduce as much as possible damages caused during the etching process itself. This surface passivation is achieved with 50 nm of SiO_2 grown with PECVD technique, followed by a post oxide annealing in N_2O at 1150 °C for three hours [36], in order to reduce the surface recombination. Another thick SiO_2 layer with a thickness of 2 μm was deposited as

intermediate dielectric, after the definition of the contacts, and before the final metal layer deposition [8].

2.2.4.7   Metallization

In the SiC process technology, different metallization techniques must be taken into consideration, based on their purpose: formation of ohmic contacts or interconnections. Before performing the metallization, a surface cleaning is required. After, there is the metal deposition followed by patterning, or the patterning followed by metal deposition. For example, a case where the patterning is performed before the metal deposition, is the *lift-off process*. In this process a sacrificial layer is first deposited on the substrate, for example photoresist, inside which windows are opened through etching that represent the pattern to realize on the substrate. At this point the target material is deposited, for example metal, over the entire wafer area, which will cover both the part of the sacrificial layer, that was not attacked by etching, and the surface of the substrate in the windows opened with etching. Finally, the sacrificial layer and metal above it are washed away, using solvents. In this way also the material deposited on the top is lifted-off and washed together with the sacrificial layer below, so as to ensure that the deposited material (metal in this case) remains only where it has a direct contact with the substrate (i.e. where deposited within windows).

The realization of a good ohmic contact requires that the material is deposited in intimate contact with the semiconductor. This means that any residual oxide, photoresist or metal contamination, must be removed from the surface of the semiconductor itself with a surface cleaning. After the metal contact realization, an annealing follows at a high temperature (typically between 800-1000 °C), in an oxygen free environment, so as to favor the reaction between metal and SiC, and to form silicides (chemical compounds formed by metals and silicon atoms), in the case of Nickel (Ni) contacts, taking care not to perform an annealing at high temperature that could otherwise damage the passivation layer.

For the metal deposition different deposition techniques can be used, such as *sputtering*, *thermal evaporation*, *EBPVD* (*electron beam physical vapor deposition*), or *CVD* (*chemical vapor deposition*). The sputtering is a process where the atoms are ejected from a solid target after an ion bombardment on the same, for example with Argon's ions, and then migrate and deposit on the substrate surface. The thermal evaporation is a process where the source material is evaporated in the vacuum, so that the vacuum itself allows the vapor particles to travel toward the substrate and condense into a solid state on it. The EBPVD is a process where a target, the anode, is bombarded with a beam of electrons emitted by an electrified tungsten filament, in conditions of ultra vacuum. After the bombardment, the target atoms are emitted in gaseous phase, which precipitate in solid form, and cover everything inside the deposition chamber, including the substrate surface. The CVD is a process that allows to deposit on the substrate a thin film of material, starting from a certain molecular precursor introduced in gaseous form into the reaction chamber, and which reacts on the substrate surface itself. The transport of the precursor takes place

using a carrier gas, such as oxygen, argon, hydrogen, etc., thanks to which also all the gaseous products of decomposition will be moved away from the system, at the end of the reaction.

Sputtering allows to obtain a good adhesion of the metal to the substrate, but having a good step coverage it can be problematic in the lift-off process. In fact, in these cases, it is preferable the use of an evaporation technique, although it could suffer of poor adhesion to the substrate (note that in integrated fabrication the quality of the ohmic contacts and the quality of the interconnections is of extreme importance to obtain high performance of devices and circuits, and to reduce the power loss).

For the photodiode realization, both evaporation technique and sputtering have been used.

The E-beam evaporation has been used to deposit the Nickel to realize the emitter (it is possible to realize a photodiode etching completely the emitter region if it is needed) and collector contact (i.e., the N^+ region contacts), and to deposit a triple layer Ni/Ti/Al with a thickness ratio of 0.1/0.15/0.85 for the base and isolation layer contacts, to minimize as much as possible the ohmic contact resistance on the P^+ region itself [8,37]. Obviously, once deposited these three layers, they will not be three separate layers, because these three types of materials will bind realizing an alloy of Ni, Ti and Al. After each metal deposition, a lift-off process is used to pattern the contacts, and an annealing step is performed for 1 min, in an environment with Argon (Ar) and at a temperature of 950 °C, when a contact on a N region has to be realized, or 820 °C, when a contact on a P region is realized, to achieve low resistance ohmic contacts to the epitaxial layer.

The sputtering is used to deposit the metal layer for the realization of the wafer interconnections. The photodiodes were produced on a wafer where other SiC circuits are realized, where the interconnections are required to be able to face up three steps each of height of about 1 µm, due to the mesa structures of the base, emitter and collector (in the case of a BJT realization), without breaking or narrowing the interconnections. This means that a good metal coverage and a proper control of the its etching has to be ensured, because a poor coverage of the steps, or an overetch, may lead to an interruption in the interconnection.

2.2.4.8   IC technology process flow

The technological process used for the realization of 4H-SiC photodiodes is the same used for the realization of bipolar integrated circuits for high temperature applications [8]. In fact, the technological process flow for the realization of a NPN BJT and of a photodiode will be shown. The base contact is realized like a grid contact with a lift-off technique, in order to have large holes in the base contact that can allow the light to better penetrate inside the base, instead to be totally reflected. Furthermore, in a photodiode the emitter is not present. Therefore, where the realization of a pin diode is needed, an emitter etching is required. In fact, the photodiode is substantially realized utilizing the base, collector, and collector plus of a NPN BJT. The N^+ region in the BJT is necessary because it is not possible to deposit the metal, of the collector contact, directly on the lightly doped collector (i.e. the N^- region). Otherwise, a *Schottky* contact would be realized and, in this

case, an ohmic contact is not realized, but a *metal-semiconductor junction* that "*rectifies*" the current is realized instead.

Another interesting thing, that will be shown in the process flow, is the presence of a P^+ *isolation layer*, and an *emitter cap* directly deposited on the emitter, with a doping higher than the emitter's one. The P^+ isolation layer serves to isolate the various devices fabricated on the same wafer through the realization of a specific contact. The *emitter cap*, theoretically, would serve to realize a better ohmic contact, reducing the emitter contact resistance, even if, in this case, given the highly emitter doping, the *cap* can be removed, and the metal can be directly deposited on the emitter itself. In fact, for the photodiode realization, when the emitter etching is realized also the *cap* will be removed. Instead, if a phototransistor has to be realized, the removal of the *emitter cap* is still more useful, in order to reduce the number of epitaxial layers that the light has to traverse, before reaching the base, if it hit the device from the top of the same.

In Figure 2.36, given the structure symmetry of the BJT, the cross section of the entire structure it is not shown, but only the half structure. The process used in the realization of bipolar circuits, shown in Figure 2.37, starts from a substrate purchased from SiCrystal [38] on which six epitaxial layers were grown by Acreo [39]. The grown epitaxial layers are, from the bottom to the top, an insulation layer, a more doped collector layer, a less doped collector layer, a base layer, the emitter layer, a more doped emitter layer. Furthermore, the process also involves the use of seven masks, three for the definition of the mesa structures of the base, emitter and collector, one to realize N-type regions contact (N regions are doped with *Phosphorus*), one to realize P-type (P regions are doped with *Boron*) regions contact, one to realize via holes and one to realize the first metallization layer.
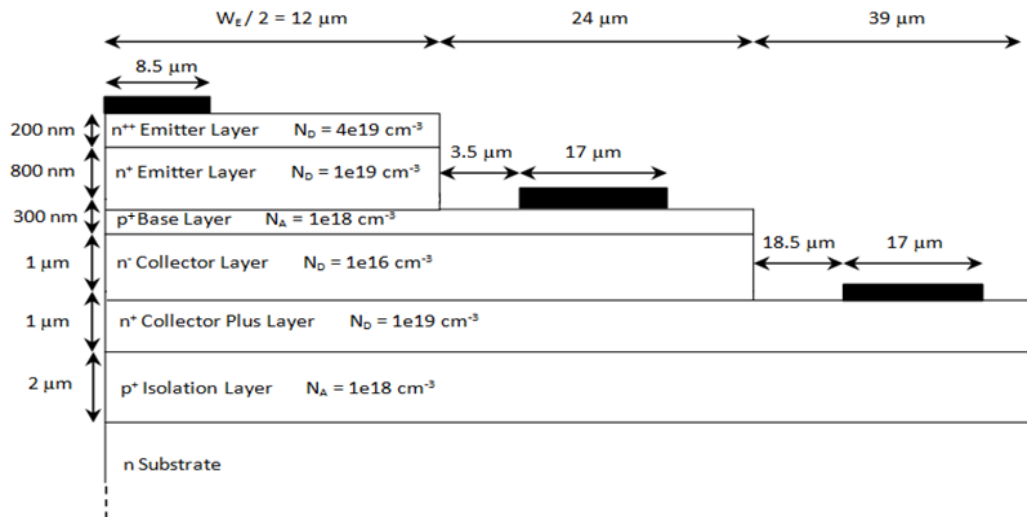
Figure 2.36. Half cross section of 4H-SiC NPN BJT. Over-etches, due to mesa structures, are neglected.
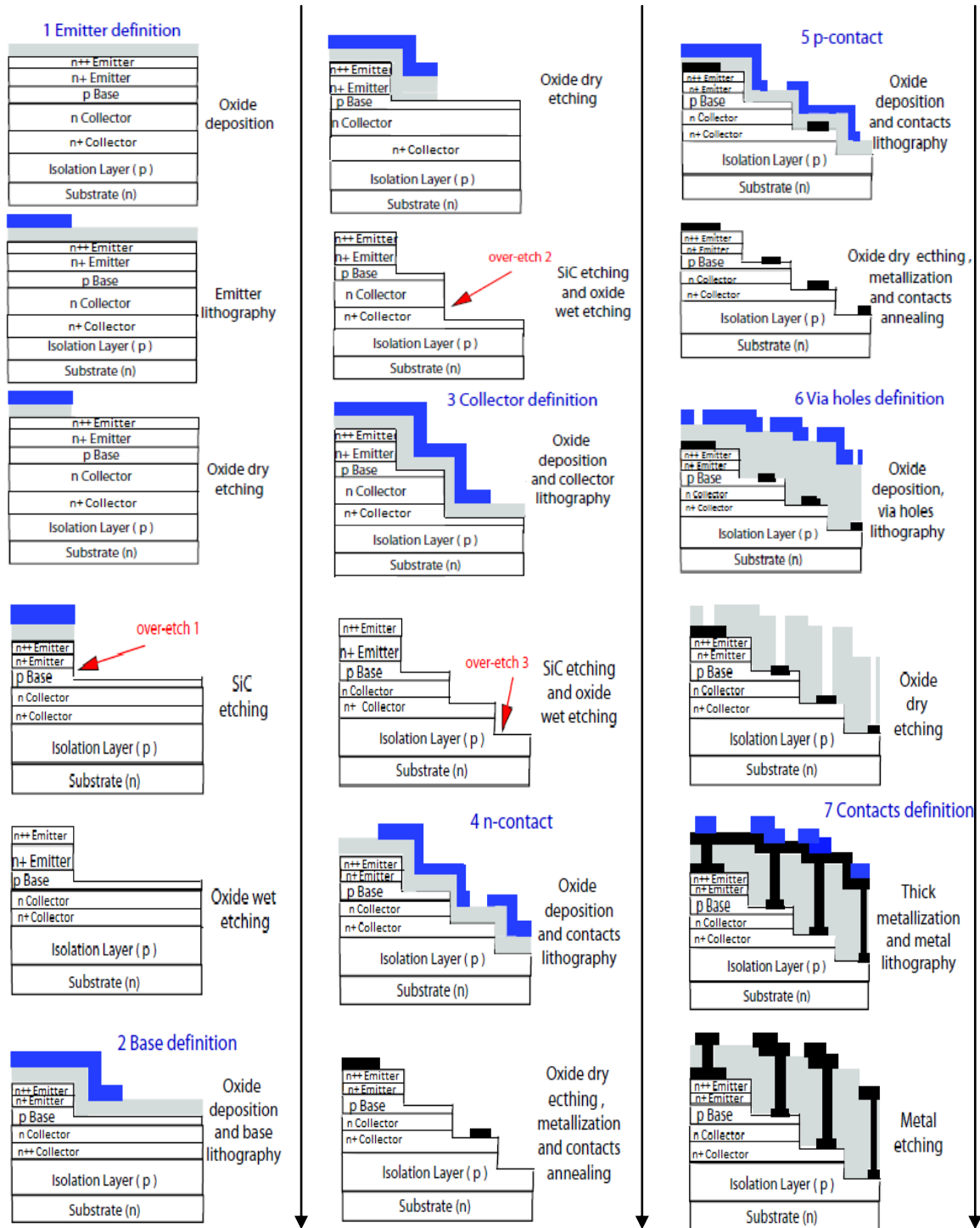
Figure 2.37. 4H-SiC BJT technology process flow [8].

The process shown in Figure 2.37, can be summarized in seven basic steps: 1) emitter etching, 2) base etching, 3) collector etching, 4) N^+ contacts metallization and annealing, for the contacts of the emitter and collector, 5) P^+ contacts metallization and annealing, for the contacts of the base and of the insulation layer, 6) via holes definition for the first level of interconnection, 7) definition of the first level of interconnection [8]. The process also provides a second level of interconnection, repeating again step 6) and 7), but, the Figure

2.37 shows only the first seven steps of the process, i.e. up to the first interconnection level.

At this point, some observations have to be made. The first thing to note is that the structure is initially formed by six epitaxial layers, grown with different thicknesses and dopings, as shown in the cross section in Figure 2.36. The reason to use an epitaxial growth, as previously anticipated, is related to the fact that the diffusivity rate of the dopant in SiC is very low, making it preferable to thermal diffusion to obtain appropriate doping concentrations. A second reason is related to the fact that, through the use of the epitaxial growth, it can grow layers with a purity level much higher than that typical of the substrate. To define the BJT contacts, different etchings of the SiC regions have to be executed. Through these etchings, the three regions of the BJT are realized as three mesa structures, with three different over-etches. The over-etch is a disadvantage of the typical etch process, due to the fact that one can never to obtain a perfect etch profile since some of the material below the etched area, will inevitably be consumed. This over-etch, in the considered BJT, is usually 100 nm for the used process [8]. Often, a little over-etch is also wanted, to be able to more precisely define the structure to build, otherwise the risk is to not completely attack the area of interest. In Figure 2.37 the over-etch is shown. Instead, they have been neglected in Figure 2.36.

The first over-etch is present in the phase of the emitter definition, where the etching has to be able to properly remove the portion of the emitter layer that is not needed, being careful to do not have a too deep over-etch, otherwise it can also etch the base, and consistently increase the resistance of the BJT base (it would reduce the section of the same).

The second over-etch is performed to define the base region (both the base that the collector under the base itself). This over-etch is made deep enough to reach the highly doped collector region. The third over-etch is obtained during the definition of the collector region, and it is also a very deep one and it reaches the isolation region, to eliminate the entire portion of the highly doped collector that it is not useful. Moreover, a dedicated contact for the P^+ isolation region has been realized. It is necessary to control the voltage drop across the collector-isolation layer junction that creates an insulation between the various devices, preventing that disturbs are transferred from one device to another.

In Figure 2.38 is shown a top view of the NPN BJT realized [8].
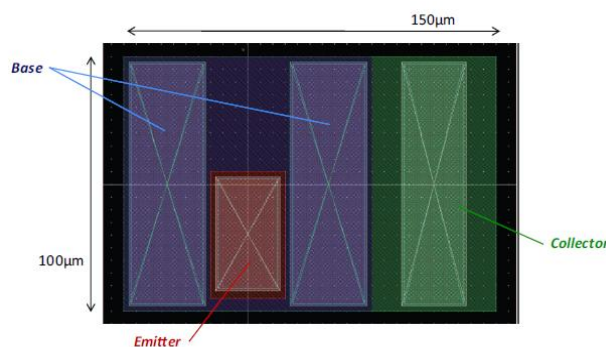
Figure 2.38. Top view of the entire NPN BJT structure [8].

In Figure 2.38, the collector contact area is 96 x 26 μm^2, the base contact (each one) is 96 x 31 μm^2 and the emitter contact is 50 x 26 μm^2.

Despite this work is focused on the investigation of the efficiency parameters of a photodiode realized in 4H-SiC, as possible future developments, the possibility of using the BJT in 4H-SiC like basic element for the photodetection (i.e. like a phototransistor) will also be investigated (through simulations).

As previously mentioned, on the same wafer, other devices are realized, including the photodiodes that have to be experimentally tested under UV light.

Compared to the process shown in Figure 2.37 for the realization of the BJT, the only two differences in the photodiode realization are the following. In the initial step, a total etching of the emitter of the devices that must work as photodiodes is realized. Furthermore, the grid base contact is realized using a lift-off technique.

Therefore, in Figure 2.39 a cross section of the entire photodiode realized is shown, in Figure 2.40 the process for the realization of the photodiode is shown, and in Figure 2.41 a top view of the device is shown.
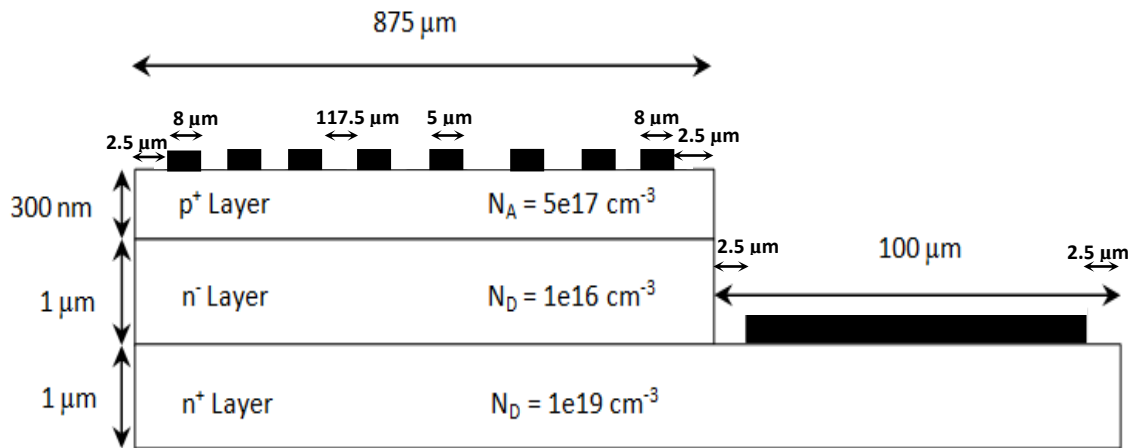
Figure 2.39. Entire cross section of 4H-SiC PIN Photodiode. Over-etches, due to mesa structures, are neglected.

Figure 2.40. 4H-SiC PIN Photodiode technology process flow [8].
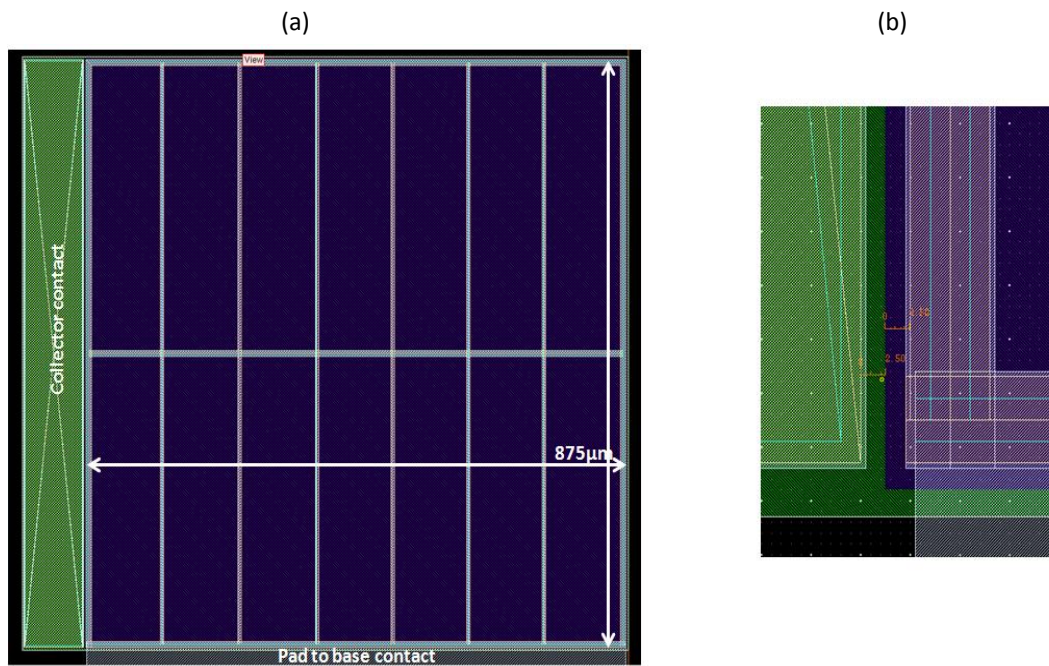
Figure 2.41. (a) Top view of the entire 4H-SiC PIN Photodiode. (b) Highlight of the distance of 2.5 μm between the base contact and the base mesa edge, and of the distance of 2.5 μm between the collector contact and the base mesa edge.

The first thing to note is the difference between the doping concentrations used to realize the BJT (see Figure 2.36) and those used to realize the PIN photodiode (see Figure 2.39). This suggests that the two devices were made on different wafers, despite the production process used is the same.

In the cross section, shown in Figure 2.39 and 2.40, only a cut of the grid of the base contact is observed, but in Figure 2.41 the presence of an appropriate *pad*, realized outside the photodiode, is also observed, necessary to contact the entire grid and to apply a voltage on the base.

The grid contact is realized in the following way. Every vertical line has a width of 5 μm, excluding the two external lines that are wide 8 μm. Each horizontal line has a width of 9 μm. The windows opened within the contact, via lift-off technique, are wide 117.5 x 423 μm^2.

In addition to that a possible design of an avalanche photodiode and of an integrated photodiode will be presented, with good quantum efficiency and responsivity. Moreover, with a device much smaller than the previous, and less metal cover, to reduce the light reflection on these regions, will be shown. The design will follow a similar structure of some structures already physically realized and commercially available [40,41].

Finally, the reason to realize the diode as a mesa structure has to be pointed out. In fact, the choice is related to the *premature breakdown* problem, also if this problem does not occur if the photodetector is used at low reverse voltages. In fact, this phenomenon is present when the reverse voltage is increased, reaching values close to the breakdown, i.e. when the pin photodiode has to be used as an avalanche photodiode. This operation is useful if the diode has to work as a simple photodetector to detect low light intensities, but not when

it has to work like the basic element of an image sensor, because the strong amplification of the dark current would be a serious problem.

An avalanche diode requires that the avalanche multiplication is spatially uniform over the entire area of the diode [31].

In fact, the diode can also be realized as a simple junction diode, i.e. growing an intrinsic epitaxial layer (the N⁻ region) on the N⁺ region, and then implanting within the intrinsic region the P⁺ region [31]. When it is reverse biased, the field which actually interests the flat region of the P⁺N⁻ junction and the one that interests the curvature of the P⁺N⁻ junction itself are different. In fact, it can be approximately said that, for the same applied voltage, the field in the curved regions of the junction will grow faster than the field inside the flat region since the curvature radius of the lateral junction (i.e. in the curvature regions) is lesser than the vertical extension of the junction, and this will cause that in the lateral zones the critical field will be reached before that in the flat region of the junction, triggering, then, the premature breakdown in these areas at a lower voltage than that calculated assuming a planar junction (like the central region of the P⁺N⁻ junction). A lot of tests on devices physically realized and commercially available both experimental and simulative were performed [40]. For this, an P⁺N⁻ epitaxial structure is better than a typical P⁺N⁻ diode realized with an implantation of the P⁺ region in the N⁻ intrinsic region.

2.2.5 4H-SiC NPN phototransistor: operation principle overview

The principle of operation of the *phototransistor* is the same of a *photodiode*, with the only difference that the photogenerated current will be amplified by exploiting the gain β of the phototransistor (direct current gain in common emitter configuration, i.e. with $V_{be} > 0$ and $V_{bc} < 0$). From this point of view, one can say that the phototransistor is a much more light sensitive device, compared to the photodiode. In fact, even in conditions of very low light intensity the phototransistor allows to detect a large collector output current. It is intuitive to understand that the phototransistor will have a much slower response than the photodiode, because it has to wait that the transistor effect is established before using the advantage of the current amplification.

Typically, the phototransistor works with a floating base, and a positive voltage is applied between the collector and emitter, causing the device to work as a two-terminal device. Despite this, the device is still working in the direct active operation condition, i.e. the base-emitter junction is forward biased and base-collector junction is reverse biased. Obviously, if a greater amplification of the collector current is required, it is possible to use the base contact to inject an appropriate base current.

As previously mentioned, the basic operation of the phototransistor is similar to that of the photodiode. Now, the light absorption task is essentially carried on in the reverse biased base-collector junction. If the base-collector junction is reverse biased, the only current flowing through the device is the reverse current of the base-collector diode, i.e. I_{CO} (often indicated also as the dark current I_D or I_{dark}), and the collector current is equal to:

$$I_C = \beta I_B + (\beta + 1) I_{CO} \tag{2.42}$$

where I_B is the base current, and β is the current gain of the transistor in active region.

If the transistor works without the base current, the collector current becomes:

$$I_C = (\beta + 1)I_{CO} \tag{2.43}$$

In practice, the light can hit the device from every part. If the light strikes from the top, i.e. on the emitter, the phototransistor should be appropriately designed realizing the emitter as a *window layer*, i.e. as a *heterojunction* transistor. In this case, the emitter bandgap will be greater than the base and collector bandgap, to allow light to easily reach the base-collector junction, as well as to reduce the emitter's thickness, to minimize the absorption in the emitter itself. In the analyzed case, a homojunction device, on which the light hits the base-collector junction, will be assumed.

Then, if it is supposed that the light hits the base-collector junction, as it happens for the photodiode, it generates a reverse photogenerated current I_{ph} linearly dependent from the light intensity, which will be superimposed to the initial reverse current I_{CO}, obtaining [31]:

$$I_C = (\beta + 1)(I_{CO} + I_{ph}) \cong \beta I_{ph} \tag{2.44}$$

Obviously, as it is shown in Eq. (2.43), if there is a base current due to an external polarization, the collector current in Eq. (2.44) is also increased of βI_B.

The only thing to understand, of course, is how it is possible that the transistor, with a zero base current, can trigger the transistor effect. In fact, under active operation, applying a positive voltage to the collector, with a grounded emitter, when in the base-collector depletion region electron-hole pairs are generated, under the field action the electrons are sent in the collector region and the holes are sent in the base region. The holes accumulated in the base region, since the emitter potential is fixed from the outside (for example, to ground), only increase the base potential [31], implying a direct polarization of the base-emitter junction, which increases as the holes are accumulated. Therefore, this causes the injection of electrons from the emitter that reach the collector region crossing the base region, maintaining the transistor effect. The photogenerated current can be seen as a base current which triggers the transistor effect when the photogenerated holes lower the potential barrier of the base-emitter side (i.e., cause an increase of the base-emitter voltage). It supports an injection of electrons that, reaching the collector, give rise, via the transistor gain, to a collector current approximately equal to βI_b, where I_b, now, is the photogenerated current in the base region due to the light absorption.

Figure 2.42 shows an equivalent circuit of the phototransistor operation, where it is noted that the base-collector junction has been modeled as a reverse-biased diode, with a base-collector junction capacitance in parallel, where the reverse current I_{ph}, crossing the base-collector junction, enters in the base contact and, thanks to the transistor effect, causes an amplification of the collector current of β. Obviously, from Eq. (2.44), it is observed that not only the photogenerated current is amplified, of β, but also the dark current I_{CO}, and this, if the device has to be used as the basic element for an image sensor, can be a serious problem. Instead, if it has to work as a simple photodetector, this is not a problem. Furthermore, the difference from a photodiode is that in a photodiode the dark current

undergoes to an increase in only two cases, if the temperature significantly increases, or if the avalanche condition is reached.
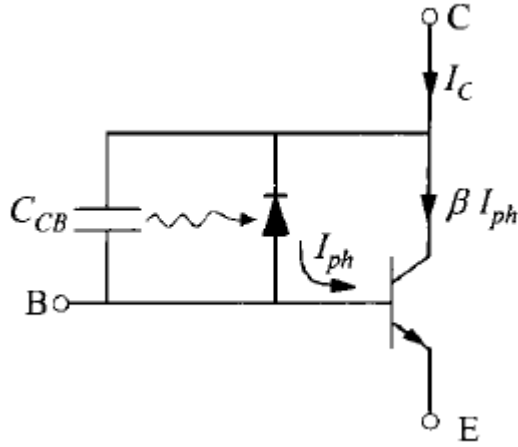
Figure 2.42. Equivalent circuit of a phototransistor [31].

The quantity $(\beta+1) \approx \beta$ in the Eq. (2.44) is defined (in addition to the name of current gain at common emitter) also as the *photocurrent gain*, since it depends on the value of the photogenerated current, unlike a typical NPN transistor. In fact, as for the case of the avalanche photodiode, the photocurrent gain is not constant (in the medium currents regime), but it varies with the photogenerated current and with the intensity of the incident radiation, and it establishes as the collector current changes by setting a certain photogenerated current.

Even for a phototransistor it is possible to define an optical gain G (similar to the one defined for the avalanche photodiode, which was nothing more than the avalanche gain itself), defined as follows [41]:

$$G = \frac{I_{Cph} - I_D}{q} \times \frac{h\,v}{P_{inc}} \tag{2.45}$$

where I_{cph} is the collector current under illumination in A, I_D is the dark current in A (i.e., the collector current without illumination), P_{inc} is the incident optical power in W, and $h\,v$ is the photon energy in J [41]. The photogenerated current I_{cph} is referred to the collector current under illumination conditions, since it is easier to measure the increase in the collector current due to the light absorption from outside, instead of the photogenerated current previously defined, i.e. I_{ph}, that would be the base current that is generated inside the transistor.

Then, the optical gain G represents of how much the collector current increases respect to its value in dark conditions, as a result of the absorption of a given incident optical power.

Therefore, the Eq. (2.45) confirms, as previously mentioned, that the current gain of the phototransistor, depending on the optical gain, is not constant, but varies with the incident radiation intensity.

Also, if it is assumed that the base region width is small, to reduce the absorption in the base region itself, and a depletion region width of the base-collector junction much greater than the absorption depth $1/\alpha$ is assumed (so that it can absorb all wavelengths of interest without any problem), where α is the absorption coefficient, it can be shown that the optical gain G and the transistor gain β (i.e., the photocurrent gain) are related by the following equation [9]:

$$G \cong \eta \, \beta \qquad\qquad (2.46)$$

where η is the external quantum efficiency.

Finally, it is important to add that the quantum efficiency η of a phototransistor is quite complex to evaluate both analytically and experimentally [42], because it is related to a photogenerated base current that not only it is not possible to measure from the outside, but it is also complex to estimate both analytically and by simulations. Typically, this value is a priori known or it is fixed to a certain default value, such that, once estimated the optical gain G, it is possible to obtain the value of the transistor gain β.

In simulations that will be presented in the follows, in addition to simulate the absorption light ability of the BJT realized at KTH (in Figure 2.36), also other solutions will be proposed, following a similar structure to the one of the previous BJT, trying to optimize the light absorption. In practice, some practical solutions already exist, but in 3C-SiC, where it is clear that to achieve high optical gains, and therefore higher transistor current gains, it is necessary to completely change the BJT structure [41] (this analysis will be carried out in what follows).

Furthermore, the phototransistors that will be simulated have not a floating base, because the simulator, in this case, will show convergence problems.

Chapter 3

Simulation results

3.1   Simulation problems in SiC devices

The physical devices simulations are often used to predict the characteristics of electronic devices, both during the design phase, before that the device is realized, and to investigate the advantages that brings a certain structure compared to another [7]. Obviously, when the simulations are carried out, it is important to have physical models that are as accurate as possible, in order to describe the physical behavior of the device itself. Unfortunately, nowadays, in the case of silicon carbide, there are not programs that are able to correctly describe the physics of the device, since not all the models' parameters, for the case of interest, are known and, therefore, it is not possible to have a good prediction of the silicon carbide device behavior, both from an electrical and from an optical point of view. Then, given that there are no models able to accurately describe the physical behavior of the simulated silicon carbide devices, one has to directly enter into the used model with simulation software parameters (which are documented in the manuals), and then modify them to fit the physical model of the simulated devices, some of which have already been discussed in Chapter 1. The parameters of interest must be manually added in the simulator using appropriate text files (see Appendix).

In addition to the parameter problems of the used physical models, there are also other problems that can arise during the silicon carbide device simulations, caused by the wide bandgap, and which have nothing to do with the simulator [7].

For example, at the equilibrium it is possible to calculate the minority concentrations through the use of the mass action law ($np = ni^2$). This means that if a N-type semiconductor is considered, where $n = N_D = 10^{18}\,\text{cm}^{-3}$, and it works at room temperature, i.e. with a $ni^2 = 10^{-18}\,\text{cm}^{-3}$, the minority concentration approximately becomes equal to $10^{-36}\,\text{cm}^{-3}$ ($p_n = ni^2/N_D$). In this case, in the numerical solution of the equations of the devices, problems may arise leading both to the cancellation of some terms and at erroneous estimations of the quantities of interest or even to convergence problems.

Then, for example, when one has to calculate the reverse current (calculation that will be fundamental to study the behavior of the pin diode) at low temperatures or when one has to study what happens near the avalanche-breakdown voltage, this can be a serious problem. A solution at this problem is to start the simulation by setting the simulation temperature around 600 K where, given the high value of ni^2, it is obtained that the influence of the minority carrier concentration is not negligible. When the avalanche condition is reached, the temperature can be reduced [7]. In fact, experimentally, it is observed that the breakdown voltage of a device increases with the temperature, but slightly [43]. Then, this

allows to assume that the breakdown voltage calculated at high temperatures is almost the same of the breakdown voltage calculated at low temperatures.

This is just one of the problems. For example, another problem to take into account, during the simulations, is the partial ionization of the dopant at room temperature. In fact, all dopants in SiC are much deeper inside the bandgap, if compared with the Si ones, and this means that, at room temperature, not all of the dopant are actually ionized and, therefore, the free carriers concentration is not equal to the dopant concentration. The incomplete ionization can lead to some unexpected effects [7], because when the temperature increases, increases the number of ionized atoms too (see the equations 1.25 and 1.26) and, therefore, this changes the device properties.

Therefore, given the many issues to take into account, in the case of simulations with silicon carbide, a lot of simulations have to be developed and particular attention has to be paid to the results and the models used.

3.2   Sentaurus TCAD: overview

As previously noted, the simulation tools are of extreme importance during the development and the optimization of a device, in order to study the properties of a device before its physical realization, to greatly reduce the cost of the project, and to investigate the behavior of the device, reproducing as closely as possible the conditions in which the device will work in order to obtain as realistic as possible results with high level of accuracy.

For the simulations of the 4H-SiC photodiode an advanced software tool will be used, i.e. *Sentaurus TCAD* [44], a program that is very useful both for the design phase and for the optimization of semiconductor devices. It is capable of both carrying out analysis in two or in three dimensions, as well as to simulate the electrical characteristics and thermal and optical properties of many semiconductor devices. Some great strengths of this simulator are surely the time calculation, as well as the rapid optimization of the performances of the device itself. Furthermore, in order to minimize the simulation time, as well as to simplify the calculations, it was decided to perform only two-dimensional simulations of the devices. Then, a single cross section of the device was simulated, where, in this case, the simulator considers the carriers movement in two dimensions, assuming a default depth (along z dimension) equal to 1 µm. Of course, this analysis will be a less accurate description of the behavior of the device itself. If the choice of a 2D analysis is correct, this can be only confirmed from a subsequent comparison between theoretical, simulations and experimental results. Inside the *Sentaurus TCAD* package, there are some basic software for the entire device construction, like *Sentaurus Structure Editor*, and the device simulation, like *Sentaurus Device*, as well as the presence of basic software for the analysis of the electrical parameters of interest, like *Inspect* and *Sentaurus Visual*.

The realization of a device in *TCAD* is done defining a *Project*, where the inserted tools are executed in sequence. Typically, the order is the following: 1) *Sentaurus Structure Editor*, 2) *Sentaurus Device*, 3) *Inspect* or *Sentaurus Visual*.

Sentaurus Structure Editor is useful for the creation of the device cross section, to fix the various doping profiles and contacts, and to generate the mesh of the structure. The mesh of the device is the domain discretization of the device. The choice of the mesh is a fundamental step, since its definition is directly related to the quality of the results that will be obtained. In fact, to simulate the device behavior, the semiconductors equations have to be solved (that are quite complex equations). However, they will not be solved in a "continuous mode", in any point of the device, but only at the chosen mesh points. Only at these points, when the equations are solved, there will be a "memory" of the electrical, optical and thermal properties of the device. Obviously, when the mesh is chosen, there will be a trade-off to take into account. If an accurate description of the device is necessary, a very dense mesh has to be used, but this entails a very high computational complexity of the simulation. Vice versa, to solve the equations in reduced times, it is necessary to reduce the number of points, and to pay this in terms of a lower accuracy of the solution. To obtain a number of points that does not significantly increase the calculation time and the computational complexity of the calculations, without neglecting the accuracy and the reliability of the result, it was chosen to use a very dense grid at the junction points, where, in fact, there are abrupt changes of fundamental quantities, such as doping profiles and minority concentrations and where, essentially, the most important part of the device operations is developed. In fact, is interesting to see better what happens near the PN junction, because it is what happens close to the junction that determines the device operation, in contrast to what occurs in the bulk material or in a uniformly doped material, where deep investigations in this area would be only a loss of time. Hence, in the rest of the device, where the characteristics are homogeneous, a grid with very spaced points is chosen. It is obvious that the grid, once defined for a certain device, does not remain the same for the other, but it changes from time to time according to the device and to the situation in exam.

The device description, within Sentaurus Structure Editor, can be directly done for a graphic via or by entering command lines, that are performed one after the other.

Sentaurus Device represents, instead, the environment in which the behavior (electrical, thermal, optical, etc.) of the device, as defined in Sentaurus Structure Editor, is simulated, from a numerical point of view. Starting from the defined mesh, this tool solves the semiconductor equations (Poisson equation for a semiconductor doped with a generic doping profile, particularized in the region of interest, and continuity equations for electrons and holes). The equations will be solved at the defined points, imposing appropriate boundary conditions, where the various electrical quantities, such as current, voltage, mobility, electric field, etc., are calculated on the basis of suitable mathematical models that describe the physics of the device itself, suitably adapted to the device in question, modifying the parameters of the same.

All the electrical quantities of interest are obtained subdividing the area of the device in many small triangles around the node of the considered mesh, by applying a particular method, i.e. the *Box Discretization method*. In this case the equations of interest are solved on a polygon, obtaining a "*discretization*" of the same equations. In this way a coupled nonlinear algebraic equations system is obtained, which will be solved applying a non-linear iterative method, such as *Newton's method* (the other that can be used is the

Gummel's method, not used for the analysis in question), whose convergence is quadratic, i.e. at each iteration the error rate decreases with quadratic rate, giving a more rapid convergence and a more accurate solution. Instead, in the case of the Gummel's method, the error decreases of the same factor at each iteration, i.e. the convergence is done with linear rate. Therefore, the quadratic method is better to obtain more accurate solutions. For more details, on like the Newton's method operates, refer to [44].

Sentaurus Device receives as input a file (with extension *.tdr*), generated by Sentaurus Structure Editor, where the description of the entire device (in terms of mesh, contacts, doping, etc.) is reported, in the form of an appropriate language. Furthermore, another parameter file is inserted in Sentaurus Device (with extension *.par*), where all the parameters of the physical models of the used materials are defined, if they are not present in the library of the simulator itself. Through appropriate command lines, several sections (such as, contacts and voltages applied to them by default, physical models included in the analysis, input files, electrical quantities to be plotted, etc.) generate as output various files that can be graphically displayed (with the extension *.plt*) or read in Linux environment (with the extension *.log*). In particular, through an appropriate section, *Solve{}*, the type of simulation to be carried out is defined, which can be of two types: *Quasi-Stationary* and *Time-Variant*. Through the use of the *Math{}* section is said at the simulator to solve the equations of interest as a system of partial differential equations through an iterative mechanism, calculating, at each iteration, an error, that when becomes sufficiently small, indicates the convergence to the solution. In this section other parameters can be also defined, such as the maximum number of iterations to be performed, the maximum committed error at n-th step, etc., to reduce the calculation time. An example of a file written in TCAD, and a simplified description of the used commands, refer to Appendix.

Finally, Inspect and Sentaurus Visual are two useful tools to graphically display the generated files (*.plt* and *.tdr*) by Sentaurus Device. The first allows, through two-dimensional graphs, the view of the macroscopic quantities, such as currents, voltages at various nodes, electric field, etc. The second is a powerful graphical tool that allows to view and analyze microscopic quantities (as well as the macroscopic ones), such as carriers densities, photonic absorption, doping profiles, mobility, bandgap, etc., i.e. it allows to do an interior investigation of the structure itself, through two-dimensional and three-dimensional graphs (depending on what kind of structure it is analyzing).

3.2.1   Optical generation: raytracing

The main purpose of this thesis is the investigation of the 4H-SiC ability to perform the photodetection at high temperatures, analyzing its efficiency parameters when the temperature changes. For this reason, it is obvious that to focus the attention on the used method to simulate the optic generation is important. It is necessary to study how the electromagnetic wave, penetrating inside the device, generates electron-hole pairs useful for the photocurrent. In particular, the method used to perform the simulations is the *Raytracing method* [44]. In Appendix is reported an example of the code written in

Sentaurus Device to carry out the optical generation, in one of the simulated devices, through the use of this method.

This method, in order to be applied, requires the use of the complex refractive index of the material in question. In fact, it is also a good practice to define the complex refractive indices of the other materials considered in the simulation, such as, for example, the silicon dioxide, because if the complex refractive index of a material/region of the device is not defined, in the appropriate *parameter file* [75], the refractive index is set to default to 1 [44].

The Raytracer implemented in Sentaurus Device works only with the simulation of linearly polarized light [44] (furthermore, it is optimized for speed). In fact, the *polarization* of an electromagnetic wave is defined as the direction of oscillation of the electric field in time domain. Defined as the *polarization plane* the plane where the electric field E oscillates, if the electric field oscillates always along one direction, perpendicular to the fluctuation of the magnetic field and the wave propagation direction, the wave is *linearly polarized*, i.e. the two components along the x and y directions of the electric field are out of phase by 0°, 180° or multiples of π (with *n* integer). If the oscillation direction of the E field rotates in the time, the polarization is called *circular* or *elliptical*. In the first case the two components are out of phase by 90° (or more correctly are out of phase by $-\pi/2+n\pi$, with *n* integer), but the two components are equal in magnitude, which implies that the wave amplitude is constant in time, but the direction of the field itself varies in time. In the second case the two components are always out of phase by 90°, but are different in amplitude, which implies that the electric field, rotates and changes in intensity. Obviously, even when the amplitudes of the two waves are not equal and the phase shift is a generic value between 0 and 2π, but fixed in time, the electric field will rotate and simultaneously change in intensity, i.e. the electric field vector, observed in the propagation direction, however, will describe an ellipse.

The Raytracer uses a recursive algorithm. It starts with a ray source and builds a binary tree that tracks the transmission and reflection of the ray. A reflection/transmission process occurs at the interfaces with different refractive indices [44].
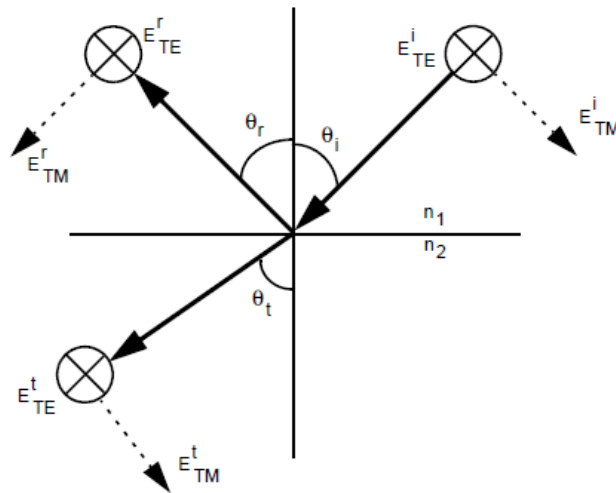
Figure 3.1. Incident ray splits into reflected and transmitted rays at the interface. The TE component of the polarization vector maintains the same direction, whereas the TM component changes direction [44].

In Figure 3.1 it is shown that when a ray arrive at the interface of two material with different refractive indices, for the Snell's law, the incident ray is split into a reflected and a transmitted ray, where the TE (s-polarized component) component of the polarization vector maintains the same direction, whereas the TM (p-polarized component) component changes direction [44]. Obviously, to apply the Snell's law, it is necessary to define an incidence plane (the plane formed from the normal to the interface and the propagation direction of the wave). Only when a plane of incidence is defined, it is possible to establish the concept of TE and TM polarization [44].

A plane wave is a wave where the electric field vector and the magnetic field vector are orthogonal to each other, and both orthogonal to the propagation direction.

A ray can be considered a plane wave traveling in a particular direction with its polarization vector perpendicular to the propagation direction. The polarization vector direction (electric field direction) indicates the direction of the plane transverse to the propagation direction along which the electric field oscillates. The length of the polarization vector represents the amplitude, and the square of its length denotes the intensity [44]. There are two limiting cases. The first case is when the electric field oscillates perpendicular to the plane of incidence (in Figure 3.1 this plane would be the plane of the sheet), and in this case one speaks of *TE polarization* (transverse electric) or *s-wave* (as already seen in Chapter 1). The second case is when the electric field oscillates parallel to the plane of incidence (or it can say that the magnetic field oscillates perpendicularly to the plane of incidence), and in this case one speaks of *TM polarization* (transverse magnetic) or *p-wave*. Obviously, given that these two polarizations are orthogonal to each other, any incident plane wave, with any polarization, can always be decomposed into a TE component and a TM component that can be separately treated (these are the two ray polarization vector components). In fact, in Figure 3.1, the TE and TM components of the electric field (i.e. the ray polarization vector) vector are indicated, respectively, with E_{TE} and E_{TM}. For these two components of the ray polarization vector it is possible to define different reflection and transmission coefficients, as shown below [44]:

1- Amplitude reflection coefficients:

$$r_{TE} = \frac{k_{1z} - k_{2z}}{k_{1z} + k_{2z}} \qquad (3.1)$$

$$r_{TM} = \frac{\varepsilon_2 k_{1z} - \varepsilon_1 k_{2z}}{\varepsilon_2 k_{1z} + \varepsilon_1 k_{2z}} \qquad (3.2)$$

2- Amplitude transmission coefficients:

$$t_{TE} = \frac{2\, k_{1z}}{k_{1z} + k_{2z}} \qquad (3.3)$$

$$t_{TM} = \frac{2\,\varepsilon_2\,k_{1z}}{\varepsilon_2\,k_{1z} + \varepsilon_1\,k_{2z}} \tag{3.4}$$

3- Power reflection coefficients:

$$R_{TE} = |r_{TE}|^2 \tag{3.5}$$

$$R_{TM} = |r_{TM}|^2 \tag{3.6}$$

4- Power transmission coefficients:

$$T_{TE} = \frac{k_{2z}}{k_{1z}}|t_{TE}|^2 \tag{3.7}$$

$$T_{TM} = \frac{\varepsilon_1\,k_{2z}}{\varepsilon_2\,k_{1z}}|t_{TE}|^2 \tag{3.8}$$

where $k_0 = 2\pi/\lambda_0$, with λ_0 the free space wavelength and k_0 the free space wave number, $k_{1z} = n_1\,k_0\,cos\theta_i$, $k_{2z} = n_2\,k_0\,cos\theta_t$, $\varepsilon_1 = n_1{}^2$ and $\varepsilon_2 = n_2{}^2$. Furthermore, for the amplitude cefficients it is considered that $1+r = t$, and for power coefficients $R+T = 1$, that can be particularized for TE and TM polarization easily substituting the above reflection and transmission coefficients [44]. Obviously, for normal incidence, $\theta_i = \theta_t =0$, $r_{TE} = - r_{TM}$ and $R_{TE} = R_{TM}$.

If the refractive index is complex, the reflection and transmission coefficients are also complex. In such cases, only the absolute value, of the complex refractive index, is taken into account [44]. In the case of 4H-SiC is useless to calculate these parameters, because, once inserted the value of the 4H-SiC complex refractive index, through an appropriate parameter file, the simulator automatically calculates these parameters, without entering these from the outside.

The raytracer automatically computes the incidence plane at each interface, decomposes the polarization vector into TE and TM components, and applies the respective reflection and transmission coefficients to these TE and TM components [44]. Hence, a plane wave with arbitrary polarization is decomposed in two waves, i.e. a s-polarized wave and p-polarized wave. The total reflected and transmitted fields will be the sum of those relative to the two polarizations.

Once inserted within the simulator the imaginary part of the 4H-SiC complex refractive index (k, the extinction coefficient), it will automatically calculate the absorption coefficient of the material, using the formula (1.42) (in the simulator it is called *Ray absorption coefficient* [44]).

When the refractive index of a material is defined in the simulator, this index is defined as *element-wise*, in the sense that is defined for material regions, i.e. the material is divided into many parts (basic elements of the simulator) and the optical absorption calculations on these elements are realized. In particular, the intensity of the ray is reduced by an

exponential factor in each element, i.e. *exp(-αL)*, where *L* is the the thickness of considered material crosses by the ray. If *I(x,y,z)*, the incident ray intensity (photons/s^{-1}) in the element, is defined, *I(x,y,z) exp(-αL)* is the intensity at the output of a single element. The *photon absorption rate*, *G^{opt}(x,y,z,t)*, in each element is [44]:

$$G^{opt}(x, y, z, t) = I(x, y, z)[1 - e^{-\alpha L}]$$
(3.9)

After that all the photon absorptions in the elements have been computed, the values are interpolated onto the neighboring vertices and are divided by its sustaining volume to obtain the final units in s^{-1} cm^{-3} [44].

At this point, the concept of an *illumination window*, to confine the light that is incident on the surface of a device structure, plays an important role in various simulation setups for photodiode devices, such as photodetectors, solar cells, and image sensors [44]. In particular, the illumination window has been described using a local coordinate system specified by the global location of its origin and the *x* and *y* directions given as vectors (in 2D the illumination window is a line, with the z dimension set to 1 μm). Also, through suitable commands, it will be also possible to set the power transported by each ray that hits the device, in W, as well as the wavelength of the monochromatic considered source. Furthermore, it is possible to decide how the rays will be distributed within the same illumination window. In particular, in the case in exam, the *Autopopulate mode* will be set. In this case, once established the number of rays to be considered within the window, the simulator will distribute them evenly within the window itself, dividing the window into appropriate sub-windows of a certain size set through appropriate techniques [44].

Rayrtracing also offers the possibility to set (with the use of *RayTraceBC* command) an appropriate reflectivity value at the discontinuity interface between two media with different refractive index, in order to perform a simulation that is as consistent as possible with the reality. To set a certain reflectivity value at the discontinuity between air and metal contacts, it allows to take into account how much power will be reflected on the metal contacts and how much power effectively penetrates inside the device. This allows the designer to understand what should be the correct dimension of the contact in order to minimize the reflection, as well as choose the most suitable material for the realization of the contacts. To calculate how much power is actually transmitted, the simulator exploits the relation *R+T* = 1, once fixed a certain reflectivity (where 1 indicates that the total power is equal to reflected power plus the transmitted power), where *R* is the reflectance and *T* is the transmittance. Then, if the first is set, the second is obtained as *T* = 1-*R*, and vice versa (obviously, if *R* = 0, the rays will be completely transmitted, and if *T* = 0, they will be completely reflected).

Finally, when raytracing is used inside the simulator, a typical power report is shown in Figure 3.2.

```
                Input      Escaped    StoppedMinInt  StoppedDepth  AbsorbedBulk  AbsorbedBC
Photons [#/s]: 4.531E+11   1.333E+11   4.142E+07     0.000E+00     6.236E+10     2.574E+11
Powers [W]:    3.000E-07   8.826E-08   2.743E-11     0.000E+00     4.129E-08     1.704E-07
```

Figure 3.2. Summary of RayTrace Total Photons and Powers [44].

In Figure 3.2 is possible to see that a typical *Raytrace* summary includes different powers. The *Input power* is calculated multiplying the input incident optical power, transported from the rays (in W/cm^2), by the defined rectangular (or circular) illumination window (in cm^2), where the third dimension is set by default to 1 μm in 2D simulation. The *Escaped power* is related to the sum of powers of the rays that are ejected from the device and are unable to re-enter in it (for example, with another subsequent reflection). The *StoppedMinInt power* and the *StoppedDepth power*, are, respectively, the sums of the powers of the rays terminated by the *MinIntensity* condition and the sums of the powers of the rays terminated by the *DepthLimit* criteria. In fact, the *Raytracing* gives also the possibility to define if to terminate the *Raytracing* when the ray intensity becomes less than *n* times respect the original intensity, where this value is set with the definition of the parameter *MinIntensity*, or if to terminate the *Raytracing* if the ray passes a material thickness of a value equal to *DepthLimit* [44]. In the next simulations these two parameters will not be used. The *AbsorbedBulk power* refers to power absorbed in bulk regions. The *AbsorbedBC power* refers to power absorbed in the *TMM contacts*, and this column is shown only if *TMM contacts* have been defined. *TMM* stands for *Transfer Matrix Method*, that is another optical generation method that is possible to use in the simulator and that is not of interest for the simulations in exam because the considered contacts are simply ohmic and with a particular reflectivity. Obviously, like it is depicted in the Figure 3.2, it is possible to repeat the same considerations, done for the powers, on the incident photons quantities, i.e. escaped photons, stopped photons, and absorbed photons.

This is only a simple introduction about the operation of the *Raytracer*, focusing the attention on the use of it in the following simulations. For more details about the commands used in the *Raytracer* section, refer to the code example in Appendix, and for more information, regarding the potentiality and the optical generation method, refer the program's user guide [44].

3.3   Photodiode simulations

In this section all the simulations made on a 4H-SiC photodiode, which is physically available at KTH, are presented. Experimental tests are subsequently conducted on this device as well. Then, simulations will be done on a suitable photodiode proposed for UV photodetection, following a typical realization already experimentally and commercially available, with reduced dimensions compared to the previous (the device will be approximately scaled to one ninth of the previous width). It will be simulated varying different technology parameters, varying the monochromatic source's considered

wavelength, as well as that in avalanche conditions. Moreover, in all the simulations, the attention will be focused on what happens when the temperature changes, so as to completely investigate the 4H-SiC ability to work as the basic element for the UV image. All simulations are performed in a wavelength range of 100 - 410 nm (looking to cover all three sub-bands of the UV band, i.e. near, middle and far ultraviolet), changing the temperature, and focusing on what happens in the temperature range of 300-800 K.

It must be underlined that to do under light simulations, well approximating a real case, it is necessary to know the spectral irradiance (spectral power density for wavelength unity of the electromagnetic spectrum) on Venus surface. Unfortunately, in literature, this quantity is not present. The only available data is that the total power outside the planet's atmosphere, calculated like the integration of the spectral power density on all the wavelengths of the electromagnetic spectrum. The total power density is almost twice the one that arrives on the Earth, i.e. 2.65 kW/m^2, since Venus is closer to the Sun 40 millions of km than the Earth (the Earth is distant 150 millions of km from the Sun). This means that the simulations will be done at an incident optical power chosen of default (1W/cm^2). In any case, the efficiency parameters of the photodetector will not change, because if the real power density reduces also the photogenerated current will be reduced. Furthermore, the purpose of these simulations is to show the 4H-SiC performance in the UV detection, independently from the incident optical power.

3.3.1   KTH's 4H-SiC photodiode

The description of such photodiode, as well as the cross section and the top view of it are shown in Chapter 2.

Following results are reported in terms of responsivity and quantum efficiency. They are obtained by setting a reverse voltage of -20 V. This voltage has been chosen because it is far enough from the value of the breakdown voltage theoretically estimated, assuming a triangular function of the electric field inside the device (the depletion region thickness is assumed equal to the intrinsic region thickness when the electric field assumes the critical electric field value). This assumption is possible due to the reduced doping in the intrinsic region. In fact, at -20 V, this region is already completely depleted, obtaining a punch-through PN junction. The breakdown voltage is confirmed to be around of -100 V by the simulations and experimental tests. Finally the considered incident optical power density is 1 W/cm^2.
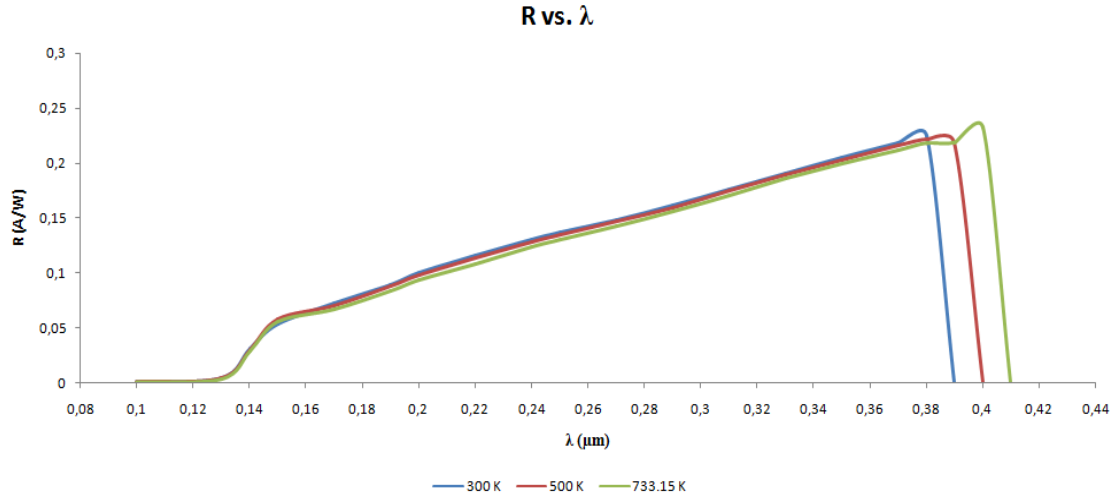
Figure 3.3. Responsivity versus wavelength at different temperatures.
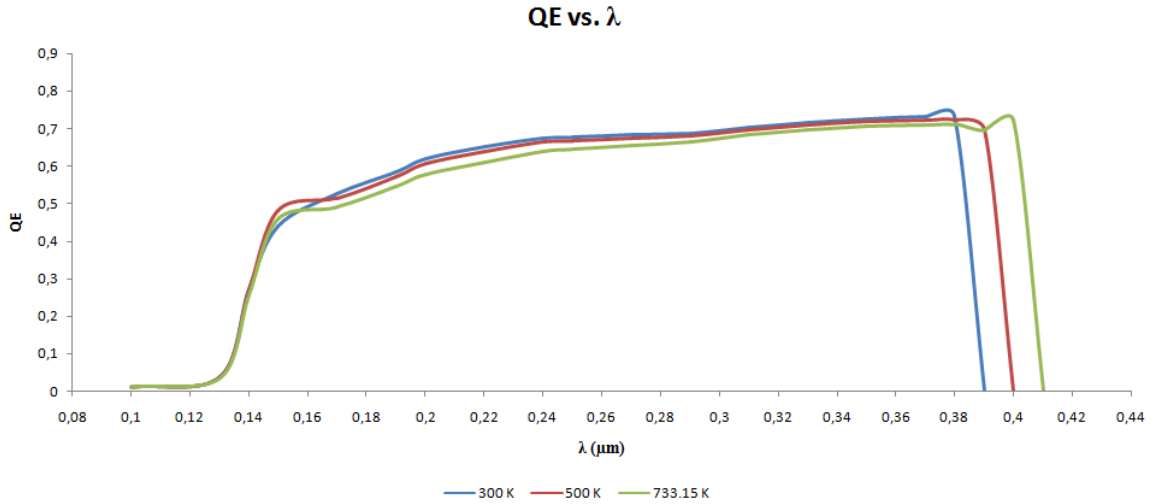
Figure 3.4. Quantum efficiency versus wavelength at different temperatures.

In Figures 3.3 and 3.4 it is clearly shown as both the responsivity and the quantum efficiency, at variation of the wavelength, appear to be almost identical (in the 100 – 380 nm) as the temperature varies. The only thing that is interesting to note is, for example, that at 300 K, with a wavelength of 390 nm, this wavelength is not absorbed by the device itself, since that at this wavelength both the responsivity and the quantum efficiency, are pratically zero. This is not surprising, since it is in agreement with how expected from the equations (1.9) and (1.33). At room temperature, the 4H-SiC bandgap is about 3.2 eV, and this implies that the critical wavelength is equal to 385 nm. When the temperature increases, the bandgap reduces, resulting in an increase of the critical wavelength. In fact, at 500 K, the bandgap is reduced to 3.16 eV, causing an absorption until a critical wavelength of 392 nm (and beyond it is blind). At 733.15 K, the bandgap is reduced to 3.09 eV, causing an absorption until the critical wavelength of 401 nm, and

therefore, an absorption of a small part of the visible spectrum (in particular, the violet-blue colors).

Moreover, the responsivity shows an almost linear trend with the wavelength, similar to that theoretically expected, in ideal operating conditions. When wavelengths in the visible range are considered, the device becomes completely blind. The quantum efficiency is quite constant with the variation of the wavelength. Also this trend is expected from the theory, because, always referring to the Eq. (2.8), if the responsivity linearly increases with the wavelength, by dividing first and second member of the equation for λ, the quantum efficiency is constant with the wavelength itself.

The responsivity and the quantum efficiency obtained values are confirmed by experimental results performed on commercially available 4H-SiC photodiodes [45,46].

In Figures 3.5 and 3.6 it is shown that the responsivity and the quantum efficiency are almost constant with the temperature variations, at a particular wavelength (as previously anticipated).
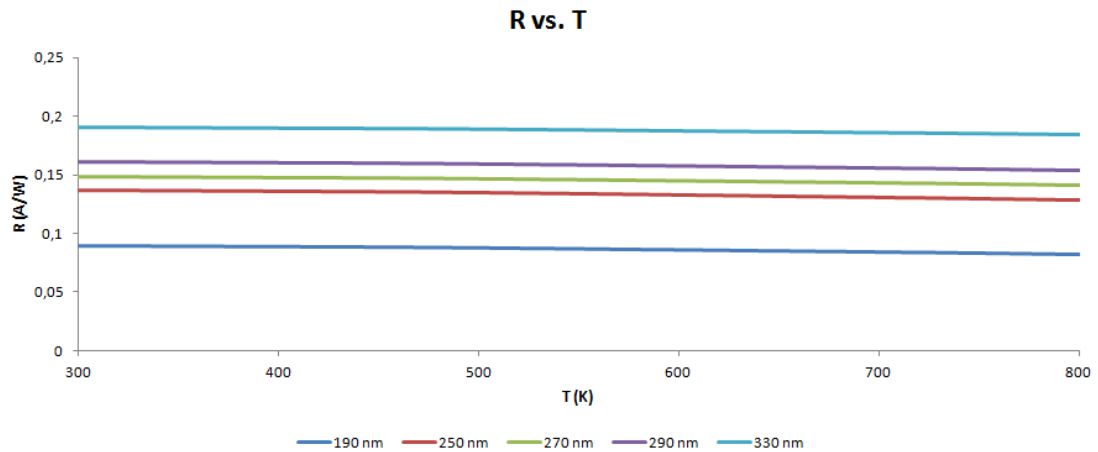
Figure 3.5. Responsivity versus temperature at different wavelengths.
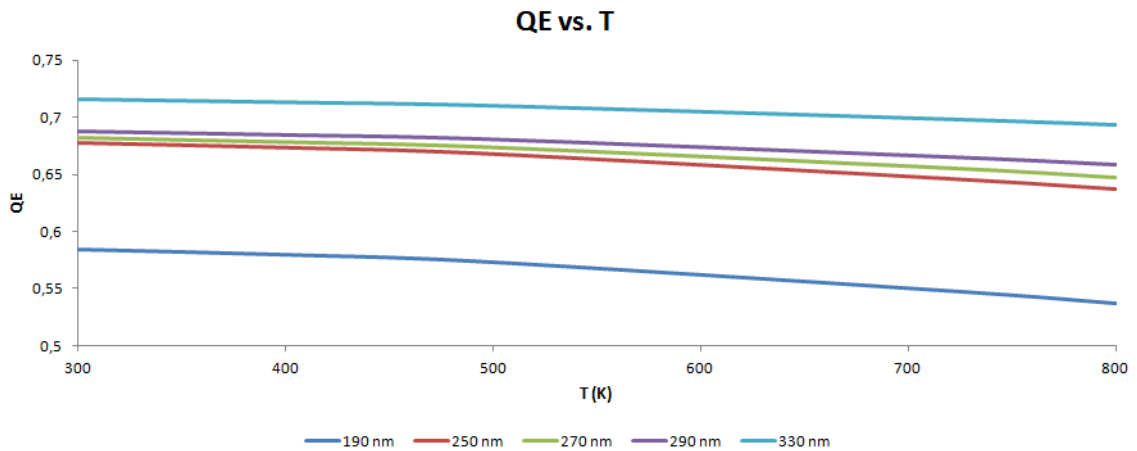
Figure 3.6. Quantum efficiency versus temperature at different wavelengths.

Obviously, as well as the quantum efficiency and the responsivity, to determine the ability of a photodetector to convert incident photons (and therefore light power) in a photogenerated current (and thus into electrical power), it is interesting to observe the trend of photogenerated current density when the temperature changes, setting an appropriate wavelength. This trend is shown in Figure 3.7.
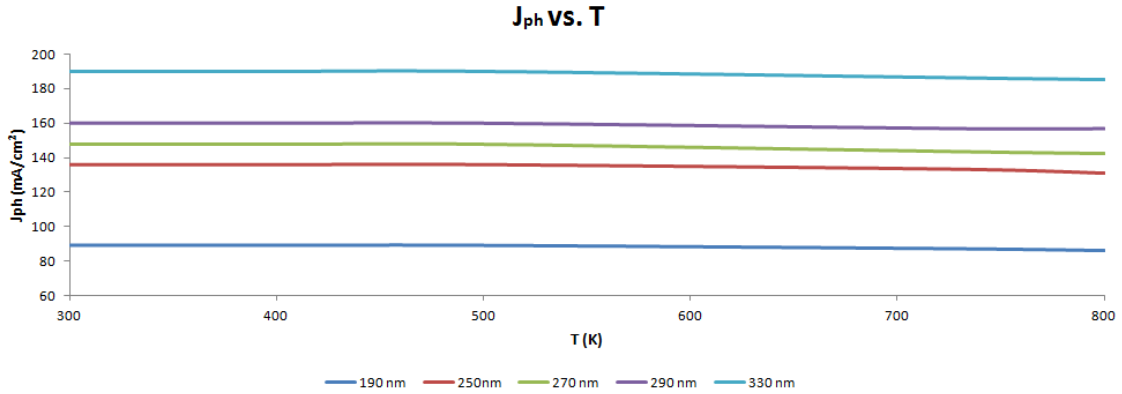
Figure 3.7. Photogenerated current density versus temperature at different wavelengths.

As can be seen from Figure 3.7, the photogenerated current is practically constant with temperature variations (fixing a certain wavelength). In particular, reasoning in terms of I_{ph}, there is a variation of the current, at 250 nm, of about 0.1 µA/100°C. Given that the J_{ph} remains constant when the temperature changes, this is in line with the fact that the quantum efficiency (the only independent variable) is quite constant with the changing wavelength. The responsivity linearly varies with the wavelength (the responsivity is quantum efficiency dependent), at a given temperature. Furthermore, by the trend of the photogenerated current density, it is observed that the device is actually able to work as a photodetector. In fact, despite it is largely covered by metal (and in particular on the N^+ contact region), the presence of a grid base contact, and therefore the presence of a large collection light exposed area (approximately equal to the area of the base region, i.e. 875 µm^2), makes this device suitable for photodetection, showing also high current density (in absolute value).

Obviously, this shows the 4H-SiC ability to absorb in the UV range, but this device, with a too large area of about 975x875 µm^2, could never be used for the realization of an image sensor. In fact, even if a simple sensor with a resolution of 1 Megapixel is created, assuming a square sensor (i.e. 1000x1000), it is obtained a sensor with an area of 0.85 m^2. It is obviously impossible to integrate this sensor.

At this point, the investigation of the dark current variation with temperature is very important, to see if this device can be equipped to work as a basic element for the UV image sensor, at high temperature. This investigation is shown in Figure 3.8.
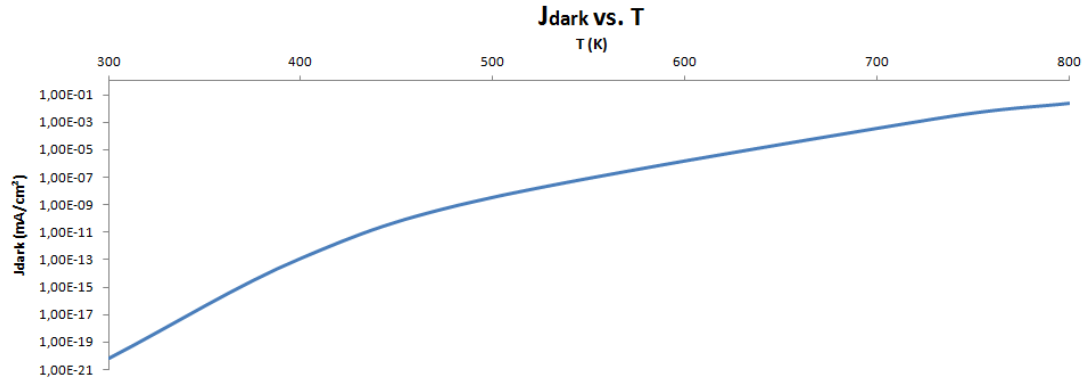
Figure 3.8. Dark current density versus temperature in log-scale.

In Figure 3.8 is shown an expected trend of the dark current density. In fact, when the temperature increases, the current density grows exponentially with it (the intrinsic concentration is temperature dependent). Making a plot of the current density in a logarithmic scale an almost linear trend is obtained.

In this analysis the current density is considered, and not the total current (current density multiplied for the total device area), because knowing the current density it is possible to compare different devices.

Moreover, at the temperature of interest, 733.15 K, it is observed that the dark current density is about 1 mA/cm^2. Then, from the simulations, 4H-SiC appears able to sensing high temperature applications. For example, reasoning with a temperature of 733.15 K, and a wavelength of 270 nm (but the same reasoning is also valid for other wavelengths), this device shows a photocurrent gain of approximately 10^5, evaluated simply as the ratio of the photogenerated current, at a certain wavelength, and the dark current, at 733.15 K. This result is very important because it shows how the 4H -SiC is able to "distinguish" a dark current from a photo-generated current. In fact, if there is an appropriate electronics, downstream the pixel (or sensor), that reads the analog voltage value produced by the light absorption, a current of the order of magnitude of pA can be considered a simple noise current by the same circuitry and it is able to recognize if this current was not generated by light absorption, and, therefore, the circuit does not perform any analog-to-digital conversion. Vice versa, if the current has a value of μA, the downstream electronics interprets this value as a current generated by light absorption, and it will proceed to a suitable analog-digital conversion.

Another interesting check is to verify that, effectively, the 4H-SiC absorbs the light radiation as theoretically predicted by the conducted analysis in Chapter 1. For example, the Figure 3.9, shows the 4H-SiC photons absorption at different wavelengths, assuming a temperature of 733.15 K.
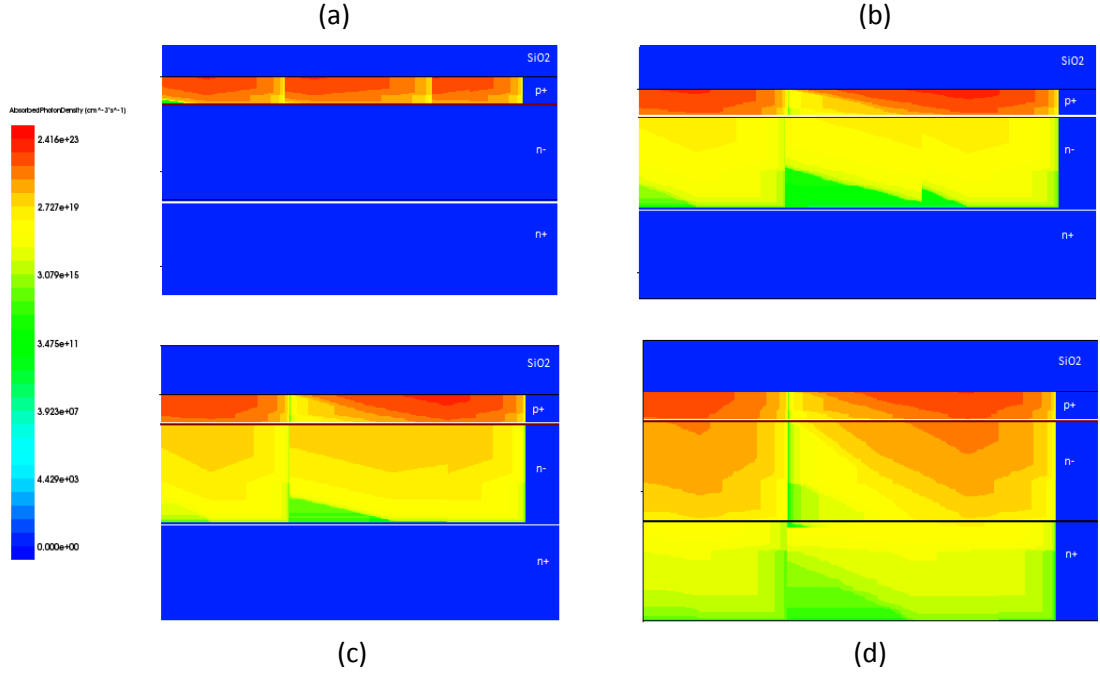
Figure 3.9. Absorbed photon density at 190 nm (a), 250 nm (b), 270 nm (c) and 330 nm (d).

In Figure 3.9 the photons absorption (it is represented a zoom of the central region of the device) at four different wavelengths is shown. For example, if the wavelength of 270 nm is taken in consideration, it is observed that the photons absorption is reduced, compared to that on the surface, where for surface absorption the interface surface SiO_2 / P^+ region is considered, where the reference is set at 0. In fact, as theoretically expected from the penetration depth evaluated in Chapter 1, the reduction of approximately 30 % takes place in a distance of about 0.15 μm (to be precise, theoretically the incident power is reduced of *1/e* at a distance of 0.133 μm from the surface). Furthermore, the electron-hole generation rate, due to the photons absorption, is in agreement with what theoretically expected. In fact, the figure shows that there is a reduction of the carriers generation when the radiation penetrates into the device, given that the generation rate is reduced in the same way the photons absorption is reduced. Assuming an unitary internal quantum efficiency, each absorbed photon generates exactly one electron-hole pair being, the pin diode, a device with an internal unity gain. In fact, Figure 2.31 shows a theoretical generation rate at the surface of the order of 10^{29} $m^{-3}s^{-1}$, while in the simulations a rate of the order of 10^{23} $cm^{-3}s^{-1}$ is obtained (which converted in meters gives the same value).

Obviously, this reasoning can also be repeated at other wavelengths and at different temperatures, remembering that, as can be seen from the penetration depth definition and from the electron-hole pairs generation rate, these parameters are temperature independent. This means that this analysis, repeated at different temperatures, would give always the same result, providing that the wavelength does not change.

Another thing that can be observed in the Figure 3.9 is that the intrinsic region N^-, with a reverse voltage of -20 V, is already completely depleted. In fact, the white lines, which represent the extension of the depleted region, touch the edges of the P^+ and N^+ regions. Of course, this is translated into an advantage in terms of absorption of the incident photons,

since if the radiation is able to reach the intrinsic region, it will certainly contribute to the useful carriers generation for the photogenerated current. Furthermore, the P^+ region is not very thick, being 300 nm, which allows the carriers collection to be enhanced.

Moreover, it must be emphasized that the simulations were carried out considering a deposition of 50 nm of SiO_2 on top of the device, as required by the production process used for the realization of the device itself, without taking into account the oxide deposition of 2 µm as intermediate dielectric after the contacts definition.

Following the analysis of the reflectance for an air/SiO_2/4H-SiC is reported (as done in section 2.2.3.2), with a deposition of silicon dioxide of 50 nm.
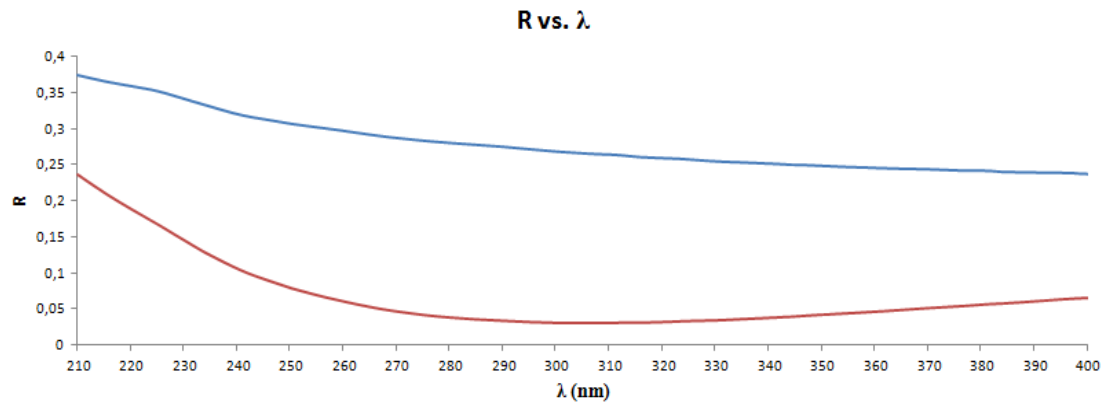
Figure 3.10. Reflectance with and without oxide deposition.

Therefore, as can be observed from Figure 3.10, with the deposition of a SiO_2 passivation layer of 50 nm, the reflectivity, in the UV range, of the incident radiation, with equal wavelength, is significantly reduced.

Finally, before concluding the analysis on this device, it must also be observed that the contacts inside the simulator are considered as ideal ohmic contacts. But, in the reality, it must be remembered that the contacts on the P^+ and N^+ regions are made in two different ways. In fact, the first is made with the deposition of a triple layer of Ni/Ti/Al, while the second with the deposition of a Ni layer. For the purpose of taking into account a contacts' reflectivity (as happens in the presence of any metal contact or, more generally, of a given discontinuity surface), trying to simplify the simulation analysis, a 3% optical incident power contacts reflectivity can be considered. This value was estimated taking simply into account the air/Ni reflectance in the UV range [27] (calculated with the formula 2.13; see Figure 3.11), and then inserting into the simulator an average value evaluated on the UV wavelengths range (i.e. about 3 %). It is possible to show that also a Au contact has a so low reflectivity air/Au, i.e. about 5%.
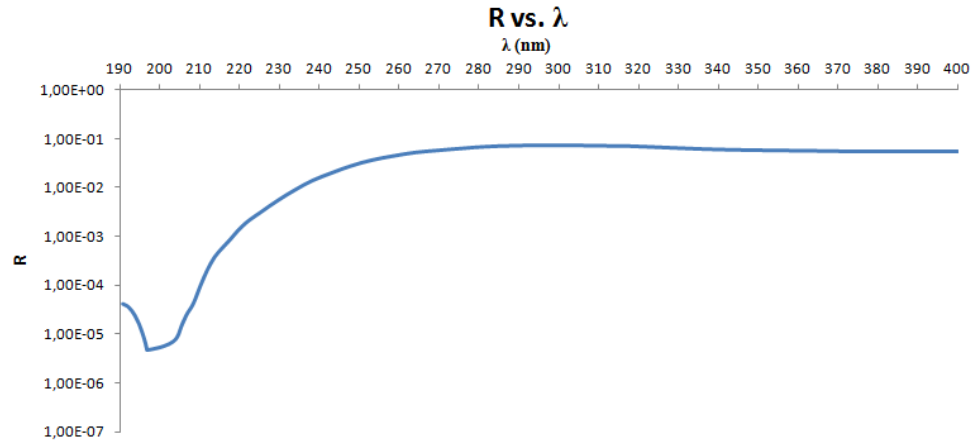
Figure 3.11. Reflectance at an air/Ni interface for different wavelengths in UV range in log-scale.

Figure 3.11 shows as the nickel, at least in the UV band, presents a very low reflectivity. This is not true in the visible and infrared band, where the reflectivity values can have values up to 35%. The investigation of a suitable material to minimize the contact reflectivity is of extreme importance. Moreover, this material has to be able to withstand to high temperatures, such as that of interest, even if it has already been experimentally demonstrated circuits working with Nickel contacts in high temperature applications [1], thanks to the material high melting point of about 1500 °C. The low reflectivity is important where the light intensity to be detected is very low, as in the case of a planet like Venus, where a large part of the solar radiation, including a part of UV radiation, is blocked by the thick layer of clouds that surrounds it. Then, a wrong choice of the used material, could lead to a high reflectivity. In fact, in Figure 3.12 the case where the contacts are completely made of Al is shown [27] that is a suitable material for high temperature applications [1], but it is clearly demonstrated that the reflectivity in the UV band is extremely high (about 42 % as an average value).
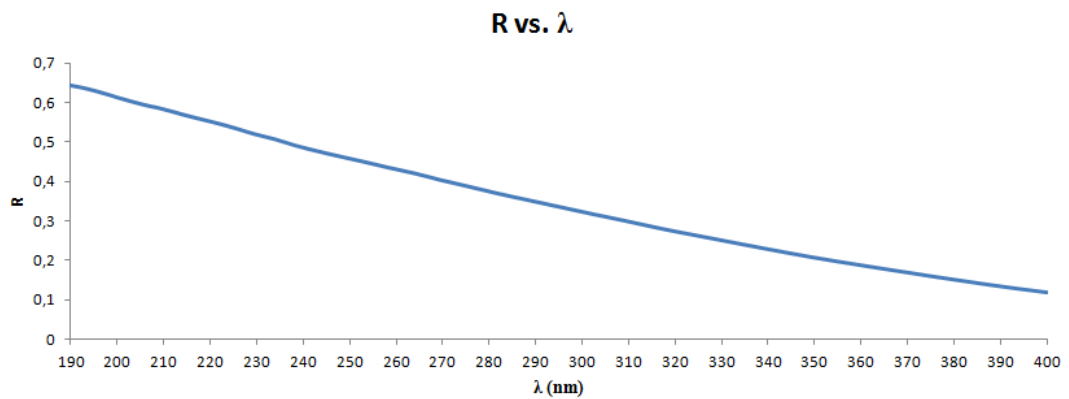
Figure 3.12. Reflectance at an air/Al interface for different wavelengths in the UV range.

Furthermore, in the choice of the right metal that has to be used for the contacts realization, one should also consider the absorption coefficient at different wavelengths within the UV range. In fact, a metal can reflect little the radiation but, in the same time, it can absorb

much the same radiation hitting on the contact, preventing that it can penetrate in the underlying device. Starting from the imaginary part k of the complex refractive index, and using it in the Eq. (1.42), it is possible to calculate the absorption coefficient of the used metal. In fact, choosing a *Nickel* contact, a *Gold* contact or an *Aluminum* contact, in terms of the absorption coefficient, it can be shown that the coefficient would be the same for all, and it is about 10^6 cm^{-1} in the UV range. In fact, in the photodiode simulations also this has been taken into account, as well as the reflection at all the discontinuity surfaces automatically calculated by raytracing method (see section 3.2.1). In particular, where the ohmic contact are defined, instead to insert a constant reflectivity in the UV range, three rectangles of different materials are considered, one upon the other, to realize the P$^+$ contact (Ni/Ti/Al), and one rectangle is considered to realize the N$^+$ contact (Ni). To calculate the absorption coefficient, in the parameter section the complex refractive indices of these materials have been inserted. In this way, also the reflection at the discontinuity surface air/Ni, for the N$^+$ contact, and air/Al, Al/Ti, Ti/Ni, for the P$^+$ contact, have been calculated (from the simulator itself, in addition to the reflectivity to the discontinuity Ni/4H-SiC). Obviously, the theoretical analysis in the section 2.2.3.2 can be also used to calculate the reflectance of a triple layer, for example, air/Al/Ti, Ti/Ni/4H-SiC, etc. Therefore, the investigation of the best contact with lower reflectivity and absorption coefficient would be the correct way to follow.

3.3.2   4H-SiC photodiode: first proposed solution

The structure that will be shown is a possible structure proposed for UV detection. This structure will present some advantages compared to the previous, including the reduction of the amount of deposited metal, for the contacts realization, and a size reduction to allow easier integration of the device, without having a significant reduction in the efficiency parameters. Obviously, being a proposed structure, different simulations will be done varying some technological parameters, such as the doping and thickness of the P$^+$ region. Furthermore, the trend of the breakdown voltage will be also investigated as the temperature changes, as well as the avalanche gain. Of course, this analysis is important if one is interested in using this structure as a simple photodetector, but not for an image sensor. The simulations will be carried out fixing, again, a reverse voltage of -20 V and an optical power density of 1 W/cm^2. In this way it is possible to compare the two different structures, for the same simulation parameters. Finally, the simulations will be done at different temperatures, to test the ability of the device to correctly work at high temperature. The simulations will be also done at different wavelengths including the UV range.

The proposed structure will follow a design similar to that of a device already on the market [40], with some modifications in the lateral dimensions and in the doping concentrations. The device is a symmetric structure, and its cross section is shown in Figure 3.13.
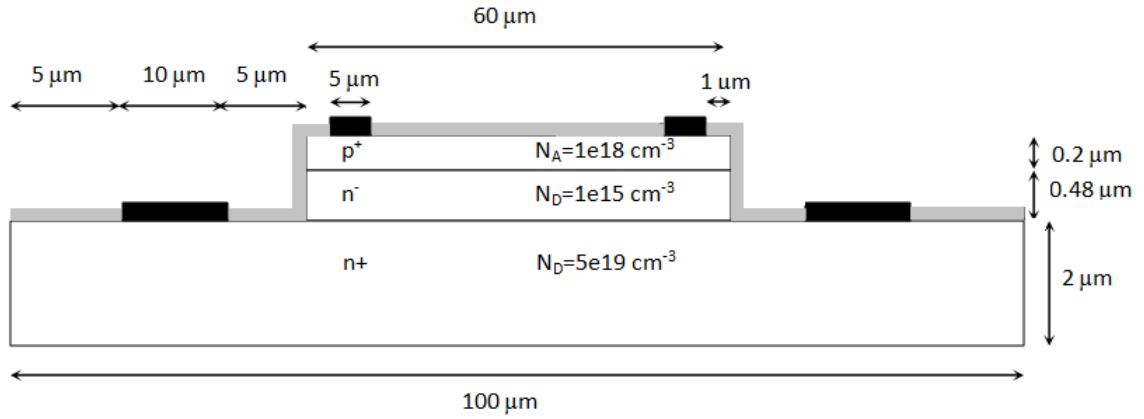
Figure 3.13. Entire cross section of the 4H-SiC photodiode.

In Figure 3.13 some differences with respect to the structure previously analyzed are shown. The N⁻ doping is reduced to have an intrinsic region completely depleted even for low reverse voltages, and to optimize as much as possible the collection of the incident photons. Moreover, the reduction of the intrinsic doping region permits to have a field profile almost constant inside this region, in order to increase the breakdown voltage. The thicknesses of the P⁺ region and the N⁻ region are reduced, both to reduce the surface absorption and to optimize the electron-hole pairs generation (see Figure 2.33). The contacts' lateral size is reduced to minimize the amount of reflected light. A double contact for both regions is realized, to optimize the carriers collection in terms of available output power. If the carriers are collected in several points, as in the case of a grid contact, a reduction of the resistance, encountered by the carriers flow, is obtained, when they cross the device regions before reaching the contact itself. In fact, if a single contact is considered, the path that they have to follow is longer than the previous, and it changes according to where they are generated. Also the encountered resistance is bigger than before. Therefore, this allows a reduction of the dissipated electrical power inside the device. The device has an oxide passivation layer of 50 nm (as before).

In particular, the choice of this oxide thickness is due to the fact that, as it was previously observed, with this thickness it is possible to obtain a substantial reflectivity reduction at the interface. This also translates in an advantage in terms of deposition time of the layer itself.

In the following figures the results of the simulations carried out are shown, in terms of, responsivity, quantum efficiency and photogenerated current, at different temperatures and different wavelengths.
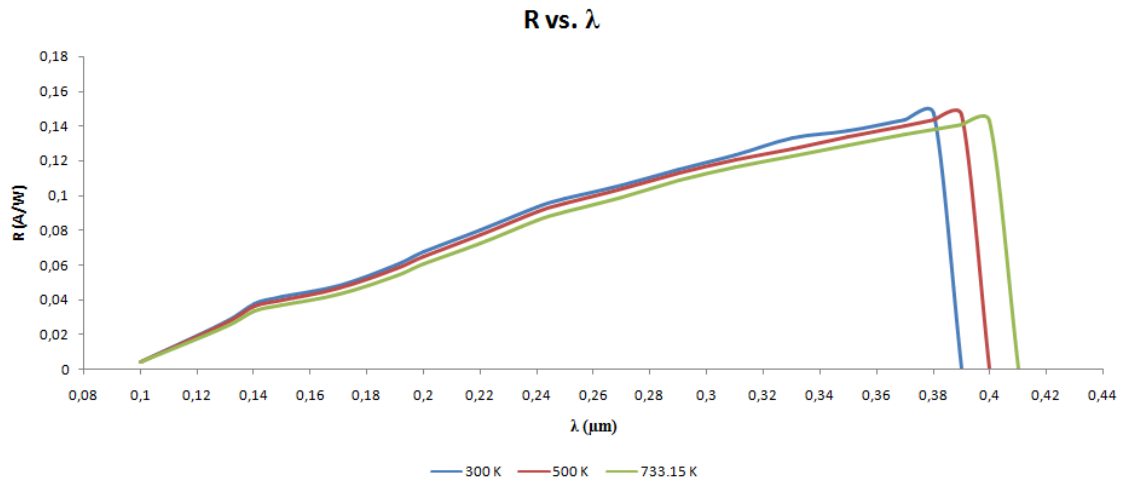
Figure 3.14. Responsivity versus wavelength at different temperatures.
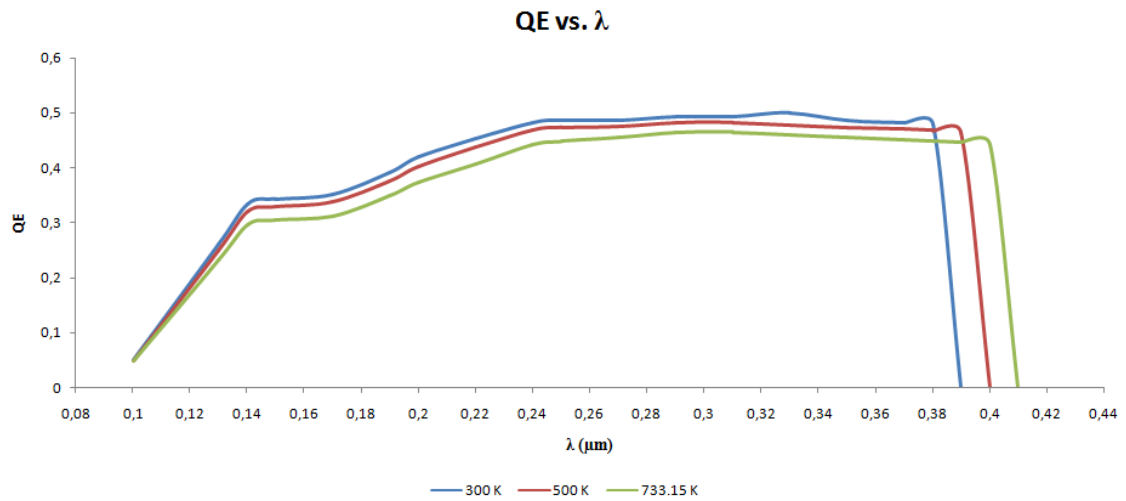
Figure 3.15. Quantum efficiency versus wavelength at different temperatures.
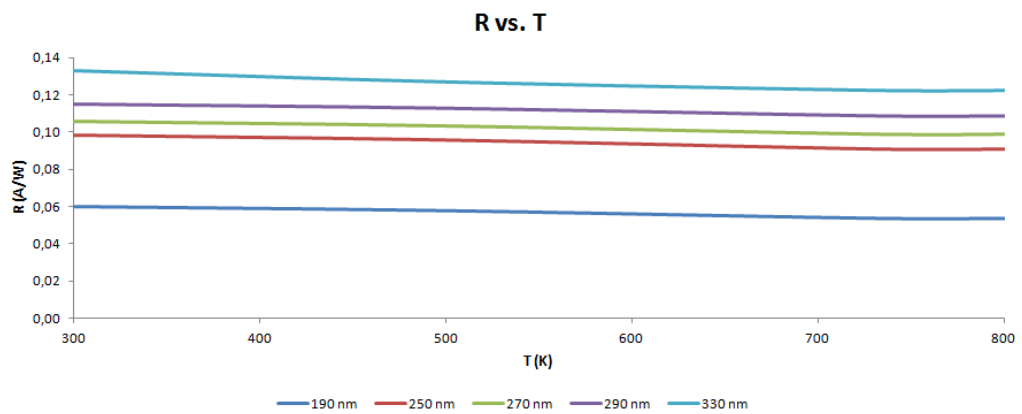
Figure 3.16. Responsivity versus temperature for different wavelengths.

107
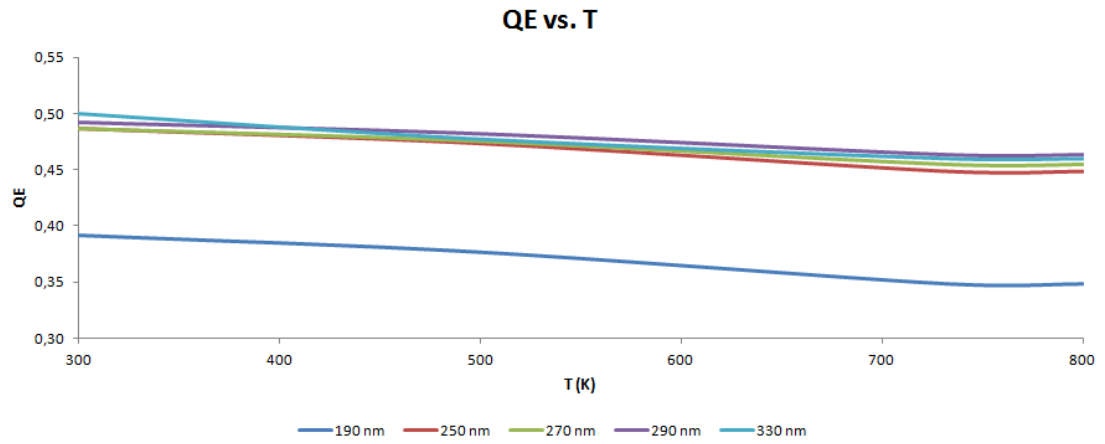
Figure 3.17. Quantum efficiency versus temperature for different wavelengths.
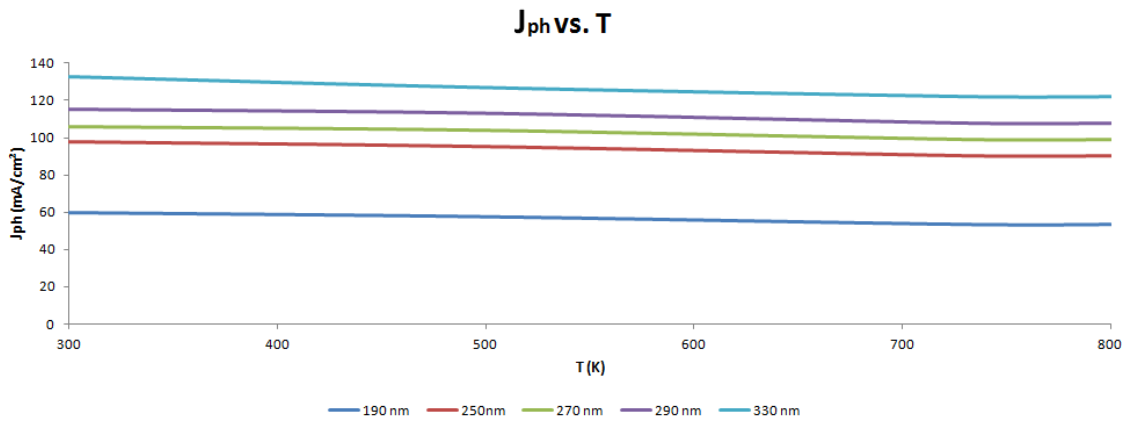
Figure 3.18. Photogenerated current density versus temperature for different wavelengths.

From the Figure 3.18 it is possible to observe that the photogenerated current density is reduced compared to the previous device, fixed a certain wavelength. The reduction of the current density is not surprising because of the reduction of the device dimensions (about one-ninth in terms of lateral dimensions). This means a smaller light collection at parity of incident optical power density. As before, the photogenerated current is quite constant when the temperature varies.

Therefore, a less effective collection area means a lower quantum efficiency (at parity of incident photons) and, being the responsivity related to the quantum efficiency, in a directly proportional way, it will be also reduced. In fact, for example, with a device with a an area of 975x875 μm^2, at a wavelength of 270 nm and a temperature of 733.15 K, the responsivity was of 15% and the quantum efficiency was of 60%. With a device with an area of 100 μm^2, at the same wavelength and temperature, a responsivity of 11% and a quantum efficiency of 45% are obtained. Furthermore, it is possible to see that there is a little increment in the quantum efficiency and in the responsivity for short wavelengths, like 100 nm. This is related to the fact that reducing the P^+ thickness, the short wavelengths

are better absorbed, because the electron-hole pairs generated can arrive in the intrinsic region without any problem.

At this point, it is important to observe the dark current trend, which is the greatest problem for an image sensor, as previously pointed out, if it has to work at high temperature.
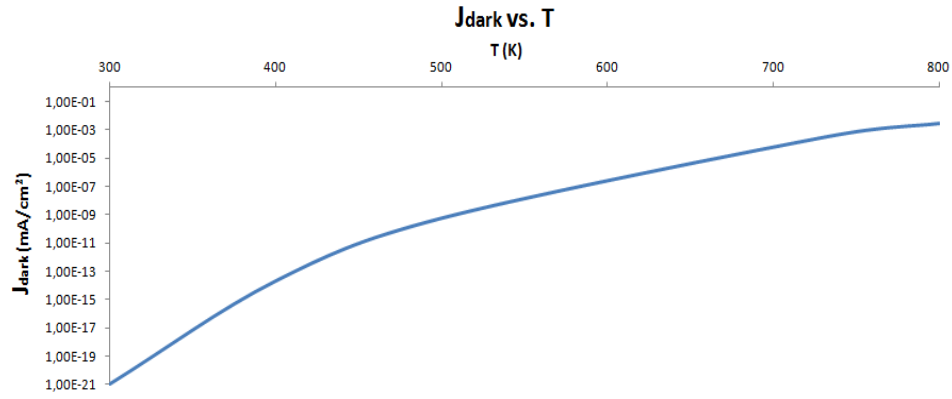
Figure 3.19. Dark current density versus temperature in log-scale.

In the second device there is an improvement in terms of reverse saturation current density (that is almost two order of magnitude smaller, at the same temperature). From Eq. (2.20) it is observed that the current density depends on the physical parameters, which do not vary if dimensions are changed, but if the temperature changes. Maybe, this reduction is related to an increase of the P^+ doping than before and, thanks to a reduction of the N^- doping, also an improvement of the mobility, and in turn of the diffusion coefficient of the holes inside the intrinsic region, is obtained. Hence, if the two devices work at the same temperature, and with the same area, it is obvious that, at a given current density, the total reverse current becomes smaller (see Figure 3.20).
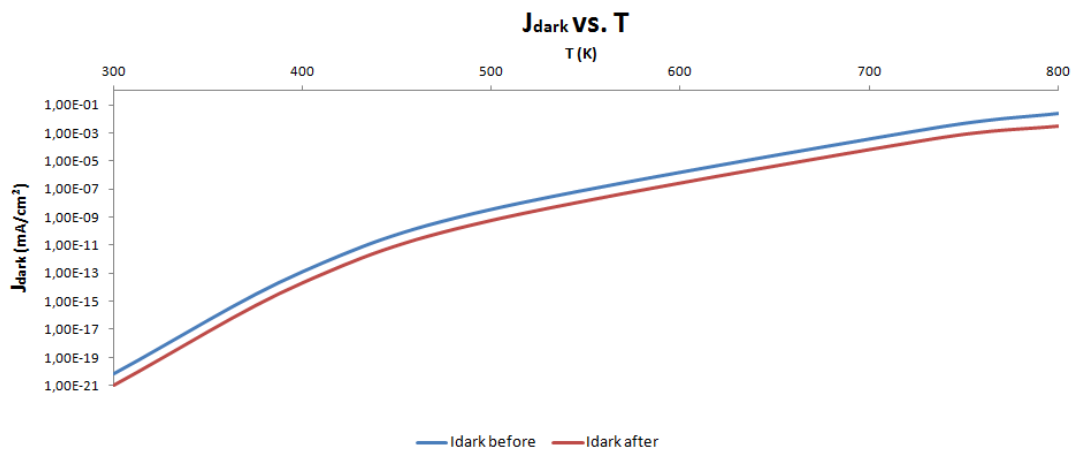
Figure 3.20. Dark current density comparison at different temperatures.

Therefore, from what has been said, there is a trade-off that has to be taken into account. If a high photogenerated current is required, at the same incident optical power, the effective

device area exposed to the light has to be increased, causing an increase in the reverse current, and therefore, a greater background noise. Conversely, if a lower dark current is required, the device area has to be reduced, and this is paid in terms of lower collecting area exposed to the light. Reasoning in terms of equal incident power density, thus a lower photogenerated current will be detected. Obviously, all depends on the sensor application. If the sensor has to work at lower temperatures, given that the 4H-SiC is characterized by very low reverse currents at reduced temperatures (such as room temperature), the device area can be increased in order to have a greater responsivity and quantum efficiency. Obviously, the only problem will be the manufacturing costs. Instead, if the device has to be used for high temperature applications, the reverse current density tends to increase a lot. In this case, to contain this effect, it is necessary to reduce the device area, and then the collection area exposed to the light, paying this in terms of quantum efficiency and responsivity.

As before, the device shows a high photodetection gain. In fact, for example, at a wavelength of 270 nm and a temperature of 733.15 K, the ratio between the photogenerated current and the dark current is 10^5. Obviously, the ratio, in term of order of magnitude, increases reducing the working temperature because the reverse current is reduced.

Although it is not of great interest for the project purposes to use this device as the basic element for the realization of an image sensor, it can be interesting to evaluate (by simulations) the breakdown voltage value varying the temperature, and the optical gain introduced by the device, under avalanche condition.
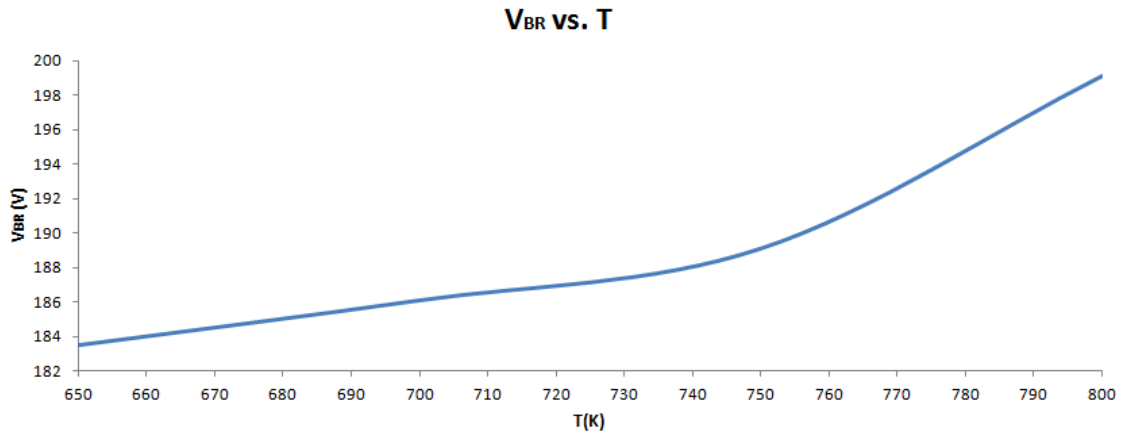
Figure 3.21. Breakdown voltage at different temperatures.

Figure 3.21 shows that the breakdown voltage increases with increasing temperature. This phenomenon is also confirmed by experimental results [47] and, probably, this is due to the fact that the carriers generation rate (see Eq. 1.24), under avalanche effect, is directly proportional to the temperature. Then, if the temperature increases, the impact ionization coefficient increases. This means that, since it is the reciprocal of the mean free path, this will be reduced and, therefore, the carriers, because of bumps, do not acquire the enough energy to trigger the avalanche condition (equal to the bandgap). This implies a shift of the breakdown voltage value to higher values. Furthermore, note that the breakdown voltage

value, evaluated via simulation, can be confirmed with an approximate theoretical calculation. In fact, at 650 K, given the low doping of the N⁻ region, assuming that the field profile is practically rectangular inside the depletion region, and neglecting the voltage drop on the P⁺ and N⁺ regions, it is possible to derive the reverse voltage simply as $E_{CR}W_D$, where E_{CR} is the 4H-SiC critical electric field, approximately equal to 2.2 MV/cm, and W_D is the depletion region width, assumed equal to the width of the intrinsic region, i.e. 0.48 μm. Developing the calculations a breakdown voltage approximately equal to 110 V is obtained. It is a little different from the simulated value (around 180 V), since the critical electric field extracted from the simulations was 4 MV/cm. To calculate the breakdown voltage, an appropriate command has been used, i.e. *BreakAtIonIntegral* [44]. In particular, this is an approximate breakdown analysis, where the avalanche generation is simulated by calculating the following ionization integrals:

$$I_n = \int_0^W \alpha_n(x) e^{-\int_x^W (\alpha_n(x') - \alpha_p(x'))\, dx'}\, dx \qquad (3.10)$$

$$I_p = \int_0^W \alpha_p(x) e^{-\int_0^x (\alpha_p(x') - \alpha_n(x'))\, dx'}\, dx \qquad (3.11)$$

where α_n and α_p are the ionization coefficients for electrons and holes, respectively, and W is the depletion zone width. In particular, the avalanche breakdown occurs if one of the two ionization integrals becomes 1 (because the avalanche can be triggered from electrons, from the holes, or both of them; see Eq. 2.39).

Analyzing the breakdown voltage, assuming that the device works at a voltage near the breakdown voltage, that at 733.15 K is approximately 190 V, the optical avalanche gain can be evaluated with its mathematical definition (see Eq. 2.38). Obviously, this gain could be investigated, as all the other parameters seen so far, with temperature variations. For example, the Figure 3.22 shows the optical gain, in avalanche conditions, as a function of the wavelength, at a fixed temperature of 733.15 K.
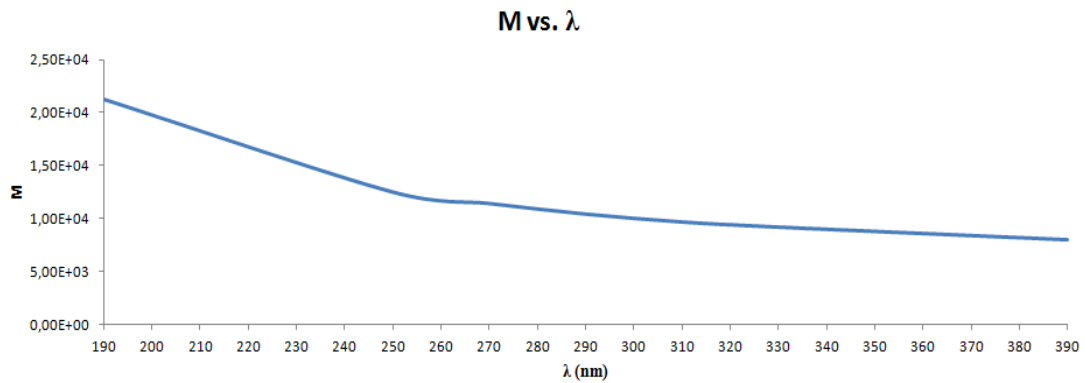
Figure 3.22. Avalanche gain at 733.15 K for different wavelengths.

Therefore, as can be seen from Figure 3.22, in avalanche conditions, with a photogenerated current value of the order of mA, and a dark current of the order of nA, and considering as

the photogenerated current and the dark current of reference the calculated values at a reverse voltage of -20 V (the first of the order of tenths of μA, and the second of the order of 10^{-13} A, at 733.15 K), optical gains in the order of 10^3-10^4 are obtained. On the other hand, when the photogenerated current is amplified, the dark current will also be amplified in the same way. This emphasizes that this condition has to be avoided at all costs, when this device has to be used as the basic element of an image sensor.

Another important thing to analyze is that, when the avalanche triggers, the breakdown has to be uniform throughout the device, i.e., the electric field has to uniformly increase throughout the entire device, without triggering any premature breakdown. In this way, an optical avalanche gain as uniform as possible is obtained. To make sure of this, the evolution of the electric field has to be observed. In Figure 3.23, it is shown that the electric field is uniform throughout the device, without presenting higher values in a point rather than another.
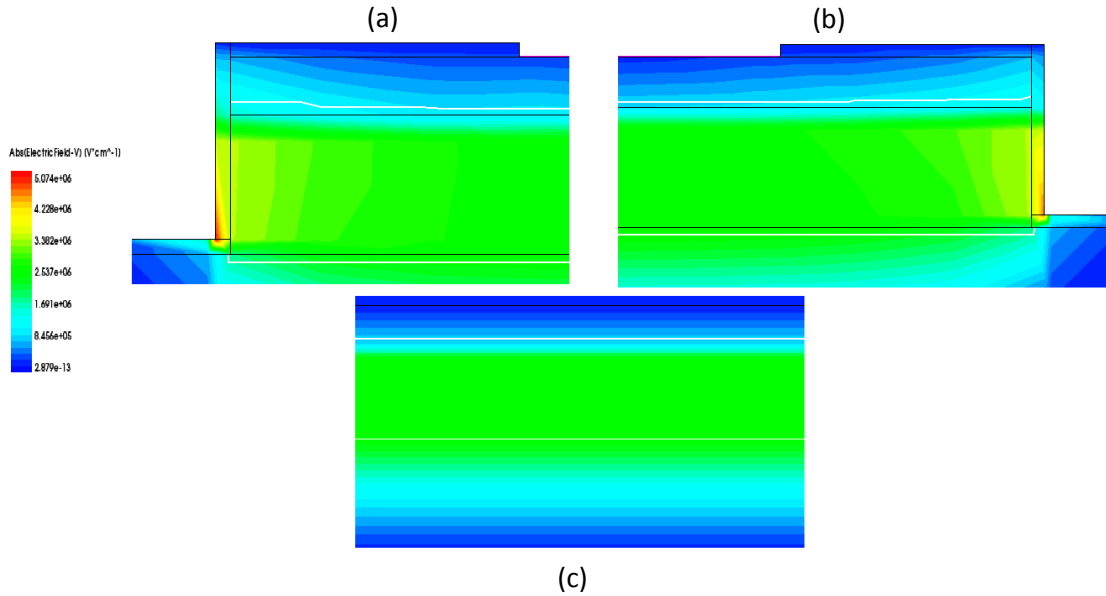
Figure 3.23. Electric field in avalanche breakdown condition, on left side (a), right side (b) and central region (c) of the device.

Therefore, as can be seen from Figure 3.23, the electric field inside the device is uniform, with a slight increase in the corners (in the oxide) of the lateral regions, but however the order of magnitude (which is what matters) does not change. This ensures an uniform avalanche gain throughout the device.

At this point, given that the device in question is only a possible proposed UV photodetector, it is also interesting to investigate what happens in terms of photogenerated current, when some technological parameters change, such as doping and thickness of the P^+ region. These two are important parameters to investigate the device light absorption.

If the doping value decreases, theoretically, the electron-hole pairs collection should be optimized, because of a greater extension of the emptied region in P^+ region. For the second parameter, from a theoretical point of view, the thickness is directly related to the ability of collecting the photogenerated carriers. If the thickness increases a lot, the

electrons photogenerated on the surface do not succeed in reaching the depletion region and being sent to the N⁺ region. This reasoning should be iterated for various temperatures, because many physical parameters, such as mobility, diffusion lengths, active dopant concentration, etc., are strictly dependent on the working temperature. Moreover, this reasoning should be iterated for different incident wavelengths. To simplify the analysis, the simulations were carried out at a fixed temperature, i.e. the one of interest, equal to 733.15 K, and at three different wavelengths, namely 190, 290 and 330 nm, in order to consider, respectively, a wavelength in each one of the UV sub-bands.

J$_{ph}$ vs. N$_A$
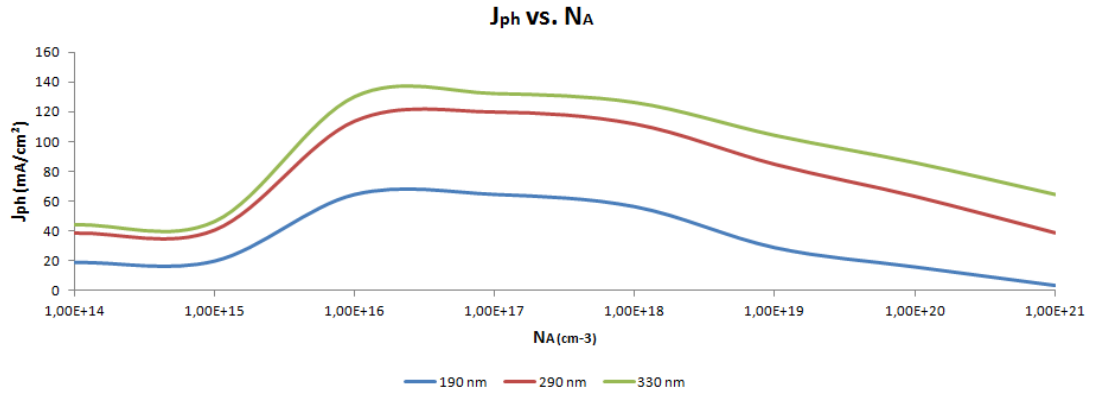
Figure 3.24. Photogenerated current density versus P⁺ doping for different wavelengths at 733.15 K.
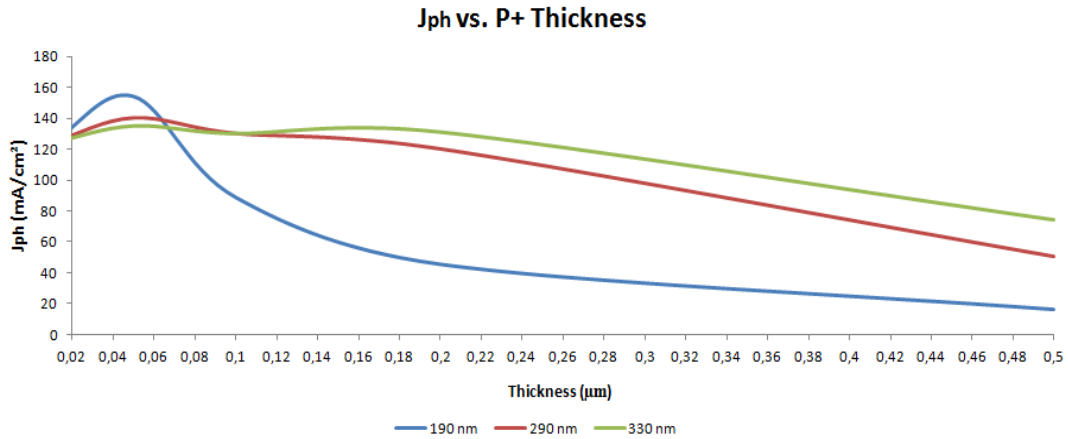
J$_{ph}$ vs. P+ Thickness

Figure 3.25. Photogenerated current density versus P⁺ Thickness for different wavelengths at 733.15 K.

In Figures 3.24 and 3.25 it is possible to observe that the photogenerated current depends, as expected, both from the value of the doping and from the thickness of the P⁺. In particular, when the value of the doping increases a lot, a strong reduction of the photogenerated current is observed. This is due to the fact that if the doping is increased, the depletion region, in the P⁺ region, will be reduced. Of course, this implies that the carriers collection is not optimized because, recalling that a lot of carriers are generated at the surface (remembering the trend of *G*), if the diffusion length is not suitable to reach the depletion region, these carriers will not contribute to the photogenerated current. This

problem is also more severe when the temperature increases, because these quantities tend to be reduced due to a mobility reduction. Therefore, a doping reduction allows a greater extension of the depletion region inside the P$^+$ region and a more efficient carriers collection, in particular of the carriers generated at the surface, that are more than those in depth. This is true if the doping is not reduced too much. In fact, if the doping is reduced a lot, the P$^+$ region could completely disappear, because it becomes all depleted. Therefore, the holes will not be collected in any region, resulting in a collapse of the photogenerated current. Also, in Figure 3.24 it is observed that the collapse of the photogenerated current is different changing the considered wavelength. Indeed, if a short wavelength is considered (for example 190 nm), in agreement with the absorption depth, these wavelength creates electron-hole pairs prevalently at the surface. Therefore, if the doping is high, the current reduction is still greater, compared with what happens in the case of a long wavelength. Vice versa, for wavelengths that penetrate deeper (i.e. long wavelengths), a doping increase causes a more contained current reduction, because they create a high quantity of electron-hole pairs (quite constant) in the entire device. From this figure, it can also be understood the choice of a P$^+$ doping of 10^{18} cm^{-3}. In fact, the current density grows when the doping decreases, up to a value of 10^{18} cm^{-3}, then it becomes constant, up to a value of 10^{16} cm^{-3}, and after it decreases. These simulations were performed with the same thickness of the P$^+$ region, i.e. 200 nm.

A similar reasoning can be done for the thickness of the P$^+$ region, where it is observed that the smaller is the thickness of this region, the higher is the photogenerated current.

In fact, if the thickness of the P$^+$ region is reduced, it optimizes the carriers collection, because, fixing a certain doping, recalling the trend of the generation rate G, it is possible to collect more carriers and, in particular, those near the surface, where the photogeneration is more intense. Moreover, if the thickness is reduced, as the temperature increases, there will not be even problems of carriers collection, due to the diffusion length reduction.

In fact, even if the diffusion length is reduced, the carriers can reach the intrinsic region because they have to cross a much smaller P$^+$ region. These simulations were performed with the same doping of the P$^+$ region, i.e. 10^{18} cm^{-3}.

Once again, fixing the same doping and temperature, all depends on the incident wavelength. In fact, from Figure 3.25 it is observed that if the wavelength is short, reasoning with the same doping, a thickness reduction would be very convenient to collect more carriers, because the used wavelength creates a lot of carriers especially at the surface (see the absorption depth). Instead, if the wavelength is long, reasoning with the same doping, also a greater thickness is fine, because this wavelength creates also deeper carriers (in a way quite constant on the entire device).

For the previous simulations, a thickness of 200 nm was chosen, because, unless working in the extreme UV, i.e. in the range 10-200 nm and, therefore, with very low wavelengths, a thickness of 200 nm is more than sufficient to have a good photocurrent density and it is realizable with typical ion implantation.

It must be kept in mind that the thickness reduction is not a trivial thing, since to reach these thicknesses special implantation techniques are required. In fact, with the standard implantations it is possible to obtain a thickness of 30 nm (i.e. *ion implantation*). Instead, if

a thickness of 5-10 nm is required, more sophisticated techniques have to be used, such as *plasma implantation* [16]. Therefore, according to the considered wavelength, a good trade-off can be chosen. If long wavelengths have to be detected, a higher doping and a greater thickness of the P^+ region (obtainable with typical *ion implantation* techniques) are preferable. Vice versa, if short wavelengths have to be detected, a smaller thickness (obtainable with *plasma implantation*) and a doping reduction of the P^+ region, ensure a higher photocurrent. Furthermore, it could be also interesting to analyze, if there is a dependence of the dark current from the doping and from the thickness of the P^+ region. As can be seen in Figures 3.26 and 3.27, the dark current does not suffer of any variation, if these two parameters change, as confirmed by results available in the literature [16].
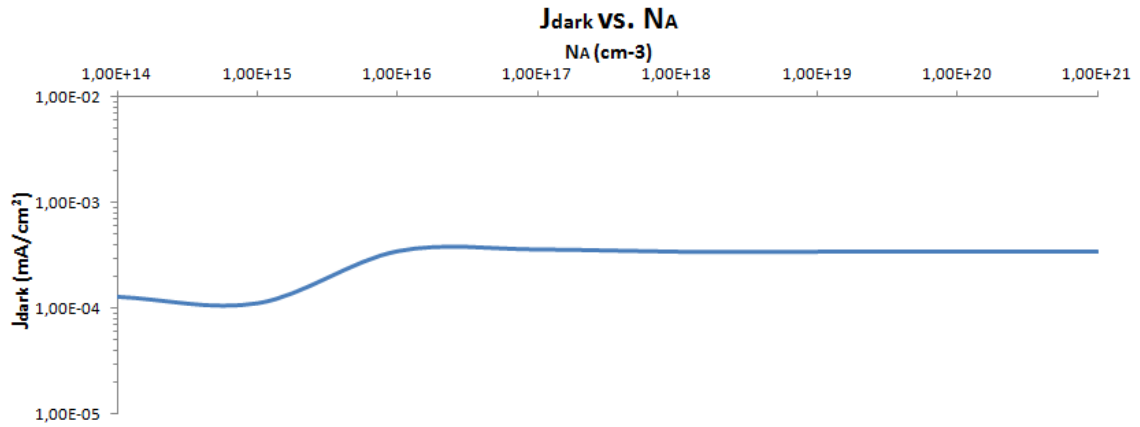
Figure 3.26. Dark current density versus P^+ doping at 733.15 K in log-scale.
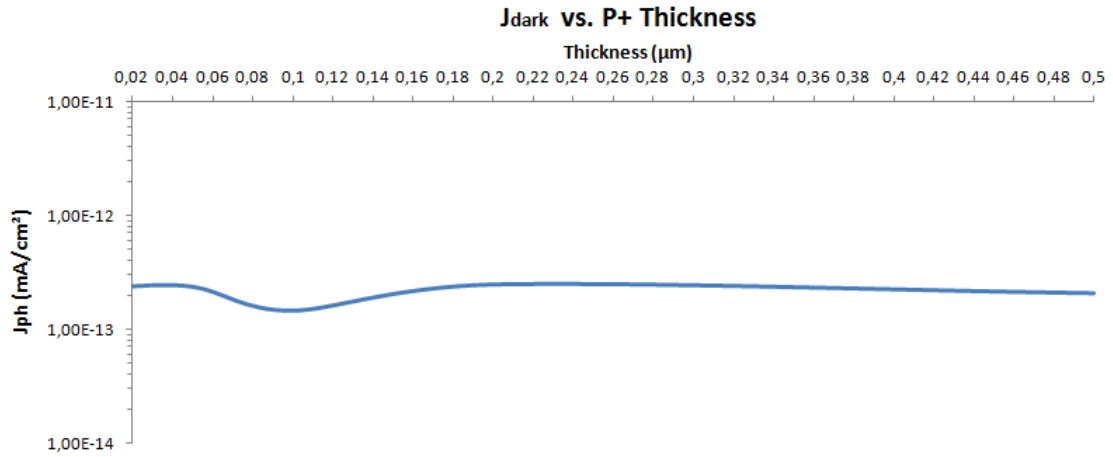
Figure 3.27. Dark current versus P^+ thickness at 733.15 K in log-scale.

Perhaps this trend of the dark current can be explained in the following way. Recalling the expression of the reverse current (see Eq. 2.20), neglecting, in first approximation, the hyperbolic tangents, for high doping and high thickness of the P^+ region, the second addend is still negligible compared to the first. When the doping of this region drops of an order of magnitude below the value of the doping of the N^- region, or the P^+ thickness becomes too small, such that the hyperbolic term cannot be considered negligible,

115

theoretically, the second term should be taken into account. When the temperature is high, the reduction of D_n (due to a strong reduction of mobility) must be taken into account, and, given that the value of L_n is higher than L_p (because μ_n is always greater than μ_p, at least 10 times at a temperature of about 700 K, as represented in Figure 1.4), the second addend, causes a small increase in the dark current. This increase is, however, limited, and, then, the current remains quite constant.

Note that, these two parameters, i.e. the thickness and the doping of the P$^+$ region, only have an impact on the electrical behavior of the device (for example, the photogenerated current variation). They have not any effect on the optical properties (for example, absorption coefficient, absorption depth, etc.), because the optical properties of the material do not depend from the temperature, or from the doping, or from the thickness.

Therefore, with these simulations, it has been clearly shown the good performances of a 4H-SiC pin diode to work in the UV photodetection and, therefore, for the realization of an UV image sensor. Finally, however, it is necessary to emphasize one important thing. The dimensions of the simulated device are smaller than the previous device, but it is still big, because, if a simple integrated square sensor of 1 Megapixel (i.e. 1000x1000) has to be realized, with a lateral dimension of 100 μm for each device, the sensor will have a dimension of 100 cm^2 (i.e. 0.01 m^2, i.e. about 85 times smaller than before). Obviously, if the device size is reduced, for example all is scaled of the 80 % (therefore the lateral dimension becomes 20 μm), the sensor would be 4 cm^2 and then easily integrated. Typically, a sensor is never present within an integrated circuit, also in a typical camera, but it is implemented as a discrete component, specifically built to detect the image, and, therefore, not integrated. Obviously, the size of the sensor is essential, even if it is a discrete component, otherwise it cannot fit the camera dimensions. Typical dimensions are, for example, of 36.0 x 23.9 mm, with a pixel size of 8.45 x 8.45 μm, or 24 x 36 mm, and with the pixel size set according to the desired resolution, i.e. on the basis of the number of pixels required by the sensor itself. Therefore, a sensor with an area of 4 cm^2, can be a good integrated solution. In this case, also the application field of the sensor is important. In fact, if the sensor has to work in a harsh environment (in terms of brightness) as that of the *Venus* surface, the amount of light that reaches the surface is extremely reduced because of the thick clouds that surround the surface and block a large part of the electromagnetic spectrum, including the visible light (in any case, the visible light is not absorbed from the 4H-SiC due to the high bandgap, and the same thing happens for the IR radiation). It is obvious that a maximization of the amount of light collected is very important, even if, in the case of the 4H-SiC, it is limited only in the UV portion of the electromagnetic spectrum. A strong reduction of the area exposed to the light (i.e. the pixels area) will penalize the performances of the sensor in terms both of quantum efficiency and responsivity, for a same incident optical power density. Increasing the size up to the maximum dimensions allowed by integrated technology would be the best choice. To understand if an UV photo would make sense on the Venus surface, it is interesting to investigate the atmosphere surrounding Venus and, therefore, what are the wavelengths that reach the surface. The Venus atmosphere is mainly composed of carbon dioxide (96.5%), CO_2, and nitrogen (3.5%), N_2. The first strongly absorbs infrared radiation (i.e., above 700 nm), while the latter strongly absorbs the wavelengths below 100 nm [48] (i.e.,

extreme UV). Moreover, in 2011, a thin ozone layer at an altitude of 100 kilometers in the Venus atmosphere has been discovered, by ESA's Venus Express spacecraft [49], where it is well known (also on the Earth) that the ozone layer (O_3) completely blocks the UV-C radiation (100-280 nm), most of the UV-B radiation (280-315 nm), and only allows the passage of UV-A radiation (315-400 nm). Then, taking into account the thick layer of clouds that surrounds Venus, causing a sunlight reflection of 76% [50], it is possible figure out how the light which arrives on Venus is reduced, both in terms of intensity and wavelength.

Therefore, it is essential in the design phase do not forget this observation, which might cause an incorrect sensor design. Moreover, it is also possible to implement solutions to improve the light absorption, such as the deposition of more *antireflective layers* on the device. These layers can improve the light absorption, thanks to a further reduction of the reflectivity on the surface. Another solution can be the use of appropriate *texturing* techniques, to specially damage the surface [16], to increase, through multiple reflection techniques, the number of collected photons, which, otherwise, would be lost. Another solution can be the use of optimized optical systems of lenses (i.e. extended well beyond the pixel size itself, as in the case of a typical microlens), to better focus the light radiation on each pixel. In this way, for the same incident power density, the light power focused on the pixel increases. Another solution can be the realization of appropriate contacts, which are not simple metal contacts, but *ITO* (*indium-tin oxide*) contacts, which seems to be the most widely used transparent conductive oxide for the manufacture of conductive transparent films. It appears to be the best material to make contacts that simultaneously combine both a good electrical conductivity and a good UV optical transparency (if suitably realized [72]). This solution is already used in some applications, as reported in [51], even if this solution is used in the case of β-SiC devices, i.e. 3C-SiC, and not α-SiC, such as the 4H-SiC.

For example, one of the best materials used as antireflective layer, both for photovoltaic applications and for photodetectors, is the *magnesium fluoride* (MgF_2). In fact, in Figure 3.29 and 3.30, respectively, the responsivity and the quantum efficiency obtained by simulations are reported, for different wavelengths, at a temperature of 470 K. In the simulations the deposition of an antireflective layer of 200 nm is considered. The thickness was chosen in agreement with typical thicknesses of antireflective layers used to realize photodetectors in 4H-SiC [40]. The MgF_2 layer covers the entire device (contacts excluded, obviously).
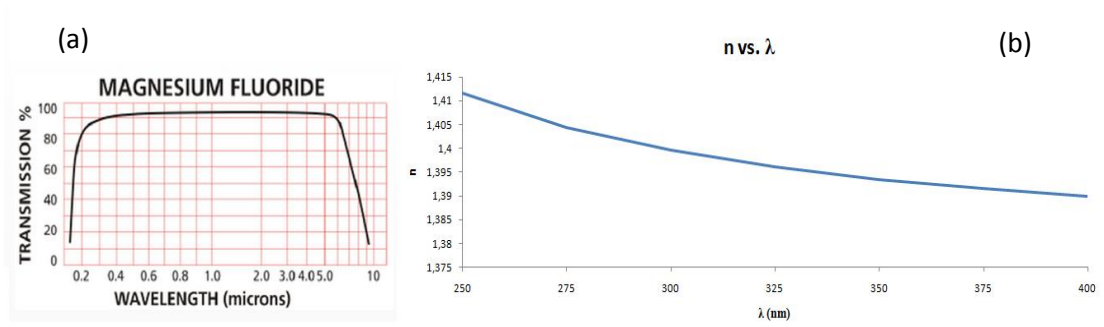
Figure 3.28. Optical properties of MgF$_2$. (a) Transmittance versus wavelength. (b) Real part of the complex refractive index.
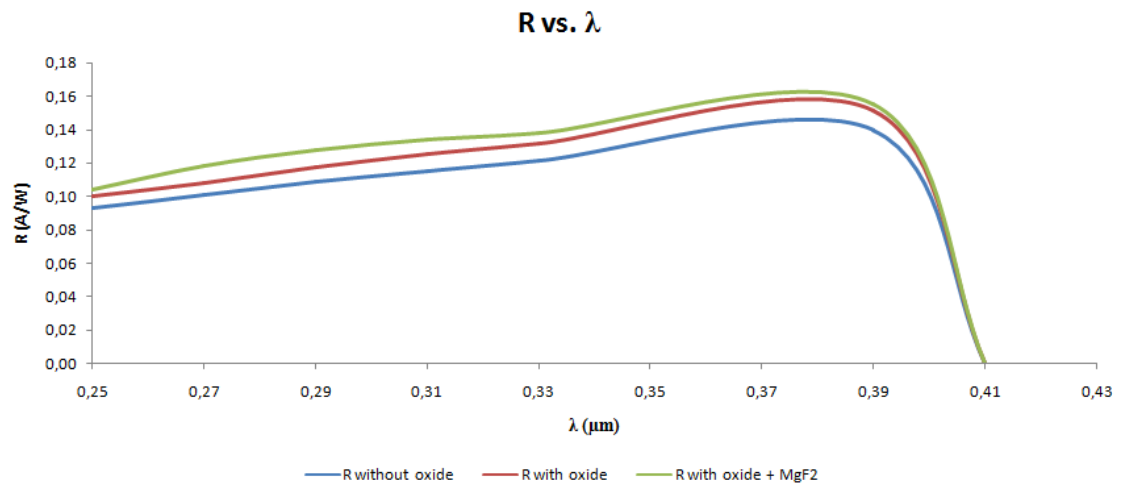
Figure 3.29. Responsivity versus wavelength at 470 K.
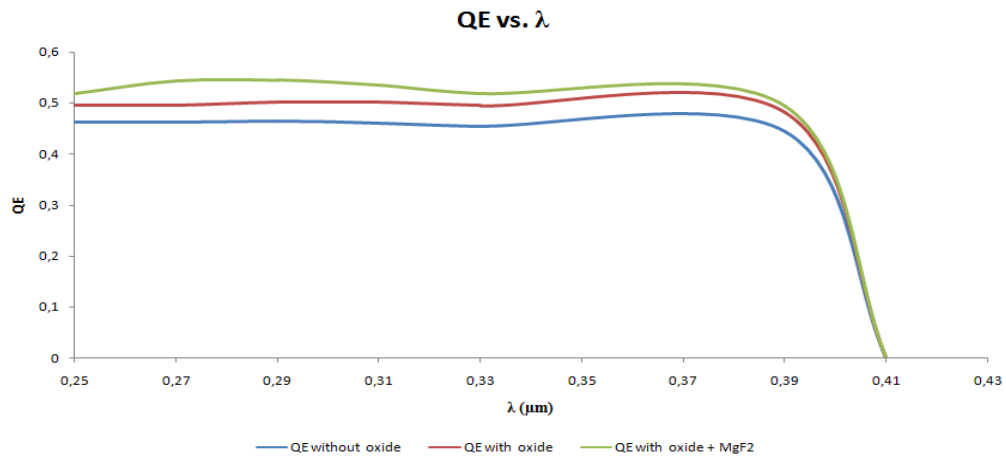
Figure 3.30. Quantum efficiency versus wavelength at 470 K.

Therefore, as can be observed from Figures 3.29 and 3.30 reported above, the responsivity and the quantum efficiency increase thanks to the deposition of a layer of 200 nm of MgF$_2$ above the SiO$_2$ layer of 50 nm. The simulations were carried out at a temperature of 470 K because, in practice, the MgF$_2$ is suitable to work in a temperature range from -100 to

200 °C [52]. Therefore, it would be useless to go beyond this value. In Figure 3.28 is reported only the real part of the complex refractive index, since the imaginary part k is zero, at the different wavelengths, not only in the UV range, but also beyond. These values [27] have been included inside the simulator, through a dedicated file. To optimize the light collection, it would be interesting to investigate other antireflective materials suitable for applications at higher temperatures.

3.3.3   4H-SiC photodiode: second proposed solution

If the objective is to realize an integrated sensor, the pixel size has to be reduced as mentioned in the previous paragraph.
For this reason, it is interesting to analyze the 4H-SiC photodiode behavior, with lateral dimensions reduced by approximately 80 %, compared to the previous device. The doping and the vertical dimensions remain unchanged, compared to the first photodiode proposed. Furthermore, the cross section will be slightly modified, to allow a simple integrated realization of the same. The cross section of the second 4H-SiC photodiode is shown in Figure 3.31.
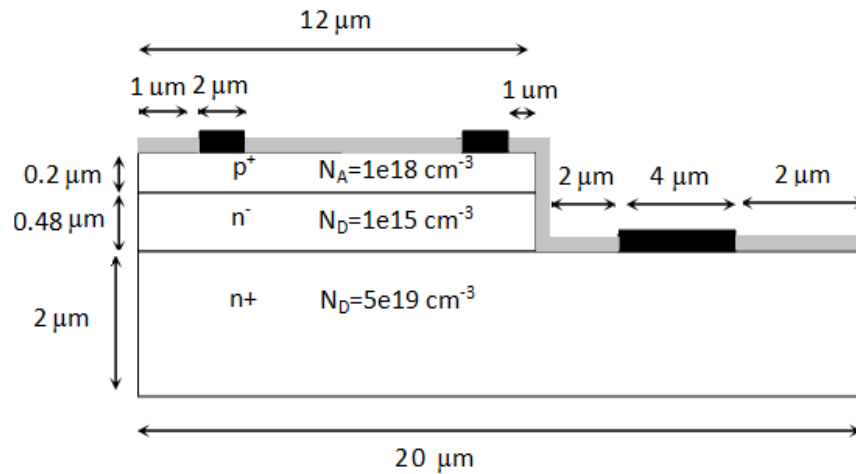
Figure 3.31. Entire cross section of the 4H-SiC photodiode proposed.

Looking at the Figure 3.31, comparing it to the previous structure, everything has been reduced, in terms of lateral size (also the contacts width). In particular, the contact of the P^+ region is always a double contact, for the reason presented in the previous paragraph, also because the doping of this region is reduced compared to that of the N^+ region, which means the resistance in this region is bigger than in the N^+ region. Instead, the contact of the N^+ region is unique because, having reduced the dimensions, one cannot easily achieve a double contact also on this region (due to the small distances involved and the possible problems of uncertainty alignment of the masks, the uncertainties of the process, etc.). The contact is distant 2 μm from the mesa structure of the intrinsic region. In any case, the contact is made wide enough to effectively collect the carriers, in terms of internal

119

dissipated power. The carriers, before being collected, encounter a minor lateral resistance, because to arrive to the contact they cover a shorter distance in a high doped region. For this reason the contact is realized on the upper side of the device, and not on the lower side, to reduce the path, that otherwise would be vertical. A large part of the devices made in SiC have always contacts on the top side of the device [1], [8], [41], [54], because this material is already intrinsically rich of defects (these defects arise during the manufacturing process) and, therefore, to reduce the losses, one tries to act also from a technological point of view. This results also in terms of easy deposition of all contacts simultaneously. This contacts are supposed to be always made of *TiAl*-based alloys, the only currently available materials that yield significantly low contact resistance - *Ohmic contact* - to the p-type SiC. These contacts show a high thermal stability. Moreover, also it can be theoretically shown that to reduce the side contact resistance, the contact length has to increase.

The oxide passivation thickness considered is always of 50 nm.

This device, simulated always with an optical incident power of 1 W/cm^2 and in a temperature range of 300-800 K, shows, despite its small size, good efficiency parameters, and good electrical properties (i.e., photogenerated current) even if, for the same incident optical power density, the actual optical power absorbed is reduced to one tenth compared to the previous simulation.
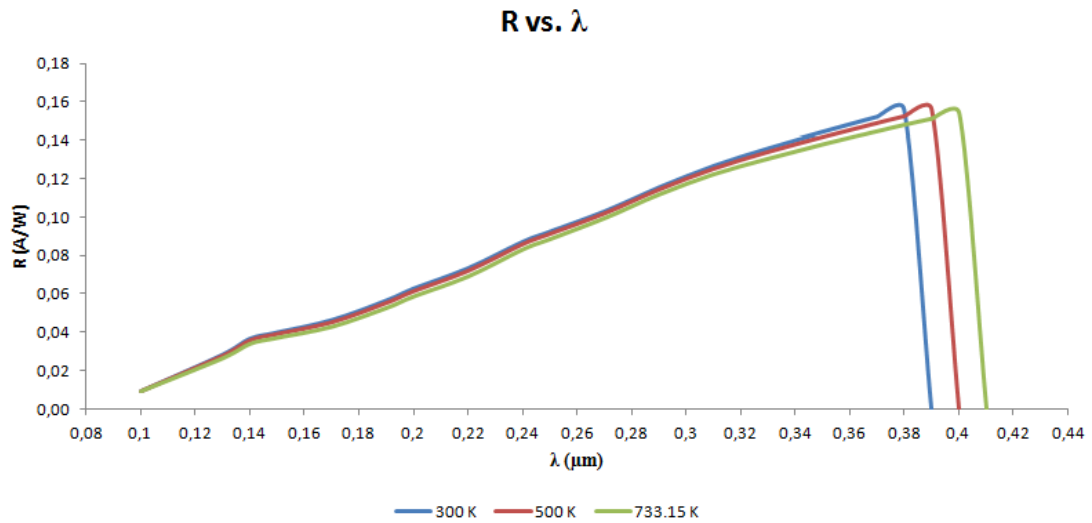
Figure 3.32. Responsivity versus λ at different temperatures.
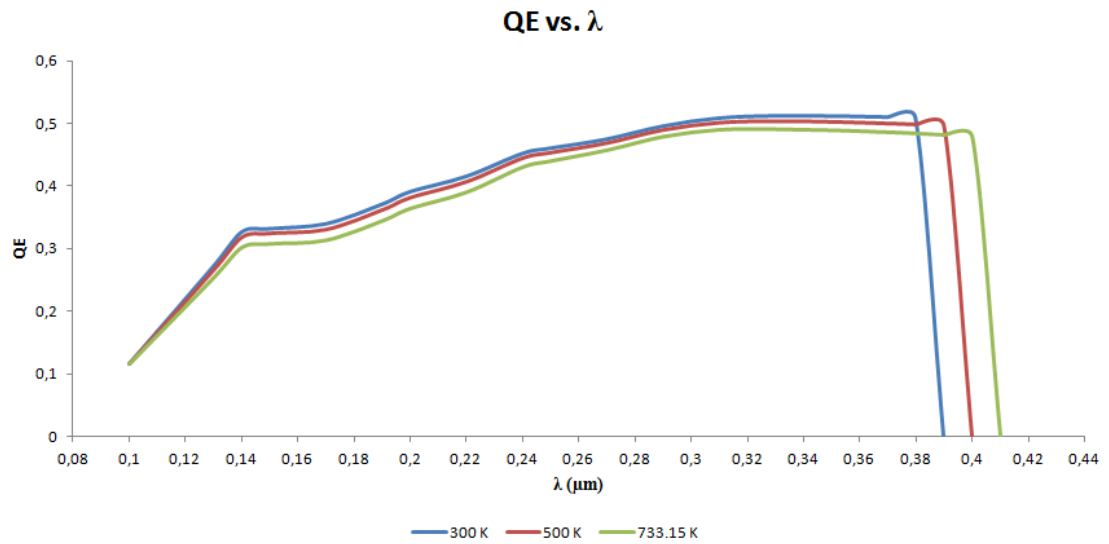
Figure 3.33. Quantum efficiency versus λ at different temperatures.
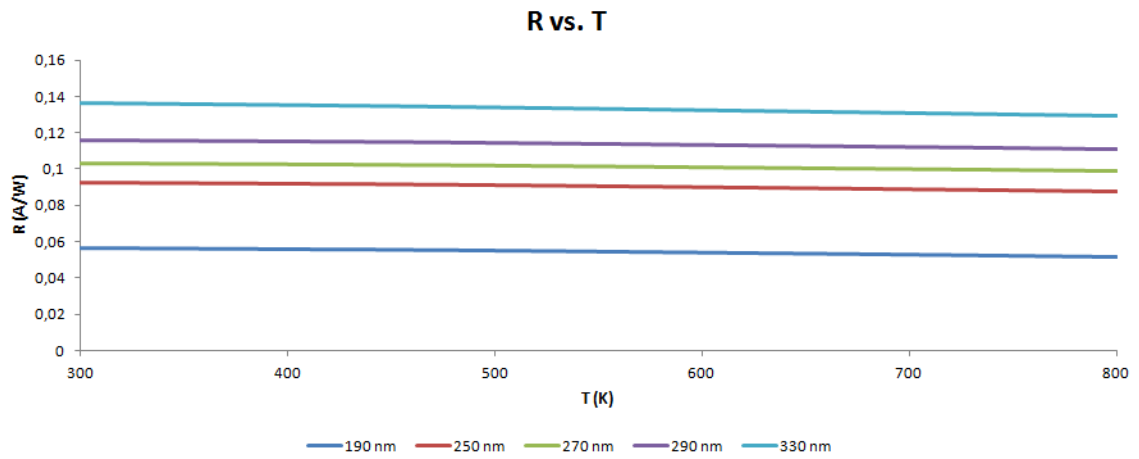
Figure 3.34. Responsivity versus temperature ad different wavelengths.
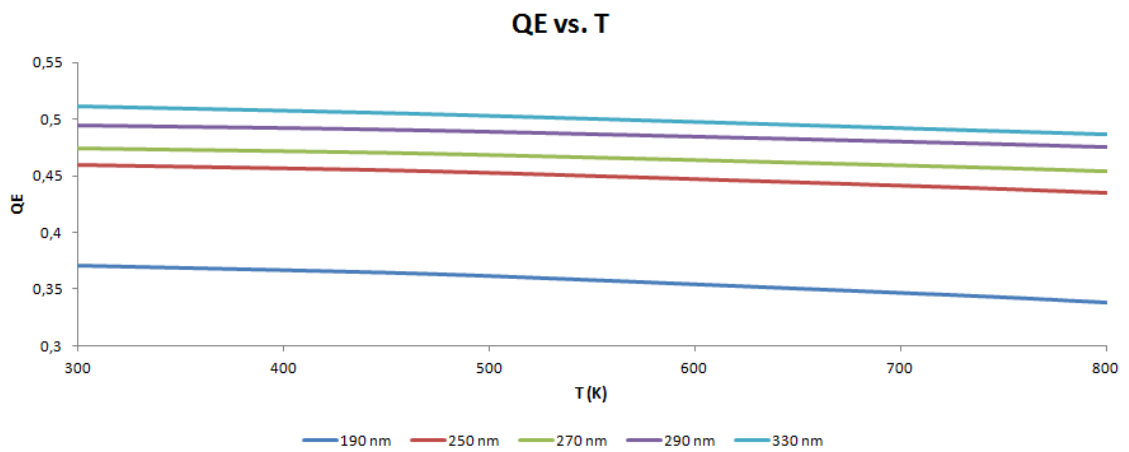
Figure 3.35. Quantum efficiency versus temperature at different wavelengths.

121
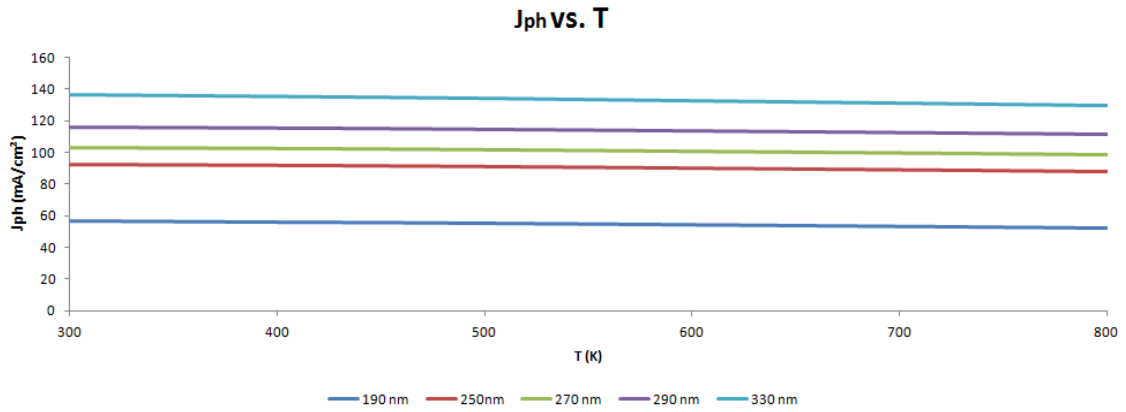
Figure 3.36. Photogenerated current density versus temperature ad different wavelengths.

Obviously, the analysis of the dark current is very important. Moreover, a comparison with the dark currents obtained in the first two devices can be very interesting, as shown in what follows.
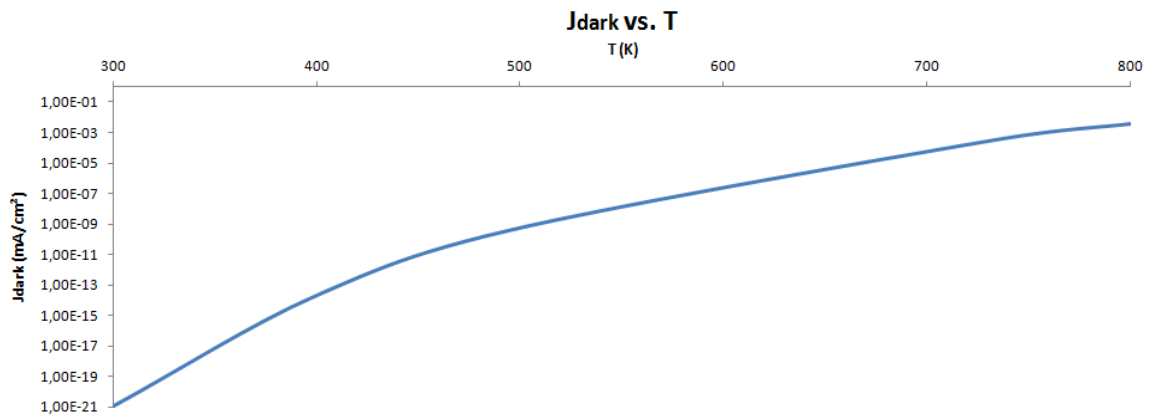
Figure 3.37. Dark current density versus temperature.
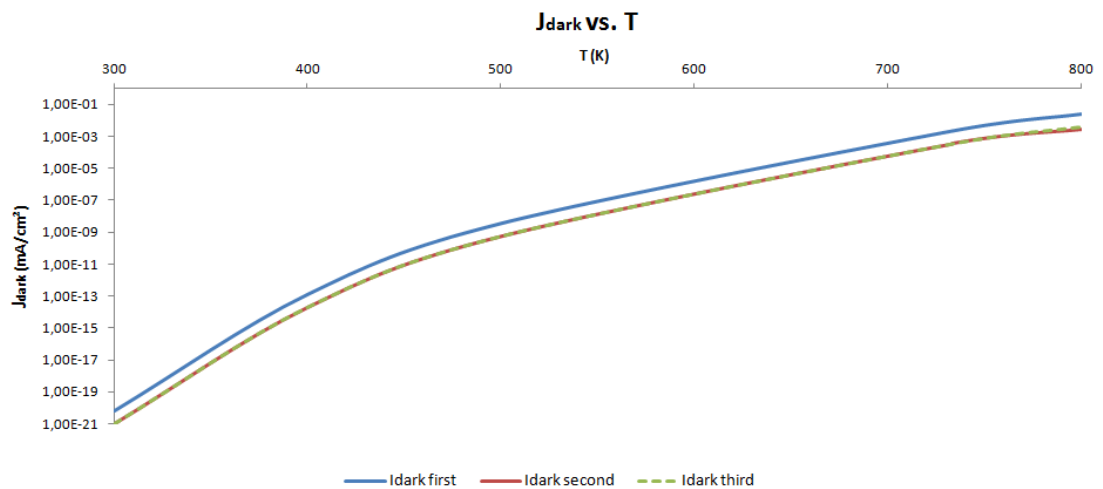
Figure 3.38. Dark current density comparison between the three devices.

122

Therefore, as seen in Figure 3.38, the third device does not allow a significant reduction of the dark current density, compared to the second device.

3.4 Phototransistor simulations

Following, for a possible future application of a phototransistor as the basic element of a pixel, the simulated phototransistors are shown. The advantage of using a phototransistor as a device for the photodetection is related to the fact that it shows an internal optical gain that allows to amplify the collector current, fixing the incident optical power. In this way, a photoconversion with a high optical gain is possible, even if in presence of low light intensities. In the pin diode, through the use of the avalanche condition, it has been observed that it is possible to obtain high photogenerated currents. However, when the avalanche condition starts, this also causes an increase in the dark current that it is not certainly favorable in the reading step of the pixels. Instead, now, the device does not work in the avalanche condition, but it is simply brought to work in direct active region, with the presence of a base polarization current (that, as discussed in the second chapter, is not important for the phototransistor operation itself). This allows a reduction of the dark current amplification. It should be noted that the base-collector junction, which plays the main role in the photogeneration, is always reverse polarized in direct active region. Thus, increasing the V_{BC} up to the junction breakdown voltage, it is possible to trigger the avalanche condition that has to be avoided.

The simulations will be carried out imposing the emitter voltage to 0 V, the collector voltage to 10 V and the base voltage to 2.5 V. This V_{be} is necessary to turn on the base-emitter junction. Due to the large bandgap, the built-in voltage is approximately 2 - 2.3 V, and so higher than the one in a typical silicon diode, where the built-in voltage is around 0.7 V. Furthermore, the transistor is polarized with a base current of 10 μA, and the analysis will be done in a temperature range of 300-500 K.

Moreover, the simulations will also be performed varying the wavelength in the UV range, and considering an incident optical power density of 1 W/cm^2 for the three cases (and considering, as before, a normal incidence of the optical rays). For matters in simulation times, a minor number of points will be considered for any phototransistors (in terms of wavelengths analyzed, the simulations will start from 190 nm), giving up, of course, a greater result accuracy, and obtaining a qualitative result of the quantities of interest. The high simulation time is related to the fact that to do one simulation (at a certain wavelength and a certain temperature), three sweeps are required, one to increase the base voltage to 2.5 V, one to increase the base current to 10 μA, and one to increase the collector voltage to 10 V (each simulation lasts at least 9-10 minutes, if a thick mesh is considered).

3.4.1 KTH's NPN BJT: test under light

First the performances of the NPN BJT, realized at KTH, was tested under UV light, whose cross-section is shown in Figure 2.36.
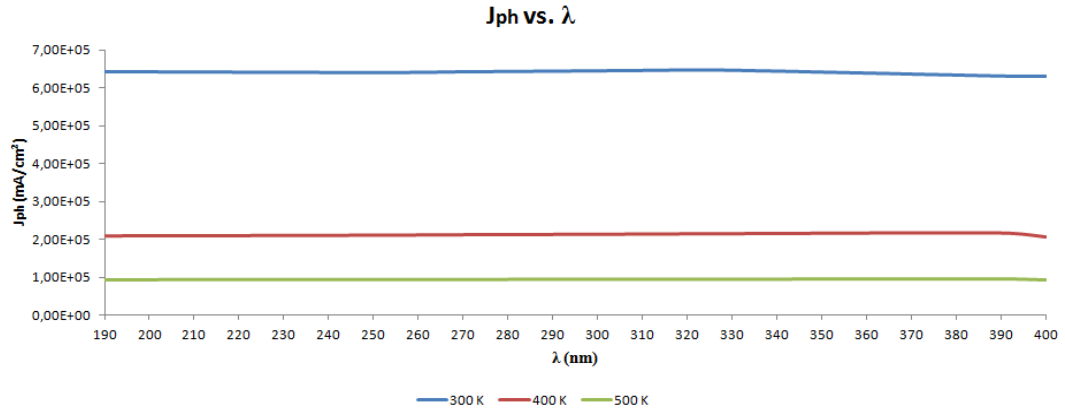
Figure 3.39. Photogenerated current density versus wavelength at different temperatures.

In Figure 3.39 the trend of the collector current, when the device is illuminated, has been reported (note that with J_{ph} the collector current density, under lighting conditions, is indicated). As can be observed, fixing a certain temperature, the current remains almost constant when the wavelength is changed (in fact, it slightly increases), while, fixing the wavelength, if the temperature increases this tends to cause a decrease in the current values. Furthermore, the photogenerated current is almost equal to the collector current at 400 nm (i.e., where the 4H-SiC is blind, and it shows the same behavior as in the dark condition). This is in agreement with the fact that this device is not, in any way, suitable to the light absorption, because it is covered almost entirely from metal, on the surface. Moreover, before that the light reaches the base-collector junction, where the photogeneration takes place, it must cross an emitter layer of about 1 μm (including the emitter cap), as well as a base layer of 300 nm. In agreement with the penetration depth, where it is clearly shown that in about 0.4/0.5 μm, all the incident power is already almost all absorbed, this performance was expected. Regarding the reduction of the collector current under illumination, when the temperature increases (reasoning at a constant wavelength), this trend follows the same trend of the non illuminated collector current (which would be, now, the dark current), as shown in Figure 3.40.
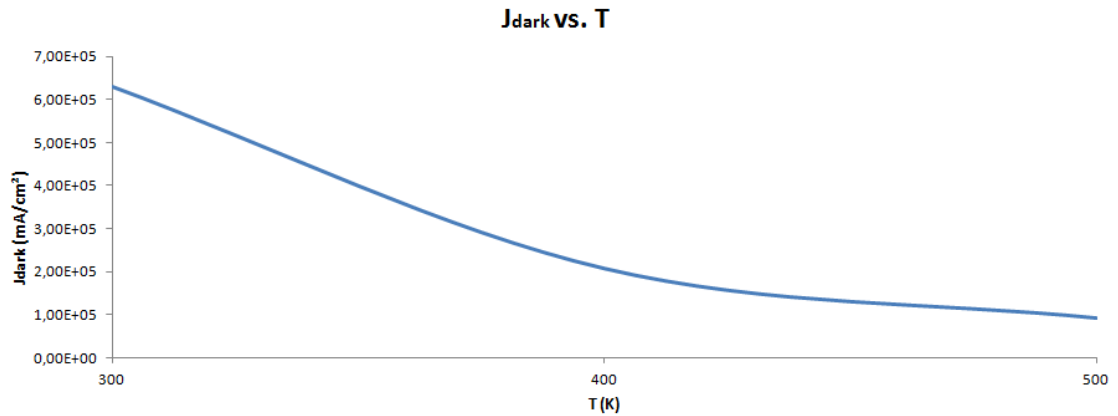
Figure 3.40. Collector dark current density versus temperature.

124

The reduction of the collector current can be explained in the same way as shown also in literature and experimentally [53,54]. Fixing a base current, the bipolar transistor gain tends to decrease when the temperature increases, for two possible reasons: the reduction of the emitter injection efficiency γ, due to an increase in the ionization degree of the base dopant, and the increase of the carriers lifetime. Indeed, the current gain β is defined as the ratio $I_C / I_B = \alpha/1$-α, in active region, where I_C is the collector current, I_B is the base current, and $\alpha = I_C/I_E$ (direct current gain at common-base), where I_E is the emitter current equal to $I_B + I_C$. However, α is defined as follows:

$$\alpha = \frac{I_{nE}}{I_E} \frac{I_{nC}}{I_{nE}} = \gamma \, \alpha_T \qquad (3.12)$$

where α_T is the base transport factor and γ is the emitter injection efficiency. Assuming a negligible recombination in the base (i.e., considering the base region width much less of the diffusion length L_n), it can be assumed that α_T is equal to 1, and, so, $\alpha \approx \gamma$.
In this case follows that:

$$\beta = \frac{\gamma}{1 - \gamma} = \frac{I_{nE}}{I_E - I_{nE}} = \frac{I_{nE}}{I_{pE}} \qquad (3.13)$$

where I_{nE} and I_{pE} are, respectively, the electrons and holes current at the forward-biased emitter junction, and I_E is the total emitter current equal to the sum of I_{nE} and I_{pE}. Applying a forward bias to the base-emitter junction equal to V_{be}, the diffusive currents I_{nE} and I_{pE} are equal to [9]:

$$I_{nE} = \frac{q \, A_E \, D_e \, n_0}{L_e} \left[\exp\left(\frac{q \, V_{be}}{k_B \, T}\right) - 1 \right] \qquad (3.14)$$

$$I_{pE} = \frac{q \, A_E \, D_h \, p_0}{L_h} \left[\exp\left(\frac{q \, V_{be}}{k_B \, T}\right) - 1 \right] \qquad (3.15)$$

where D_h and L_h are the diffusion constant and the diffusion length of the holes in the emitter, and D_e and L_e are the diffusion constant and the diffusion length of the electrons in the base, and n_0 and p_0 are, respectively, the equilibrium minority carrier densities in the base and in the emitter, equal, respectively, to ni^2/N_A and ni^2/N_D. Using the Eq. (3.13), (3.14) and (3.15) it is obtained that:

$$\beta = \frac{I_{nE}}{I_{pE}} = \frac{D_e L_h N_D}{D_h L_e N_A} \qquad (3.16)$$

from which, inverting the Eq. (3.13), it is obtained that:

$$\gamma = \frac{1}{1 + \dfrac{D_h L_e}{D_e L_h} \dfrac{N_A}{N_D}} \tag{3.17}$$

where, it is clear that if the carrier lifetime and ionization degree are increased, with the increase of the temperature, γ is reduced, and from Eq. (3.13), also β is reduced. Accordingly, for the same base current, the collector current is reduced, when the temperature increases, both in term of collector dark current and in term of collector photogenerated current. Note that in the Eq. (3.16), in place of the diffusion lengths, the quantities W_B and W_E must to be considered, that are, respectively, the physical base and emitter width, in the case that it is assumed that $W_B \ll L_e$ and $W_E \ll L_h$.

At this point it is interesting to derive the performance of the internal optical gain of the phototransistor, and the gain β under lighting conditions, following the Eq. (2.45) and (2.46).
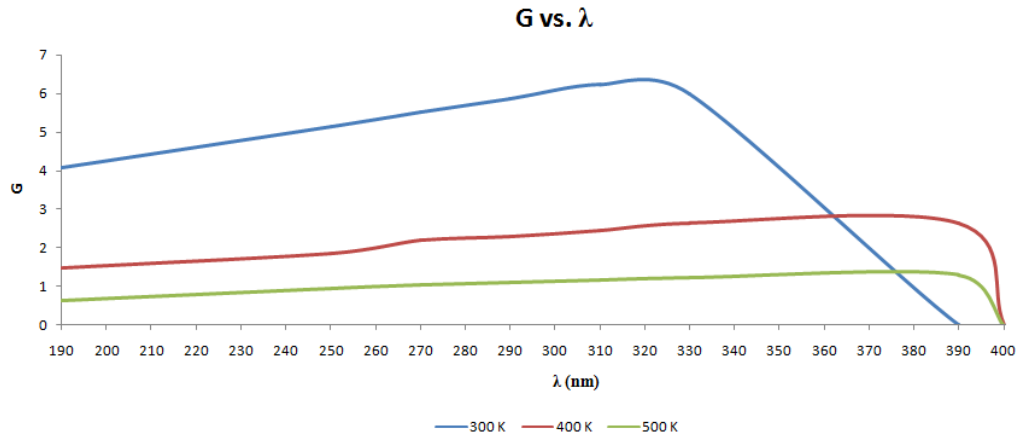
Figure 3.41. Gain versus λ at different temperatures.
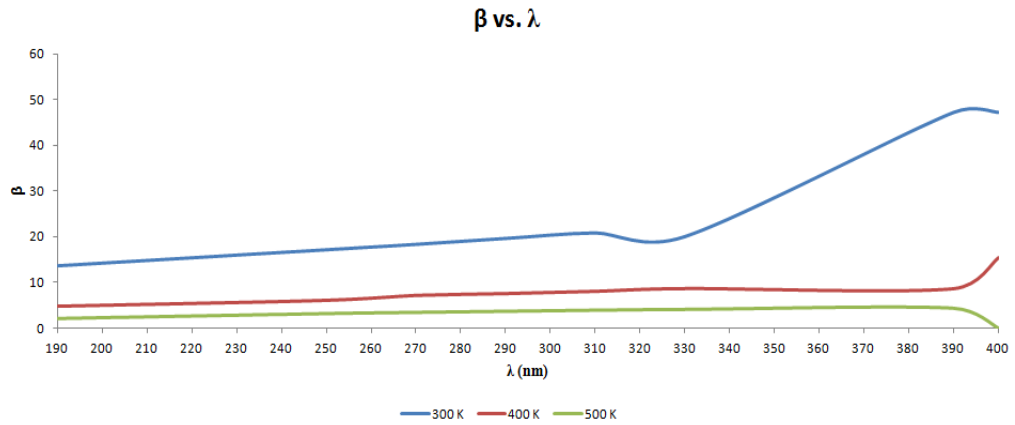
Figure 3.42. Phototransistor gain versus λ at different temperatures.

126

Hence, from Figures 3.41 and 3.42 it is confirmed what previously mentioned. In fact, both G and β are directly proportional to the collector current which, if the temperature increases, tends to be reduced, causing both a reduction in G and β, for the same incident wavelength.

From Figure 3.41 it is noted that the internal optical gain is very low on almost all the wavelengths of interest. This explains why this device is not absolutely suitable for the photodetection, due to the light reflection on three contacts which cover almost the entire upper surface, and to the fact that light does not directly hit on the base to reach the collector. In fact, if the light strikes on the emitter, because of the thicker layer to cross, it will surely be lost.

In addition a strange trend for gain β is observed from Figure 3.42. In particular, it is observed that, under illumination, the gain appears to be lower than the gain of the transistor in light absence. Obviously, in light absence the gain is the same presented at 400 nm (and also at 390 nm at room temperature due to the bandgap extension, as happened in diode). Beyond this wavelength the 4H-SiC does not absorb. Probably this strange behavior is related to the fact that, from Eq. (2.44), because of low internal optical gain, the collector current is little increased (because the light that is collected is not so much), while the photogenerated current, that is added to the polarization base current ($I_b = I_{bpolarization} + I_{ph}$; see Figure 2.42), tends to increase causing a consistent increase in the base current and, therefore, a β reduction.

Note, also, that, according to Eq. (2.46), once calculated the internal optical gain, the knowledge of the quantum efficiency is required to calculate β. Since it is difficult to analytically calculate the quantum efficiency of a phototransistor [42], it has been set to a default value constant and equal to 0.3. In particular, this value of quantum efficiency was chosen because from the previous simulations of the diode available at KTH, it is obtained that the quantum efficiency reaches about a 0.7 value, with a light exposure area of about 975 μm^2. If, now, the area is approximately reduced of 6 times (since the lateral size passes from about 975 μm to 150 μm), it can be assumed that, considering the same incident optical power density, the amount of collected light is reduced of six times than before and, therefore, also the quantum efficiency is reduced in the same way. But, however, in this way, the device shows a QE about 0.1. However, compared to previous diode, the collector is not completely covered by metal and the base contact is only 17 μm wide (even if, before, the base contact was made with inner holes and it extended across the entire base). Moreover, it will be assumed that the light mainly invests the base region, and not the emitter, otherwise the light would be all lost, because it crosses a thickness of 1 μm, and it is reflected, in part, by the contact (remember, however, that a Nickel contact reflects a little the ultraviolet radiation). Under this assumption, it can be considered that the quantum efficiency is slightly higher and, therefore, it has been set at 0.3. This is only an assumption. Probably, as result of this assumption, this is a best case (or the worst case) for QE value.

Furthermore, analyzing the G and β trends, it is also possible to understand why an analysis range of 300 - 500 K was chosen. In fact, at 500 K, both G and β are so low that it has not any sense to raise the temperature even more. In the future, it would be interesting

to investigate how to optimize the device to obtain a device that is able to exhibit high optical G and transistor β gains, at higher temperatures.

3.4.2 NPN phototransistor: first proposed solution

As previously done for the photodiode, possible realization solutions of the phototransistor will be analyzed, trying not to vary much from previously used BJT realization technology. The cross section of the proposed solution is shown in Figure 3.43.
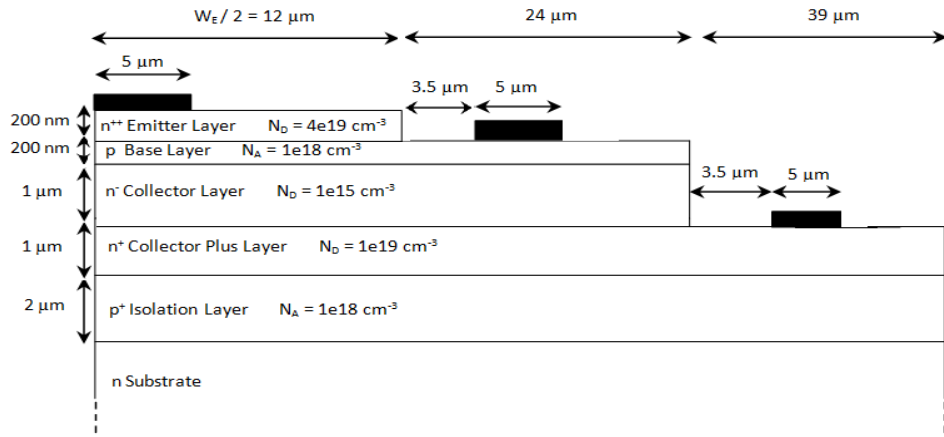
Figure 3.43. Half cross section of the proposed BJT.

Compared to the previous BJT, for the same lateral dimensions, the following changes were made. Emitter cap etching, since it is useless because of the high emitter doping of 10^{19} cm^{-3}, allows to obtain a good *ohmic* contact, and to avoid a *Schottky* contact. Reduction of the lateral size of the emitter, base and collector contacts to 5 µm, allows to further reduce the reflection to the contacts. Reduction of the emitter and base thicknesses to 200 nm to allow the light to penetrate more easily into the region and to reach the base-collector depletion region where the photogeneration takes place in the most efficient way. The dopings are unchanged, apart from the collector doping that has been reduced at 10^{15} cm^{-3}, in order to have a greater extension of the base-collector depletion region and, therefore, a better light absorption. Also a reduction to 3.5 µm of the distance of the collector contact from the edge of the base mesa structure has been done (the same distance of the base contact from the edge of the emitter mesa structure). In fact, in this way, the light absorbed within the collector plus, generating electron-hole pairs, permits the holes generated therein to reach the depletion region and, under the field action, sent in the P$^+$ region, even if the temperature increases, causing a reduction of the mobility and thus of the diffusion length. Moreover, if the contact is closer, it also reduces the internal resistance that the carriers meet in the lateral path, resulting in a reduction of the power dissipation. In Figure 3.43 the over-etch and the oxide of 50 nm deposited are not shown, as previously.

In the Figure 3.44, 3.45, 3.46 and 3.47 are shown, respectively, the photogenerated current density, the optical gain G, and the transistor gain β, for different wavelengths and

temperatures, and the dark current for different temperatures. When β is calculated, a quantum efficiency of 30 % is considered, although it is now probably increased. In fact, if a high optical gain will be obtained, this could be explained by a high quantum efficiency, improved compared with the previous case. Obviously, to compare the different devices, the same test conditions have been chosen and, therefore, the same quantum efficiency was considered.
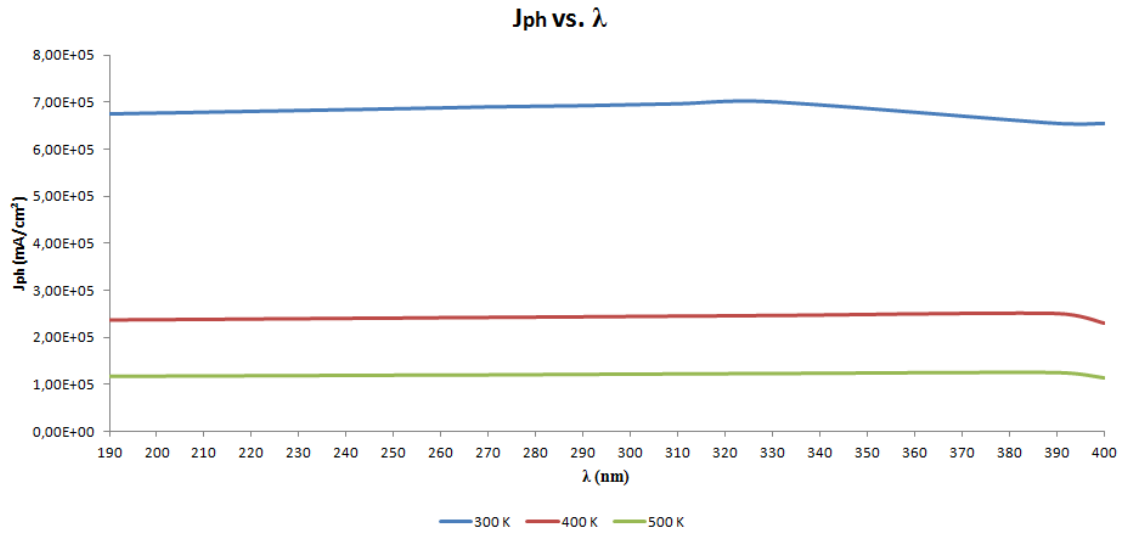
Figure 3.44. Photogenerated current density versus wavelength for different temperatures.
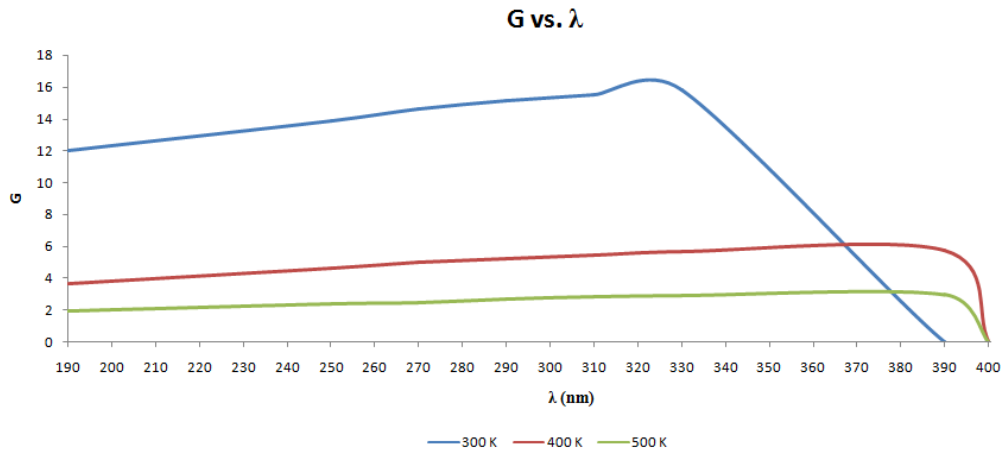
Figure 3.45. Optical gain versus wavelength for different temperatures.
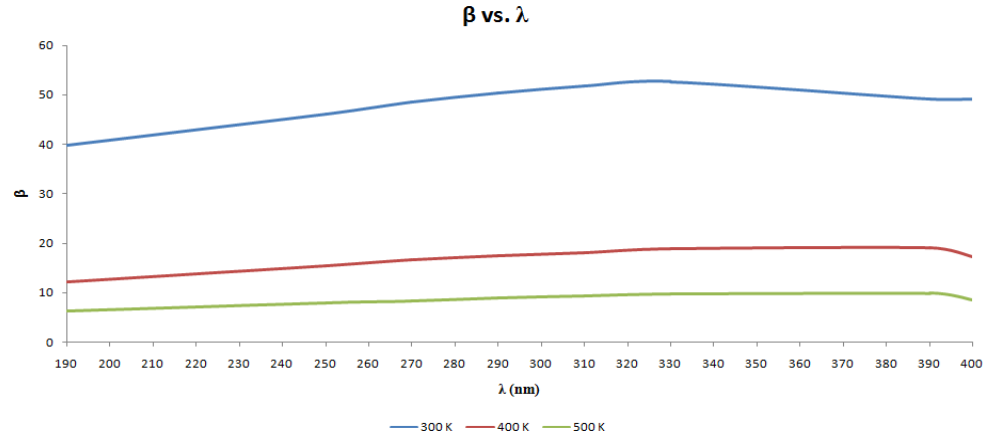
Figure 3.46. Transistor gain versus wavelength for different temperatures.
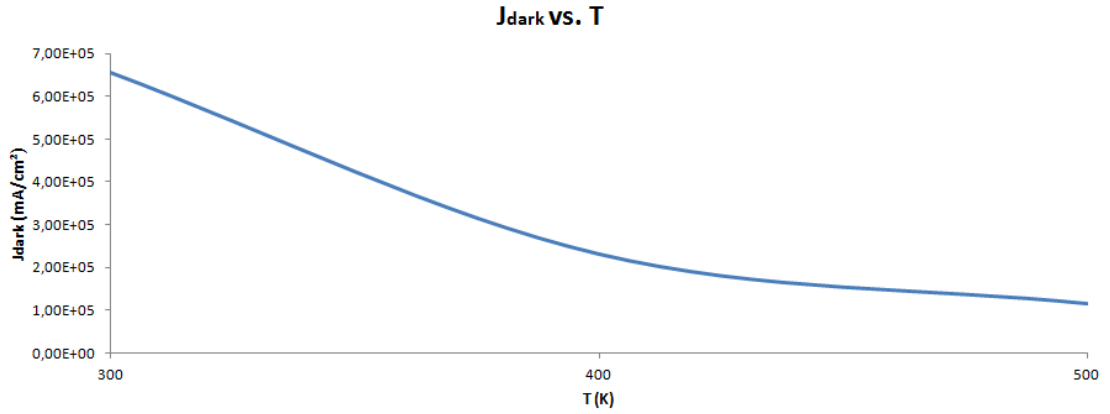
Figure 3.47. Dark current density versus temperature.

In the Figure 3.44 is shown that the photogenerated current tends to increment for the same temperature, even if this change is not noticeable in this figure. Instead, it is observed in Figure 3.45 that with the proposed structure, the optical gain is increased compared to the previous device. This justifies the fact that the light is collected in a more efficient way than before. In fact, also in Figure 3.46, where the transistor gain is shown, it is observed that it does not undergo a reduction as before, but it results to be higher than the dark current value and, furthermore, it linearly increases with the incident wavelength. Finally, Figure 3.47 shows the dark collector current density, where it is observed that it is practically the same as before (in fact, the lateral dimension, and the physical parameters, are the same).

To compare the two structures, below are reported two graphs where the optical gain G and the gain β of the two transistors are compared, where the obtained improvements are more emphasized.
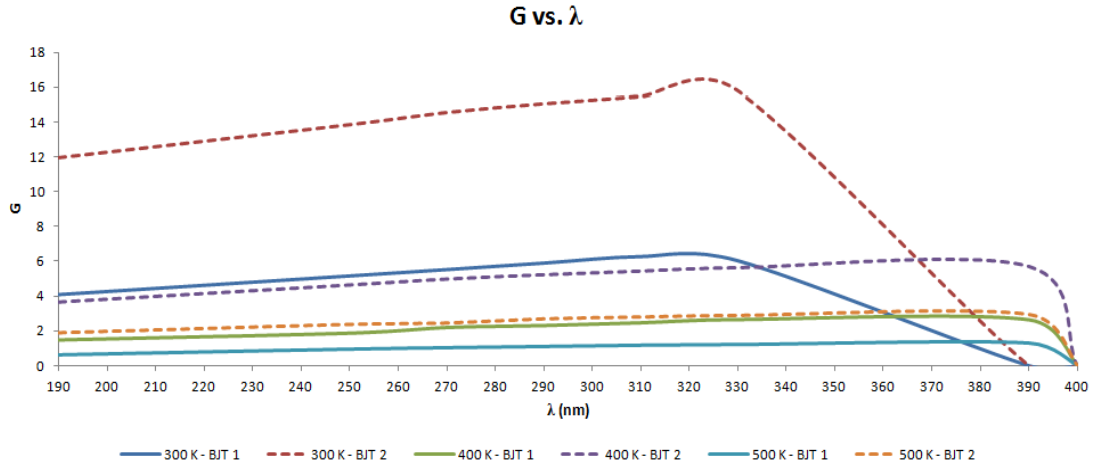
Figure 3.48. Comparison between the optical gains G of the two phototransistors.
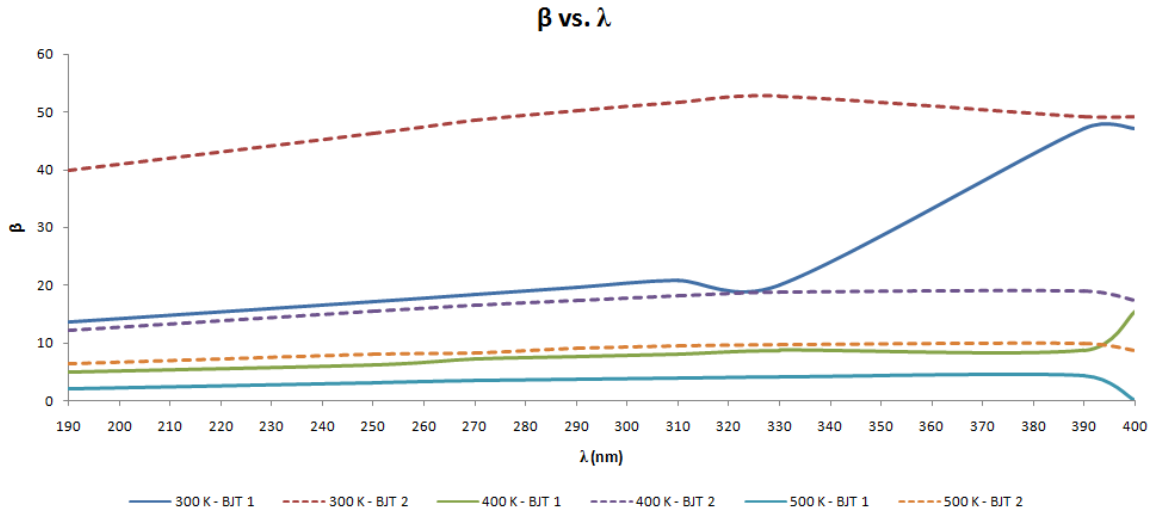
Figure 3.49. Comparison between the gains β of the two phototransistors.

3.4.3 NPN phototransistor: second proposed solution

To increase, even more, both the optical gain and the transistor gain, under lighting conditions, another solution will be shown.

In this phototransistor version, the doping of the first BJT will be considered. In fact, for the changes that will be adopted, it is useless to reduce the collector doping, because, in terms of light collection inside the depletion region advantages, this will be offset due to a collector thickness reduction. However, this time, the half cross-section dimensions are increased to 120 μm. An emitter etching is considered, reducing the size to 5 μm, in order to exploit it to trigger the transistor effect, reducing the light absorption at the same time, exposing as much as possible the base to have a better light collection. Given the emitter reduced size, the emitter contact will be extended on all the emitter region. The base contact is displaced as most as possible from the emitter mesa structure, reducing its width

to 2 μm, in order to have almost the entire base exposed to light. The distance between the collector contact and the base mesa structure is reduced to 2 μm (to have the same advantage in the structure previously presented). The collector thickness is reduced to 500 nm to compensate its doping concentration increase, to obtain a better light absorption. In figure 3.50 is shown a half cross section of the device.
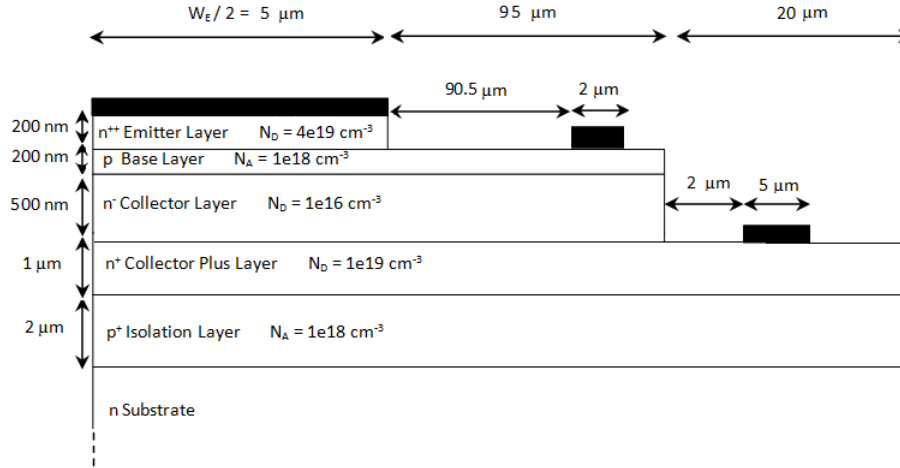
Figure 3.50. Half cross section of the proposed BJT.

In Figures 3.51, 3.52, 3.53 and 3.54 are shown, respectively, the trend of the photogenerated current, optical gain, and transistor gain when the wavelength changes, and the collector dark current when the temperature changes. The gain β is calculated, again, setting a quantum efficiency of 0.3. Of course, the assumption that the quantum efficiency is always the same from one device to another, and equal to 0.3, is necessary to do comparisons between the different devices, for a same quantum efficiency. But this assumption, will surely lead to estimate a not accurate gain β for the transistor. Moreover, when G increases, this is a clear manifestation of a better light absorption, and therefore of a higher QE, which would lead, in fact, to an estimation of a lower β value compared to that calculated assuming the QE always equal to 0.3. But in the conducted analysis it is interesting to understand as the structure presented is more suitable to absorb the light, in terms of G, compared to another. Only a careful knowledge of QE would conduct to an exact estimation of the gain β, while it is possible to calculate G without the knowledge of QE.

Furthermore, the phototransistor is suitably optimized to absorb the light. Then, the analysis will be also done at higher temperatures, up to 733.15 K, because, even if there will be a gain reduction, rising the temperature, it will be more limited than before.
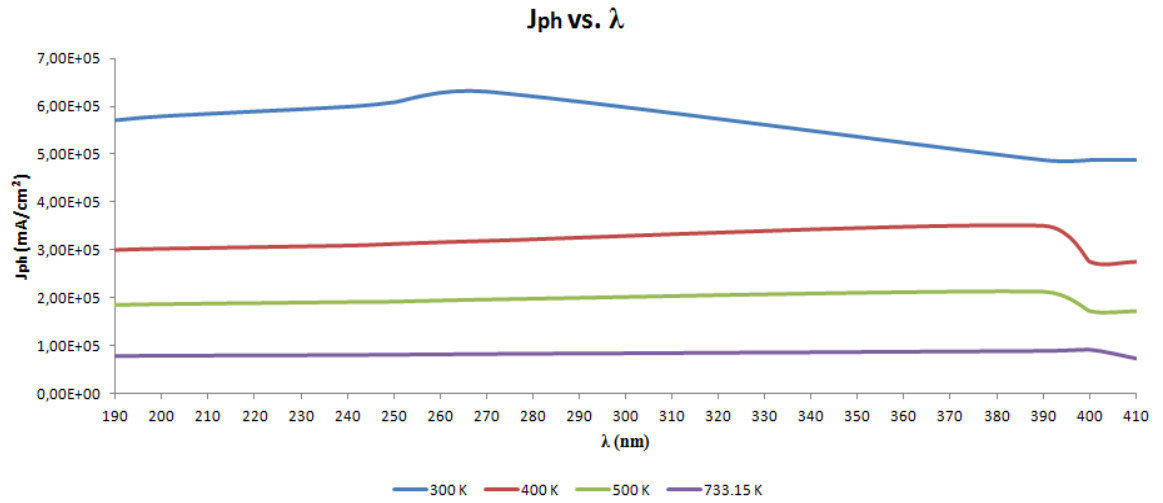
Figure 3.51. Photogenerated current density versus wavelength for different temperatures.
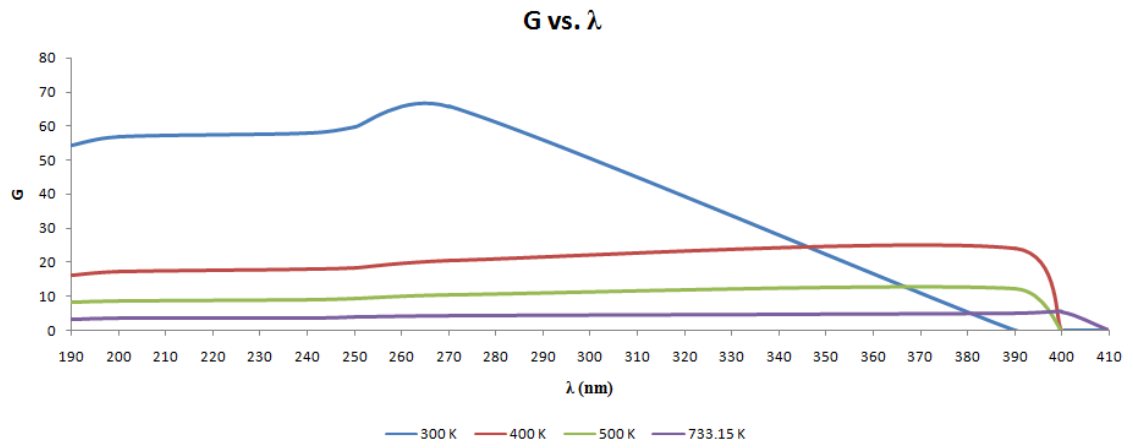
Figure 3.52. Optical gain versus wavelength for different temperatures.
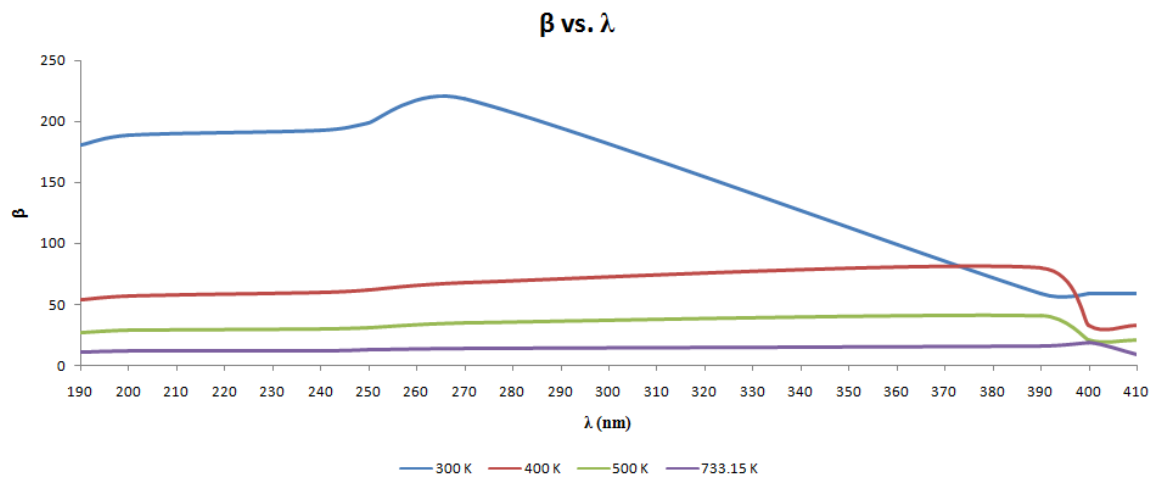
Figure 3.53. Transistor gain versus wavelength for different temperatures.

133
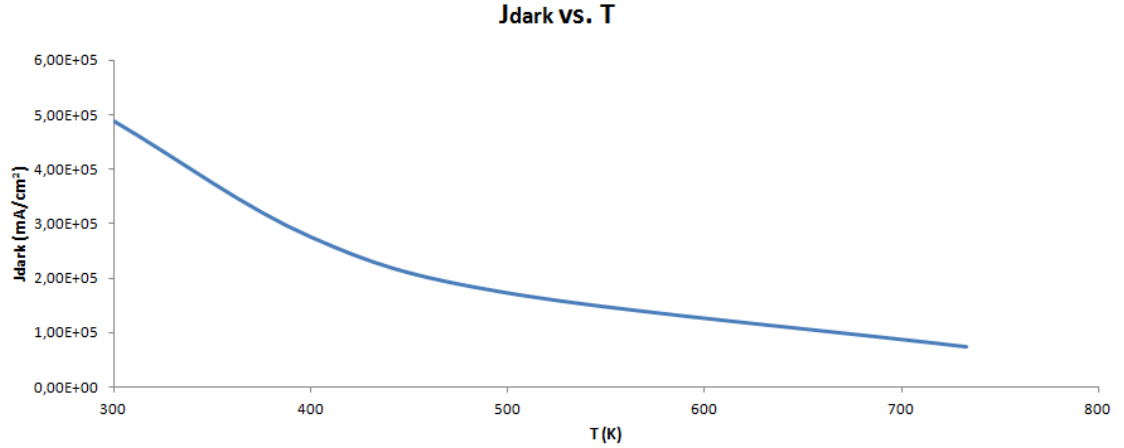
Figure 3.54. Dark current density versus temperature.

As can be seen from the figures presented above, both the optical gain *G* and the transistor gain *β*, under illumination, have significantly improved, achieving even transistor gains that pass from the value of about 50 without lighting to values of about 200 under lighting, at room temperature, thanks to an optical gain of about 60 from 190 to 270 nm, at room temperature. Furthermore, this time, the simulations were carried out up to a temperature of 733.15 K because, when the temperature increases beyond, the gains collapse. However their values are around, respectively, 5 and 10. Instead, with regard to the dark current, it varies little compared to the previous case. In particular, it is noted that the collector current, without light, varies little from a device to another, because even the transistor gain, in dark conditions, varies little for the three transistors. This implies that, at constant base current, the collector current varies little from one structure to another.

To complete the analysis, the best thing is to do a comparison between the three structures, to directly compare, fixing a certain wavelength, the various transistors in terms of the internal optical gain and the transistor gain, as shown in Figure 3.55 and 3.56, respectively.
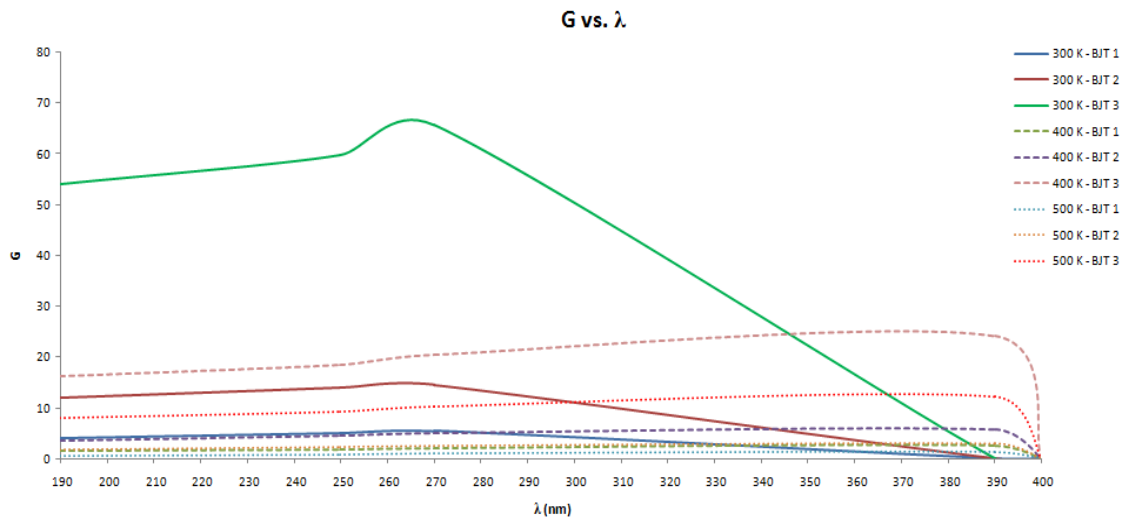
Figure 3.55. Comparison between the optical gain G of the three phototransistors.

134
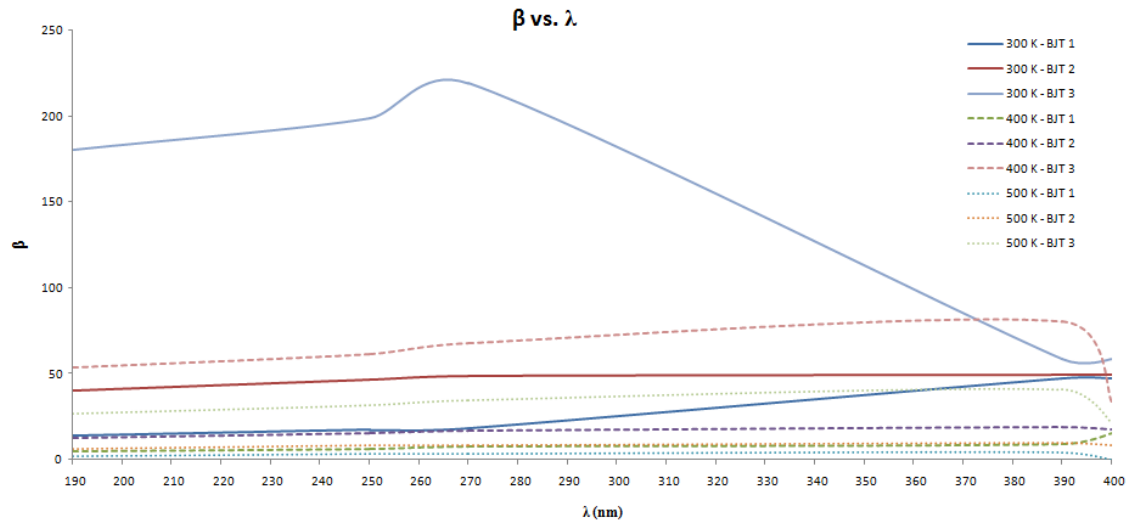
Figure 3.56. Comparison between the gain β of the three phototransistors.

Obviously, the presented structures are only possible proposals of 4H-SiC phototransistors. Unfortunately, in literature, there are a few practical solutions, apart from some phototransistor's models, but not in 4H-SiC, but in 3C-SiC [41], which show very high internal optical gains G, up to about 150, with a V_{CE} of 10 V, an incident optical power of 10 µW, and an incident wavelength of 500 nm. Of course, to achieve these gains, the structure has to be completely modified, as shown in Figure 3.57.

(a)   (b)
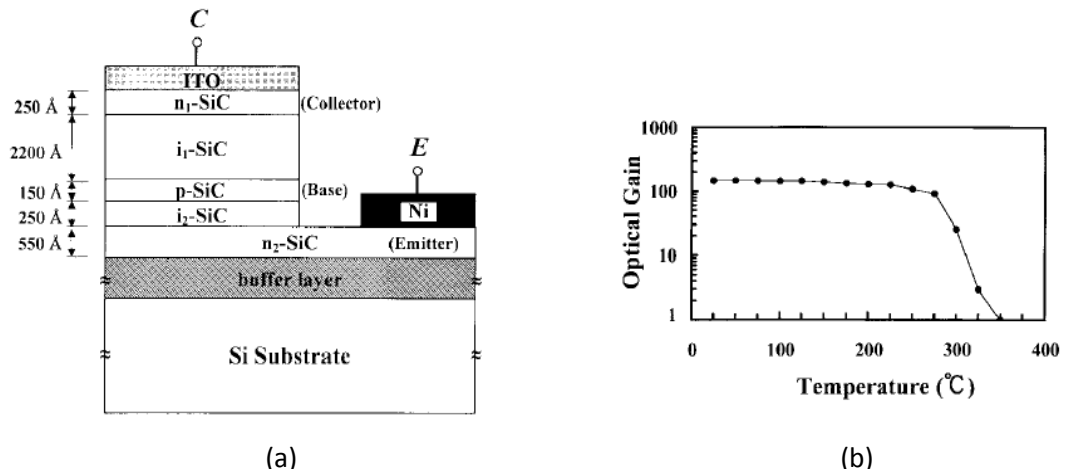
Figure 3.57. (a) Cross section of the β-SiC phototransistor. (b) Optical Gain of the β-SiC phototransistor as a function of temperature.

As it can be seen from Figure 3.57, the phototransistor structure is completely changed. The interesting things to note are two. The base contact is not present, to minimize the reflection on the base, and the transistor works with a floating base. The collector is moved on top of the device, so that the base-collector junction, where the photogeneration occurs, is directly exposed to the incident light, so as to collect the photons as efficiently as possible in the depletion region of the base-collector junction. Collector, base and emitter

135

regions are all reduced in thickness, respectively, to 25 nm, 15 nm and 55 nm, because, as observed for the pin diode, if the collector is made thicker, it only worsen the light collection. The collector contact is made in ITO, to reduce the light reflection of the contact directly light exposed almost to zero. The emitter contact size is reduced, compared to collector contact size, and it is made in Nickel, and moved to the right end of the device, to collect the light that hits the emitter. Also a buffer layer is deposed, before the active layers deposition, to improve the quality of the SiC substrate film, in order to reduce the defects and, therefore, the occurrence of recombination. Furthermore, two intrinsic layers are inserted between the collector and the base, and between the base and the emitter, to achieve a phototransistor as the series of two *back-to-back* diodes, a nip and a pin diode (looking the device from the top to the bottom). In particular the first intrinsic region is very thick, i.e. 220 nm, compared to the second, that is 25 nm.

The presence of these two intrinsic layers allows to obtain high internal optical gains. In fact, since the collector thickness is extremely reduced, the light absorption at the surface is minimized (also thanks to the transparent collector contact). Therefore, the light can reach the first intrinsic region without any problem, and, applying a positive V_{CE}, this region is completely depleted (since it is reverse biased and given the low doping of the intrinsic regions themselves, equal to 2×10^{14} cm^{-3}). The generated charges will be separated and sent to the corresponding regions. Furthermore, the high thickness of the first region permits to collect all the wavelengths, even the longest, without any problem. The same applies to the second intrinsic region, which is less thick than the previous, since it is not directly light exposed as the first. This region allows, however, to collect all the carriers generated through the light absorption in the emitter region. Once photogenerated, the holes move toward the intrinsic region (which, for the low doping, will be almost completely depleted, even if this pin diode is directly polarized [41]), and they are sent in the base region under the electric field action, in a more efficient way.

These changes allow to obtain high internal optical gains in this structure and, therefore, for the same quantum efficiency, high transistor gains, under illumination, with $V_{CE} > 0$, and a little optical incident power, even at high temperatures (up to 300 - 350 °C) [41]. Remembering that the bandgap of 3C-SiC is smaller than 4H-SiC, being 2.4 eV at room temperature, allows us to say that it absorbs up to a critical wavelength of 516 nm, absorbing, then, up to the green of the visible range. Of course, the advantage of using the 4H-SiC, over the 3C-SiC, is also related to electrical and thermal reasons, such as high critical electric fields, high saturation velocity, and, in particular, high thermal conductivity, compared to the 3C-SiC, that makes it more suitable for use at high temperatures applications.

For more information about the manufacturing process, and other technological details on the phototransistor (as the doping, for example), refer to [41].

3.5 CMOS technology in 4H-SiC

After a detailed analysis of the 4H-SiC performances in the absorption of the ultraviolet radiation, to realize an UV photography, at very high temperature, it is interesting to focus the attention on a "baseline" of a CMOS image sensor. Obviously, this baseline has to be developed for high temperature applications. This will be only a theoretical investigation.

3.5.1 MOSFET in 4H-SiC: mobility behavior

Before going any further, a small digression on the typical behavior of a MOSFET in 4H-SiC has to be done. This is just a simple introduction to the problem, because MOS technology in 4H-SiC is not present at KTH nowadays and thus this analysis cannot have, at the moment, experimental confirmations. Typically, in a semiconductor only two model types of mobility are taken into account: carriers mobility due to *scattering by impurities* and carriers mobility due to *phonon scattering*. The first is important when the doping concentration is very high. The second takes into account the atom vibrations around lattice positions. In quantum mechanics, the vibrations are quantized, i.e. particles are introduced to model the vibrations, the so-called *phonons*. The energy transfer from electrons to the lattice is called phonon scattering. In particular, the first mechanism is dominant at low temperatures, where it can be shown that, in this case, the electrons and the holes mobilities increases with the temperature, according to a trend directly proportional at the temperature as $T^{3/2}$. Instead, the second mechanism is dominant at high temperatures, where it can be shown that, in this case, the carrier mobilities decreases with the increasing temperature, according to a trend directly proportional to the temperature as $T^{-3/2}$ [56]. Note that the *electron-electron* and *electron-hole scattering* are ignored. These are important at high carrier concentrations. Moreover, the *scattering by crystalline defects* is also ignored. It is important in polycrystalline materials. Furthermore, for a typical MOSFET, other factors have to be taken into account, such as the mobility dependence by the vertical component of the electric field (induced in the channel when a gate voltage different from zero is applied). This dependence causes that the carriers flow is not perfectly laminar (as tipically it is assumed), because this component of the field accelerates the electrons to the oxide-semiconductor interface and, this collisions with the surface will slow down the carriers (i.e. the mobility is reduced). Furthermore, in the channel there is also the presence of a horizontal component of the field, due to the application of the source-drain voltage, responsible of the carriers transport within the channel itself (remember that, now, the current is a drift current). The drift speed of the carriers is related to the field applied from the outside and, for high fields (i.e. high voltages), tends to saturate to a constant value, equal to the saturation speed (this is not only true for the MOS, as seen in Chapter 1). In the case of a MOSFET made in 4H-SiC, another factor that must be taken into account is the *Coulomb mobility* factor, which is related to the *Coulomb scattering* of the mobile charges in the inversion channel at the interface SiC - SiO_2, due to the Coulombic interaction with the high density of occupied interface traps and with the fixed oxide charges. The *Coulomb scattering* mechanism is

very important for SiC MOSFETs because of the extremely large densities of occupied traps found in devices with a SiC-SiO$_2$ interface. This will cause a high amount of coulomb scattering, causing a mobility degradation [57]. *Coulomb scattering*, also known as *Rutherford scattering*, is so-called because it is a type of scattering which is based simply on the presence of static electric forces, i.e. the *Coulomb forces*, i.e. on the force exerted on a particle in the presence of an electric field.

Therefore, to characterize the real mobility in a 4H-SiC MOSFET, there is need of a highly detailed physical description that brings into account all the scattering phenomena in the device. In particular, the total mobility, μ_{TOTAL} (as seen also in Chapter 1), can always be calculated through the sum of all the mobility factors, using the *Matthiessen's rule*, which, in this case, provides the following result [57]:

$$\frac{1}{\mu_{TOTAL}} = \frac{1}{\mu_{LF}} + \frac{1}{\mu_{HF}} = \frac{1}{\mu_B} + \frac{1}{\mu_{SP}} + \frac{1}{\mu_{SR}} + \frac{1}{\mu_C} + \frac{1}{\mu_{HF}} \qquad (3.18)$$

where μ_{LF} is the total *low field mobility*, in each point of the device, calculated by considering the *bulk phonon mobility* μ_B, *surface phonon mobility* μ_{SP}, *surface roughness mobility* μ_{SR}, and *Coulomb mobility* μ_C, and μ_{HF} is the *high field mobility component*, due to the high lateral field on the scattering of charged carriers in the inversion layer.

In the analysis that follows the *Coulomb mobility* will be considered, since, as it will be seen, especially with low fields, it will dominate, causing a mobility trend slightly different from what is expected, when the temperature rises. For more details on the models that can be used to model such mobility components refer to [57].

A model that can be suitable to describe the *Coulomb scattering*, due to the scattering caused by occupied traps and fixed charges at a temperature T, suitable for any distribution of mobile charges in the inversion layer, any distribution of fixed charges inside the oxide, and any variation of occupied trap density along the SiC-SiO$_2$ interface of the MOSFET, for a mobile charge at a depth z inside the semiconductor, is reported following [57]:

$$\frac{1}{\mu_C(z,T)} = \frac{m^* q^3 (N_f + N_{it})}{16\,\pi\,\bar{\varepsilon}\,\hbar\,k_B\,T}\,F \qquad (3.19)$$

where N_{it} are the occupied traps and N_f are the fixed charges located at the interface, q is the electronic charge, m^* is the density of states effective mass, $\hbar$ is Planck's constant, k_B is Boltzmann's constant, $\bar{\varepsilon}$ is the avarage of the permittivity of 4H-SiC and SiO$_2$, and F is the form factor that takes into account the depth dependence of the Coulomb mobility [57].

Therefore, the important thing to note, from Eq. (3.19), is that the *Coulomb scattering*, when present, appears to be directly proportional to the temperature, which means that as the temperature increases, the mobility tends to increase.

Then, if the mobility follows Eq. (3.19), the mobility behavior is in contrast with the behavior predicted from Eq. (1.13) and (1.14), where, when the temperature increases, the mobility should always be reduced. Instead, taking into account also the *Coulomb's term*, the higher is the temperature the higher is the mobility. Of course, it has to be understood when an effect dominates on the other. A typical trend of the mobility can be extracted

through experimental tests and simulations, considering complex models within the simulator that accurately describe the interface trap states density [57], as well as accurately describe the amount of fixed oxide charge. In this trend it is observed that the mobility, in NMOS and PMOS, follows a temperature and gate voltage dependent law as is shown in Figure 3.58 [58].
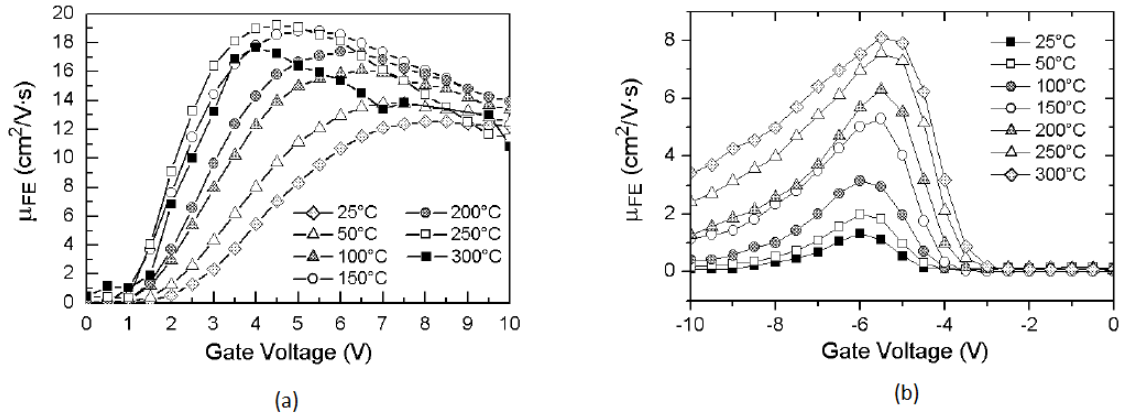
Figure 3.58. Temperature and field dependence of 4H-SiC NMOS mobility (a) and 4H-SiC PMOS mobility (b) [58].

As seen in Figure 3.58, fixing a certain temperature, the mobility first increases when the applied voltage increases (i.e. for low applied gate voltages), and after it tends to decrease with the increasing of the same voltage. Furthermore, if it works at low voltages, fixing a certain gate voltage, when the temperature increases, the mobility increases, instead of reducing. Instead, for high voltages, fixing a gate voltage, the mobility decreases increasing the temperature (as it is usually thought). Therefore, since the mobility, instead of reducing with increasing temperature, tends to increase at low voltages, there is a clear presence of the *Coulomb scattering* which appears to be the dominant term in the mobility definition.

The reason of this trend can be explained as follows. At low gate voltages, there is less inversion charge, with a significant amount of occupied traps. In fact, from extracted values of the occupied interface trap density [57] and of inversion layer mobile charge density, it is possible to see that the density of occupied traps is much higher than the inversion charge density. This means that most of the charge induced in the semiconductor, during the inversion, gets trapped (in fact, less than 30 % of the induced charge is available for the conduction). This is translated in a mobility and in a current reduction. Obviously, a significant current improvement is expected if the number of interface trap states is reduced, in way to obtain an increase in mobile charge. Of course, this means that, at low voltages, there is a very large amount of Coulombic scattering of the mobile charges by occupied traps and fixed oxide charges, causing that the Coulomb scattering becomes the dominant mobility degradation mechanism. This effect can also be seen in the following way. When a positive gate voltage is applied, for example in the case of a NMOS, the holes are moved away from the oxide-semiconductor interface, giving rise to a space-charge region formed by negative acceptors ions, that are not compensated by holes.

When the gate voltage exceeds the threshold voltage, electrons at the interface are induced to move from the substrate to the gate, to form the inversion region, also called channel region. These uncompensated acceptors ions, i.e. negative ions, give rise to an electric field, exerting a certain force, i.e. the Coulomb force, on the negative charge in the channel. This causes the Coulomb scattering. In any case, since the Coulomb mobility is directly proportional to the temperature, fixing a gate voltage, the mobility increases with the increase in temperature. Instead, at higher gate voltages, the inversion charge is so high that it effectively screens the occupied traps and the fixed oxide charges. In fact, since the charge in the channel is very high, the effect of the field, exerted by negative not compensated ions on the electrons, will be less than before. This causes a reduction in the amount of Coulomb scattering, and the high field mobility mechanism becomes the dominant scattering. In this way, the classic trend of the mobility is restored, i.e. fixing a gate voltage the mobility is reduced when the temperature increases [57]. In reality, very near to the oxide-semiconductor interface, the Coulomb scattering is still the dominant mechanism, also if this effect is not much significant [57]. TCAD [44] allows the possibility to include in the analysis a possible Coulomb scattering on the surface, but the problem is that it needs the appropriate parameters of interest to be set, as reported in [57]. Then, it is observed that it is very difficult to do simulations of MOSFETs in 4H-SiC, both due to the fact that, in the analysis, particular models have to be included (more details are present in [57]), and because these analysis can also become unnecessary, since, as also noted in [7], [47], [58] and [59], often, the simulation results will be contradicted by experimental tests, as occurs on the performances of the threshold voltage V_{TH} (see Figure 3.59 [57]), or the mobility performances. In fact, in Figure 3.58 it is observed that the mobility of the SiC MOSFET, in the inversion layer, presents unacceptable values (at most of the order 50 cm^2/Vs), if compared with the bulk mobility, that still remains around values of 500-1000 cm^2/Vs. This effect is presumed to be due to the high density of interface trap states SiC/SiO$_2$, especially close to the conduction band edge [7]. This causes a sharp fall in the amount of carriers available for conduction. Furthermore, after the simulations made to predict a certain result, the SiC MOSFET is extremely unstable, in practice, because it shows, for example, a shift of the threshold voltage due to generation/annihilation of the defects at the SiO$_2$/SiC interface, or for the presence of charge trapping in the oxide [7]. In fact, to make an accurate analysis of a 4H-SiC MOSFET, a combination of simulation and experimental results would be needed, as well as analytical calculations, which allows to evaluate the performances of the density of trap states at the interface, in terms of energy (in eV), both in the mid-gap and at the band-edge, to obtain an estimate of the amount of fixed charge in the oxide, taking into account, also, as these quantities vary with temperature (however, the effect on fixed oxide charge, when the temperature varies, is negligible [57]). Moreover, a fairly accurate estimation should be made regarding the charge density within the channel region, the charge density within the depletion region, the density of interface trap states occupied (as already mentioned), as well as the comparison of the mobile inversion charge density with the occupied interface trap density at different gate voltages and varying the temperature [57].

Therefore, given the complicated analysis which concerns the MOSFET operation, in this section only a literature investigation will be done, to extract some values of interest that

will be used later to make a simulation in OrCAD PSPICE [60], and analyze the complete operation of a pixel, putting together all the data previously obtained, combining both the data obtained by the simulations of the pin photodetector and the experimental data taken from the literature to build the LEVEL 1 model of a 4H-SiC MOSFET.

Figure 3.59 shows some trends of the variables of interest, extracted through a combination of analytical work, simulations and experimental results available in the literature. This behaviors show how to make a simulation of a SiC MOSFET can be really complex, due to all the things that should be taken into account. Furthermore, not being currently available this type of technology at KTH, it is also useless to do simulations, because these have no experimental confirmation. This suggests, even more, that it is best to only do an investigation of what is available nowadays.
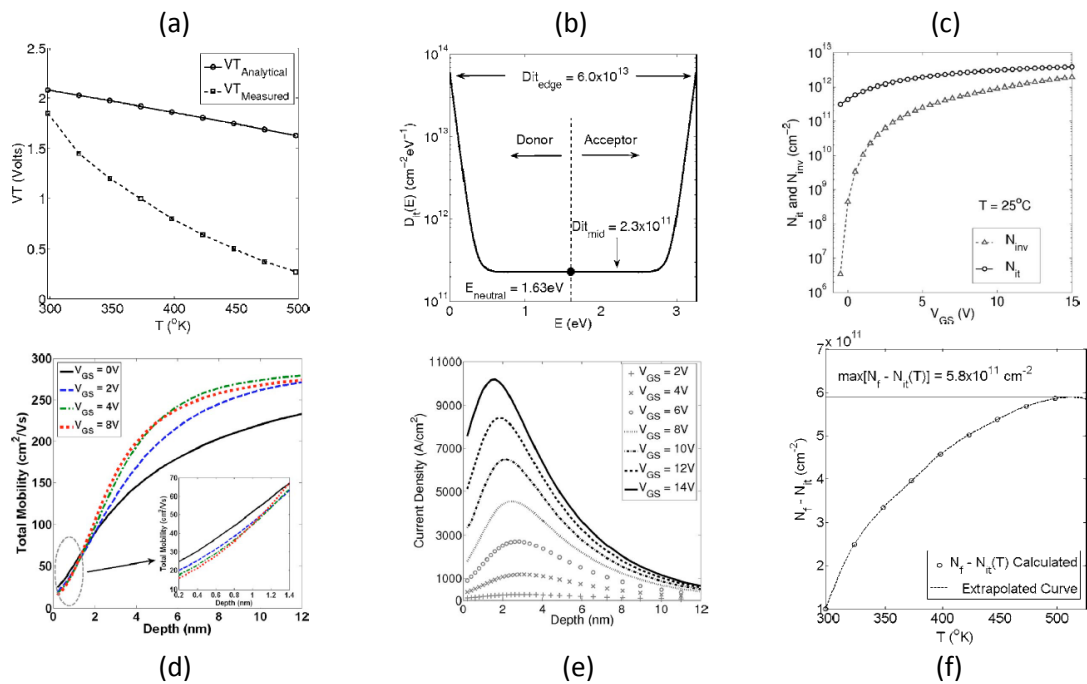
Figure 3.59. Numerical and experimental characterization of 4H-SiC lateral NMOSFET. (a) Analytically calculated and experimentally measured threshold voltages. (b) Interface trap density of states profile extracted by comparing simulated I_D-V_{GS} characteristics to experimental measurement. (c) Comparison of the mobile inversion charge density and occupied interface trap density at different gate voltages at room temperature. (d) Total mobility versus depth at different gate biases, with $V_{DS} = 0.25$ V and T = 25 °C. The inset shows the mobility near the surface at different gate biases. (e) Current density variation with depth for a 4H-SiC MOSFET at room temperature. The current density is high at the center of the channel and it is plotted versus the distance into the device. (f) Extrapolation to get an estimation of the fixed charge N_f [57].

Figure 3.59 shows the trends of some quantities of interest of a 440x10 μm^2 4H-SiC lateral MOSFET. Note that, typically, a MOSFET is realized with big dimensions, because, in this way, it is possible to balance the strong mobility reduction (this is even more important in a SiC MOSFET). The quantities behavior can be briefly explained as follows.

The threshold voltage, as also previously mentioned, is proved to be experimentally much smaller, fixing a certain temperature, than the one obtained by analytical results and it reduces quickly increasing the temperature itself. This is a justification of the fact that, in

analytical calculations, the high amount of trapped charge in the oxide is not taken into consideration. In fact, the real trend of the threshold voltage is the following:

$$V_{TH} = \Phi_{GS} + 2\,\Phi_F - \frac{Q_{SUB}}{C_{OX}} - \frac{Q_{OX}}{C_{OX}} \qquad (3.20)$$

where Φ_{GS} is the difference between the gate's and substrate's extraction works, $2\Phi_F$ (where Φ_F is the Fermi's potential) is the voltage to induce the strong inversion, Q_{SUB} is the charge in the substrate depletion, Q_{OX} is the charge trapped in the oxide, and C_{OX} is the oxide capacitance (ε_{OX}/t_{OX}, where ε_{OX} it is the dielectric constant of the oxide, and t_{OX} is the oxide thickness). These quantities are equal to:

$$\Phi_F = \pm V_T \ln\left(\frac{N_{SUB}}{n_i}\right) \qquad Q_{SUB} = \pm\sqrt{2\,q\,N_{SUB}\varepsilon_{SiC}|2\,\Phi_F + V_{SB}|} \qquad (3.21)$$

where N_{SUB} is the substrate doping, and V_{SB} is the source-body voltage (it is taken into account when the body effect is considered and it is ≥ 0 for a NMOS, and ≤ 0 for a PMOS). Furthermore, the sign of Φ_{GS} is + if a P$^+$ gate is considered (i.e., for example, using a polycrystalline doped gate), and - if a N$^+$ gate or a metal gate are considered. Instead, the sign of Φ_F is + for a NMOS and - for a PMOS, while Q_{SUB} has sign - for a NMOS and + for a PMOS. The sign of Q_{OX} is always +.

Using simple mathematical manipulations, it is possible rewrite the Eq. (3.20) as follows:

$$V_{TH} = V_{T0} + \gamma\left[\sqrt{|2\,\Phi_F + V_{SB}|} - \sqrt{|2\,\Phi_F|}\right] \qquad (3.22)$$

where V_{T0} is V_{TH} when $V_{SB}=0$ and γ is equal to $\frac{\sqrt{2\,q\,N_{SUB}\varepsilon_{SiC}}}{C_{OX}}$. Note that in Eq. (3.20), if the extraction works of metal and semiconductor are equal, Φ_{GS} is zero. Instead, in this equation, a non-zero amount was considered, to consider a general case where the extraction works are different. In fact, when, for example, a N$^+$ gate is considered, the Fermi level of the metal is practically coincident with the conduction band, while, if one considers a NMOS, the Fermi level of the semiconductor is very close to the valence band. Therefore, the extraction work Φ_M of electrons in the metal is less than the extraction work Φ_S in the semiconductor, and their difference defines, precisely, the *flat band voltage* V_{FB}. In fact, with a zero gate voltage, at thermodynamic equilibrium, the Fermi level must be constant throughout the device, because there is no current flow. To achieve alignment, there will be a shift of electrons from the metal to the semiconductor, or equivalently of holes in the opposite direction, that causes to form, on the semiconductor side, a negatively charged region composed from the acceptors ionized atoms, while, on the metal side, a layer emptied of electrons is formed, with a positive charge. In this way, since the system must be globally neutral, this layer of electrons compensates the negative charge $-q\,N_A\,x_p$ in the semiconductor. This implies, therefore, that the bands are not flat at equilibrium, but curved, to justify the transferring of electrons from the metal to the semiconductor. Applying a gate voltage exactly equal to the flat band voltage, there will be a shift of the Fermi level of the metal, with respect to that of the semiconductor, so that the jump of

potential on the structure is deleted, and the bands are flat. Note that the same problem occurs even when the oxide presents positive ions accumulated at the oxide-semiconductor interface due to manufacturing problems. These charges attract electrons to the interface, having a channel charge different from zero, even when the gate voltage is zero. This will cause, however, the bands to bend, and to restore the initial situation, a negative voltage on the gate that serves to repel the electrons at the interface has to be applied, to cancel the charge in the channel, and to restore the condition of flat band. Then from Eq. (3.20) can be observed very clearly why if trapped charges are present in the oxide the V_{TH} drastically collapses, for a certain temperature value. This phenomenon is very important in the production of 4H-SiC MOSFETs, due to the high electronics defects density SiC-SiO$_2$ interface, which naturally arise during the manufacturing phase of the device. Generally, they are excess or deficit sites of oxygen or impurities, which lead to the emergence of electronic states within the bandgap oxide that can trap the carriers in the channel. As predicted from Eq. (3.20) and (3.21), when the temperature increases, the V_{TH} will reduce because Φ_F will reduce, due to the increase of n_i.

In any case, since the mobile charges gain more energy with an increase in temperature (that it is a kinetic energy of the carriers that varies like *3/2 k_B T* when there is a temperature variation), less carriers are trapped. Therefore, the occupied traps density N_{it} decreases with an increase in temperature. On the other hand, the fixed oxide charge N_f remains practically constant. Hence, from a plot of the difference $N_f - N_{it}$ as a function of the temperature, as depicted in Figure 3.59 (f), it is possible to estimate the value of N_f as the maximum of the curve, where N_{it} is the minimum (increasing the temperature). The estimated value of N_f is around 5.8×10^{11} cm^{-2} [57]. Furthermore, Figure 3.59 (b) shows the trend of occupied interface traps. In particular, it is observed, that the density of occupied traps depends on the applied voltage (or energy), as in the subthreshold and near-threshold regions, for example for a NMOS operation. In the subthreshold and near-threshold regions, the electron Fermi level is closer to the center of the bandgap. In fact, remembering that the Shockley relationships can be generalized by introducing the *quasi-Fermi* levels for electrons, E_{Fn}, and for holes, E_{Fp}, i.e. $n = n_{ie} \exp\left(\frac{E_{Fn} - E_i}{k_B T}\right)$ an $p = n_{ie} \exp\left(-\frac{E_{Fp} - E_i}{k_B T}\right)$, where E_i is always in the middle of the bandgap, and the position of the quasi-Fermi levels in the band curve depends on the carrier concentrations. n_{ie} is the effective intrinsic concentration (it is considered when the bandgap temperature dependence is taken into account) equal to the root of $n_{ie}^2 = KT^3 exp(-E_g/KT)$, where K is the Boltzmann constant. In particular $E_{Fn} = E_F = E_{Fp}$ if the system is in thermodynamic equilibrium, i.e. $p = p_0$, $n = n_0$ and $p_0 n_0 = ni^2$, or out from thermodynamic equilibrium, but with $p = p_0$ and $n = n_0$. Instead, if $E_{Fn} > E_{Fp} > E_F$, i.e. $n > n_0$, an injection of electrons will arise, and if $E_{Fn} > E_F$ and $E_{Fp} < E_F$, i.e. $n > n_0$ and $p > p_0$, an injection of electrons and holes will arise. Because of this, the interface traps in the midgap region, of the 4H-SiC band gap, become occupied, the electron Fermi level is closer to the center of the band gap. Therefore, the comparison of the simulated subthreshold and near-threshold I_D-V_{GS} characteristics of the device with the experimental data gives an estimation of the midgap states density for the interface traps. Above the threshold, in deep inversion, the electron Fermi energy is closer to the conduction band edge (in a PMOS, the hole Fermi

energy is closer to the valence band edge), causing traps at energies closer to the band edge to be occupied. Hence, states density of traps can be extracted near the band edge by comparing the simulated and measured I_D-V_{GS} characteristics in the linear region (i.e. in triode region, for small V_{DS}).

The extracted values indicate that the density of trap states at the interface, in the midgap (Dit_{med}), is equal to 2.3×10^{11} cm^2/eV, and, at the edge of the band (Dit_{edge}), it is equal to 6×10^{13} cm^2/eV [57]. In particular, the density of states for interface trap states lying in the upper half of the 4H-SiC band gap can be approximated as $D_{it}(E) = D_{it_{mid}} +$ $+D_{it_{edge}} exp\left(\frac{E-E_c}{\sigma_{it}}\right)$, where E is the energy, E_c is the energy of the conduction band edge, and σ_{it} determines the shape of the D_{it}-E curve. Instead, the density of occupied acceptor-like interface traps is given by $N_{it} = \int_{E_{neutral}}^{E_c} D_{it}(E) f_n(E) dE$, where $f_n(E)$ is the probability density function describing the occupancy of the traps, and $E_{neutral}$ is the energy at the neutral point. The midgap neutrality assumed, at room temperature, is 1.63 eV. Interface traps lying above the midgap are acceptor type, while those lying below the midgap are donor type [57]. In Figure 3.59 (f) it is noted that the difference N_f - N_{it} grows with increasing of temperature, which means that, given that N_f (fixed charge) is almost constant with temperature, while N_{it} (occupied traps), instead, tends to decrease when the temperature increases. Furthermore, in Figure 3.59 (c), it is observed that, at low temperatures, for example, at room temperature, the density of occupied traps is much higher than the inversion charge density. This means that most of the induced charge in the semiconductor during inversion is trapped. In fact, maybe, less than 30% of the induced charge is available for conduction, causing a reduction in the current of the 4H-SiC MOSFETs. A significant improvement in current values is expected due to an increase in the number of mobile charge, if the number of interface trap states is reduced [57]. As said about the *Coulomb scattering*, and for what is shown in Figure 3.59 (d) (that represents the trend of mobility starting from the interface oxide-semiconductor, until it gets in the bulk), it is observed that the mobility change, also, inside the channel, and, in particular, it is extremely low at the surface, compared to the one at the bottom of the inversion layer, and it varies with the gate voltage. Obviously, the previously considered mobility trend causes a variation of the current density within the device. In fact, as can be observed from Figure 3.59 (e), fixing a certain voltage value, the current density, on the surface, is very low, and tends to increase moving deeper in the layer, and it presents a maximum where the carriers mobility is maximum (typically a value around 75 cm^2/Vs), then decreasing again going deeper (obviously, in the bulk there is no current flow). Moreover, it is observed that reducing the gate voltage, the current maximum is reduced and it shifts to the right, i.e. more in depth. In fact, at low gate voltages, the few carriers induced in the channel are affected by the *Coulomb scattering* effect on the surface, which will cause a collapse of the surface mobility, at an equal distance from the surface, presenting its peak more in depth, as in the case of the current (since it is related to the mobility in a directly proportional way) [57].

Moreover, from what has been said up to now, in a 4H-SiC MOSFET, as observed in Figure 3.58 and 3.59, the increase of the mobility, up to a certain value of the gate voltage, and the strong reduction of the threshold voltage, at the increase of the temperature (that

causes also an increase in the degree of ionized dopant in the source and drain [7] causing, therefore, the presence of a greater amount of carriers), for a certain drain voltage, cause an increase of the saturation current of the 4H-SiC MOSFET.

3.5.2 4H-SiC CMOS technology: possible implementation

At the state of the art, there are very few CMOS technologies realized in 4H-SiC commercially available (as mentioned earlier, they are complex to realize), on which the experimental tests were conducted at high temperature. Some examples are reported in [47] and [58], where in the first case the experimental tests are conducted up to 350 °C and in the second case up to 300 °C. For example, the following structure (see Figure 3.60) shows good characteristics at high temperature, and a future perspective could be to investigate if it can be able to withstand even higher temperatures (up to, at least, 460 °C, i.e. the Venus temperature).
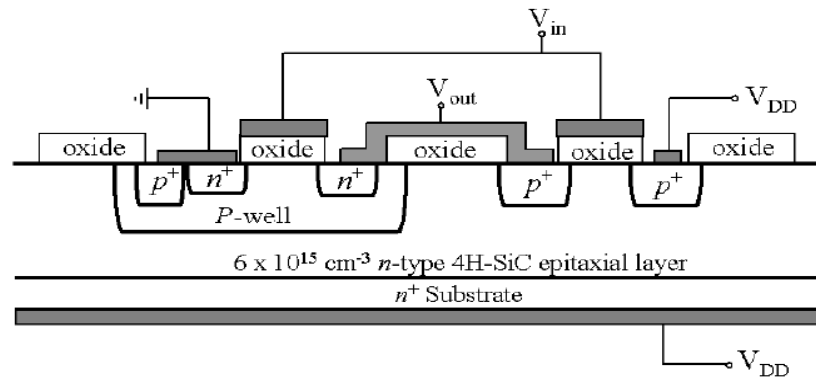
Figure 3.60. Cross-section of a 4H-SiC CMOS Inverter [58].

Figure 3.60 shows a cross section of a 4H-SiC CMOS inverter. A N^- epitaxial layer of 10 μm (it is doped 6×10^{15} cm^{-3}) is grown on a N^+ wafer, of 3 inch, in 4H-SiC. The p-well and the implanted regions of the source and drain of the PMOS are made with an implantation of Aluminum. The p-well is realized to completely eliminate the body effect for the NMOS, connecting the source and the body to the lowest potential of the circuit, i.e. 0 V in the case in exam. Instead, for the PMOS, directly made in the epitaxial layer N^-, source and body are connected at the higher potential of the circuit, indicated with V_{DD} in Figure 3.60. It would be interesting to observe what changes if these implantations are made with Boron. The N^+ implantations, for the NMOS, are made with Nitrogen. It would be interesting to observe what changes if they are made with Phosphorous. Furthermore, the N^+ regions of source and drain of the NMOS are doped 10^{20} cm^{-3}, and they are extended to a depth of about 300 nm, while the P^+ regions of the source and drain of the PMOS are doped 10^{19} cm^{-3}, and they are extended 500 nm in depth. Instead, with regard to the p-well, the implantation is carried out with a peak doping of 4×10^{19} cm^{-3}, and the well is extended to about 600 nm in depth. All the implants were activated at 1650 °C under a Si overpressure. The channel length, for both the devices, is 3 μm, and the width (of the device and, obviously, of the gate) is 50 μm. A 800 nm thick field oxide was then deposited with CVD technique, and patterned to open the active region. The gate oxides,

40 nm thick, both for NMOS and PMOS devices, were simultaneously thermally grown, at 1175 °C in dry O_2, with post-oxidation annealing in wet O_2 at 950 °C and NO (Nitrogen monoxide) at 1175 °C (in order to reduce the interface state density, and, in turn, to increase electron channel mobility [58]). Furthermore, a 400 nm thick P^+ polysilicon film was deposited via CVD, and patterned as the gate electrode. Source and drain ohmic contacts were formed with annealed Ni films. Finally, following a CVD deposition of a 500 nm thick SiO_2 film, vias were opened in this dielectric intermetal, and a 4 µm thick Al overlayer was deposited by e-beam evaporation, and patterned using a wet etch [58].

Given that the purpose of the investigation is the possible realization of a pixel in 4H-SiC, which follows the scheme proposed in Figure 2.16, only NMOS will be used (and not PMOS). This means that it is interesting to focus the attention, not much on how all the structure, in Figure 3.60, behaves, such as CMOS logic inverter (for more details see [58]), but on how the NMOS technology works, when the temperature changes. For completeness, although it is not of actual interest, it will be also reported the analysis of the PMOS, separately tested from the NMOS [58].

Figure 3.61 shows I-V characteristics of NMOS at different temperatures and different gate voltages [58].

Figure 3.61. I-V Characteristics of 4H-SiC NMOSFET at (a) 25 °C , (b) 200 °C and (c) 300 °C. (d) Threshold voltage (V_{TH}) versus temperature [58].

As seen from Figure 3.61, fixing a certain drain and gate voltage (with the source to ground), the drain current increases when the temperature increases.

The only thing to note is that, for low gate voltages, also below the V_{TH} value, when the drain voltage increases, around 10 V, a slight increase in the drain current due to loss mechanisms is observed, related to the excessive doping of the NMOS p-well. Indeed, typically, it is good practice to slightly increase the doping of the substrate to avoid, for example, punch-through phenomena. In fact, given that the drain-well junction is a reverse

biased junction, if the voltage applied on the drain is increased, the depletion region can reach the source-well depletion region. If the two depletion regions come to contact, the current flow will no longer be under the control of the gate voltage (a phenomenon especially important in small channel devices). But if the doping is increased very much, as in this case, and in general in power devices, up to the order of 10^{19} cm^{-3}, this can trigger loss phenomena, which can lead to increases the current that passes through the reverse biased drain-well junction. The more dangerous loss mechanism is the *Band-to-Band Tunneling Current* [61].

Indeed, when the doping is very high, this causes a strong narrowing of the bands, that causes the electrons, even if they have not the potential energy sufficient to overcome the barrier, to even pierce it due to tunnel effect (quantum effect), related to a thickness reduction of the barrier itself (for a same height). In this case, the high electric field ($> 10^6$ V/cm) across the reverse-biased *pn* junction causes a significant increase of the current flow through the junction because of electrons tunneling, directly, from the valence band of the *p* region to the conduction band of the *n* region, as shown in Figure 3.62 [61].
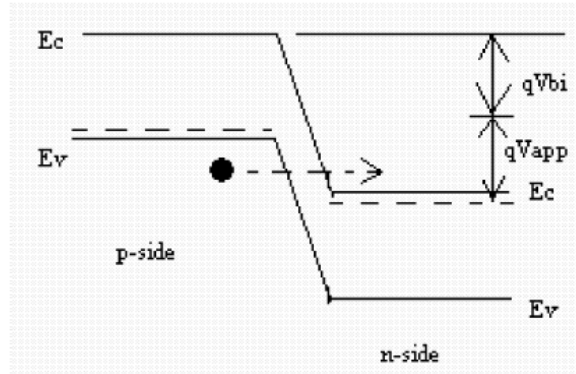
Figure 3.62. Tunneling current in reverse-biased pn junction [61].

The tunneling current density is given by the following equation [61]:

$$J_{b-b} = \frac{\sqrt{2\,m^*}q^3}{4\,\pi^3\,\hbar^2}\frac{E\,V_{app}}{E_g^{1/2}}\exp\left(-\frac{4\,\sqrt{2\,m^*}}{3\,q\,\hbar}\frac{E_g^{3/2}}{E}\right) \tag{3.23}$$

where V_{app} is the applied reverse bias, m^* is the electron effective mass, E_g is the bandgap energy, E is the electric field at the junction, q is the electronic charge, and $\hbar$ is $1/2\pi$ times the Planck's constant h. From the Eq. (3.23), it is observed that, due to the 4H-SiC high bandgap, the tunneling current is lower than in a silicon device. In any case, if the substrate doping is increased, the tunneling current increases. In fact, assuming an abrupt junction, the electric field at the junction is given by:

$$E = \sqrt{\frac{2\,q\,N_A\,N_D\left(V_{app} + V_{bi}\right)}{\varepsilon_{SiC}\left(N_A + N_D\right)}} \tag{3.24}$$

Thus, for a high p-well doping, E is increased, and the tunneling current exponentially increases (remember that the built-in voltage is equal to $V_{bi} = V_T \ln \frac{N_A N_D}{n_i^2}$).

Therefore, the only way to solve this problem is to proceed with an appropriate engineering of the p-well implant, to minimize the drain leakage current. For example, a solution would be to make a gradual implant. In such a way, the surface doping is reduced, while the depth doping increases, to prevent any punch-through phenomena, when the drain voltages come up to 10-15 V values. In this way the mobility is not reduced, because it is directly related to the doping. Furthermore, also the threshold voltage is reduced. Both the improvements permit to have a higher current. A possible 4H-SiC CMOS solution, able to efficiently work up to 350 °C, can be the structure given in [47]. In this structure it is observed that the two MOSFETs are made in two separated well epitaxially grown on a 4H-SiC N$^+$ substrate (the which profile, unfortunately, is not shown). It is observed that the reverse currents that affect the source-well and the drain-well junctions are quite small (order of 10^{-11} A) up to breakdown voltage around 80 V (SiC advantage). The breakdown voltage tends to slightly increase when the temperature increases, as in the case of the pin diode. Unfortunately, during experimental tests, it is observed, after a temperature of 350 °C, that both transistors begin to become unstable, because of excessive gate leakage [47]. Probably, this is due to the presence of another leakage mechanism, typical of MOSFETs, especially when the gate thicknesses is too small (the thickness reduction is necessary, in modern technologies, to increase, for example, C_{OX}, and then the current). In this case, the electric field across the gate oxide (V_{OX}/t_{OX}) grows so high that it can cause a direct carriers tunneling from the substrate to the gate (as well as from the gate to the substrate), through the gate oxide, creating a *gate-oxide tunneling current*.

To understand this tunneling phenomenon, a NMOS transistor with a N$^+$ polysilicon gate and a P substrate is considered. In Figure 3.63 (a) an energy-band diagram in flat-band condition is shown, where Φ_{OX} (carrier tunneling barrier height) is the SiC-SiO$_2$ interface barrier height for the electrons in the conduction band in the substrate. When a positive bias is applied to the gate, the energy-band diagram changes as shown in Figure 3.63 (b). Due to the small oxide thickness, which results in a small width of the potential barrier, the electrons in the channel can tunnel into or through the SiO$_2$ layer, and, hence, they can rise the gate current. On the other hand, if a negative gate bias is applied, electrons from the N$^+$ polysilicon can tunnel into or through the oxide layer and they can rise the gate current (see Figure 3.63 c) [61]. For example, in a NMOS, when a positive gate voltage is applied, the primary sources of gate dielectric direct tunneling leakage current in the transistor are electron tunneling from the conduction band of the substrate in the gate (dominant mechanism), electron tunneling from the valence band of the substrate in the gate (weak mechanism), and hole tunneling from the valence band of the gate (if a N$^+$ poly-gate is considered) in the substrate (negligible mechanism) [77]. This means that Φ_{OX} should be changed for any considered carrier type in the Eq. (3.25).
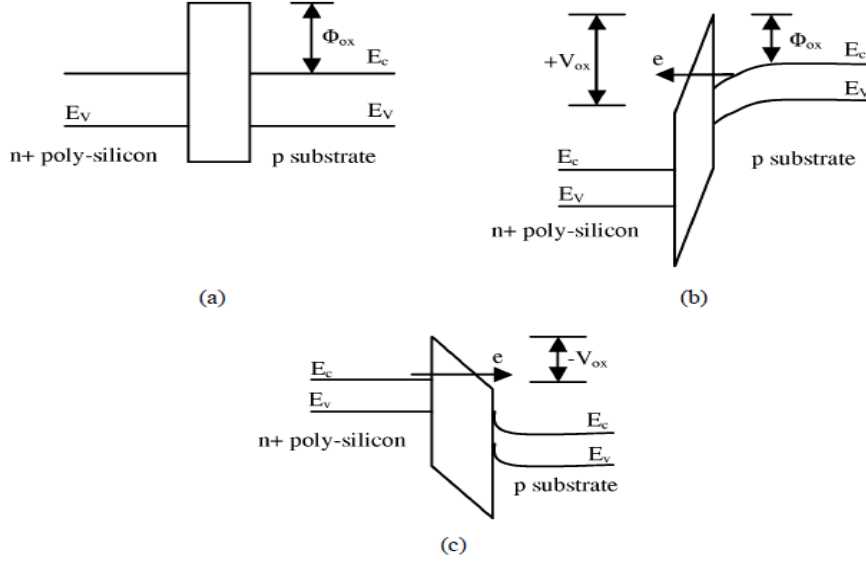
Figure 3.63. Tunneling of electrons through a NMOS oxide. (a) Flat-band energy diagram. (b) Energy-band diagram with positive gate bias shows electron tunneling from the substrate to the gate. (c) Energy-band diagram with negative gate bias shows electron tunneling from the gate to the substrate [61].

Assuming the voltage across the gate oxide is less than the barrier height of carriers ($V_{OX} < \Phi_{OX}$) [77], the equation that governs the current density of the direct tunneling is given by [61]:

$$J_{DT} = \frac{q^3}{16\,\pi^2\,\hbar\,\Phi_{OX}}\,E_{OX}{}^2\,\exp\left\{-\frac{4\,\sqrt{2\,m^*}\Phi_{OX}{}^{3/2}}{3\,\hbar\,q\,E_{OX}}\,\left[1 - \left(1 - \frac{V_{OX}}{\Phi_{OX}}\right)^{3/2}\right]\right\} \qquad (3.25)$$

where E_{OX} is the field in the gate oxide and m^* is the effective mass of tunneling carriers in the gate oxide [77]. Therefore, when the oxide thickness is reduced, the field across the oxide increases, and the tunneling increases. Furthermore, it is observed that, at a constant temperature, given the greater bandgap of a SiC device compared to a Si one, a SiC device has always a disadvantage in terms of direct tunneling, since the barrier seen by the electrons, in the first case, is smaller than in the second case.

Furthermore, tests beyond a temperature of 350 °C are not present in literature, because of the strong reduction of the threshold voltage. Moreover, in some experimental tests, it is observed that, for high temperatures, the gate oxide is stressed a lot, and this will cause an oxide breakdown before of the nominal time to breakdown (evaluated by project), also if the same maximum field, that it can sustain, is considered. This effect is more significant for reduced oxide thicknesses. In fact, this problem, nowadays, has to be taken into account, because it sets limits in terms of oxide scaling.

Moreover, to understand the gate tunneling temperature dependence, the electron density for tunneling from the conduction band (that is the dominant tunneling mechanism) has to be considered. It is possible to show [77] that the carrier density N for electron tunneling is

equal to $N = \frac{\varepsilon_{OX}}{t_{OX}}\left[S\ln\left(1 + e^{\frac{V_{ge}-V_{TH}}{S}}\right) + V_T\ln\left(1 + e^{\frac{V_{FB}-V_g}{V_T}}\right)\right]$, where S is the subthreshold

slope, V_{ge} is the effective gate voltage, considering the voltage drop across the polysilicon

depletion region (V_{poly}), that it is zero for a metal gate, i.e. $V_{ge} = V_g - V_{poly}$, V_{FB} is the flat band voltage and V_g is the gate voltage. The subthreshold slope is an important MOS parameter because it determines the reduction rate of the current respect to V_{GS} when $V_{GS}<V_{TH}$. This slope is defined as nV_T, with n a swing parameter [77]. In fact, it is defined as $n\ V_T\ ln(10)$, and for this it is a measure of how to reduce the V_{GS} to obtain a current reduction of a factor 10, and it is expressed in mV/dec. In an ideal transistor with n=1, $V_T\ ln(10)$ is equal to 60 mV/dec (at room temperature). This means that the subthreshold current, where it is possible to show, assuming that in this case the source-body-drain regions form a parasitic bipolar transistor, this current is equal to $Is[exp(V_{GS}/nV_T)][1-exp(--V_{DS}/V_T)](1+\lambda V_{DS})$, decreases of a factor 10 for a V_{GS} reduction of 60 mV.

In any case, N provides a measure of the number of free carriers (mobile charge density) available for tunneling. N is inversely proportional to the oxide thickness. This means that, reducing the oxide thickness, N increases. Furthermore, when the temperature increases S is increased and V_{TH} is reduced. Hence, N increases with increased die temperature, thereby enhancing the gate oxide leakage current density [77].

In Figure 3.64 the trend of the drain and gate current of the NMOS proposed in [47] is shown. In fact, as said before, only the NMOS analysis of the CMOS structure is interesting
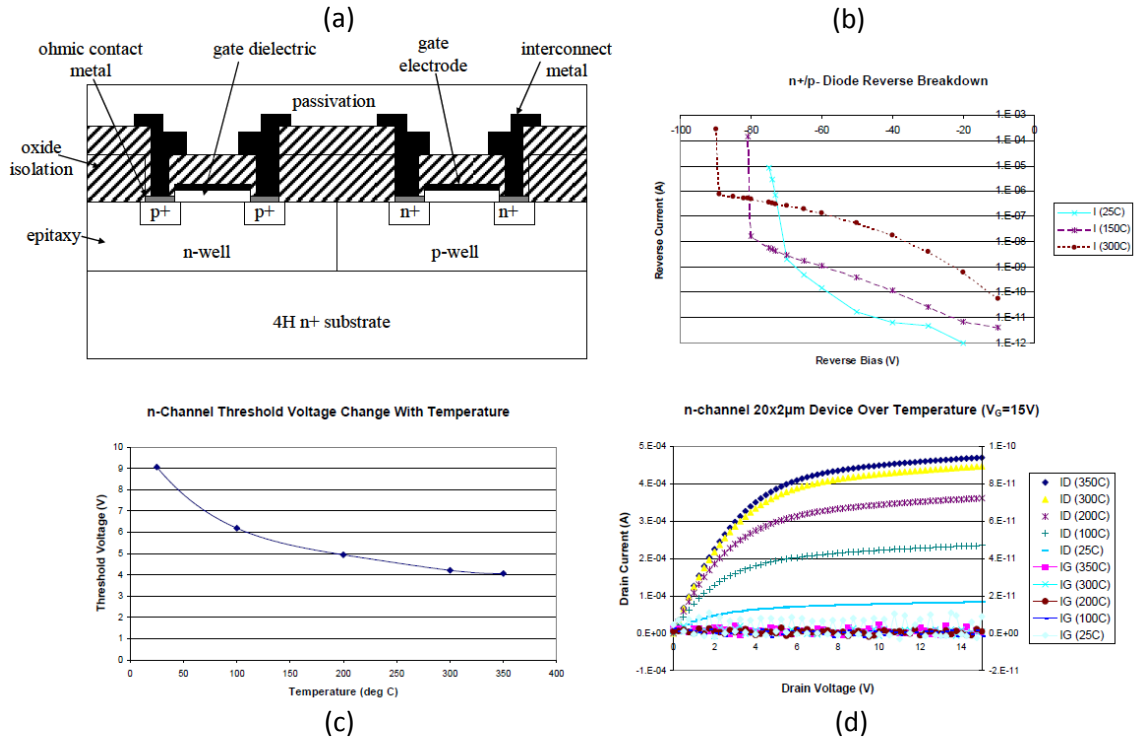
Figure 3.64. (a) 4H-SiC CMOS process architecture, with a NMOS 20x2 µm. (b) Reverse N$^+$/P$^-$ characteristics versus temperature. (c) NMOS threshold voltage. (d) NMOS drain (on the left) and gate current (on the right).

As seen in Figure 3.64 (d), with the same gate voltage (15 V), the drain current increases, increasing the temperature, and it is of the same order of magnitude as that analyzed in [58]. Furthermore, also the gate current tends to increase, as noted before.

Returning to the structure proposed in [58], through a *TLM technique* (for more details see [8]) the sheet resistance of the N$^+$ source and drain regions of the NMOS was extracted, where it is observed that at 25 °C it is equal to 6700 Ω/sq, while at 300 °C it falls to the value of 3200 Ω/sq, as a result of greater ionization of donor atoms with the growing temperature.

For completeness, also the analysis of the PMOS transistor proposed in [58] will be reported (see Figure 3.65), when the temperature varies from 25 °C to 300 °C.
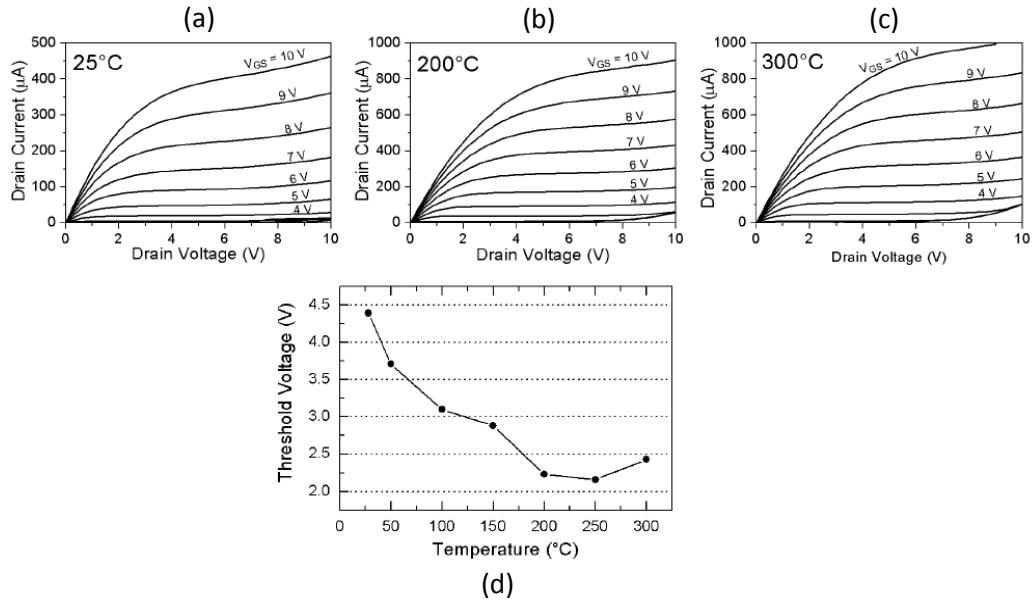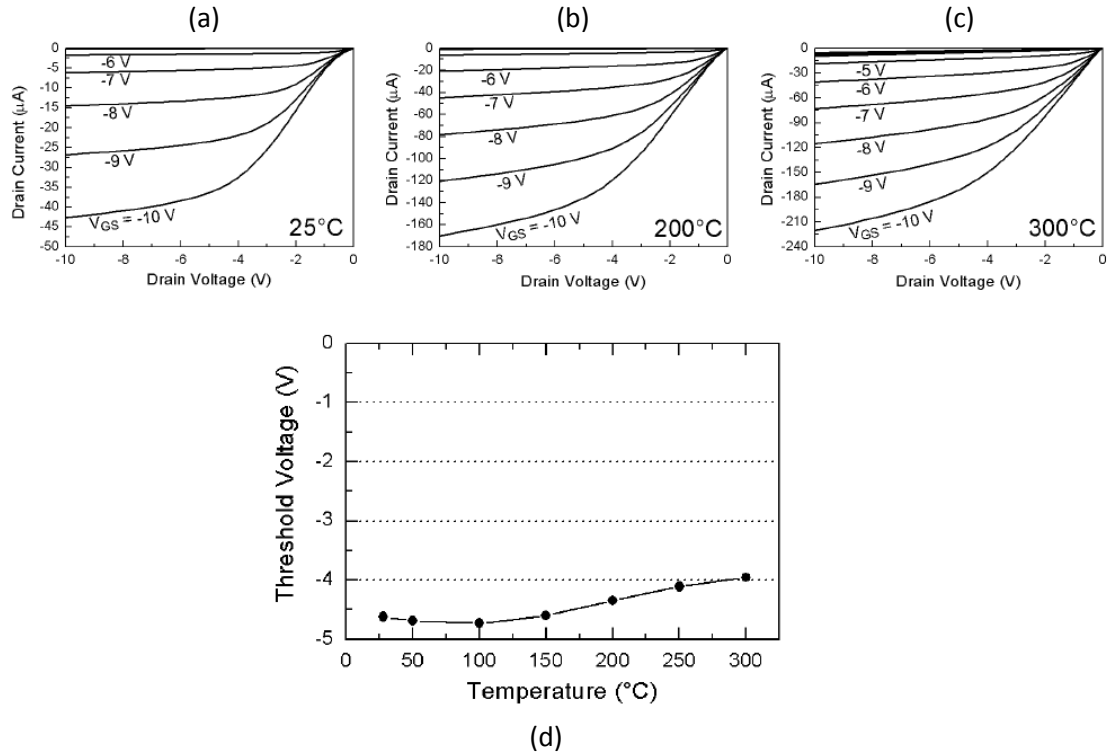

Figure 3.65. I-V Characteristics of 4H-SiC PMOSFET at (a) 25 °C , (b) 200 °C and (c) 300 °C. (d) Threshold voltage (VTH) versus temperature [58].

In Figure 3.65 it is noted that at low temperatures (around 25 °C), the I-V characteristic, in the triode region, is slightly non-linear, due to the non-linear nature of the ohmic contacts of the P$^+$ source and of the drain region of the PMOS (this is a typical behavior in the case of realization of an ohmic P$^+$ contact in 4H-SiC). Instead, when the temperature becomes higher, due to the increase of the ionized acceptor dopant amount, the sheet resistance of P$^+$ regions drops from the value of 41 kΩ/sq, at 25 °C, to 5 kΩ/sq, at 300 °C (extracted by TLM test), resulting in a more ohmic contact, and the I-V characteristic becomes more linear in the triode region.

Compared to NMOS, the PMOS threshold voltage appears to be quite stable when the temperature increases in the range of 25-300 °C, moving from a maximum value of -4.7 V at 100 °C to a minimum value of -4 V at 300 °C. Furthermore, as shown in Figure 3.58 (b), as for the NMOS, the mobility increases (up to a certain value of gate voltage) when the temperature increases, which, together with the number of carriers increase, due to the

increase of the degree of the acceptor ionized dopant amount, causes an increase in the saturation current when the temperature increases.

3.5.3   4H-SiC NMOS: parameters extraction

At this point one must extract the NMOS parameters, in order to simulate a pixel in PSpice. In particular, parameters needed to construct a simple LEVEL 1 model will be extracted [60].

To perform such an extraction, it is necessary to remember, first of all, that when $V_{DS} < V_{GS}\text{-}V_{TH}$, the MOSFET works in the triode region, where the current I_D is equal to:

$$ I_D = \frac{C_{OX}\,\mu_n W}{L}\left[(V_{GS} - V_{TH})V_{DS} - \frac{V_{DS}^2}{2}\right] = K_n\left[(V_{GS} - V_{TH})V_{DS} - \frac{V_{DS}^2}{2}\right] \quad (3.26) $$

where W and L are, respectively, the width and the channel length of the NMOS.

For low V_{DS} values it is possible to neglect the term $V_{DS}^2/2$ in parentheses of Eq. (3.26) and, in this case, the drain current will be linearly dependent both from the output voltage V_{DS}, and the input voltage V_{GS}.

In these conditions, the MOSFET behavior is similar to that of a controlled resistor. In fact, the channel resistance, also called the *conduction resistance* (or *on resistance*), will be equal, simply, starting from Eq. (3.26), at V_{DS}/I_D.

For example, for the NMOS shown in Figure 3.60, the I_D-V_{GS} characteristics experimentally measured, for a drain voltage V_{DS} of 50 mV (setting the source to ground), for a temperature range of 25-300 °C, are shown in Figure 3.66 (the measurement setup is the same in Figure 3.67).
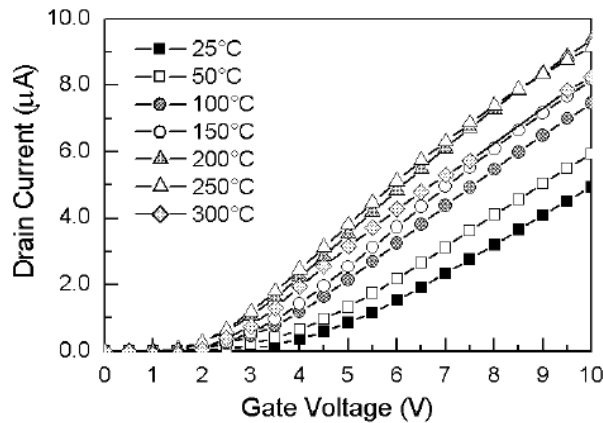
Figure 3.66. I$_D$-V$_G$ characteristics of a 4H-SiC NMOS, at VD=50 mV, from 25 °C to 300 °C [58].

From the Figure 3.66 it is noted that the drain current, as a function of the gate voltage, increases when the temperature increases, as previously explained, due to the increase of the mobility and to the V_{TH} reduction.

Setting a certain temperature, to extract the basic parameters of the NMOS, i.e. V_{TH}, μ_n and K_n, the following procedure is used.

It is possible calculate K_n evaluating the slope of the curves in Figure 3.66.

In fact, by setting a given value of V_{DS}, starting from the Eq. (3.26), it is obtained that:

$$\frac{\partial I_D}{\partial V_{GS}} = K_n V_{DS} \quad \rightarrow \quad K_n = \frac{1}{V_{DS}} \frac{\partial I_D}{\partial V_{GS}} \tag{3.27}$$

Setting a certain oxide thickness value t_{OX} (and, then, a certain oxide capacitance per unit of area $C_{OX} = \varepsilon_{OX}/t_{OX}$), a width W, and a channel length L, starting from the value of K_n, it is possible to extract the mobility value μ_n, in this way:

$$\mu_n = \frac{K_n}{C_{OX}} \frac{L}{W} \tag{3.28}$$

where the trend of the extracted mobility and of the threshold voltage, with the variation of the gate voltage V_G and the temperature, has been already shown in Figure 3.58 and 3.61.

Finally, the threshold voltage V_{TH} can be calculated as the intercept of the I_D-V_{GS} curve and the V_{GS} voltages axis (i.e., at $I_D = 0$). Moreover, recalling that the threshold voltage is defined as in Eq. (3.22), from the I_D-V_{GS} curve for $V_{SB}=0$, one obtains the V_{TO}. Repeating the graph for different values of V_{SB} it is possible to obtain the threshold voltage V_{TH} for different V_{SB} values. In particular, plotting the values V_{TH} in function of V_{SB}, it is also possible to measure the parameters γ and $2\Phi_F$, starting from the following set of equations:

$$\begin{cases} (1) & V_{TH} = V_{T0} + \gamma \left[\sqrt{2\ \Phi_F + V_{SB}} - \sqrt{2\ \Phi_F} \right] \\ (2) & \frac{\partial V_{TH}}{\partial V_{SB}} = \gamma \left[\frac{1}{2\sqrt{2\ \Phi_F + V_{SB}}} \right] \end{cases} \tag{3.29}$$

In fact, once calculated V_{TO}, as the intercept of the x axis with the I_D-V_{GS} graph for $V_{SB}=0$, and calculating the slope $\frac{\partial V_{TH}}{\partial V_{SB}}$ from the graph V_{TH}-V_{SB}, substituting the equation (1) (calculated for a certain V_{SB} value) in the equation (2), of the system (3.29), rewriting the equation (1) in term of γ (i.e. $\gamma = \frac{V_{TH} - V_{T0}}{\left[\sqrt{2\ \Phi_F + V_{SB}} - \sqrt{2\ \Phi_F}\right]}$), and setting a certain V_{SB} value, it is possible to calculate the value of $2\Phi_F$ from the equation (2) of the system (3.29). Once calculated the value $2\Phi_F$, from the equation (1) of the system (3.29), for a certain V_{SB} value, it is possible to calculate the γ value.

PSpice includes different models for the MOS transistor. In the following the simplest model will be presented, i.e. the LEVEL 1 model.

In the LEVEL 1 model the drain current, for the different operation regions of an enrichment NMOS, is equal to:

$$
\begin{cases}
(1) & I_D = 0 & V_{GS} < V_{TH} \\[2mm]
(2) & \dfrac{K_n'}{2}\dfrac{W}{L}\left[2\,(V_{GS} - V_{TH})V_{DS} - V_{DS}{}^2\right] & V_{DS} < V_{GS} - V_{TH} \\[2mm]
(3) & \dfrac{K_n'}{2}\dfrac{W}{L}(V_{GS} - V_{TH})^2(1 + \lambda V_{DS}) & V_{DS} > V_{GS} - V_{TH}
\end{cases}
\qquad (3.30)
$$

where V_{TH} is equal to Eq. (3.22), and K'_n is equal to $\mu_n\,C_{OX}$. It is noted that in the equation (3) of the system (3.30), also the NMOS channel modulation is taken into account. It takes into account that, when the channel is in pinch-off, the effective channel length L', on which always falls a constant voltage equal to V_{GS}-V_{TH}, i.e. the pinch-off voltage V_{DSsat}, has to be considered. This length is smaller than the physical length L, which implies an increase of the current when the outside voltage V_{DS} increases, through a direct proportionality factor λ. This factor can be calculated from experimental data, tracing the I_D-V_{DS} characteristics versus V_{GS} (as in Figure 3.61) in the saturation region (Eq. 3 of the system 3.30), and observing that the tangents lines to the saturation characteristics pass all through the same point, i.e. they intercept the negative voltages axis V_{DS} (at $I_D = 0$). This point is equal to $V_{DS} = -1/\lambda$. Therefore, it is possible to calculate the value of λ simply as the absolute value of the intercept of the tangent lines with the x-axis of the voltages V_{DS} (see Figure 3.67). It must be emphasized that the term $1+\lambda V_{DS}$ in the Eq. (3) in the system (3.30) comes out from the fact that L' is considered, instead of the channel length L. On L' V_{DSsat} falls, and $L'= L-\Delta L = L(1-\Delta L/L)$. Remembering that $1/1$-x is about $1+x$ (because the Taylor series of the quantity $1/1$-x is about $1+x$, at the first order), if one considers that $\Delta L/L$ is proportional to V_{DS} as λV_{DS}, the equation above is obtained. Obviously, this shows that to reduce the effect of the channel modulation, i.e. to ensure that the variation ΔL affects less, in percentage, the channel length L has to be increased. In fact, in the technology analyzed, a very large L was considered, i.e. 3 µm. In fact, as shown in Figure 3.61 the channel modulation is not so important in pinch-off. Typical values of λ vary between 0.01 to 0.03 V^{-1} (in silicon devices).
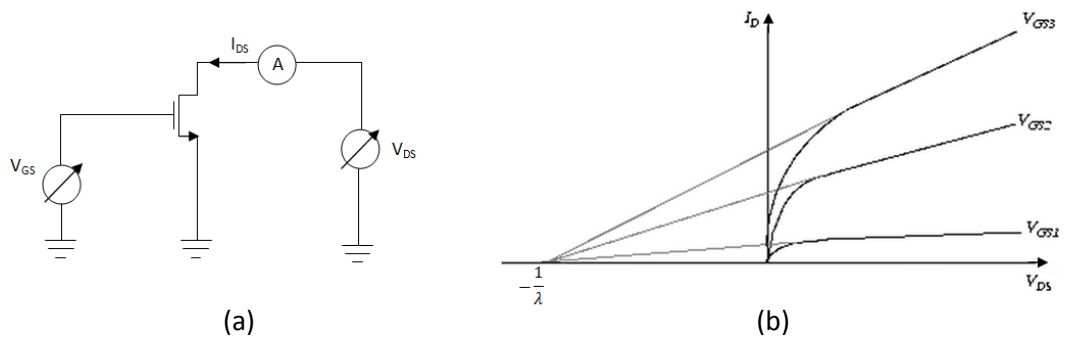
Figure 3.67. Experimental measurement. (a) Measurement setup. (b) Extraction procedure of λ.

In the pixel simulation shown after, some parameters are taken from literature [58], and some parameters are taken from Si technology, because they are not available for SiC technology.

In a suitable form in PSpice, known as the .MODEL form, all the electrical parameters previously extracted from experimental measurements, i.e. λ, V_{TO}, t_{OX}, μ_n, N_{SUB} (substrate doping) are put, while the amount K'_n, γ and $2\Phi_F$ are calculated by Spice automatically, as

$$\gamma = \frac{\sqrt{2\,q\,N_{SUB}\varepsilon_{SiC}}}{C_{OX}}, \quad K'_n = \mu_n\,C_{OX} \text{ (with } C_{OX} = \varepsilon_{OX}/t_{OX}\text{), and } \Phi_F = V_T \ln\left(\frac{N_{SUB}}{n_i}\right), \text{ respectively.}$$

If it is not only of interest the MOSFET static analysis, but also the analysis of what happens in the transient behavior, the parasitic effects must also be included in the model.

In fact, Spice allows to realize DC and transient analysis of linear and nonlinear circuits, as well as small signals and the frequency domain analysis.

Once extracted the NMOS electrical parameters, in order to simulate a NMOS in PSpice, there is the need to derive the capacitive parameters, since the LEVEL 1 Spice model of a NMOS also provides the presence of five capacitances, as shown in Figure 3.68.
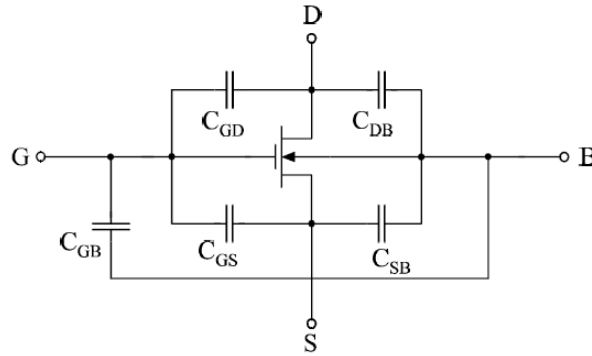
Figure 3.68. Capacitances included in a NMOS Spice Model.

C_{DB} and C_{SB} are the junction capacitances of the reverse biased junctions source-body and drain-body. An advantage of the CMOS structure is that the source and the body, both of the NMOS and PMOS, are at the same potential, so the junction is short-circuited and, therefore, the junction capacitance is limited to the value of zero voltage on the junction.

From the PN junction theory, it can be shown that the value of a *junction capacitance* depends from the reverse voltage value, on the same junction, according to the following relationship:

$$C(V) = \frac{C_{j0}}{\left(1 - \frac{V}{\varphi_0}\right)^m} \tag{3.31}$$

where V is the reverse voltage applied on the junction, φ_0 is the built-in voltage, C_{j0}, i.e. $C_j(V=0)$, is the capacitance per unit of area of the junction for $V = 0$, equal, for the PN junctions theory, at $\sqrt{\frac{\varepsilon q}{2\varphi_0}\frac{N_A N_D}{N_A + N_D}}$, and m depends on the junction type (in particular, m = 0.5 for "*abrupt*" *junction*, and m = 0.33 for *gradual junction*). Therefore, the first three parameters that have to be inserted in the .MODEL section of a NMOS, in PSpice, are *CJ*,

that corresponds to C_{j0} of the previous equation (expressed in F/m^2), *PB*, that corresponds to φ_0 of the previous equation (expressed in *V*), and *MJ*, that corresponds to *m* of the previous equation (dimensionless). Obviously, to calculate the total junction capacitance, PSpice also requires other two parameters, i.e. the drain and source areas, indicated, as *AS* and *AD* (expressed in m^2), that are defined for every MOS.

Typically, when PSpice builds the MOSFET model (and, in particular, even more important in the implantation cases), the capacitances contributions of the source-body and drain-body regions, are divided into two separate contributions, considering the contribution due to the "*flat*" region of the junction, and the contribution due to the *perimetric* region of the junction (see Figure 3.69), in the following way (for example, considering the drain-body junction, since for the source-body is exactly the same):

$$C_{db} = \frac{A_D C_j}{\left(1 - \frac{V}{PB}\right)^{M_j}} + \frac{P_D C_{jSW}}{\left(1 - \frac{V}{PB}\right)^{M_{jSW}}} \tag{3.32}$$

where *AD* and *PD* are, respectively, the area and the perimeter of the junction, and C_j and C_{jSW} are the junction capacitance for unity of area and perimeter, respectively. These capacitance values are technology dependent and, therefore, they must be provided by the designer or manufacturer. Unfortunately, this technology is not being treated at KTH, at the moment, and so for the perimeter capacitance an assumption will be done. The parameter that should be inserted in the .MODEL section are C_j and C_{jSW}, and for every MOS the values of *AD*, *AS*, *PS*, and *PD* should be defined. It should be noted that the parameters defined in the section .MODEL will be valid for all devices, while others, such as area and perimeter of the source and drain diffusion, must be defined for each device. On the other hand, typically, at least for a silicon process, the perimetric contribution is very low, since a typical value of the capacitance for unity of perimeter is around 10^{-10} F/m and, also considering a big perimeter, for example of about 100 μm, the perimeter capacitance will be of the order of the *fF* at V=0, i.e. very low. Instead, the capacitance for unit area is very big. Typically, for a silicon technology, it is around 10^{-4} F/m^2 and, this means that it is not possible to neglect this contribution.
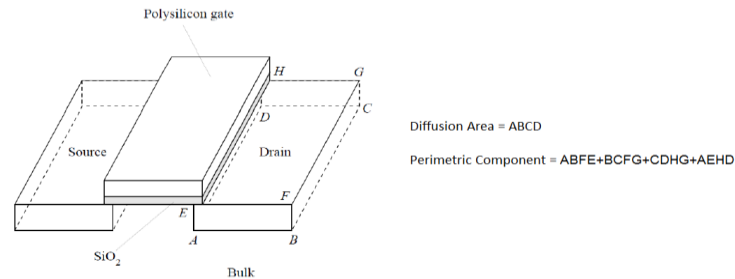
Figure 3.69. Area and perimetric diffusion components.

Regarding the other three capacitances C_{GS}, C_{GD} and C_{GB}, they are given by the sum of two contributions. The first contribution takes into account the capacitance between the channel and the underlying channel, which value is $C_G = WLC_{OX}$, with $C_{OX} = \varepsilon_{OX}/t_{OX}$ the oxide

capacitance, with ε_{OX} the dielectric constant of the silicon dioxide, equal to 3.45×10^{-11} F/m, and t_{OX} the thickness oxide. Depending on the operating region of the device, PSpice automatically distributes the C_G in three capacities connected between the gate-drain, gate-substrate and the gate-source. It is possible to theoretically demonstrate that, depending on the operating region of the device, the MOS capacitances are different, and they are equal to the values reported in the Table 3.1 [63] (where is considered for them, not the theoretical value of the channel L, but the effective channel length L_{eff}, after the drive-in phase, i.e. after the source and drain implantations).

Operation Region	C_{gb}	C_{gs}	C_{gd}
OFF	$C_{OX}WL_{eff}$	0	0
Triode	0	$\frac{1}{2}C_{OX}WL_{eff}$	$\frac{1}{2}C_{OX}WL_{eff}$
Saturation	0	$\frac{2}{3}C_{OX}WL_{eff}$	0

Table 3.1. MOSFET capacitance according to the operation region [63].

Therefore, to take into account the first contribution of the capacitance, the value of the oxide thickness t_{OX} must be given to PSpice (in the .MODEL section).

The second contribution is due to the overlap of the gate and the channel, the drain and the source regions, which gives rise to three capacitive contributions known as *overlap capacitances*. If with δ is indicated, for example, the overlap amount between the gate and the source region, the amount $C_{GSoverlap}$ (gate-source overlap capacitance) is equal to $W\delta C_{OX}$, where the amount δC_{OX} is defined as CGSO in PSpice. An identical reasoning can be done for the gate-drain and gate-substrate overlap capacitances, obtaining, CGDO and CGBO, remembering that CGBO must be in units of channel length, and not in units of channel width, as in the first two cases.

Finally, the other three values in the .MODEL section of the NMOS are CGDO, CGSO and CGBO.

This is the simplest model (and, obviously, the less accurate) that can be considered for the simulation of a NMOS in PSpice (other models, more accurate, are the LEVEL 2 and the LEVEL 3). Of course, the purpose of the simulation, that will be presented below, is to show only the *pixel* response for 4H-SiC technology typical values, doing also comparisons between the values of capacitance (and thus the ability to work at high frequencies) that would arise in a typical silicon technology and a possible 4H-SiC technology. Many parameters of the 4H-SiC CMOS technology are not known (they are not reported by the manufacturers, being a manufacturing secret), and therefore they will be assumed equal to a certain value for assumption (based, however, on the values available in the literature, when possible, or on value of the Si technology). Therefore, if the I_D-V_{DS} characteristics shown in Figure 3.61 are not in complete agreement with what it is obtained in the PSpice simulator, this is not surprising, since a lot of data are not known, such as the width of the source and drain region, the overlapping, the channel modulation parameter, etc., and therefore they will be assumed to have a certain value. Furthermore, the above shown procedures has also the purpose to be helpful for fast calculation of

important NMOS parameters if the CMOS technology, in 4H-SiC, will start to be developed at KTH in the future.

3.5.4   Pixel operation: PSpice simulation

To realize the Pixel operation simulation it is possible to follow two ways, as regarding the modeling of the MOS: to introduce only electrical parameters, such as the threshold voltage, the mobility, the Fermi's Potential, etc., neglecting all the capacitive effects (i.e., setting them to zero as default PSpice values), considering, thus, an ideal MOS, without any signal delays, or to introduce also the parasitic parameters, making the appropriate assumptions, since some values are not available in the literature (for the given technology).

In particular the two parameters on which assumptions will be done are the width of the open window to perform the source and drain implantation (in order to estimate the source-body and drain-body junction and perimetric capacitance), and the source-gate and drain-gate overlapping (in order to evaluate the two overlapping gate-source and drain-source capacitances).

In the available silicon technologies, to minimize the overlapping, the MOS transistors are produced with *self-alignment techniques*. In particular, the gate is realized before the realization of the source and drain implantations. In this way, when the source and drain implantations are performed, the thin oxide layer, under the gate region, will act as a mask for the doping process, making sure that the drain and source regions are automatically aligned with the already present gate. After the implantation process, the annealing step (or the so-called *drive-in*) follows, which allows, the dopant activation and the reparation of the crystalline damages produced during the implantation, even for a slight dopant diffusion under the gate region. With this technique the overlapping is reduced compared to the standard gate realization after the source and drain implantation (which is greater because of possible uncertainties introduced during the alignment of the masks). This is an advantage because the self-aligned gates permit that the parasitic overlap capacitances between gate and source and gate and drain to be substantially reduced, making the MOS transistors faster, smaller and more reliable.

Unfortunately for the manufacturing processes of the SiC MOSFET it is not possible to use self-aligned structures [7], because, to achieve a self-aligned gate, a highly doped gate contact, made with a doped polysilicon, is required, deposited and patterned before the realization of the source and drain. This means that the gate will be present during the annealing step that follows the source and drain implantation. Even if the polysilicon has not exceptional conductive properties, it is preferred to a metal gate because there are not technological processes that allows to align the metal gate in a MOS structure with good precision, due to the high contamination of the metal, for example from aluminum, introduced during the various stages of thermal annealing. Instead, the polysilicon can be easily deposited via CVD, and it is tolerant to subsequent manufacturing steps, which involve extremely high temperatures above 900-1000 °C, where the metal cannot resist. However, the annealing step of a SiC process (as discussed in Chapter 2), occurs at

1500-1700 °C (compared to 900-1000 °C in a silicon process). This give rise to doubts about the polysilicon gate [7] (even if it has a better behavior than a metal gate) and the gate oxide resistance to high temperature. Therefore, for a SiC process, it is not possible to use the self-aligned structures, and the gate is always deposited after the realization of the source and the drain. In the actual technology for the realization of lateral MOSFET (LMOSFET) in SiC, the obtained overlapping vary between 0.5 and 2 μm [64]. The overlapping is always made sufficiently large, in order to deal with any alignment tolerance during the masking for the gate realization. Therefore, for the following PSpice simulation an overlapping of 0.5 μm will be considered.

Unfortunately, for the presented structure in Figure 3.60, the area of the drain and source are not reported in [58]. Indeed, in [58], only the implantation depth is reported, i.e. 300 nm, but not the lateral extension of the open window to perform the implantation. Then, in the following simulation, it will be assumed that the open window, to perform the implantation, is square, and therefore, given that W (channel width) is equal to 50 μm, it will be assumed that the lateral dimension of the drain and source is equal to 50 μm. Obviously, it is noticed that this high extension will cause the presence of a high drain and source capacitances, as well as the presence of a high lateral resistance towards the contacts for the carriers, both in the drain region and in the source region. This will cause a high voltage drop inside these regions, reducing the effective voltage V_{DS} on the channel, and then the drain current. However, any internal drop, in the following simulation, will be neglected.

At this point, using the capacitances equations shown above, one can evaluate the various 4H-SiC NMOS capacitances, and compare them with those that would be obtained in a Si technology, reasoning with the same size. Obviously, for a silicon device, there are not mobility problems at the interface, as in SiC devices. This allows to make them with reduced size, even if to make a good comparison they must be of the same size. In the Table 3.2 a comparison between the capacitances that would be obtained in a Si technology and a 4H-SiC technology at a temperature of 300 K is shown.

Parameter	Unity	Si	4H-SiC
ε_r	(adim)	11.9	10
ni^2	(cm^{-3})	10^{20}	10^{-16}
AS	(m^2)	2.5×10^{-9}	2.5×10^{-9}
AD	(m^2)	2.5×10^{-9}	2.5×10^{-9}
PS	(m)	2×10^{-4}	2×10^{-4}
PD	(m)	2×10^{-4}	2×10^{-4}
PB	(V)	1.17	3.31
CJ	(F/ m^2)	1.70×10^{-2}	9.25×10^{-3}
CJSW	(F/m)	10^{-10}	10^{-10}
CGSO	(F/m)	4.31×10^{-10}	4.31×10^{-10}
CGDO	(F/m)	4.31×10^{-10}	4.31×10^{-10}
CGBO	(F/m)	4.31×10^{-8}	4.31×10^{-8}
CSB	(F)	4.25×10^{-11}	2.31×10^{-11}
CDB	(F)	4.25×10^{-11}	2.31×10^{-11}
CG	(F)	2.16×10^{-12}	2.16×10^{-12}
CGTOT	(F)	4.35×10^{-12}	4.35×10^{-12}

Table 3.2. Capacitance comparison between Si and SiC technology.

The Table 3.2 shows the comparison between the calculated capacitances in the case of a Si technology and of a 4H-SiC technology, making the following assumptions. The first assumption is that the source and the drain area are square, with a side of 50 μm. The

perimeter capacitance, in the case of a NMOS made in 4H-SiC, is equal to that typical of a Si technology (because this value depends from the technology used and, unfortunately, there are no data in the literature for the silicon carbide). The calculations were carried out considering for the drain and the source, and p-well doping, the values of the structure presented in Figure 3.60. Furthermore, the total gate capacitance was calculated as follows:

$$C_{g,TOT} = W\ L\ C_{OX} + W\ CGDO + W\ CGSO + L\ CGBO \qquad (3.33)$$

where WLC_{OX} is the CG in the Table 3.2. Instead, the source-body capacitance for V=0 (for the drain-body capacitance is the same) was calculated as follows:

$$C_{sb} = AS\ CJ + PS\ CJSW \qquad (3.34)$$

The fundamental thing that is noted from Table 3.2 is that, reasoning with the same gate capacitance (since they are assumed to be equal because the channel size is assumed equal, both in length and width), and perimeter capacitance, the source-body and drain body capacitances, in a 4H-SiC device is half than the one a Si device. This analysis can be repeated up to the operation limit of the Si technology (200-300 °C), where the SiC is still working well, where it is noted that the capacitances are equal to 42 pF, for Si, and 23 pF for the 4H-SiC (the other parameters, as t_{OX}, C_{OX}, etc., will be shown after, in the PSpice simulation).

The capacitance reduction to a half of its value is a big advantage, both in terms of signal propagation delays within the circuit, and of dynamic power dissipation. For example, if a CMOS inverter is considered (in addition to the advantage that, if made in SiC, it can work at very high temperatures, compared to the Si) supposing equal propagation delays tp_{LH} and tp_{HL} (time between a change of 50% of the input and a variation of 50% of the output), equal to $C_T\ V_{DD}\ /\ 2\ K\ (V_{DD}\text{-}V_{TH})^2$. Hence, the delays are proportional to the total load capacitance C_T on the output node of the CMOS logic. This capacitance is equal to the sum of the eventual gate capacitance of the downstream MOSFETs, and the NMOS and PMOS drain-body capacitances of the inverter itself (plus a possible interconnection capacitance, which is neglected in this analysis). If the inverter works alone (without anything downstream), the C_T will include only the drain-body capacitance, and this means that it will be reduced by half in the SiC case compared to Si one, as well as the switching times. The same applies, for example, also for the dynamic power dissipation (since, an ideal CMOS logic does not dissipates a static power), equal to $a\ f\ C_T\ VDD^2$, where a is the activity factor (ratio between the number of times that the port is switched and the number of cycles), and f is the working frequency. In fact, halving the C_T, the dissipated power halves, if the same frequency is considered. Furthermore, for the same dissipated power, the operation frequency can be increased. In fact, as known from the theory, one of the biggest SiC advantages is to work at high frequencies, thanks to its low dielectric constant, compared to Si [7].

At this point one has all the elements to proceed to the implementation of a PSpice simulation to simulate the operation of a 3T pixel in 4H-SiC, in *soft-reset* operation. Regarding the MOS that make up the pixel, the electrical parameters will be extracted from [58] and, in particular, the parameters at a temperature of 300 °C are inserted. Instead, the

capacitive parameters, for a temperature of 300 °C, have been analytically calculated with the above equations. Figure 3.70 shows the schematic of the Pixel realized in PSpice, and the Table 3.3 shows the electrical and capacitive parameters evaluated at 300 °C.
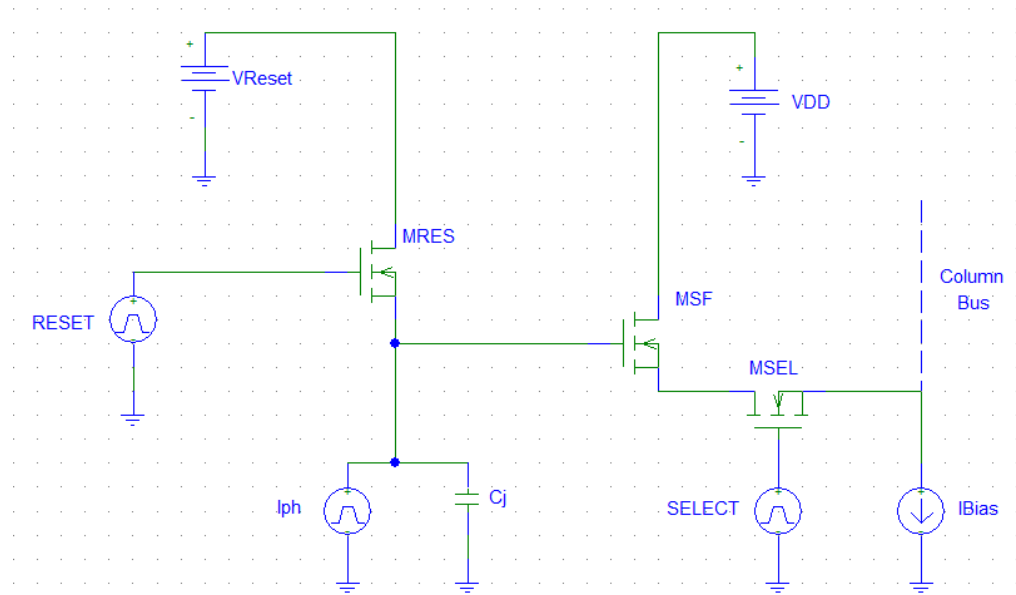
Figure 3.70. PSpice 3T Pixel schematic.

Parameter	Unity	Value
LAMBDA	(V^{-1})	0.02
KP	(A/V^2)	8.625×10^{-7}
TOX	(m)	0.04×10^{-6}
NSUB	(cm^{-3})	4×10^{19}
PB	(V)	3.04
UO	(cm^2/Vs)	10
MJ	$(adim)$	0.5
MJSW	$(adim)$	0.5
VTO	(V)	2.5
AD	(m^2)	2.5×10^{-9}
AS	(m^2)	2.5×10^{-9}
PS	(m)	2×10^{-4}
PD	(m)	2×10^{-4}
CJ	(F/m^2)	9.49×10^{-3}
CJSW	(F/m)	10^{-10}
CGSO	(F/m)	4.31×10^{-10}
CGDO	(F/m)	4.31×10^{-10}
CGBO	(F/m)	4.31×10^{-8}

Table 3.3. PSpice parameters at 300 °C.

Table 3.3 shows all the parameters before considered, with the addition of the channel modulation (LAMBDA) with a value of 0.02 V^{-1}, since that the I-V NMOS curves in [58] show a slight channel modulation effect, when the voltage increase around 10 V. Since typical λ values vary between 0.01 and 0.03 V^{-1} (in Si technology), a λ value equal at

0.02 V^{-1} has been assumed (because this value is not given in [58], and it should be experimentally measured, as shown before).

As shown in Figure 3.70, the photodiode (that is the diode realized at KTH) was modeled as a current generator with in parallel a capacitance, which is its junction capacitance, with a reverse voltage of 10 V across the same. The capacitance is calculated from Eq. (2.41), and it is equal to about 70 pF, assuming that the intrinsic region is completely depleted (in fact, this has been confirmed by the simulations). The photogenerated current, extracted from a simulation of the photodiode at 300 °C, at a wavelength of 250 nm (obviously the same analysis can be repeated for other wavelengths and temperatures), is equal to 1.3 μA. The voltage supply *Reset* and V_{DD} (which, theoretically, could also be different), are both equal to 10 V. The *Reset* and *Select* signals, that pilot the turn on of M$_{RES}$ and M$_{SEL}$ respectively, are modeled with two square wave of 10 V of magnitude, the *Reset* with a period of 0.4 ms, with an on-state of 0.25 ms, and the *Select* with a period of 0.4 ms, a delay of 0.3 ms (so that it can read the output signal after that it is available on the source of M$_{SF}$), and an on-state of 0.05 ms (this is the time in which the signal is read, and it can be fixed by a correct circuit design). The on-state of the *Reset* was chosen to give the time to load, to the steady-state value *Reset*-V_{TH}, the junction capacitance C_j, and discharge up to a certain value (the discharging time is not fixed and it can be varied according to the circuit design).

The photodiode behavior has been modeled with a square wave current generator, with a magnitude of 1.3 μA, with a period of 0.4 ms, an on-state (i.e. the *integration time*) of 0.15 ms, and a delay of 0.25 ms. These values were chosen assuming that during the junction capacitance charge phase, via the MOS, the photodiode does not absorb light (i.e., it does not generate current). Instead, when the MOS is OFF, after 0.25 ms, the photodiode absorbs light and it gives rise to a photocurrent of 1.3 μA, that discharge the capacitance C_j, for 0.15 ms. Instead, the *Column Bus* was modeled simply as a constant current generator of 2 μA, I_{Bias}. This current value, and the M$_{SEL}$ gate voltage, will bring M$_{SEL}$ itself in the triode region operation. I_{Bias} polarizes the transistor M$_{SEL}$, when it is turned on. On the other hand, if the source of M$_{SEL}$ is floating, PSpice gives an error during the simulation.

In Figure 3.71 the trends of the voltage signals inside the pixel circuit are shown (starting from a steady-state condition, reached after about 100 μs), that are completely in agreement with the theory shown in the Chapter 2 (see Figure 2.17), as confirmation of the good operation of the 4H-SiC *pixel* at 300 °C. Obviously, it is possible to repeat this test at higher temperature, like the Venus temperature, without any problem, because in the previous simulations it is clearly shown that the 4H-SiC photodiode can work at this temperature. The only problem will be the knowledge of the electrical parameters of the 4H-SiC NMOS that are not known, at this temperature, in literature.
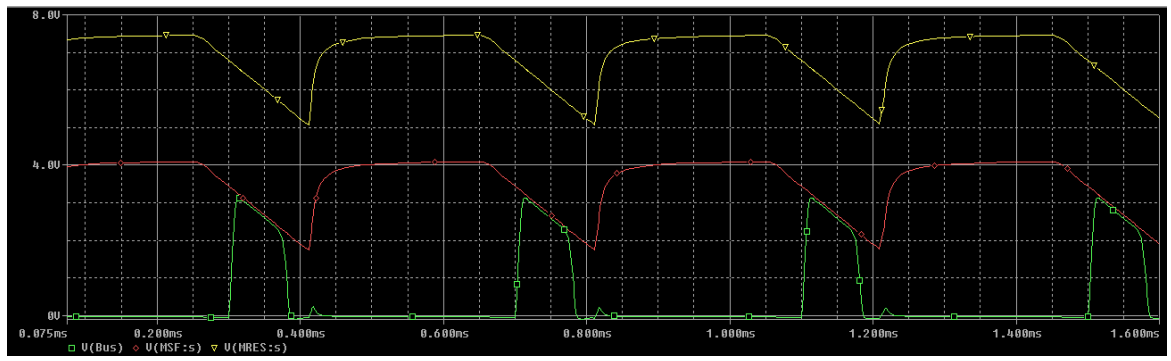
Figure 3.71. Voltages inside the pixel at 300 °C and λ = 250 nm.

Chapter 4

Experimental results

4.1   Measurement equipment

In this chapter the results of the experimental tests will be presented. These tests are carried out on some photodiodes available at KTH (seen in Chapter 2). The tests are realized in a temperature range from 25 °C to 500 °C, in order to include an analysis at the temperature of interest, i.e. the Venus temperature. The objective of these measurements will be to observe if what predicted during the theoretical and simulative analysis is actually confirmed by experimental analysis. In addition, this will confirm the ability of the 4H-SiC to absorb in the UV range and, therefore, that it can be used for the realization of a photodiode for UV photography, useful for the planet investigation.

Obviously, before showing the obtained results, it is fair to briefly present the equipment used. In Figure 4.1 it is shown the measurement setup.
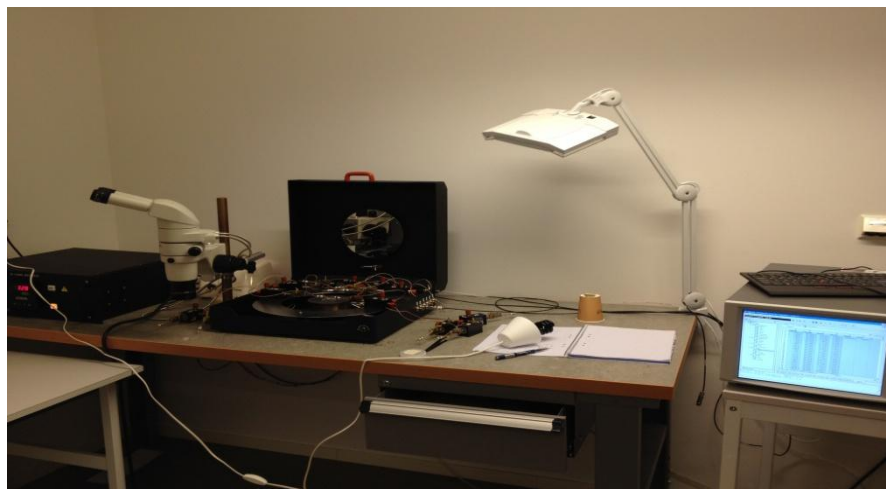
Figure 4.1. Measurement Setup.

The measurement setup essentially consists of four parts: a *Thermal Probing System*, a *Semiconductor Characterization System*, a *Cooling System* (which it is not possible to see in the Figure 4.1), and an *UV lamp*.

The Thermal Probe Station, *Model S-1060 Series*, used to perform the measurement of the reverse current of the device under test, is made by *Signatone* [65]. It is a Probe for the wafers characterization and packaged devices which, through the use of a *Hot Chuck Systems*, allows to realize measurements on the devices from a temperature of 25 °C up to a temperature of 600 °C, with an accuracy of ± 1 °C, a resolution of 1 °C, and a uniformity of $\pm\, 1$ °C. The Hot Chuck system (the part of the probe station that supports the device

during the measurement) is necessary because both at low temperature and high temperatures (the temperature is manually varied from the outside by a suitable heat generator), the device can move on the chuck, and the probe (i.e., the probe contacts) can destroy the device itself, due to fluctuations. In fact, by means of a vacuum system, when the temperature rises beyond a certain value, a high stability of the component is obtained during the measurement, to prevent scratches on the wafer. For this reason, the probes contact have to lift before the temperature increases, because the temperature change can cause air fluctuations and move the sample.

Furthermore, the Probe Station is equipped with a *Stereoscopic Zoom Microscope, SMZ1000*, one of Nikon's most advanced stereomicroscopes, that incorporates a powerful combination of advanced microscope optics, with high *NA* objectives (*NA* stands for numerical aperture, which is a parameter that represents the maximum useful angle to the system to receive or emit light) and exclusive Nikon illumination system [66]. Obviously, the microscope is positioned above the wafer during the positioning of the device, while it is moved away when making the high temperature measurement, to preserve its integrity, since it cannot withstand high working temperatures.
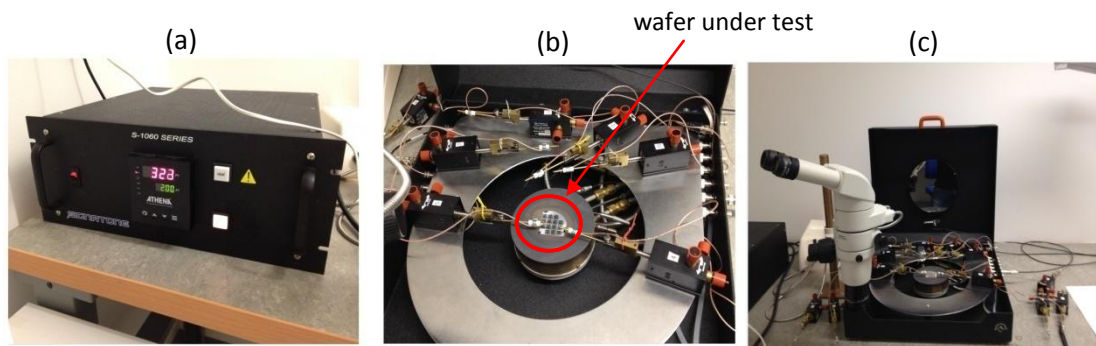
Figure 4.2. Probe station parts. (a) Heat Generator. (b) Vacuum Chuck with the wafer upside.
(c) Stereomicroscope SMZ1000.

To measure the photodiodes under test reverse current, and to extract the obtained data, saved in a *.xls* file (an Excel file), the probe station is connected to a Semiconductor Characterization System, *Model 4200-SCS*, by *KEITHLEY* [67]. The *Model 4200-SCS* is a total system solution, and a powerful single box solution, for electrical characterization of devices, materials and semiconductor processes. This advanced parameter analyzer provides intuitive and sophisticated capabilities for semiconductor device characterization by combining measurement sensitivity and accuracy with an embedded Windows-based operating system and the Keithley Interactive Test Environment. In fact, among the various required tests (in terms of fundamental electrical measurements), at the beginning of the characterization of the same there is always a DC measurement to extract the I-V characteristic of a device to have a complete picture of a device operation. Other measurements could be C-V measurements needed to evaluate, changing the applied voltage on the device, the trend of the junction capacitance value, etc. In Figure 4.3 the front panel of the *4200-SCS* is shown (for more detail see [67]).

Figure 4.3. 4200-SCS front panel.

When the work temperature has to be reduced (for example, from 500 °C to 25 °C), the probe station's chuck must be cooled. To do this, it is connected to a chiller (that performs a liquid cooling), *ThermoChill II*, by *Thermo Scientific* [68]. It allows to control the coolant temperature in an extremely reliable way (the refrigerant is water, which has the task to transfer, in an optimal way, the heat from the hot source, to a cold source). The chiller is used when the system works at a temperature equal or above 300 °C, to both cool the chuck when the temperature is reduced from a temperature equal or above 300 °C and to keep a stable temperature at high temperature. In fact, when the temperature is below 300 °C, the cooler does not come into action. When the temperature arrives at 300 °C, due to the heat generator instability, the chuck can arrive, for example, to 305-310 °C. In this case, the chiller sends water to the chuck through a pump that allows the water circulation. The water continuously circulates under the chuck and cools it, until the temperature is not lowered to 300 °C. After each cooling cycle, the water returns back to the chiller and it is cooled, for a next cooling. The same applies when the temperature has to be reduced under the 300 °C. After having set the cooling operation of the heat generator, to reduce the temperature, the chiller works to reduce the temperature with the cool water circulation under the chuck, at a temperature of 22 °C, for example. In figure 4.4 the chiller used is shown (for more details see [68]).

Figure 4.4. Recirculating Chiller.

166

Finally, to test the device under ultraviolet radiation, it is used a *compact fluorescent UV lamp* (*compact* because the pipe has been made to occupy little space), also called compact fluorescent light, produced by *Velleman* [69]. This type of lamp is a fluorescent lamp (i.e. it uses a fluorescent material) designed to replace an incandescent lamp because it is larger at least from eight to fifteen times an incandescent lamp but it allows to produce the same amount of light of an incandescent lamp using one-fifth or one-third of the total consumed electrical power. The basic operation principle, of a common *CFL*, is simple. In the lamp pipe the inner surface is coated with a fluorescent material with the aspect of white powder. After, a vacuum is practiced and a noble gas at low pressure is introduced (such as argon, xenon, neon, krypton), in addition to a small quantity of mercury, which partly evaporates mixing to the gas. At the ends of the tube there are two electrodes, through which it is possible to obtain, applying an external voltage, a passage of current that lead the gas to emit ultraviolet radiation. The material in the tube invested by such radiation, being fluorescent, emits in turn also visible radiation, i.e. light. Visible radiation, having a wavelength greater than the ultraviolet, carries only a part of the energy that was carried from the ultraviolet radiation, while the remaining energy is converted into heat, which goes to heat the pipe. These types of lamps, however, do not emit only UV light, but also visible light, while, in the test that will be performed, a lamp that emits UV light only is required.

Obviously, in the case of an UV lamp, visible light must be filtered as much as possible. In this case the lamp takes the name of *Black Light* lamp, or *UV-A light* (long-wave UV), or *Wood's lamp*, and it has a filter for the violet color (in fact, if the short wavelength of the violet is filtered, also the long wavelength of the white light is filtered), inside the tube. This filter blocks most of the visible light, causing the lamp to present a violet glow during operation (because this is the last color that the human eye can perceive, and that could pass the filter having a wavelength around 400 nm).

The only difference between a standard CFL and a black light lamp is in the fluorescent material, typically *phosphors*. Typical phosphors are transition metal compounds, or rare earth compounds of various types inserted in the lamp, chosen according to the type of emission desired, i.e. emissions UV-A or UV-B (because the UV-C are almost always completely blocked), instead of emitting white light. Note that both the fluorescence that the phosphorescence are radiative processes by which one can verify the relaxation of an excited molecule. The distinction between the two processes concerns the radiation life time. In the case of the fluorescence, the luminescence ceases almost immediately after removing the exciting radiation. Instead, in the phosphorescence, the radiation continues to be emitted, at least for a short period of time, typically over 1 ms, after the exciting source removal.

CFL lamps radiate a *spectral power distribution* different from a lamp to another, depending on the type of used fluorescent material. The spectral power distribution, or energy distribution, is the distribution of the radiated energy from the lamp at the different wavelengths of the electromagnetic spectrum. Then, according to the type of lamp used, most part of the radiated energy can be more concentrated in a given portion of the spectrum than in another. Unfortunately, for the lamp used in the tests nor the spectrum,

nor the *radiant power* (that is the total energy radiated by the lamp in all directions in the time unit) are reported, by the manufacturer.

For this reason, the spectrum of the lamp was manually measured through the use of a *spectrometer*. In general, the *spectrometer* is an instrument capable of measuring the spectrum of the electromagnetic radiation, i.e. the properties of light according to its wavelength. The spectral lines can be observed through a *dispersion prism* or through a *diffraction grating*, where both devices allow to "angularly disperse" the light beam to be analyzed, and to relate the dispersion angle with the wavelength component of the light beam. A lot of spectrometers, once decomposed the incident electromagnetic radiation into its wavelengths, measure the intensity, at different wavelengths, through the use of a photodiode. For more detail see [56].

The spectrometer used is a *COMPACT CCD Spectrometer*, by *THORLABS* [70], which allows to detect radiation in the range 200-1000 nm, with a resolution of 2 nm. It measures the emission spectrum of the lamp through the use of an optical fiber that is placed on a small portion of the outer surface of the lamp. The light that enters in the optical fiber is transmitted to the spectrometer, where a first spherical mirror focuses the light on a diffraction grating. The diffracted light impacts on a second spherical mirror, which projects the spectrum on a CCD array, and the data are transferred to a computer through the use of an analog-digital converter (for more details see [70]). In Figure 4.5 the spectrometer used and the operation basic principle of the same are shown.
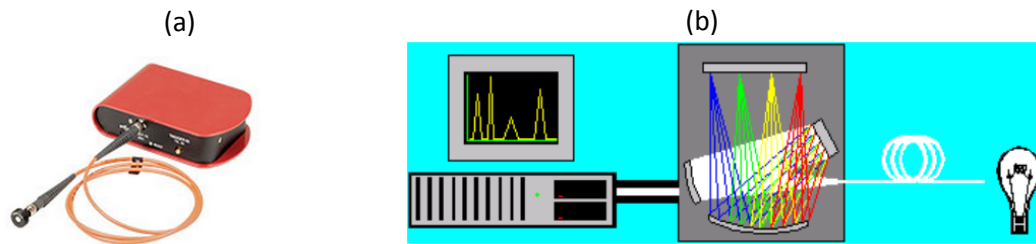
Figure 4.5. (a) Fiber-based spectrometer. (b) Basic operation principle of the used spectrometer.

In Figure 4.6 the lamp spectrum used for the test is shown. In this Figure it is shown that the spectrum is in *arbitrary unit*, i.e. the spectral intensity of the radiation has been normalized to a reference measurement value, which in this case could be the maximum of the detected intensity. In general, it is not possible to know this value because it depends on the system type, unless from a detailed prior knowledge of the "arbitrary units" definition. Obviously, this is not a problem because, even if the reference value is not known, the objective of the measure is only to compare multiple measurements performed in similar environment, through the use of a dimensionless quantity defined as the ratio between the measurement and the reference value.
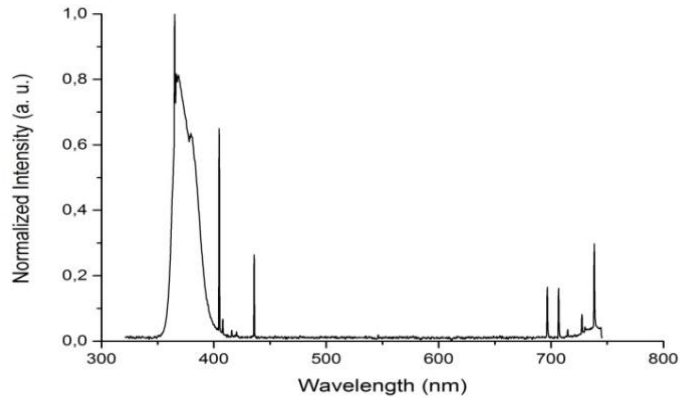
Figure 4.6. UV lamp spectrum.

From the spectrum of the black light fluorescent lamp analyzed, it is observed that the used lamp is of *wide-band* type (or broad-band), since it produces radiation in the 350-400 nm band (unlike a *narrow-band* lamp that has a very tight spectrum, at most 2 nm), with a peak around 360 nm (i.e. in the UV-A range). Furthermore, it is also noted that there are weak intensity peaks at certain wavelengths in the visible range. Typically, the *wide-band* lamp are done of lead-activated calcium metasilicate (silicates are a class of minerals primarily composed of oxygen and silicon). But, inside the lamp, other substances are present which serve for the lamp operation, such as, for example, the mercury. In fact, when the mercury "relaxes", it has an emission spectrum in the visible range at different wavelengths (404 nm, around 700 nm, etc.) and this emitted light crosses the filter and reaches the spectrometer, due to leakages through the filter that blocks visible radiation. Note that thanks to the effects due to the mercury vapor that passes through the filter, because of losses introduced by the same, the lamp has its violet color. In Figure 4.7 is reported the UV lamp used, as well as a photo of a UV light test configuration.

(a)   (b)
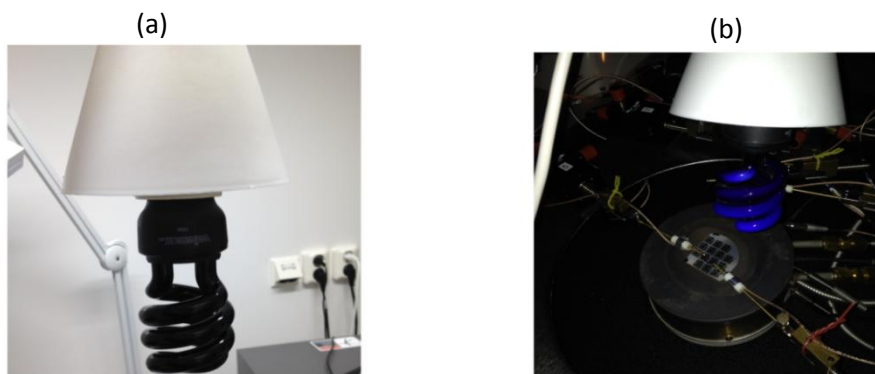
Figure 4.7. (a) UV lamp. (b) UV illumination test.

One last thing to note is that some measurements, and, in particular, measurements up to 200 °C, were also performed on a probe station, the *Cascade 12000*, by *CASCADE MICROTECH* [71], almost identical to the one presented in Figure 4.2. The principal

difference is that this probe station has a chamber, where the device under test is inserted on the chuck, and it is fully closed. With a hole on the top, a microscope, with a camera inside, is inserted. During the positioning of the probe contacts (realized in aluminum, both for this probe station and for the previous), this camera inside the microscope can be used to perform a zoom on the device, to contact it more easily. As for the microscope in Figure 4.2, this microscope must be removed when the measurement is done, because the measurement require more time, compared to the simple positioning of the device, and, therefore, the microscope and the camera will surely not resist at these high work temperatures. Figure 4.8 shows the probe station and a zoom of the device performed with the camera inside the microscope, with the device placed on the chuck (the upside contact is the pad for the base contact, and the right contact is the collector contact).
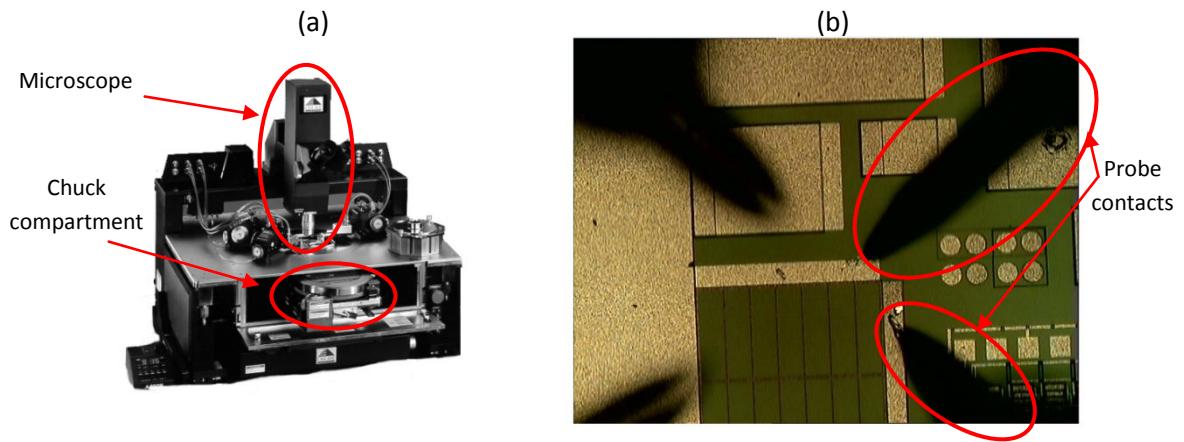
Figure 4.8. (a) Cascade 12000 probe station. (b) Tested device zoom.

4.2   Experimental analysis

Through the use of the measuring apparatus described in Section 4.1, the measurements were made, both in dark conditions and under UV light, on 14 photodiodes on 14 Dies (belonging to a cut piece of the EB12rw wafer) shown in Figure 4.7.

The experimental tests are carried out in a temperature range of 25-500 °C and in a voltages range -4 ÷ 3 V, without doing a sweep, in reverse, up to -20 V, as done in the simulations, because as observed, both in simulations and in the experimental tests the reverse current results to be almost constant with the reverse applied voltage. Therefore, in order to reduce the data acquisition time, the range of voltages considered has been narrowed. Moreover, it is a good idea to make a sweep with positive voltages to see if the photodiode correctly works, in order to observe if the diode is working well in ON state, and if the light absorption, as theoretically expected, acts only on the reverse current and not on the direct current, i.e. the exponential portion of the I-V characteristic (in logarithmic scale a linear trend would be).

An important thing to immediately notice is the resolution (the resolution constitutes the lower limit at which it has still sense to evaluate the measured value) used by the instrument (i.e. 4200-SCS). In particular, if a voltage source is applied, and a current

flowing through the device is measured, the chosen instrument resolution was 1 pA (this resolution is possible to manually set), with a full scale of 1 µA (the full scale is the maximum value that the instrument can measure) and an accuracy of ± (0.050 % rdg + +100 pA) [67] (*rdg* stands for *reading*). The accuracy is the proximity of measurement results to the true value. This means that if one wants to measure a current lower than this resolution value, the instrument will measure always currents of the order of pA (minimum detectable value) when, instead, the current is well below this measured value. This is important to stress, especially in photodiode operation, because this could lead to a wrong interpretation of the measured dark current, considering it higher than its actual value.

Furthermore, when the effective current is under this value, the instrument will not show a stable current value of the order of pA, but it will show a floating current measurement, because it is measuring only noise (thermal, etc.). In fact, the resolution of the instrument is limited by fundamental noise limits [67]. Therefore, the instability that occurs in the reading constitutes a limit to the resolution of the measurement. Of course, this involves a measure of a random current at the variation of voltage and temperature. Instead, when the current will begin to rise above the minimum detectable value of the instrument, following the increase in temperature (for the same applied voltage), the current will appear quite stable, because the measurement shows the actual current.

From [67] it is possible to see that also a resolution of 100 fA, or lower than this, is possible to set. Apart that the choice of the resolution is related at the current range that is possible to detect, a lower resolution causes also a slower measurement. Furthermore, if a so low resolution is set, for chuck and probe contacts leakage currents (always > 100 fA), the instrument is not able to detect a current of 100 fA, but the measurement is limited from this leakage currents. Hence, the measurement does not change a lot even if a lower resolution is chosen.

In the following figures the I-V characteristics of the photodiode varying the temperature are shown.
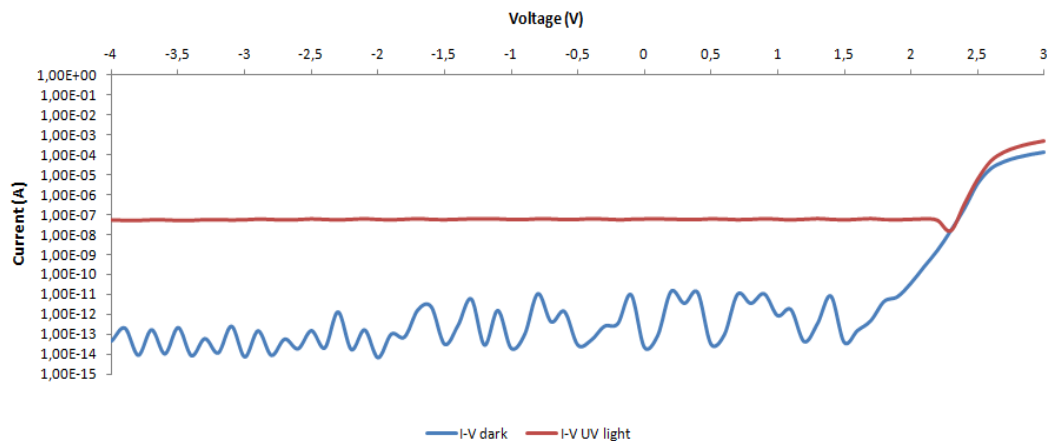
Figure 4.9. I-V characteristic in dark and under UV light at 25 °C.

171
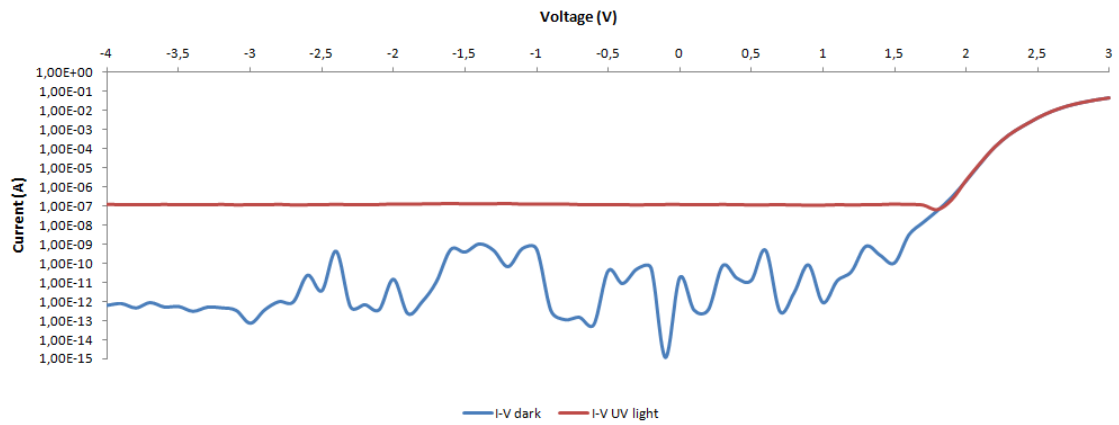
Figure 4.10. I-V characteristic in dark and under UV light at 200 °C.
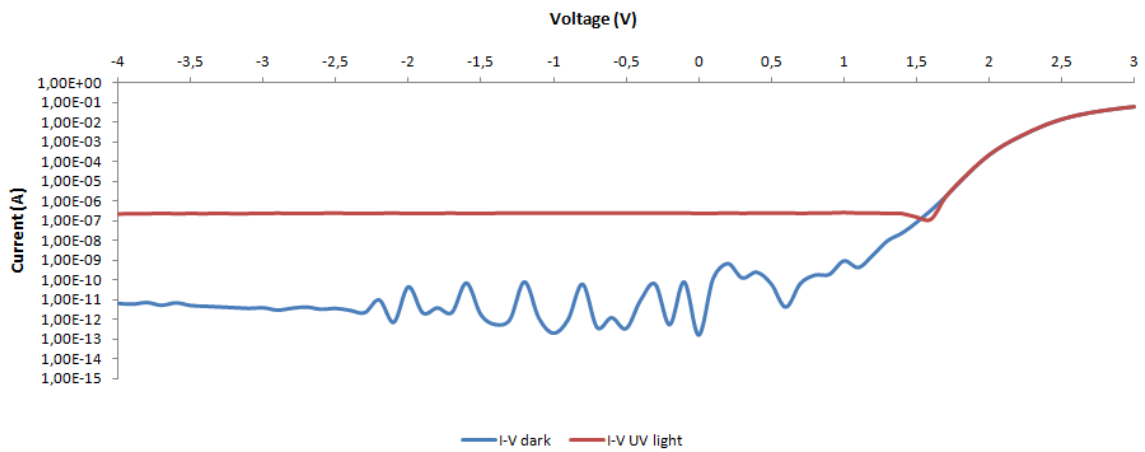
Figure 4.11. I-V characteristic in dark and under UV light at 300 °C.
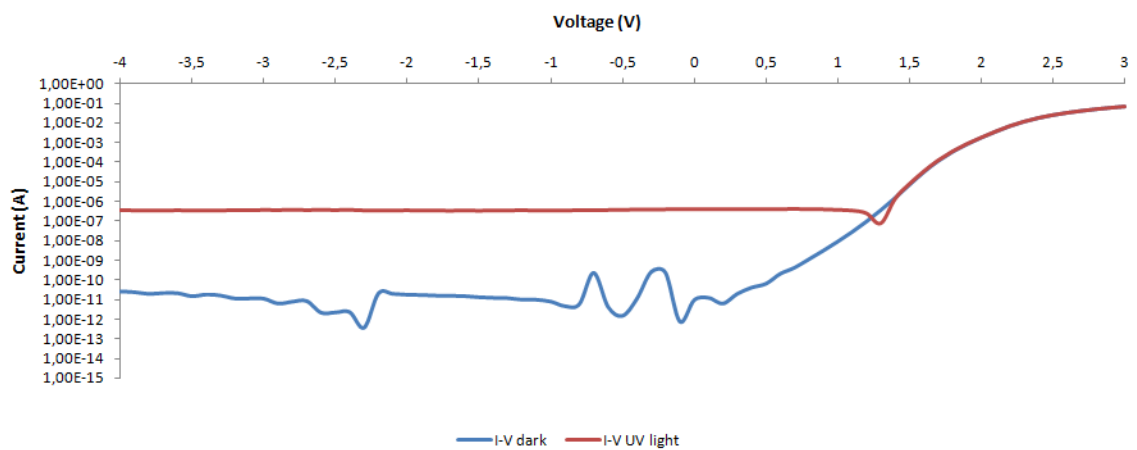
Figure 4.12. I-V characteristic in dark and under UV light at 400 °C.

172
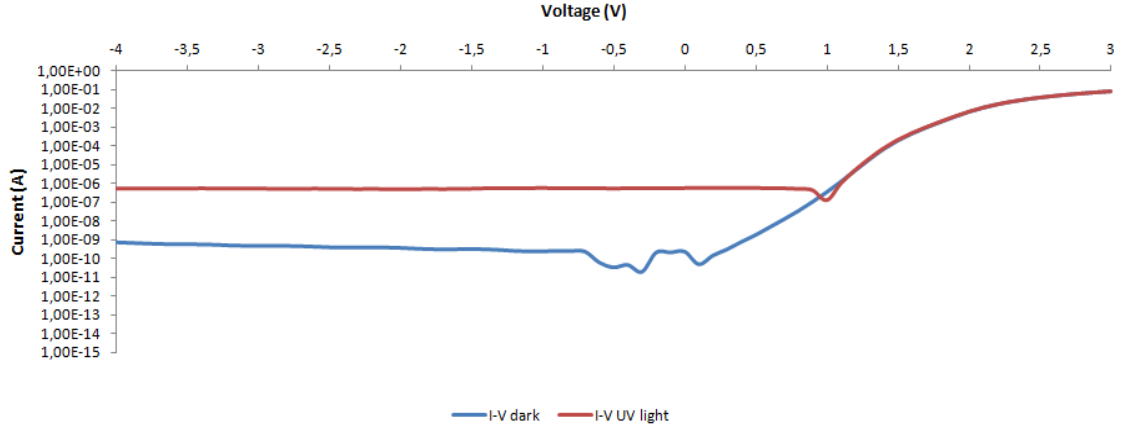
Figure 4.13. I-V characteristic in dark and under UV light at 500 °C.

From the above figures, it is observed that in the direct operation of the diode, as theoretically expected, the illumination does not cause any change of the current through the device. Moreover, as happens for a typical PN junction, it is observed that the ON voltage decreases with the increasing temperature. In fact, it can be shown that, reasoning at the same current value, the ON voltage of a diode is reduced with the following law:

$$\left.\frac{\partial V}{\partial T}\right|_{I=cost} = \frac{V - 3\,V_T - E_G/q}{T} \tag{4.1}$$

that in the case of a 4H-SiC diode (as the diode with an I-V characteristic as that shown in the Figure 4.9), with a V ≈ 2.5 V (that is possible to estimate, approximately, with the built-in voltage formula), an energy gap E_g of 3.2 eV, and at a temperature T of 300 K, the voltage variation with the temperature is ≈ - 2.6 mV/°C (instead, for a typical silicon diode the voltage variation with temperature is ≈ - 2 mV/°C).

Furthermore, from the I-V characteristic in the direct region, it is also possible to observe another typical diode behavior, i.e. the effect of the parasitic series resistance R (related to the resistances presented by the neutral regions plus the contact resistances), which shows his effect at high voltages (and, then, at high current). In fact, due to the ohmic drops on the neutral regions and on the contacts, the voltage applied to the space charge region is lower than the external voltage. Thus, indicating with V_a the external voltage applied, the voltage that actually drops on the depletion region, and that has to be inserted in the formula of the current in the forward operation, i.e. $I = I_O\,[exp(V/V_T\,)-1]$, will be $V = V_a - RI$. This means that with an increase in the external voltage, the current increases, the drop on the parasitic resistance increases too, and this will reduce the voltage that actually drops on the PN junction, resulting in a current reduction, which instead of increasing (as one might think), stabilizes itself at an almost constant value.

Regarding the analysis in reverse polarization conditions, it is observed what is mentioned earlier. In particular, with regard to the dark current, from 25 °C to 400 °C, it is observed that the measured current is practically the background noise of the instrument (due to the

173

cables, the electronic devices inside the instrument, etc.), which randomly varies, varying the applied voltage. In fact, even if the reverse current is increasing due to the increase of temperature, the real reverse current value is below the instrument minimum detectable value (i.e. the resolution). In this case, if the actual current is below this limit, up to temperatures of 400 °C (as actually happens in the case of the 4H-SiC, because of its low intrinsic concentration, even at very high temperatures), the instrument will return an average current value of pA (i.e., the limit imposed by the instrument). At 500 °C, however, since the temperature increase, the dark current overcomes the instrument resolution, and this makes that the measured current is actually the device reverse current in dark condition, given that it exceeds by two orders of magnitude the minimum detectable value, i.e. it is approximately 10^{-10} A. During the measurements in dark conditions, the light in the room has been turned off, to do not to have any disturb from the light of the lamps present inside the measurement room.

At each temperature of interest, a test was also performed under UV illumination, to derive the photogenerated current value for the same temperature and voltage range. It is observed that the photogenerated current remains almost constant varying the temperature (in fact, only a slightly increase with temperature is shown), around the order of 10^{-7} A as theoretically predicted and as predicted in the simulations in the Chapter 3. Moreover, it is also observed that its value is practically constant with the reverse applied voltage (obviously in the reverse voltages range, because in the direct range the current varies with an exponential law), being the photegenerated current much higher than the instrument resolution value, the noise does not disturb the measurement in any way.

To compare the measurements obtained with *TCAD* simulations, of course, it is needed to know the actual absorbed power by the photodiode, from which, dividing by the collecting area (i.e. the base area, neglecting the reflection of the base contact, in the UV range), it allows to derive the absorbed optical power density. Unfortunately, the only available data from the measurements is the photogenerated current, while nothing is known about the actually absorbed optical power. This means that a comparison between the simulations (where it is assumed a given incident optical power) and the experimental tests, in terms of test under the UV light, cannot be done. The only thing that is possible to compare is the increase of the photogenerated current with the temperature. It is possible to calculate it for a default incident power, and it is always the same. On the other hand, one can compare the dark currents. Furthermore, to make a comparison between the simulated values and the experimental values, a particular value of reverse voltage at which to make the comparison has to be set. For this, the comparison value, fixed in the simulations, is -2.5 V (at this value the measured dark current, beyond 400 °C, is quite constant too).

Therefore, in Table 4.1 the obtained results are shown.

Temperature (°C)	I_{dark} measured (A)	I_{dark} simulated (A)	I_{ph} measured (A)
25	1×10^{-12}	7.33×10^{-33}	5.62×10^{-8}
200	1×10^{-12}	1.44×10^{-22}	1.18×10^{-7}
300	1×10^{-12}	1.89×10^{-17}	2.54×10^{-7}
400	1×10^{-12}	1.82×10^{-14}	3.43×10^{-7}
500	4.23×10^{-10}	8.42×10^{-11}	5.63×10^{-7}

Table 4.1 Comparison between the measured and simulated quantities.

In the Table 4.1 it is observed how the dark currents are very different up to 400 °C, while they tend to coincide at 500 °C, when the dark current measured value exceeds the minimum detectable value by the instrument. Furthermore, the agreement at high temperature between simulated and measured dark currents shows that the *TCAD* simulations for the dark current can be considered quite satisfactory.

Obviously, how it is shown in the reported above I-V characteristics, the measured dark current oscillates and it is not stable. This means that to do a comparison, the instrument resolution of 1 pA has to be considered up to 400 °C. Instead, any problem is present in the simulations, because the current is quite constant, both at -2.5 V, at -4 V, and also beyond, as shown in the Figure 4.14. Thus, the value at -2.5 V was considered.
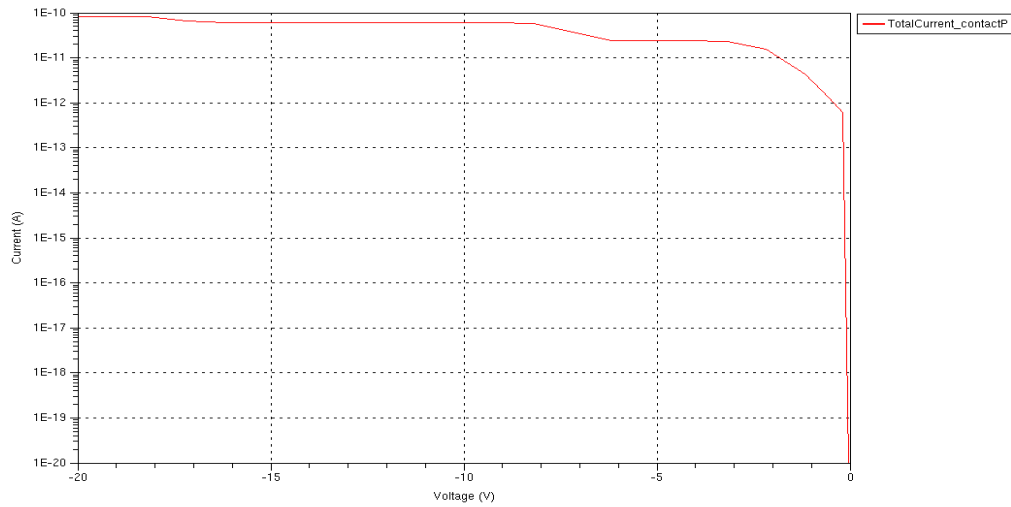
Figure 4.14. Simulated dark current at 500 °C.

Also for the I_{ph}, since it is quite constant, a reference value of -2.5 V is considered.

To better observe what has been said, in Figure 4.15 and 4.16 the measured and simulated values are shown, when the temperature varies from 25 °C to 500 °C.
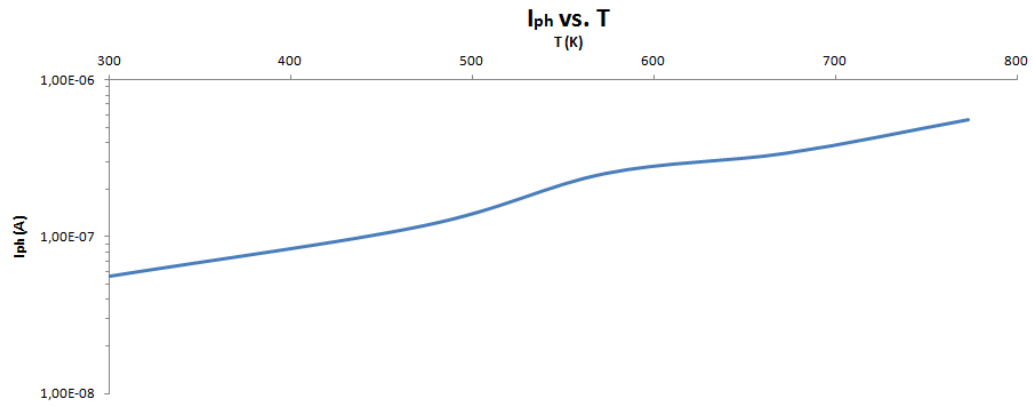
Figure 4.15. Photogenerated measured current versus temperature in log-scale.
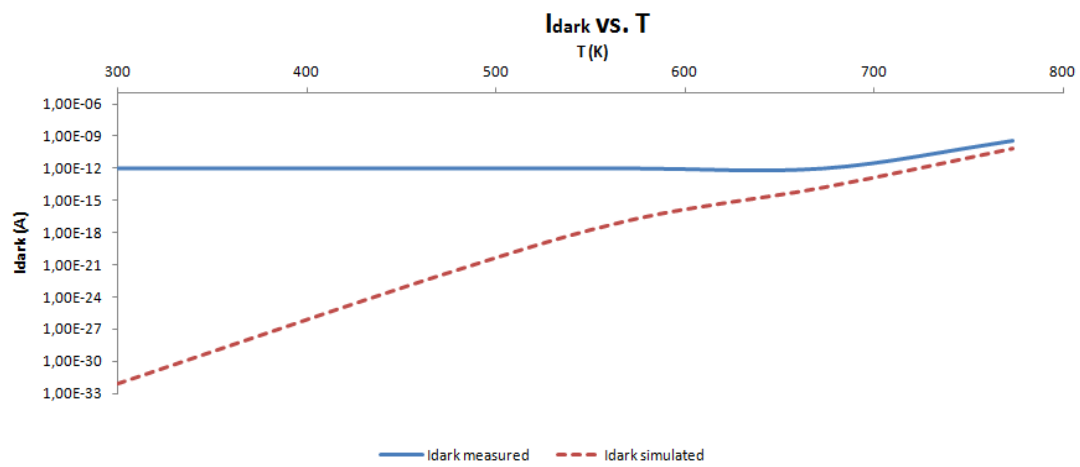
Figure 4.16. Comparison between the simulated dark current and the measured dark current versus temperature in log-scale.

Obviously, since below 500 °C the measured dark current oscillates around the minimum value measured by the instrument, it does not have much sense to make a comparison between the measured value and the simulated one, except if one considers an average value of the measured dark current, or the current limit of 1 pA. Vice versa, when the temperature exceeds 500 °C, the comparison has sense, because the measured value is beyond the minimum detectable current. In fact, the two currents tend to coincide, as shown in Figure 4.16.

Furthermore, from the Table 4.1 it is possible to see that the photogenerated current has a variation of about 0.1 μA/100 °C, i.e. it is quite constant when the temperature increases, as confirmed by simulations. Moreover, it is checked that the second term in the Eq. (2.36) does not give any problems when the temperature increases.

Also at 500 °C there is a little deviation from the actual dark current value but, in this case, this little deviation is due to the instrument itself (i.e. instrument accuracy), measurement precision (i.e. measurement table stabilization), and to device stabilization (for example, air fluctuations and vibrations as previously anticipated). In fact, even if the measured current is beyond the minimum measurable value, the instrument is characterized from a certain accuracy. Moreover, the measurement table of the probe station shown in Figure 4.1 is not very stable. Furthermore, since the possible device vibration, during the

measurement itself (due to the temperature increase), if the instrument samples in this instant, obviously, the measured voltage is different from the actual value.

One last thing has to be noticed, regarding the reason why the tests were not performed up to 600 °C. In fact, even if the probe station allows to perform tests up to 600 °C, in this case the tests were stopped at a temperature of 500 °C, for security reasons, and in particular to avoid a possible destruction of the wafer. Given that the realized measurement is a measure that takes a long time (because it has to do both a dark condition measurement and an UV light measurement, for different voltages), if it works at very high temperatures for a long time, this could cause an overheating both of the device and of the chuck, causing the wafer destruction. In fact only one device was tested at 600 °C and an increase of the reverse current up to 0.1 A, at -1 V, was observed. After all, the temperature of interest is 460 °C. Thus stop the analysis at 500 °C is more than sufficient.

Chapter 5

Conclusions and future works

The first deep analysis, both simulative and experimental, at KTH, of the 4H-SiC performance in UV light absorption has been completed.

If the initial purpose of this work was "the possibility to create an UV image sensor in 4H-SiC" that can withstand high temperatures, such as that of Venus, after this deep investigation, both theoretical, simulative and experimental, the answer is positive. Obviously, there are still some things to investigate more in depth, such as the ability of the 4H-SiC MOSFETs to work well at high temperature above 300-350 °C for the sensor operation. Furthermore, also all the downstream electronics required to convert and reading the output signal generated by the single pixel has to be investigated (buffer, A/D converters, control unit, etc.).

Moreover, this analysis should be completed with other extreme conditions tests, such as high pressure test, radioactive bombardment test, etc., to check that this sensor is able to withstand in harsh environments. Also the investigation of a suitable lens to focus the UV light on the sensor is of big interest (and of all the optics that precedes the sensor itself).

Furthermore, during the course of this work, not only the ability of 4H-SiC photodiodes to absorb well the UV light was presented, in a wide temperature range, but it was also analyzed the ability of the 4H-SiC bipolar transistors to work well under UV light (properly optimizing the layout). This, obviously, lays the foundation to realize other optoelectronic components in 4H-SiC, that can work at high temperatures, such as LEDs, optocouplers (for power control systems applications), photomultipliers, solar cells, etc.

A LED works in the opposite way of a photodiode, because it will produce photons through the spontaneous emission phenomenon, i.e. from the recombination of electron-hole pairs, also if these devices are typically realized with direct bandgap semiconductors, otherwise the optical emission is very inefficient (in fact, nowadays, this market is dominated by direct bandgap materials, i.e. GaN). Hence, a deep investigation to improve the optical emission can be interesting.

The optocouplers is an electronic component that allows to transfer a signal between two circuits maintaining the galvanic isolation between the same. Normally it realizes an optically coupling with a LED and a photosensitive element, such as a floating base phototransistor, which detects the brightness variations related to the input signal produced by the LED, resulting in the transfer of information from one circuit to another without electrical continuity between them. The only problem can be the LED behavior if realized in 4H-SiC.

The photomultiplier is an extremely sensitive electronic detector for ultraviolet light. It is so sensitive to be able to detect a single photon, and its operation is mainly based on the photoelectric effect and on the secondary emission.

A solar cell works with the same basic operation principle of a photodetector, with the difference that, now, the fourth quadrant of the I-V characteristic is used. In fact, the I_{ph} is the same of the photodetector analyzed before, and the ON voltage is very high, around 2-2.5 V, respect to a silicon device, that is about 0.7 V, when the UV light is absorbed. This means that the maximum output power is very high compared to the one of a silicon cell, if they are compared in an UV operation at high temperature.

Furthermore, through the use of appropriate *texturization* techniques using *KOH* etching, i.e. *potassium hydroxide etching* (currently used especially in photovoltaic applications for silicon cells), properly optimized for the SiC. An attack of the surface directly exposed to the light is possible to appropriately choose the geometry of the damaged surfaces (i.e. trapezoidal, triangular, etc.) and to improve, due to successive reflections, the absorption of the incident photons (up to 99.9%). This permits a greater optic generation which, in principle, will also mean a greater photogenerated current, fixing an incident power. Obviously, this can be confirmed both with simulations and with experimental measurements.

Moreover, in the carried out analysis no thermal problems were considered for the device in question, thanks to the high thermal capacity of the silicon carbide, that has already been demonstrated by many circuits (analogical and digital), reported in the literature, able to withstand without any problem at high temperatures. In any case, for an accurate analysis of the device itself, it would be interesting to make an accurate electro-thermal analysis, if it is possible.

Finally, another issue that has been overlooked is the noise analysis in the device (as well as the intrinsic noise source during the operation of the device itself, i.e. the dark current), because it is difficult to model, both with TCAD and PSpice. In fact the noise is a random quantity, since, in principle, one should also distinguish the noise from the external disturbs. In fact, noise usually refers to random source signals coming from the inside of the device or the circuit, and which are described in probabilistic terms, while the disturbs are signals coming from the outside, and that can be described in deterministic terms, i.e. like interference. Thus, here is why it is extremely complicated to take into account this type of analysis.

Typically, regarding the internal noise sources, the three main noise sources that are taken in consideration, from a theoretical point of view, are the *Johnson noise* or *thermal noise* (that arises from the random motion of the carriers with an average energy $k_B T$, and that proportionally depends on the temperature in question), the *generation-recombination noise* or *shot noise* (due to fluctuations in the generation-recombination processes, which causes a fluctuation of the carrier concentration, and therefore fluctuations in the conductivity of the semiconductor) and the *Flicker noise* (due to surface and interface defects and traps in the bulk of the semiconductor which are activated, or not, depending on the temperature value). These three noise sources, in all cases, give rise to a noise current that is superimposed on the dark current. These three noise sources act depending on the value of the working switching frequency of the photodetector. In particular, it can be observed that if the working frequencies are very low (< 1 kHz), Flicker noise is the dominant contribution, at medium frequencies the generation-recombination noise dominates, while at high-frequency Johnson noise dominates. If the switching time of the

order of tens of ms are considered, the generation-recombination noise and the Johnson noise are the two fundamental noise contributions. In particular, regarding the generation-recombination noise, the probability of the thermal generation of electron-hole pairs is proportional to $exp(-E_g/2k_BT)$, which means that even if the temperature increases, the high 4H-SiC bandgap will ensure that this noise contribution is negligible compared to the Johnson noise (and it is lower to the one of a silicon device reasoning with the same temperature). The power spectral density of the Johnson noise is constant with frequency and equal to $2\,R_C\,k_B\,T$, being R_C the resistance of the photoconducting channel [9]. Thus, to make a correct simulation of the device, taking into account the various noise contributions, the circuit in Figure 2.34 should be modified by adding two current generators in parallel to the I_{ph} current generator, that represent the Flicker noise and the generation-recombination noise, and a conductance, that represents the Johnson noise [9]. In the future, this analysis could be performed to estimate even better the performances of the circuit at the variation of the considered temperature and wavelength (or frequency).

Appendix

ISE-TCAD parameters and codes

A.1   SiC material properties for ISE-TCAD simulations

Material = "SiliconCarbide"
{
* 4H-SiC model for ISE
* isotropic version (c-axis)
* created by Erik Danielsson 001016
*
* based on
* [1] Ulf Lindefelt, "Physical Models for 4H-SiC - version 4:9601/4H"
* [2] Band offsets and electronic structure of SiC/SiO2 interfaces
* [3] Silicon Carbide conference 97 - Theory I session

Epsilon
{ * Ratio of the permittivities of material and vacuum

  * epsilon() = epsilon
    epsilon = 9.98 # [1]
}

RefractiveIndex
{ * Optical Refractive Index

  * refractiveindex() = refractiveindex
    refractiveindex   = 2.74092 # [1]
}

ComplexRefractiveIndex
{
    Formula = 3 * Read data from TableODB
}

Kappa
{ * Lattice thermal conductivity
    Formula = 0

```
  * Formula = 0:
  * kappa() = 1/(1/kappa + 1/kappa_b * T + 1/kappa_c * T^2)
  * Fitted data from [1]
    1/kappa = -1.3482e-02          # [W/(K cm)]
    1/kappa_b = 4.1268e-04         # [W/(K^2 cm)]
    1/kappa_c = 8.3063e-07         # [W/(K^3 cm)]


  * Formula = 1:
  * kappa() = kappa + kappa_b * T + kappa_c * T^2
    kappa    = 4.55                # [W/(K cm)]
    kappa_b= 0.0000e+00            # [W/(K^2 cm)]
    kappa_c= 0.0000e+00            # [W/(K^3 cm)]
}



LatticeHeatCapacity
{ * Lattice Heat Capacity
  * c()  = cv + cv_b * T + cv_c * T^2 + cv_d * T^3
    cv   = -9.2188e+02      # []
    cv_b = 1.1581e+01       # []
    cv_c = -1.6773e-02      # []
    cv_d = 1.1162e-05       # []
}


 Ionization
{
      E_As_0         = 0.1                # [eV]
      alpha_As       = 3.1000e-08         # [eV cm]
      g_As           = 2                  # [1]
      Xsec_As        = 1.0000e-12         # [cm^2/sec]


      E_P_0          = 0.065              # [eV]
      alpha_P        = 3.1000e-08         # [eV cm]
      g_P            = 2                  # [1]
      Xsec_P         = 1.0000e-12         # [cm^2/sec]


      E_Sb_0         = 0.1                # [eV]
      alpha_Sb       = 3.1000e-08         # [eV cm]
      g_Sb           = 2                  # [1]
      Xsec_Sb        = 1.0000e-12         # [cm^2/sec]


      E_B_0          = 0.191              # [eV]
      alpha_B        = 3.1000e-08         # [eV cm]
      g_B            = 4                  # [1]
```

```
        Xsec_B          = 1.0000e-12          # [cm^2/sec]


*       E_Al_0          = 0.191               # [eV]
*       alpha_Al        = 3.1000e-08          # [eV cm]
*       g_Al            = 4                   # [1]
*       Xsec_Al         = 1.0000e-12          # [cm^2/sec]


        E_In_0          = 0.2                 # [eV]
        alpha_In        = 3.1000e-08          # [eV cm]
        g_In            = 4                   # [1]
        Xsec_In         = 1.0000e-12          # [cm^2/sec]


        E_N_0           = 0.065               # [eV]
        alpha_N         = 3.1000e-08          # [eV cm]
        g_N             = 2                   # [1]
        Xsec_N          = 1.0000e-12          # [cm^2/sec]


        E_NDopant_0        = 0.1              # [eV]
        alpha_NDopant      = 3.1000e-08       # [eV cm]
        g_NDopant          = 2               # [1]
        Xsec_NDopant       = 1.0000e-12       # [cm^2/sec]


        E_PDopant_0        = 0.191            # [eV] (Al)
        alpha_PDopant      = 3.1000e-08       # [eV cm]
        g_PDopant          = 4               # [1]
        Xsec_PDopant       = 1.0000e-12       # [cm^2/sec]


        NdCrit             = 1.0000e+22       # [cm-3]
        NaCrit             = 1.0000e+22       # [cm-3]
}


Bandgap
{ * Eg = Eg0 + dEg0 + alpha Tpar^2 / (beta + Tpar) - alpha T^2 / (beta + T)
  * dEg0(<bgn_model_name>) is a band gap correction term.  It is used together with
  * an appropriate BGN model, if this BGN model is chosen in Physics section
  * Parameter 'Tpar' specifies the value of lattice
  * temperature, at which parameters below are defined
  * Chi0 is electron affinity.
    Chi0      = 3.91        # [eV]
    Bgn2Chi  = 0.5          # [1]
    Eg0       = 3.19        # [eV]
    dEg0(Bennett)           = 0.0000e+00         # [eV]
    dEg0(Slotboom)          = 0.0000e+00         # [eV]
    dEg0(OldSlotboom)       = 0.0000e+00         # [eV]
```

```
    dEg0(delAlamo)          = 0.0000e+00          # [eV]
   alpha                    = 3.3000e-04          # [eV K^-1]
     beta                   = 0.0000e+00          # [K]
     Tpar                   = 300                 # [K]
}


OldSlotboom
{ * deltaEg = dEg0 + Ebgn ( ln(N/Nref) + [ (ln(N/Nref))^2 + 0.5]^1/2 )
  * dEg0 is defined in BandGap section
    Ebgn = 9.0000e-03       # [eV]
    Nref = 1.0000e+17       # [cm^-3]
}



Slotboom
{ * deltaEg = dEg0 + Ebgn ( ln(N/Nref) + [ (ln(N/Nref))^2 + 0.5]^1/2 )
  * dEg0 is defined in BandGap section
    Ebgn = 6.9200e-03       # [eV]
    Nref = 1.3000e+17       # [cm^-3]
}


delAlamo
{ * deltaEg = dEg0 + Ebgn  ln(N/Nref)
  * dEg0 is defined in BandGap section
    Ebgn = 0.0187   # [eV]
    Nref  = 7.0000e+17      # [cm^-3]
}


Bennett
{ * deltaEg = dEg0 + Ebgn (ln(N/Nref))^2
  * dEg0 is defined in BandGap section
    Ebgn = 6.8400e-03       # [eV]
    Nref = 3.1620e+18       # [cm^-3]
}


bgnLindefelt
{ * Lindefelt bandgap narrowing model from
  * J. Appl. Phys. Vol 84, no 5, (1998), p. 2628
  * Searchpath: ~erikd/ise/lib
      Ebgn = 0              # [eV]
      Nref = 1e18           # [cm^-3]
      Apc = -1.57e-2        #
      Bpc = -3.87e-4        #
      Apv = 1.30e-2         #
```

```
        Bpv = 1.15e-3          #
        Anc = -1.50e-2         #
        Bnc = -2.93e-3         #
        Anv = 1.90e-2          #
        Bnv = 8.74e-3          #
}


eDOSMass
{
 * For effective mass specificatition Formula1 (me approximation):
 * or Formula2 (Nc300) can be used :
      Formula = 1    # [1]
 * Formula1:
 * me/m0 = [ (6 * mt)^2 *  ml ]^(1/3) + mm
 * mt = a[Eg(0)/Eg(T)]
 * Nc(T) = 2(2pi*kB/h_Planck^2*me*T)^3/2 = 2.540e19 ((me/m0)*(T/300))^3/2
 * Nc(300) = 1.66e19
      a        = 0.1494        # [1]
      ml       = 0.5           # [1]
      mm       = 0.0000e+00# [1]
}


hDOSMass
{
 * For effective mass specificatition Formula1 (mh approximation):
 * or Formula2 (Nv300) can be used :
      Formula = 1    # [1]
 * Formula1:
 * mh =  m0*{[(a+bT+cT^2+dT^3+eT^4)/(1+fT+gT^2+hT^3+iT^4)]^(2/3) + mm}
 * Nv(T) = 2(2pi*kB/h_Planck^2*mh*T)^3/2 = 2.540e19 ((mh/m0)*(T/300))^3/2
 * Nv(300) = 3.30e19
      a        = 1.19          # [1]
      b        = 0             # [K^-1]
      c        = 0             # [K^-2]
      d         = 0            # [K^-3]
      e        = 0             # [K^-4]
      f         = 0            # [K^-1]
      g        = 0             # [K^-2]
      h         = 0            # [K^-3]
      i        = 0             # [K^-4]
      mm       = 0             # [1]
}
```

ConstantMobility:
{ * mu_const = mumax (T/T0)^(-Exponent)
   mumax   = 900 ,   1000   # [cm^2/(Vs)]
   Exponent = 3 ,3   # [1]
}

DopingDependence:
{
 * For doping dependent mobility model three formulas
 * can be used. Formula1 is based on Masetti et al. approximation.
 * Formula2 uses approximation, suggested by Arora.
     formula   = 2 ,   2   # [1]
 * If formula=1, model suggested by Masetti et al. is used:
 * mu_dop = mumin1 exp(-Pc/N) + (mu_const - mumin2)/(1+(N/Cr)^alpha)
 *   - mu1/(1+(Cs/N)^beta)
 * with mu_const from ConstantMobility
 * If formula=2, model suggested by Masetti et al. is used:
 * mu_dop = Ar_mumin (T/T0)^Ar_alm + Ar_mud*(T/T0)^Ar_ald /
 *   (1 + (Ni/(Ar_N0*(T/T0)^Ar_alN))^(Ar_a*(T/T0)^Ar_ala))
 *
 * Formula = 1
   mumin1   = 20 , 5   # [cm^2/Vs]
   mumin2   = 0.0000e+00 , 0.0000e+00   # [cm^2/Vs]
   mu1   = 0.0000e+00 , 0.0000e+00   # [cm^2/Vs]
   Pc   = 0.0000e+00 , 0.0000e+00   # [cm^3]
   Cr   = 4.5000e+17 , 1.0000e+19   # [cm^3]
   Cs   = 3.4300e+20 , 6.1000e+20   # [cm^3]
   alpha   = 0.45 , 0.5   # [1]
   beta   = 2 , 2   # [1]

 * Formula   = 2
   Ar_mumin = 0 , 15.9   # [cm^2/Vs]
   Ar_alm   = 0 , 0   # [1]
   Ar_mud   = 1141 , 108.1   # [cm^2/Vs]
   Ar_ald   = -2.15 , -2.15   # [1]
   Ar_N0   = 1.94e+17 , 1.76e+19   # [cm^3]
   Ar_alN   = 0 , 0   # [1]
   Ar_a   = 0.61 , 0.34   # [1]
   Ar_ala   = 0 , 0   # [1]
}

HighFieldDependence:
{ * Caughey-Thomas model:
 * mu_highfield = mu_lowfield / (1 + (mu_lowfield E / vsat)^beta)^1/beta

* beta   = beta0 (T/T0)^betaexp.
       beta0   = 2 , 2   # [1]
       betaexp   = 0.0000e+00 , 0.0000e+00   # [1]

     * Smoothing parameter for HydroHighField Caughey-Thomas model:
     * if Tl < Tc < (1+K_dT)*Tl, then smoothing between low field mobility
     * and HydroHighField mobility is used.
         K_dT = 0.2 , 0.2   # [1]
      * Transferred-Electron Effect:
      * mu_highfield = (mu_lowfield+(vsat/E)*(E/E0_TrEf)^4)/(1+(E/E0_TrEf)^4)
          E0_TrEf = 4.0000e+03 , 4.0000e+03   # [1]
          Ksmooth_TrEf = 1 , 1   # [1]

     * For vsat either Formula1 or Formula2 can be used.
         Vsat_Formula = 1 , 1 # [1]
     * Formula1 for saturation velocity:
     *   vsat = vsat0 (T/T0)^(-Vsatexp)
     * (Parameter Vsat_Formula has to be not equal to 2):
         vsat0 = 2.5000e+07 , 2.5000e+07   # [1]
         vsatexp = 0.5 ,0.5   # [1]
     }

vanOverstraetendeMan * Impact Ionization:
{ * G_impact = alpha_n n v_drift_n + alpha_p p v_drift_p
  * with alpha = gamma a exp(-b gamma/E) for E<E0 (low) and E>E0 (high)
  * with gamma = tanh(hbarOmega/(2kT0)) / tanh(hbarOmega/(2kT))
  * Values below fitted to data from [1]
       a(low)   = 3.1260e+07 , 5.79000e+06   # [1/cm]
       a(high) = 3.1260e+07 , 5.79000e+06   # [1/cm]
       b(low)   = 2.750e+07 , 1.9000e+07   # [V/cm]
       b(high) = 2.750e+07 , 1.9000e+07   # [V/cm]
       E0 = 4.0000e+05 , 4.0000e+05   # [eV]
}

Scharfetter
{ * SRH recombination parameters (mostly silicon values)
  * R = (n*p - ni^2)/(tau_n*(p + p1) + tau_p*(n + n1))
  * p1/n1 = ni*exp(-/+Etrap/(k*T))
  * and tau_n,p is given by the expression below
  * tau_SRH = tau_dop(Ni) * f(T) / (1 + g_c(F)), c=n,p
  * g_c(F) is a field dependent term defined elsewere
  * tau_dop(Ni) = taumin + (taumax - taumin) / (1 + (Ni/Nref)^gamma)
  * f(T) = (T/300)^Talpha for TempDependence
  * f(T) = exp(Tcoeff*(T/300 - 1)) for ExpTempDependence

```
        taumin = 0 , 0                # [s]
        taumax= 1e-7 , 1e-7           # [s]
        Nref    = 1e+16 , 1e+16       # [cm^-3]
        gamma = 1, 1                  # [1]
        Talpha = -1.5  , -1.5         # [1]
        Tcoeff = 2.55  , 2.55         # [1]
        Etrap   = 0                   # [eV]
}


Auger * coefficients:
{ * R_Auger = ( C_n n + C_p p ) ( n p - ni_eff^2 )
 * with C_n,p = ( A + B (T/T0) + C (T/T0)^2 ) ( 1 + H exp(-{n,p}/N0 ) )
        A = 5e-31 , 2e-31       # [cm^6/s]
        B = 0 , 0               # [cm^6/s]
        C = 0 , 0               # [cm^6/s]
        H = 0 , 0               # [cm^6/s]
        N0 = 1e+18 , 1e+18    #[cm^(-3)]
}


TableODB
{ * Each entry of the table consists of three values:
 *complex refractive index n + i*k (unitless)
 *refractive index = n,  absorption coefficient = 4*pi*k/wavelength
 *WAVELEN(um) n                        k
0.10551932        0.557485774          1.211573517  ;
0.10574431        0.561747188          1.218412863  ;
0.10597026        0.55615434           1.230072213  ;
0.10619717        0.550679005          1.241703413  ;
0.10642506        0.567604311          1.245268908  ;
0.10665394        0.563496218          1.247656999  ;
0.10688379        0.573076419          1.263382991  ;
0.10711464        0.570735921          1.265033395  ;
0.10734649        0.578729948          1.282126496  ;
0.10757935        0.584943695          1.299176326  ;
0.10781322        0.584462911          1.301305842  ;
0.1080481         0.597170657          1.304903366  ;
0.10828402        0.591966614          1.315851235  ;
0.10852096        0.58685748           1.326778693  ;
0.10875895        0.596014952          1.341258298  ;
0.10899798        0.605739468          1.3487069    ;
0.10923806        0.601959603          1.362433618  ;
0.10947921        0.595864552          1.370034512  ;
0.10972142        0.608103384          1.384517867  ;
0.1099647         0.609582086          1.401706217  ;
```

0.11020907	0.614417049	1.407220065 ;
0.11045452	0.627719678	1.422442264 ;
0.11070107	0.623040664	1.432651273 ;
0.11094872	0.629665052	1.44790472 ;
0.11119749	0.627438981	1.453217009 ;
0.11144737	0.625130254	1.457936156 ;
0.11169838	0.634287203	1.476279193 ;
0.11195052	0.638288144	1.487784176 ;
0.1122038	0.641612178	1.499652022 ;
0.11245823	0.640421048	1.512262913 ;
0.11271382	0.649580799	1.523451743 ;
0.11297057	0.653302537	1.541085398 ;
0.11322849	0.663913727	1.545743005 ;
0.1134876	0.659676573	1.555246984 ;
0.11374789	0.667797138	1.571337971 ;
0.11400938	0.672231248	1.583301882 ;
0.11427207	0.678202741	1.595120359 ;
0.11453598	0.684575003	1.610882657 ;
0.11480111	0.689563628	1.618835383 ;
0.11506747	0.700762963	1.628910289 ;
0.11533507	0.701826152	1.6422728 ;
0.11560392	0.712657695	1.655738805 ;
0.11587402	0.718542106	1.668997531 ;
0.11614539	0.724382339	1.682150342 ;
0.11641803	0.728790638	1.68805681 ;
0.11669195	0.739833124	1.699450809 ;
0.11696717	0.74365365	1.711636863 ;
0.11724369	0.751169222	1.725197148 ;
0.11752152	0.759633683	1.736883224 ;
0.11780067	0.762357039	1.750570837 ;
0.11808114	0.776688691	1.764201044 ;
0.11836296	0.791751388	1.783880674 ;
0.11864612	0.794786593	1.793946969 ;
0.11893065	0.811408316	1.812546125 ;
0.11921654	0.814086191	1.826796739 ;
0.11950381	0.821839952	1.836720149 ;
0.11979246	0.832148996	1.860664385 ;
0.12008252	0.845946486	1.876466215 ;
0.12037398	0.857712099	1.904660086 ;
0.12066686	0.87438854	1.926980882 ;
0.12096117	0.882168819	1.949105391 ;
0.12125692	0.893805431	1.972437109 ;
0.12155412	0.907812142	1.99527514 ;
0.12185278	0.9209342	2.020611244 ;

0.12215291	0.934124715	2.041670635	;
0.12245452	0.93949236	2.064050846	;
0.12275762	0.956467771	2.089040593	;
0.12306223	0.976441532	2.106767207	;
0.12336836	0.986749402	2.129709929	;
0.12367601	1.001605656	2.152004621	;
0.1239852	1.012583835	2.169805526	;
0.12429594	1.018822217	2.192865411	;
0.12460824	1.03809236	2.206908641	;
0.12492212	1.056538357	2.226639463	;
0.12523758	1.063188608	2.240745415	;
0.12555463	1.079087323	2.25318651	;
0.1258733	1.087144193	2.272789585	;
0.12619359	1.098196736	2.285838155	;
0.12651551	1.111571822	2.297773252	;
0.12683908	1.120046588	2.311729733	;
0.12716431	1.134530094	2.320661228	;
0.12749121	1.147620155	2.324906884	;
0.12781979	1.156875751	2.340350722	;
0.12815008	1.168759728	2.350423218	;
0.12848207	1.179142077	2.357854117	;
0.12881579	1.195628541	2.363543443	;
0.12915125	1.199244715	2.372810124	;
0.12948846	1.20949164	2.385365806	;
0.12982743	1.226056478	2.390530169	;
0.13016819	1.242317405	2.401733235	;
0.13051074	1.251870261	2.407274216	;
0.13085509	1.265197318	2.420661945	;
0.13120127	1.279431901	2.424439314	;
0.13154928	1.290786522	2.433690581	;
0.13189915	1.308603275	2.441870703	;
0.13225088	1.328674844	2.453403114	;
0.13260449	1.34114204	2.459933327	;
0.13296	1.353541778	2.466466166	;
0.13331742	1.372443427	2.477613965	;
0.13367677	1.390385929	2.486212588	;
0.13403805	1.409195552	2.497563233	;
0.1344013	1.426634763	2.505960245	;
0.13476652	1.447573356	2.510422001	;
0.13513373	1.462449946	2.51159707	;
0.13550295	1.48317279	2.516203793	;
0.13587419	1.497908565	2.517496787	;
0.13624747	1.512595759	2.518842181	;
0.13662281	1.527222827	2.520237998	;

0.13700022	1.541801896	2.521682591	;
0.13737972	1.562053363	2.526600623	;
0.13776133	1.579612319	2.522989314	;
0.13814507	1.594004687	2.524613028	;
0.13853095	1.608341457	2.526276359	;
0.13891899	1.619484482	2.533065334	;
0.13930921	1.639272014	2.538257815	;
0.13970163	1.650270363	2.545046615	;
0.14009627	1.666710604	2.555281636	;
0.14049314	1.683034912	2.565493425	;
0.14089227	1.702954564	2.569965807	;
0.14129368	1.716185633	2.572647105	;
0.14169737	1.733100572	2.569697957	;
0.14210338	1.74682692	2.571671497	;
0.14251172	1.757743978	2.566525646	;
0.14292242	1.775188097	2.562649562	;
0.14333549	1.783534751	2.561250907	;
0.14375096	1.786613948	2.556346885	;
0.14416884	1.791754231	2.559742804	;
0.14458915	1.788448431	2.564370837	;
0.14501193	1.793576929	2.567751584	;
0.14543718	1.792354031	2.580609031	;
0.14586494	1.792706424	2.585967193	;
0.14629522	1.791049633	2.593294967	;
0.14672805	1.795110389	2.609513615	;
0.14716344	1.788780056	2.618821126	;
0.14760143	1.794466908	2.641427925	;
0.14804203	1.793977048	2.655619259	;
0.14848527	1.808428331	2.678184652	;
0.14893117	1.809569692	2.698605653	;
0.14937976	1.819476465	2.722698038	;
0.14983106	1.825105764	2.740961702	;
0.15028509	1.849382716	2.769237518	;
0.15074188	1.858462971	2.787709564	;
0.15120146	1.883005017	2.811253794	;
0.15166385	1.899003445	2.832356631	;
0.15212908	1.917574176	2.856617006	;
0.15259717	1.938771553	2.876311029	;
0.15306815	1.968493855	2.913674323	;
0.15354204	1.99195384	2.928724995	;
0.15401888	2.023686093	2.96121519	;
0.15449869	2.05310425	2.986219526	;
0.1549815	2.073825801	3.002139812	;
0.15546734	2.109074355	3.028639073	;

0.15595623	2.126800879	3.040279918 ;
0.1564482	2.157681916	3.060706006 ;
0.15694329	2.181628636	3.073316369 ;
0.15744152	2.21240362	3.091522243 ;
0.15794293	2.238064329	3.108824849 ;
0.15844754	2.278839064	3.130892441 ;
0.15895538	2.303905907	3.148047399 ;
0.1594665	2.337056014	3.170867517 ;
0.1599809	2.368307627	3.186984627 ;
0.16049864	2.404791217	3.21244312 ;
0.16101974	2.455349132	3.233988151 ;
0.16154423	2.515328296	3.258324176 ;
0.16207216	2.582106735	3.263898771 ;
0.16260354	2.631470276	3.28441103 ;
0.16313842	2.702682907	3.306064865 ;
0.16367683	2.750811057	3.31117071 ;
0.16421881	2.831779373	3.311131894 ;
0.16476439	2.88904468	3.304301615 ;
0.1653136	2.95215137	3.287390714 ;
0.16586649	2.995715005	3.265764595 ;
0.16642309	3.053688986	3.225015725 ;
0.16698343	3.095340643	3.197357299 ;
0.16754757	3.143320496	3.16539946 ;
0.16811553	3.17042997	3.146505394 ;
0.16868735	3.203353147	3.117197681 ;
0.16926307	3.233734885	3.091142395 ;
0.16984274	3.247235305	3.076664936 ;
0.17042639	3.269157107	3.053689276 ;
0.17101407	3.276865226	3.039143911 ;
0.17160581	3.293691225	3.027996348 ;
0.17220167	3.300861134	3.022062909 ;
0.17280167	3.316395157	3.023097226 ;
0.17340587	3.32223868	3.029237502 ;
0.17401432	3.335410983	3.064998602 ;
0.17462704	3.348619708	3.100450605 ;
0.1752441	3.384286613	3.173688056 ;
0.17586553	3.445779557	3.254746804 ;
0.17649139	3.52874911	3.340015012 ;
0.17712171	3.683641851	3.424828067 ;
0.17775656	3.878627313	3.46497328 ;
0.17839597	4.068724652	3.426774036 ;
0.17904	4.250630113	3.349529275 ;
0.1796887	4.43119556	3.193957434 ;
0.18034211	4.534810341	3.061911956 ;

0.18100029	4.641900923	2.857625619 ;
0.1816633	4.689007828	2.720300427 ;
0.18233118	4.712287476	2.56583773 ;
0.18300399	4.716370324	2.466126322 ;
0.18368178	4.708302067	2.34295078 ;
0.18436461	4.701411149	2.257493476 ;
0.18505254	4.687604002	2.149279247 ;
0.18574562	4.675820329	2.084316615 ;
0.18644391	4.665229177	2.004805047 ;
0.18714747	4.645901352	1.91240931 ;
0.18785636	4.639657278	1.860198821 ;
0.18857065	4.624168848	1.778172526 ;
0.18929038	4.611155288	1.724547213 ;
0.19001563	4.597212665	1.658328765 ;
0.19074646	4.583680422	1.61062603 ;
0.19148293	4.565723587	1.547960551 ;
0.19222512	4.549563594	1.498949264 ;
0.19297307	4.524633556	1.43584777 ;
0.19372688	4.508483887	1.396218808 ;
0.19448659	4.486830025	1.346827262 ;
0.19525228	4.47146298	1.304921907 ;
0.19602403	4.449342068	1.265118508 ;
0.1968019	4.428312554	1.215862687 ;
0.19758598	4.406635251	1.175169876 ;
0.19837632	4.38643165	1.138038934 ;
0.19917301	4.371288678	1.103428612 ;
0.19997613	4.350328853	1.065645876 ;
0.20078575	4.335402486	1.039670484 ;
0.20160195	4.312151282	1.0022967 ;
0.20242482	4.296292737	0.975854128 ;
0.20325443	4.271245886	0.946309369 ;
0.20409086	4.253458467	0.925439858 ;
0.20493421	4.233978511	0.899340889 ;
0.20578456	4.216763665	0.881479328 ;
0.206642	4.19652091	0.852236907 ;
0.20750661	4.18296295	0.831474015 ;
0.20837849	4.171498878	0.802566439 ;
0.20925772	4.161220961	0.777817384 ;
0.21014441	4.140832403	0.743628261 ;
0.21103864	4.120225895	0.709564251 ;
0.21194051	4.111305391	0.688652321 ;
0.21285013	4.089474146	0.665754301 ;
0.21376759	4.077582601	0.649869116 ;
0.21469299	4.059839903	0.625747581 ;

0.21562643	4.044824325	0.614934 ;
0.21656803	4.027135026	0.5904545 ;
0.21751789	4.015861698	0.580176852 ;
0.21847612	4.004444621	0.56218033 ;
0.21944283	3.991876548	0.541043786 ;
0.22041813	3.979380463	0.519768094 ;
0.22140214	3.96816088	0.489857911 ;
0.22239498	3.952342603	0.462852081 ;
0.22339676	3.940145462	0.441096659 ;
0.2244076	3.926637164	0.409816322 ;
0.22542764	3.906574916	0.38123165 ;
0.22645699	3.89354163	0.361948101 ;
0.22749578	3.863816214	0.336980314 ;
0.22854415	3.848906106	0.324450627 ;
0.23174804	3.771193444	0.311881376 ;
0.23283606	3.751473726	0.298906532 ;
0.23393434	3.722840936	0.288105245 ;
0.23504303	3.703252103	0.277481784 ;
0.23616229	3.679274856	0.26946886 ;
0.23729225	3.655260765	0.262280877 ;
0.23843308	3.630941199	0.257262497 ;
0.23958493	3.607521349	0.254401821 ;
0.24074796	3.59304616	0.251854543 ;
0.24192234	3.573756628	0.249191563 ;
0.24310824	3.561274827	0.245068141 ;
0.24430581	3.544139213	0.240567582 ;
0.24551525	3.534008168	0.235719602 ;
0.24673672	3.51433972	0.232171635 ;
0.2479704	3.504513566	0.227893254 ;
0.24921648	3.491225521	0.223798204 ;
0.25047515	3.477829537	0.220200557 ;
0.2517466	3.47082622	0.215579794 ;
0.25303102	3.457766935	0.210385782 ;
0.25432862	3.449993709	0.203559792 ;
0.25563959	3.433021766	0.198213133 ;
0.25696415	3.425823409	0.191875039 ;
0.2583025	3.413541582	0.185434976 ;
0.25965487	3.398113363	0.178953712 ;
0.26102147	3.384353519	0.174352353 ;
0.26240254	3.370704683	0.171726702 ;
0.2637983	3.357040725	0.169506433 ;
0.26520898	3.346637402	0.166408826 ;
0.26663484	3.332897196	0.164358505 ;
0.26807611	3.319179654	0.163320476 ;

0.26953304	3.312195623	0.16161636	;
0.2710059	3.30171742	0.159147478	;
0.27249495	3.291252333	0.157263846	;
0.27400044	3.280801847	0.155983209	;
0.27552267	3.273740392	0.154195183	;
0.2770619	3.263159793	0.151828299	;
0.27861843	3.256004265	0.149210493	;
0.28019254	3.248859566	0.146896162	;
0.28178455	3.241694622	0.144478446	;
0.28339474	3.23446307	0.141284655	;
0.28502345	3.227190902	0.137663068	;
0.28667098	3.219899341	0.133872197	;
0.28833767	3.216049337	0.129589119	;
0.29002386	3.205226804	0.125374903	;
0.29172988	3.194390738	0.121910571	;
0.29345609	3.183588221	0.11947368	;
0.29520286	3.175703228	0.11705124	;
0.29697054	3.168984441	0.113940288	;
0.29875952	3.158134744	0.111960074	;
0.30057018	3.147312532	0.111023293	;
0.30240293	3.142573158	0.109526488	;
0.30425816	3.136262132	0.107098828	;
0.3061363	3.125319028	0.10530445	;
0.30803776	3.117999663	0.10412445	;
0.309963	3.112852529	0.101837462	;
0.31191245	3.108805583	0.098397919	;
0.31388658	3.092341547	0.096727672	;
0.31588586	3.086827991	0.096265487	;
0.31791077	3.08131405	0.095949324	;
0.31996181	3.075697216	0.093879527	;
0.32203948	3.070048686	0.09131777	;
0.32414431	3.064407005	0.088996011	;
0.32627684	3.053014433	0.087390678	;
0.32843762	3.042098449	0.086272685	;
0.3306272	3.036498722	0.08575831	;
0.33284617	3.030909808	0.08569869	;
0.33509514	3.026553038	0.085400783	;
0.33737469	3.01411997	0.085960414	;
0.33968548	3.008514217	0.086416411	;
0.34202814	3.008483771	0.086049991	;
0.34440333	3.001134516	0.084666315	;
0.34681175	2.997060693	0.083083069	;
0.34925408	2.991386886	0.082737543	;
0.35173106	2.980093259	0.083581277	;

0.35424343	2.978102234	0.08344408	;
0.35679194	2.974344315	0.082547605	;
0.35937739	2.962934869	0.082298468	;
0.36200058	2.962917259	0.082211206	;
0.36466235	2.957870411	0.082446141	;
0.36736356	2.9514532	0.081951155	;
0.37010507	2.951395723	0.080973554	;
0.37288782	2.939900082	0.080700022	;
0.37571273	2.938977599	0.080742364	;
0.37858076	2.934110385	0.080397452	;
0.38149292	2.934075395	0.079865023	;
0.38445023	2.922527433	0.079978719	;
0.38745375	2.920056755	0.079758724	;
0.39050457	2.916669622	0.078877634	;
0.39360381	2.910821471	0.077984858	;
0.39675264	2.910773857	0.077165047	;
0.39995226	2.901305191	0.076953297	;
0.4032039	2.899098982	0.076647952	;
0.40650885	2.893258702	0.076719721	;
0.40986843	2.887419451	0.077143278	;
0.413284	2.883369941	0.077409422	;
0.41675697	2.881529044	0.076874117	;
0.42028881	2.87564796	0.076819208	;
0.42388103	2.869789397	0.077596286	;
0.42753517	2.866778814	0.078617855	;
0.43125287	2.863937364	0.079102638	;
0.43503579	2.858058198	0.079979127	;
0.43888566	2.852189696	0.081400617	;
0.44280429	2.851373776	0.082658402	;
0.44679351	2.846324063	0.08337069	;
0.45085527	2.846315847	0.08344998	;
0.45499156	2.84038917	0.084087069	;
0.45920444	2.836914544	0.085053672	;
0.46349607	2.834498216	0.086024044	;
0.46786868	2.828577099	0.087340734	;
0.47232457	2.828640994	0.08904983	;
0.47686615	2.824246684	0.090880872	;
0.48149592	2.822763498	0.091835536	;
0.48621647	2.816848313	0.093778568	;
0.4910305	2.810987622	0.097166917	;
0.4959408	2.8111613	0.100885353	;

}

}

A.2   Sentaurus device: parameter section

#define ParFileDir.

Material="SiliconCarbide" {
        Insert= "sic.par"
}

Material="SiO2"{
ComplexRefractiveIndex
{
Formula=3
}

TableODB
{ * Each entry of the table consists of three values:
  *complex refractive index n + i*k (unitless)
  *refractive index = n, absorption coefficient = 4*pi*k/wavelength
  *WAVELEN(um) n   k

0.21   1.5384   0   ;
0.215   1.5332   0   ;
0.22   1.5285   0   ;
0.225   1.5242   0   ;
0.23   1.5202   0   ;
0.235   1.5166   0   ;
0.24   1.5133   0   ;
0.245   1.5103   0   ;
0.25   1.5074   0   ;
0.255   1.5048   0   ;
0.26   1.5024   0   ;
0.265   1.5001   0   ;
0.27   1.498   0   ;
0.275   1.496   0   ;
0.28   1.4942   0   ;
0.285   1.4924   0   ;
0.29   1.4908   0   ;
0.295   1.4892   0   ;
0.3   1.4878   0   ;
0.305   1.4864   0   ;
0.31   1.4851   0   ;
0.315   1.4839   0   ;
0.32   1.4827   0   ;
0.325   1.4816   0   ;

0.33	1.4806	0	;
0.335	1.4796	0	;
0.34	1.4787	0	;
0.345	1.4778	0	;
0.35	1.4769	0	;
0.355	1.4761	0	;
0.36	1.4753	0	;
0.365	1.4745	0	;
0.37	1.4738	0	;
0.375	1.4731	0	;
0.38	1.4725	0	;
0.385	1.4719	0	;
0.39	1.4713	0	;
0.395	1.4707	0	;
0.4	1.4701	0	;
0.405	1.4696	0	;
0.41	1.4691	0	;
0.415	1.4686	0	;
0.42	1.4681	0	;
0.425	1.4676	0	;
0.43	1.4672	0	;
0.435	1.4668	0	;
0.44	1.4663	0	;
0.445	1.466	0	;
0.45	1.4656	0	;
0.455	1.4652	0	;
0.46	1.4648	0	;
0.465	1.4645	0	;
0.47	1.4641	0	;
0.475	1.4638	0	;
0.48	1.4635	0	;
0.485	1.4632	0	;
0.49	1.4629	0	;
0.495	1.4626	0	;
0.5	1.4623	0	;
0.505	1.4621	0	;
0.51	1.4618	0	;
0.515	1.4615	0	;
0.52	1.4613	0	;
0.525	1.461	0	;
0.53	1.4608	0	;
0.535	1.4606	0	;
0.54	1.4603	0	;
0.545	1.4601	0	;

0.55	1.4599	0	;
0.555	1.4597	0	;
0.56	1.4595	0	;
0.565	1.4593	0	;
0.57	1.4591	0	;
0.575	1.4589	0	;
0.58	1.4587	0	;
0.585	1.4586	0	;
0.59	1.4584	0	;
0.595	1.4582	0	;
0.6	1.458	0	;
0.605	1.4579	0	;
0.61	1.4577	0	;
0.615	1.4576	0	;
0.62	1.4574	0	;
0.625	1.4572	0	;
0.63	1.4571	0	;
0.635	1.457	0	;
0.64	1.4568	0	;
0.645	1.4567	0	;
0.65	1.4565	0	;
0.655	1.4564	0	;
0.66	1.4563	0	;
0.665	1.4561	0	;
0.67	1.456	0	;
0.675	1.4559	0	;
0.68	1.4558	0	;
0.685	1.4556	0	;
0.69	1.4555	0	;
0.695	1.4554	0	;
0.7	1.4553	0	;
0.71	1.4551	0	;
0.72	1.4549	0	;
0.73	1.4546	0	;
0.74	1.4544	0	;
0.75	1.4542	0	;
0.76	1.454	0	;
0.77	1.4539	0	;
0.78	1.4537	0	;
0.79	1.4535	0	;
0.8	1.4533	0	;
0.81	1.4531	0	;
0.82	1.453	0	;
0.83	1.4528	0	;

0.84	1.4527	0	;
0.85	1.4525	0	;
0.86	1.4523	0	;
0.87	1.4522	0	;
0.88	1.452	0	;
0.89	1.4519	0	;
0.9	1.4518	0	;
0.91	1.4516	0	;
0.92	1.4515	0	;
0.93	1.4513	0	;
0.94	1.4512	0	;
0.95	1.4511	0	;
0.96	1.4509	0	;
0.97	1.4508	0	;
0.98	1.4507	0	;
0.99	1.4505	0	;
1	1.4504	0	;
1.01	1.4503	0	;
1.02	1.4502	0	;
1.03	1.45	0	;
1.04	1.4499	0	;
1.05	1.4498	0	;
1.06	1.4497	0	;
1.07	1.4496	0	;
1.08	1.4494	0	;
1.09	1.4493	0	;
1.1	1.4492	0	;
1.11	1.4491	0	;
1.12	1.449	0	;
1.13	1.4489	0	;
1.14	1.4487	0	;
1.15	1.4486	0	;
1.16	1.4485	0	;
1.17	1.4484	0	;
1.18	1.4483	0	;
1.19	1.4482	0	;
1.2	1.4481	0	;
1.21	1.4479	0	;
1.22	1.4478	0	;
1.23	1.4477	0	;
1.24	1.4476	0	;
1.25	1.4475	0	;
1.26	1.4474	0	;
1.27	1.4473	0	;

1.28	1.4471	0	;
1.29	1.447	0	;
1.3	1.4469	0	;
1.31	1.4468	0	;
1.32	1.4467	0	;
1.33	1.4466	0	;
1.34	1.4465	0	;
1.35	1.4464	0	;
1.36	1.4462	0	;
1.37	1.4461	0	;
1.38	1.446	0	;
1.39	1.4459	0	;
1.4	1.4458	0	;
1.41	1.4457	0	;
1.42	1.4455	0	;
1.43	1.4454	0	;
1.44	1.4453	0	;
1.45	1.4452	0	;
1.46	1.4451	0	;
1.47	1.445	0	;
1.48	1.4449	0	;
1.49	1.4447	0	;
1.5	1.4446	0	;
1.51	1.4445	0	;
1.52	1.4444	0	;
1.53	1.4443	0	;
1.54	1.4441	0	;
1.55	1.444	0	;
1.56	1.4439	0	;
1.57	1.4438	0	;
1.58	1.4437	0	;
1.59	1.4435	0	;
1.6	1.4434	0	;
1.61	1.4433	0	;
1.62	1.4432	0	;
1.63	1.4431	0	;
1.64	1.4429	0	;
1.65	1.4428	0	;
1.66	1.4427	0	;
1.67	1.4426	0	;
1.68	1.4424	0	;
1.69	1.4423	0	;
1.7	1.4422	0	;
1.71	1.442	0	;

1.72	1.4419	0	;
1.73	1.4418	0	;
1.74	1.4417	0	;
1.75	1.4415	0	;
1.76	1.4414	0	;
1.77	1.4413	0	;
1.78	1.4411	0	;
1.79	1.441	0	;
1.8	1.4409	0	;
1.81	1.4407	0	;
1.82	1.4406	0	;
1.83	1.4405	0	;
1.84	1.4403	0	;
1.85	1.4402	0	;
1.86	1.4401	0	;
1.87	1.4399	0	;
1.88	1.4398	0	;
1.89	1.4397	0	;
1.9	1.4395	0	;
1.91	1.4394	0	;
1.92	1.4392	0	;
1.93	1.4391	0	;
1.94	1.4389	0	;
1.95	1.4388	0	;
1.96	1.4387	0	;
1.97	1.4385	0	;
1.98	1.4384	0	;
1.99	1.4382	0	;
2	1.4381	0	;
2.01	1.4379	0	;
2.02	1.4378	0	;
2.03	1.4376	0	;
2.04	1.4375	0	;
2.05	1.4373	0	;
2.06	1.4372	0	;
2.07	1.437	0	;
2.08	1.4369	0	;
2.09	1.4367	0	;
2.1	1.4366	0	;
2.11	1.4364	0	;
2.12	1.4363	0	;
2.13	1.4361	0	;
2.14	1.436	0	;
2.15	1.4358	0	;

```
2.16        1.4357       0       ;
2.17        1.4355       0       ;
2.18        1.4353       0       ;
2.19        1.4352       0       ;
2.2         1.435        0       ;
2.21        1.4349       0       ;
2.22        1.4347       0       ;
2.23        1.4345       0       ;
2.24        1.4344       0       ;
2.25        1.4342       0       ;
2.26        1.434        0       ;
2.27        1.4339       0       ;
2.28        1.4337       0       ;
2.29        1.4335       0       ;
2.3         1.4334       0       ;
2.31        1.4332       0       ;
2.32        1.433        0       ;
2.33        1.4328       0       ;
2.34        1.4327       0       ;
2.35        1.4325       0       ;
2.36        1.4323       0       ;
2.37        1.4322       0       ;
2.38        1.432        0       ;
2.39        1.4318       0       ;
2.4         1.4316       0       ;
2.41        1.4314       0       ;
2.42        1.4313       0       ;
2.43        1.4311       0       ;
2.44        1.4309       0       ;
2.45        1.4307       0       ;
2.46        1.4305       0       ;
2.47        1.4304       0       ;
2.48        1.4302       0       ;
2.49        1.43         0       ;
2.5         1.4298       0       ;
}
}

Material="MgF2"{

ComplexRefractiveIndex
{
Formula=3
}
```

TableODB
{ * Each entry of the table consists of three values:
 *complex refractive index n + i*k (unitless)
 *refractive index = n, absorption coefficient = 4*pi*k/wavelength
 *WAVELEN(um) n   k

0.25	1.4117	0	;
0.275	1.4044	0	;
0.3	1.3996	0	;
0.325	1.3961	0	;
0.35	1.3935	0	;
0.375	1.3915	0	;
0.4	1.3899	0	;
0.425	1.3886	0	;
0.45	1.3875	0	;
0.475	1.3865	0	;
0.5	1.3857	0	;
0.525	1.385	0	;
0.55	1.3844	0	;
0.575	1.3839	0	;
0.6	1.3834	0	;
0.625	1.383	0	;
0.65	1.3826	0	;
0.675	1.3823	0	;
0.7	1.3819	0	;
0.725	1.3816	0	;
0.75	1.3814	0	;
0.775	1.3811	0	;
0.8	1.3809	0	;
0.825	1.3807	0	;
0.85	1.3805	0	;
0.875	1.3803	0	;
0.9	1.3802	0	;

}
}

Material="Nickel"{

ComplexRefractiveIndex
{
Formula=3
}

TableODB
{ * Each entry of the table consists of three values:
 *complex refractive index n + i*k (unitless)
 *refractive index = n, absorption coefficient = 4*pi*k/wavelength
 *WAVELEN(um) n   k

0.19077	1.0131	1.4269 ;
0.19225	1.0121	1.4427 ;
0.19375	1.01	1.46 ;
0.19528	1.0073	1.4785 ;
0.19683	1.0044	1.4981 ;
0.1984	1.0018	1.5187 ;
0.2	1	1.54 ;
0.20163	1.0015	1.5644 ;
0.20328	1.0038	1.5883 ;
0.20496	1.0068	1.6105 ;
0.20667	1.01	1.63 ;
0.2084	1.0131	1.6456 ;
0.21017	1.02	1.67 ;
0.21197	1.0294	1.6994 ;
0.21379	1.04	1.73 ;
0.21565	1.0494	1.7556 ;
0.21754	1.06	1.78 ;
0.21947	1.0744	1.805 ;
0.22143	1.09	1.83 ;
0.22342	1.1044	1.8544 ;
0.22545	1.12	1.88 ;
0.22752	1.1388	1.91 ;
0.22963	1.16	1.94 ;
0.23178	1.1838	1.9656 ;
0.23396	1.21	1.99 ;
0.23619	1.2394	2.0163 ;
0.23846	1.27	2.04 ;
0.24078	1.2994	2.0563 ;
0.24314	1.33	2.07 ;
0.24554	1.3644	2.0863 ;
0.248	1.4	2.1 ;
0.25051	1.4356	2.1069 ;
0.25306	1.47	2.11 ;
0.25567	1.5006	2.1113 ;
0.25833	1.53	2.11 ;
0.26105	1.5613	2.1056 ;
0.26383	1.59	2.1 ;
0.26667	1.6113	2.0956 ;
0.26957	1.63	2.09 ;

0.27253	1.65	2.08	;
0.27556	1.67	2.07	;
0.27865	1.6913	2.0656	;
0.28182	1.71	2.06	;
0.28506	1.7219	2.0456	;
0.28837	1.73	2.03	;
0.29176	1.7363	2.0188	;
0.29524	1.74	2.01	;
0.2988	1.7413	2.005	;
0.30244	1.74	2	;
0.30617	1.7356	1.9894	;
0.31	1.73	1.98	;
0.31392	1.7263	1.9781	;
0.31795	1.72	1.98	;
0.32208	1.7063	1.9831	;
0.32632	1.69	1.99	;
0.33067	1.6744	2.0025	;
0.33514	1.66	2.02	;
0.33973	1.6488	2.0444	;
0.34444	1.64	2.07	;
0.3493	1.6344	2.0894	;
0.35429	1.63	2.11	;
0.35942	1.625	2.1388	;
0.36471	1.62	2.17	;
0.37015	1.6144	2.1994	;
0.37576	1.61	2.23	;
0.38154	1.6094	2.265	;
0.3875	1.61	2.3	;
0.39365	1.61	2.3294	;
0.4	1.61	2.36	;
0.40656	1.6094	2.3988	;
0.41333	1.61	2.44	;
0.42034	1.6144	2.4794	;
0.42759	1.62	2.52	;
0.43509	1.625	2.5638	;
0.44286	1.63	2.61	;
0.45091	1.635	2.6594	;
0.45926	1.64	2.71	;
0.46792	1.6444	2.7588	;
0.47692	1.65	2.81	;
0.48627	1.6581	2.8681	;
0.496	1.67	2.93	;
0.50612	1.6888	2.9944	;
0.51667	1.71	3.06	;

0.52766	1.7294	3.1244 ;
0.53913	1.75	3.19 ;
0.55111	1.7744	3.2588 ;
0.56364	1.8	3.33 ;
0.57674	1.8238	3.4031 ;
0.59048	1.85	3.48 ;
0.60488	1.8819	3.5638 ;
0.62	1.92	3.65 ;
0.6359	1.9669	3.7338 ;
0.65263	2.02	3.82 ;
0.67027	2.0775	3.915 ;
0.68889	2.14	4.01 ;
0.70857	2.2081	4.0988 ;
0.72941	2.28	4.18 ;
0.75152	2.3575	4.2456 ;
0.775	2.43	4.31 ;
0.8	2.4819	4.3881 ;
0.82667	2.53	4.47 ;
0.85517	2.5906	4.5463 ;
0.88571	2.65	4.63 ;
0.91852	2.6956	4.7344 ;
0.95385	2.74	4.85 ;
0.992	2.7931	4.9713 ;
1.03333	2.85	5.1 ;
1.07826	2.9113	5.2331 ;
1.12727	2.97	5.38 ;
1.18095	3.0213	5.5469 ;
1.24	3.06	5.74 ;
1.30526	3.11	5.98 ;
1.37778	3.18	6.23 ;
1.45882	3.27	6.51 ;
1.55	3.38	6.82 ;
1.65333	3.49	7.13 ;
1.77143	3.59	7.48 ;
1.90769	3.69	7.92 ;
2.06667	3.84	8.35 ;
2.25455	3.9	8.92 ;
2.48	4.03	9.64 ;
}		
}		

Material="Titanium"{

ComplexRefractiveIndex
{
Formula=3
}

TableODB
{ * Each entry of the table consists of three values:
 *complex refractive index n + i*k (unitless)
 *refractive index = n, absorption coefficient = 4*pi*k/wavelength
 *WAVELEN(um) n   k
206.63   1.16   1.21   ;
210.14   1.18   1.22   ;
213.76   1.21   1.22   ;
217.51   1.23   1.21   ;
221.39   1.24   1.21   ;
225.42   1.24   1.19   ;
229.59   1.18   1.15   ;
233.92   1.35   1.21   ;
238.42   1.26   1.2   ;
243.1   1.25   1.2   ;
247.96   1.24   1.21   ;
253.02   1.22   1.22   ;
258.29   1.21   1.23   ;
263.79   1.18   1.25   ;
269.52   1.17   1.28   ;
275.51   1.15   1.31   ;
281.77   1.13   1.33   ;
288.33   1.1   1.37   ;
295.19   1.05   1.44   ;
302.39   1.04   1.53   ;
309.95   1.04   1.61   ;
317.9   1.06   1.73   ;
326.26   1.11   1.83   ;
335.08   1.17   1.9   ;
344.39   1.24   1.96   ;
354.23   1.3   2.01   ;
364.65   1.37   2.06   ;
375.7   1.44   2.09   ;
387.44   1.5   2.12   ;
399.94   1.55   2.15   ;
413.27   1.59   2.17   ;

```
427.52              1.63           2.21   ;
442.79              1.68           2.25   ;
459.19              1.71           2.29   ;
476.85              1.75           2.34   ;
495.92              1.78           2.39   ;
516.58              1.81           2.47   ;
539.04              1.86           2.56   ;
563.55              1.92           2.67   ;
590.38              2.01           2.77   ;
619.9               2.11           2.88   ;
652.53              2.22           2.99   ;
688.78              2.36           3.11   ;
729.29              2.54           3.23   ;
774.87              2.74           3.3    ;
826.53              2.98           3.32   ;
885.57              3.17           3.28   ;
953.69              3.28           3.25   ;
1033.17             3.35           3.3    ;
1127.09             3.47           3.4    ;
1239.8              3.62           3.52   ;
}
}

Material="Aluminum"{

ComplexRefractiveIndex
{
Formula=3
}

TableODB
{ * Each entry of the table consists of three values:
  *complex refractive index n + i*k (unitless)
  *refractive index = n,  absorption coefficient = 4*pi*k/wavelength
  *WAVELEN(um) n              k
183.68              0.102          2.07             ;
185.05              0.1044         2.085002         ;
186.44              0.1062         2.103344         ;
187.86              0.1076         2.124184         ;
189.29              0.1088         2.146683         ;
190.75              0.11           2.17             ;
192.23              0.1113         2.193295         ;
193.73              0.1129         2.215727         ;
195.25              0.1148         2.237511         ;
```

196.8	0.1168	2.258863	;
198.38	0.119	2.28	;
199.98	0.1213	2.301136	;
201.6	0.1236	2.322489	;
203.25	0.1258	2.344273	;
204.93	0.128	2.366705	;
206.64	0.13	2.39	;
208.38	0.1318	2.414375	;
210.14	0.134	2.44	;
211.94	0.1364	2.465625	;
213.77	0.139	2.49	;
215.63	0.1415	2.509375	;
217.52	0.144	2.53	;
219.44	0.1464	2.559375	;
221.4	0.149	2.59	;
223.4	0.1519	2.615	;
225.43	0.155	2.64	;
227.5	0.1585	2.669375	;
229.6	0.162	2.7	;
231.75	0.1649	2.73	;
233.93	0.168	2.76	;
236.16	0.1719	2.79	;
238.43	0.176	2.82	;
240.75	0.1796	2.85	;
243.11	0.183	2.88	;
245.52	0.1865	2.909375	;
247.97	0.19	2.94	;
250.48	0.1934	2.975	;
253.03	0.197	3.01	;
255.64	0.2009	3.039375	;
258.3	0.205	3.07	;
261.02	0.2089	3.109375	;
263.8	0.213	3.15	;
266.63	0.2179	3.185	;
269.53	0.223	3.22	;
272.49	0.2279	3.259375	;
275.52	0.233	3.3	;
278.62	0.2384	3.339375	;
281.78	0.244	3.38	;
285.02	0.2494	3.425	;
288.34	0.255	3.47	;
291.73	0.2609	3.51	;
295.2	0.267	3.55	;
298.76	0.2734	3.59375	;

302.4	0.28	3.64	;
306.14	0.2868	3.689375	;
309.96	0.294	3.74	;
313.89	0.3019	3.789375	;
317.91	0.31	3.84	;
322.04	0.3179	3.894375	;
326.28	0.326	3.95	;
330.63	0.3348	4.005	;
335.1	0.344	4.06	;
339.69	0.3538	4.11375	;
344.4	0.364	4.17	;
349.25	0.3744	4.23375	;
354.24	0.385	4.3	;
359.38	0.3958	4.365	;
364.66	0.407	4.43	;
370.11	0.4191	4.49375	;
375.71	0.432	4.56	;
381.49	0.4457	4.63375	;
387.45	0.46	4.71	;
393.6	0.4747	4.784375	;
399.95	0.49	4.86	;
406.51	0.5062	4.938125	;
413.28	0.523	5.02	;
420.29	0.5401	5.10875	;
427.54	0.558	5.2	;
435.04	0.5773	5.29	;
442.8	0.598	5.38	;
450.86	0.6203	5.48	;
459.2	0.644	5.58	;
467.87	0.6686	5.69	;
476.87	0.695	5.8	;
486.22	0.7238	5.915	;
495.94	0.755	6.03	;
506.06	0.789	6.15	;
516.6	0.826	6.28	;
527.6	0.867	6.42	;
539.07	0.912	6.55	;
551.05	0.963	6.7	;
563.57	1.02	6.85	;
576.68	1.08	7	;
590.41	1.15	7.15	;
604.81	1.22	7.31	;
619.93	1.3	7.48	;
635.82	1.39	7.65	;

652.55	1.49	7.82	;
670.19	1.6	8.01	;
688.81	1.74	8.21	;
708.49	1.91	8.39	;
729.32	2.14	8.57	;
751.43	2.41	8.62	;
774.91	2.63	8.6	;
799.9	2.8	8.45	;
826.57	2.74	8.31	;
855.07	2.58	8.21	;
885.61	2.24	8.21	;
918.41	1.86	8.44	;
953.73	1.47	8.95	;
991.88	1.37	9.49	;
1033.21	1.26	10	;
1078.13	1.21	10.6	;
1127.14	1.2	11.2	;
1180.81	1.21	11.8	;
1239.85	1.21	12.5	;
1305.11	1.23	13.2	;
1377.61	1.26	14	;
1458.65	1.33	14.9	;
1549.81	1.44	16	;
1653.14	1.59	17.1	;
1771.22	1.77	18.3	;
1907.46	1.99	19.8	;
2066.42	2.27	21.4	;
2254.28	2.62	23.3	;
2479.7	3.07	25.6	;

```
}
}
```

A.3   Source codes for KTH's photodiode simulations

A.3.1   Sentaurus Device Editor: source code for photodiode design

```
; Structure Definition

(sdegeo:create-rectangle (position 0 0 0 )  (position 870 0.3 0 ) "SiliconCarbide" "Base" )
(sdegeo:create-rectangle (position 0  0.3  0 )   (position  870  1.3  0 ) "SiliconCarbide"
"Collector" )
```

(sdegeo:create-rectangle (position 0 1.3 0)   (position 970 2.3 0) "SiliconCarbide" "CollectorPlus")

; Passivation oixde (thickness = 50 nm)

(sdegeo:create-rectangle (position 0 -0.05 0.0) (position 2.5 0 0.0) "SiO2" "Ox1")
(sdegeo:create-rectangle (position 10.5 -0.05 0.0) (position 127.5 0 0.0) "SiO2" "Ox2")
(sdegeo:create-rectangle (position 132.5 -0.05 0.0) (position 249.5 0 0.0) "SiO2" "Ox3")
(sdegeo:create-rectangle (position 254.5 -0.05 0.0) (position 371.5 0 0.0) "SiO2" "Ox4")
(sdegeo:create-rectangle (position 376.5 -0.05 0.0) (position 493.5 0 0.0) "SiO2" "Ox5")
(sdegeo:create-rectangle (position 498.5 -0.05 0.0) (position 615.5 0 0.0) "SiO2" "Ox6")
(sdegeo:create-rectangle (position 620.5 -0.05 0.0) (position 737.5 0 0.0) "SiO2" "Ox7")
(sdegeo:create-rectangle (position 742.5 -0.05 0.0) (position 859.5 0 0.0) "SiO2" "Ox8")
(sdegeo:create-rectangle (position 867.5 -0.05 0.0)   (position 870.05 0   0.0) "SiO2" "Ox9")

(sdegeo:create-rectangle (position 870 0 0.0) (position 870.05 1.25 0.0) "SiO2" "Ox10")
(sdegeo:create-rectangle (position 870 1.25 0.0) (position 872.5 1.3 0.0) "SiO2" "Ox11")
(sdegeo:create-rectangle (position 967 1.25 0.0) (position 970 1.3 0.0) "SiO2" "Ox12")

; Doping Profile

(sdedr:define-constant-profile "ConstantProfileDefinition_1" "BoronActiveConcentration" 5e17)
(sdedr:define-constant-profile-region   "ConstantProfilePlacement_1" "ConstantProfileDefinition_1" "Base")

(sdedr:define-constant-profile   "ConstantProfileDefinition_2" "PhosphorusActiveConcentration" 1e16)
(sdedr:define-constant-profile-region   "ConstantProfilePlacement_2" "ConstantProfileDefinition_2" "Collector")

(sdedr:define-constant-profile   "ConstantProfileDefinition_3" "PhosphorusActiveConcentration" 1e19)
(sdedr:define-constant-profile-region   "ConstantProfilePlacement_3" "ConstantProfileDefinition_3" "CollectorPlus")

; Contact definition

(sdegeo:define-contact-set "contactP" 4 (color:rgb 1 0 0) "##")
(sdegeo:set-current-contact-set "contactP")

(sdegeo:define-contact-set "contactN" 4 (color:rgb 0 0 1) "##")
(sdegeo:set-current-contact-set "contactN")

```
(sdegeo:define-2d-contact (list (car (find-edge-id (position 2.6 0 0)))) "contactP")
(sdegeo:define-2d-contact (list (car (find-edge-id (position 128 0 0)))) "contactP")
(sdegeo:define-2d-contact (list (car (find-edge-id (position 250 0 0)))) "contactP")
(sdegeo:define-2d-contact (list (car (find-edge-id (position 372 0 0)))) "contactP")
(sdegeo:define-2d-contact (list (car (find-edge-id (position 494 0 0)))) "contactP")
(sdegeo:define-2d-contact (list (car (find-edge-id (position 616 0 0)))) "contactP")
(sdegeo:define-2d-contact (list (car (find-edge-id (position 738 0 0)))) "contactP")
(sdegeo:define-2d-contact (list (car (find-edge-id (position 860 0 0)))) "contactP")
(sdegeo:define-2d-contact (list (car (find-edge-id (position 873 1.3 0)))) "contactN")

(sdegeo:create-rectangle (position 2.5 -0.1 0)  (position 10.5 0 0) "Nickel" "Ni1" )
(sdegeo:create-rectangle (position 127.5 -0.1 0)  (position 132.5 0 0) " Nickel " "Ni2" )
(sdegeo:create-rectangle (position 249.5 -0.1 0)  (position 254.5 0 0) " Nickel " "Ni3" )
(sdegeo:create-rectangle (position 371.5 -0.1 0)  (position 376.5 0 0) " Nickel " "Ni4" )
(sdegeo:create-rectangle (position 493.5 -0.1 0)  (position 498.5 0 0) " Nickel " "Ni5" )
(sdegeo:create-rectangle (position 615.5 -0.1 0)  (position 620.5 0 0) " Nickel " "Ni6" )
(sdegeo:create-rectangle (position 737.5 -0.1 0)  (position 742.5 0 0) " Nickel " "Ni7" )
(sdegeo:create-rectangle (position 859.5 -0.1 0)  (position 867.5 0 0) " Nickel " "Ni8" )
(sdegeo:create-rectangle (position 872.5 1.2 0)  (position 967.5 1.3 0) " Nickel " "Ni9" )

(sdegeo:create-rectangle (position 2.5 -0.25 0)  (position 10.5 -0.1 0) "Titanium" "Ti1" )
(sdegeo:create-rectangle (position 127.5 -0.25 0)  (position 132.5 -0.1 0) "Titanium" "Ti2")
(sdegeo:create-rectangle (position 249.5 -0.25 0)  (position 254.5 -0.1 0) "Titanium" "Ti3")
(sdegeo:create-rectangle (position 371.5 -0.25 0)  (position 376.5 -0.1 0) "Titanium" "Ni4")
(sdegeo:create-rectangle (position 493.5 -0.25 0)  (position 498.5 -0.1 0) "Titanium" "Ti5")
(sdegeo:create-rectangle (position 615.5 -0.25 0)  (position 620.5 -0.1 0) "Titanium" "Ti6")
(sdegeo:create-rectangle (position 737.5 -0.25 0)  (position 742.5 -0.1 0) "Titanium" "Ti7")
(sdegeo:create-rectangle (position 859.5 -0.25 0)  (position 867.5 -0.1 0) "Titanium" "Ti8")

(sdegeo:create-rectangle (position 2.5 -1.1 0)  (position 10.5 -0.25 0) "Aluminum" "Al1" )
(sdegeo:create-rectangle (position 127.5 -1.1 0) (position 132.5 -0.25 0) "Aluminum" "Al2")
(sdegeo:create-rectangle (position 249.5 -1.1 0) (position 254.5 -0.25 0) "Aluminum" "Al3")
(sdegeo:create-rectangle (position 371.5 -1.1 0) (position 376.5 -0.25 0) "Aluminum" "Al4")
(sdegeo:create-rectangle (position 493.5 -1.1 0) (position 498.5 -0.25 0) "Aluminum" "Al5")
(sdegeo:create-rectangle (position 615.5 -1.1 0) (position 620.5 -0.25 0) "Aluminum" "Al6")
(sdegeo:create-rectangle (position 737.5 -1.1 0) (position 742.5 -0.25 0) "Aluminum" "Al7")
(sdegeo:create-rectangle (position 859.5 -1.1 0) (position 867.5 -0.25 0) "Aluminum" "Al8")
```

; Window for mash definition

```
(sdedr:define-refeval-window "RefEvalWin_1" "Rectangle" (position 0 0 0) (position 870 2.3 0) )
(sdedr:define-refeval-window "RefEvalWin_2" "Rectangle" (position 870 1.3 0) (position 970 2.3 0) )

(sdedr:define-refinement-size "RefinementDefinition_1" 0.4 0.4 0.2 0.2 )
(sdedr:define-refinement-placement "RefinementPlacement_1" "RefinementDefinition_1" "RefEvalWin_1" )
(sdedr:define-refinement-size "RefinementDefinition_2" 1 1 0.5 0.5 )
(sdedr:define-refinement-placement "RefinementPlacement_2" "RefinementDefinition_2" "RefEvalWin_2" )
(sde:set-meshing-command "snmesh -a -c boxmethod")
(sdedr:append-cmd-file "")
(sde:build-mesh "snmesh" "-a -c boxmethod"
"/afs/ict.kth.se/home/m/a/marcocr/TEST/tmp/tmp/photo2.tmp/photo2")

; Save

(sdeio:save-dfise-bnd (get-body-list)
"/afs/ict.kth.se/home/m/a/marcocr/TEST/tmp/tmp/photo2.tmp/photo2.bnd")
(sde:save-model "/afs/ict.kth.se/home/m/a/marcocr/TEST/tmp/tmp/photo2.tmp/photo2")
(sdeio:save-tdr-bnd (get-body-list)
"/afs/ict.kth.se/home/m/a/marcocr/TEST/tmp/tmp/photo2.tmp/photo2.tdr")
```

A.3.2 Sentaurus Device: source code for photodiode simulation

```
Electrode{
        { name="contactP"    voltage=0 }
        { name="contactN"    voltage=0 }
}

*--  RayTraceBC {
*--        {
*--          Name= "contactP"
*--          Reflectivity= 0.03     # medium reflectance value in the UV
*--        }
*--        {
*--          Name= "contactN"
*--          Reflectivity= 0.03
*--        }
*--              }
```

```
File{
 Grid    = "photo2_msh.tdr"
 Plot    = "photo2_des.tdr"
 Current = "photo2_des.plt"
 Output  = "photo2_des.log"
 Parameter= "sic.par"
}

Plot{
   *--Density and Currents, etc.
       eDensity hDensity
       TotalCurrent/Vector eCurrent/Vector hCurrent/Vector
       eMobility hMobility
       eVelocity hVelocity
       eQuasiFermi hQuasiFermi

 *--Temperature
       eTemperature Temperature * hTemperature

 *--Fields and charges
       ElectricField/Vector Potential SpaceCharge

 *--Doping Profiles
       Doping DonorConcentration AcceptorConcentration

 *--Generation/Recombination
       SRH Band2Band * Auger
       AvalancheGeneration eAvalancheGeneration hAvalancheGeneration
        eIonIntegral hIonIntegral MeanIonIntegral
       eLifeTime hLifeTime
       AugerRecombination SRHRecombination

 *--Band structure/Composition
       BandGap
       BandGapNarrowing
       Affinity
       ConductionBand ValenceBand

 *--Optical Generation
       ComplexRefractiveIndex QuantumYield
       OpticalIntensity AbsorbedPhotonDensity OpticalGeneration
        OpticalAbsorption QuantumEfficiency
       RayTraceIntensity RayTrees
}
```

```
Physics{
      Temperature = 300
      Mobility(
                  DopingDependence
                  HighFieldSaturation
                  )
      Recombination(
                  SRH(DopingDependence TempDependence )
                  Auger
                           )
      IncompleteIonization (Dopants="BoronActiveConcentration
      PhosphorusActiveConcentration" )
      EffectiveIntrinsicDensity(NoBandGapNarrowing)
      Fermi

Optics (
      EffectiveIndex (
                     Absorption(ODB)        #absorption based on ODB table; the absorption
                                                      coefficient is automatically calculated
                     )

      ComplexRefractiveIndex (WavelengthDep(Real Imag))
      OpticalGeneration (
       QuantumYield (StepFunction (Bandgap))    # absorption depends on the amplitude of
                                                      the bandgap, based on the temperature
      ComputeFromMonochromaticSource
                          )
      Excitation (
                     Wavelength = 0.360          # Incident light wavelength [um]
                     Intensity = 1               # Incident light intensity [W/cm2]
                     Polarization = 0.5          # Unpolarized light
                     Theta = 0                   # Normal incidence y direction
                     Window ("L1")(
                            Origin= (0, -1.5)
                            Line(x1=0 x2=970)        # Illumination window covering the
                                                          entire width of photodiode
                                   )
             )
             OpticalSolver (
             RayTracing (
                            RayDistribution(
                                   Mode= Autopopulate
```

217

```
                        NumberOfRays= 300              # Number of rays in the
                                                          illumination window
                                    )
                    )
                  )
            )
}

Physics (MaterialInterface="SiO2/SiliconCarbide") {
                Traps(FixedCharge Conc=9e+11)
                Traps (
                    (Donor Uniform EnergyMid=0.7975 EnergySig=0.7975
                    fromValBand Conc=11e11 eXsection=1e-15
                    hXsection=1e-15)
                    (Acceptor  Uniform  EnergyMid=0.7975  EnergySig=0.7975
                    fromCondBand Conc=11e11 eXsection=1e-15
                    hXsection=1e-15)
                    )
                                        }              # Traps and fixed charge
                                                          definition


Math{

        Extrapolate                             # In quasi-stationary bias ramps,
                                                      by default Sentaurus
                                                 Device uses linear interpolation
                                                   to predict (by extrapolation)
                                                    an initial guess for  the next
                                                      solution based on the
                                                 values of the previous solutions

        Derivates                        # For most of the problems, Newton iterations
                                                  converge best with full derivatives

        Iterations=15                            # Sets the number of iterations for the
                                                          Newton algorithms used
                                                            during its application

        NotDamped=5                              # Number of Newton iterations
                                                      before Bank-Rose damping is
                                               applied (this damping method try to achieve
                                                      convergence of the coupled
                                          iteration far from the final solution by changing
```

218

the solution by smaller amounts than a normal
Newton iteration would)

ComputeIonizationIntegrals(WriteAll)   # calculates the ionization integrals
                                                    for electrons and holes

BreakAtIonIntegral   # It is used to terminate the quasi-stationary
                                                    simulation when the largest ionization
                                                    integral is greater than one
}

Solve {
    Optics   # Solve the Optical problem

    Poisson   # Solve Poisson's equation
                                                    for electrons and holes

    Coupled{Poisson Electron Hole }   # Solve coupled equations (Poisson's equations
                                                    and continuity equations) using the
                                                    Newton iteration, using the solution of
                                                    the Poisson's equation of the previous step

    Quasistationary(
            InitialStep=1e-2 MinStep=1e-10 MaxStep=0.05 Decrement=3
            Goal { Name="contactP" Voltage=-2.5}
)
                                             # QuasiStationary acts on the variables at
                                                    the electrodes (voltage in this case) and
                                                    gradually change them following a ramp as
                                                    specified in the optional parameters

        {
        Coupled { Electron Hole Poisson }   #calculation of a new solution,
                                                    starting from that calculated up to
                                                    this point, by changing the boundary
                                                    conditions of the device
        }
    }

Bibliography

[1] L. Lanni et al., Design and characterization of high-temperature ECL-based bipolar integrated circuits in 4H-SiC, IEEE Trans. Electron Dev., vol. 59, 2012.

[2]   F. Taylor, Introduction to the Venus Express special issue, Planetary and Space Science, vol. 54, 2006.

[3]   F. Taylor, Venus before Venus Express, Planetary and Space Science, vol. 54, 2006.

[4] J. Cressler and A.H. Mantooth, Editors, Extreme Environment Electronics, CRC Press, 2012.

[5]   A. Basilevsky, Analysis of Suspicious Objects in TV Panorama Taken by Venera-9 Spacecraft, Solar System Research, vol. 46, 2012.

[6] www.ict.kth.se/MAP/EKT/WOV/

[7] C-M. Zetterling, editor. Process technology for silicon carbide devices, Copyright2003, IEE, London, UK, 2002.

[8] L. Lanni, SiC bipolar junction transistor circuits for low voltage and high temperature applications, Master's Thesis at department of Microelectronics and Applied Physics, Stockholm, Sweden, September 8,2009.

[9] Pallab Bhattacharya, Semiconductor Optoelectronic Devices Second Edition, Prentice-Hall, 1997.

[10] B. K. Ridley, Quantum Processes in Semiconductors, Oxford University Press, New York, 1982.

[11] www.ioffe.ru/SVA/NSM/Semicond/SiC

[12] Charles Kittel, Introduction to Solid State Physics, John Wiley and Sons, third edition, 1967.

[13] N.D. Arora, J.R. Hauser, and D.J. Roulston, Electron and hole mobilities in silicon as a function of concentration and temperature, IEEE Transactions on Electron Devices, 1982.

[14] M. Bakowski, U. Gustafsson, and U. Lindefelt, Simulation of sic high power devices, Physica Status Solidi A, 1997.

[15] Wei Liu, Electro-thermal simulations and measurement of silicon carbide bipolar transistors, PhD thesis, Department of Microelectronics and Information Technology KTH, Royal Institute of Technology, 2004.

[16] Stéphane Biondo, Wilfried Vervisch, Laurent Ottaviani, and Olivier Palais, Influence on electrical characteristics of the design of 4H-SiC ultraviolet photodetectors: Theroretical analysis and simulations, Journal of Applied Physics 111, 2012.

[17] Y. Okuto and C.R. Crowell, Phys. Rev. 10, 1974.

[18] H. E. Nilsson, E. Bellotti, K. F. Brennem, and M. Hjelem, Mater. Sci. Forum 338-342, 2000.

[19] U. Lindefelt, Doping-induced band edge displacements and band gap narrowing in 3c-, 4h-, 6h-sic, and si, Journal of Applied Physics, 1998.

[20] Handbook of Optics, 2nd edition, Vol. 2, McGraw-Hill, 1994.

[21] S. Zollner, R. Liu, E. Duda, D. Reed, T. Remmel, J. Christiansen, Optical Properties of bulk and epi SiC for power devices, American Physical Society, 1998.

[22] William West, Absorption of electromagnetic radiation in AccessScience, McGraw-Hill.

[23] www.goodfellow-ceramics.com/corporate/pdf/fused-quartz-and-silica.pdf

[24] www.uqgoptics.com/materials_optical_spectosil.aspx

[25] Rainer Waser. Nanoelectronics and Information Technology Advanced Electronic Materials and Novel Devices Second, corrected edition. WILEY-VCH Verlag GmbH & Co. KGaA, 2005.

[26] T. Reiner, B. Mishori, T. Leitner, A. Horovitz, Y. Vainbaum, M. Hakim, A. Lahav, S. Shapira and A. Fenigstein. Tower Semiconductor LTD Migdal HaEmek, CMOS Image Sensor 3T Nwell Photodiode Pixel Spice Model, Israel, 2004.

[27] www.filmetrics.com/refractive-index-database

[28] www.americanscientist.org/issues/pub/sunshine-on-a-cloudy-day

[29] Xiaping Chen, Huili Zhu, Jiafa Cai, and Zhengyun Wu, High-performance 4H-SiC-based ultraviolet p - i - n photodetector, Journal of Applied Physics, 2007.

[30] Patrik Ščajev and Kęstutis Jarašiūnas, Temperature- and excitation-dependent carrier diffusivity and recombination rate in 4H-SiC, Institute of Applied Research, Vilnius University, 2013.

[31] S. M. Sze, Kwok K. Ng. Physics of Semiconductor Devices, Third Edition.John Wiley & Sons, Inc., Hoboken, New Jersey, 2007.

[32] www.diee.unica.it/~vanzi/fotolitografia[1].pdf

[33] www.semi1source.com/glossary/default.asp?searchterm=outdiffusion

[34] Fan Ren, John C. Zolper, Wide Energy Bandgap Electronic Devices, World Scientific Publishing Co. Pte. Ltd. 5 Toh Tuck Link, Singapore, 2003.

[35] W. J. Choyke, H. Matsunami, G. Pensl, (Eds.), Silicon Carbide Recent Major Advances, Springer-Verlag Berlin Heidelberg, 2004.

[36] R. Ghandi, B. Buono, M. Domeij, R. Esteve, A. Schöner, J. Han, S. Dimitrijev, S.A. Reshanov, C.-M. Zetterling, and M. Östling, Surface-passivation effects on the performance of 4H-SiC BJTs. IEEE Transactions on Electron Devices, vol. 58, 2011.

[37] R. Ghandi, H.-S. Lee, M. Domeij, B. Buono, C.-M. Zetterling, and M. Östling, Fabrication of 2700-V 12-mΩcm^2 non ion-implanted 4H-SiC BJTs with common-emitter current gain of 50, IEEE Electron Devices Letters, vol. 29, 2008.

[38] SiCrystal AG, www.sicrystal.de.

[39] Acreo AB, www.acreo.se.

[40] Han-Din Liu, Xiaoguang Zheng, Qiugui Zhou, Xiaogang Bai, Dion C. Mcintosh, and Joe C. Campbell, Double Mesa Sidewall Silicon Carbide Avalanche Photodiode, IEEE Journal of quantum electronics, vol. 45, 2009.

[41] Kuen-Hsien Wu, Yean-Kuen Fang, Jyh-Jier Ho, Wen-Tse Hsieh, W. H. Chuang, and J. D. Hwang, A High Optical-Gain β-SiC Bulk-Barrier Phototransistor for High-Temperature Applications, IEEE Photonics Technology Letters, vol. 10, 1998.

[42] JUN HU, 4H-SiC Detectors for Low Level Ultraviolet Detection, PhD's Thesis in Electrical and Computer Engineering, Graduate School-New Brunswick Rutgers, the State University of New Jersey, 2008.

[43] Xiangyi Guo, Ariane L. Beck, Xiaowei Li, Joe C. Campbell, David Emerson, and Joe Sumakeris, Study of Reverse Dark Current in 4H-SiC Avalanche Photodiodes, IEEE Journal of quantum electronics, vol. 41, 2005.

[44] Sentaurus TCAD Version G-2012.06 from Synopsys Inc. available at www.synopsys.com, 2012.

[45] Handin Liu, Dion Mcintosh, Xiaogang Bai, Huapu Pan, Mingguo Liu, Joe C. Campbell, and Ho Young Cha, 4H-SiC PIN Recessed-Window Avalanche Photodiode With High Quantum Efficiency, IEEE photonics technology letters, vol.20, 2008.

[46] Alexey Vert, Stanislav Soloviev, Alexander Bolotnikov, and Peter Sandvik, Silicon Carbide Photomultipliers and Avalanche Photodiode Arrays for Ultraviolet and Solar-blind Light Detection, Micro and Nanostructures Technologies General Electric Global Research Center Niskayuna, NY, USA, IEEE SENSORS 2009 Conference.

[47] David T. Clark, Ewan P. Ramsay, A.E. Murphy, D.A. Smith, R.F. Thompson, R.A.R. Young, J.D. Cormack, C. Zhu, S. Finney, J. Fletcher, High Temperature Silicon Carbide CMOS Integrated Circuits, Materials Science Forum, Vols. 679-680, 2011.

[48] irina.eas.gatech.edu/EAS8803_Fall2009/Lec6.pdf

[49] www.esa.int/Our_Activities/Space_Science/Venus_Express

[50] archive.oapd.inaf.it/pianetav/L15_02S.html

[51] Kuen-Hsien Wu, Yean-Kuen Fang, Jyh-Jier Ho, Wen-Tse Hsieh, W. H. Chuang, and J. D. Hwang, A High Optical-Gain β-SiC Bulk-Barrier Phototransistor for High-Temperature Applications, IEEE photonics technology letters, vol. 10, 1998.

[52] mpfpi.com/stock-products/viewports/extended-range/magnesium-fluoride.aspx

[53] Pavel A. Ivanov, Michael E. Levinshtein, Anant K. Agarwal, Sumi Krishnaswami, and John W. Palmour, Temperature Dependence of the Current Gain in Power 4H-SiC NPN BJTs. IEEE transactions on electron devices, vol. 53, 2006.

[54] Luigia Lanni, Bengt Gunnar Malm, Mikael Östling, and Carl-Mikael Zetterling, 500 °C Bipolar Integrated OR/NOR Gate in 4H-SiC, IEEE transactions on electron devices, vol. 53, 2006.

[55] refractiveindex.info/legacy/?group=METALS&material=Nickel

[56] R. Vaglio, Elementi di fisica dello stato solido, Liguori Editore, 2010.

[57] Siddharth Potbhare, Neil Goldsman, Gary Pennington, Aivars Lelis, and James M. McGarrity, Numerical and experimental characterization of 4H-silicon carbide lateral metal-oxidesemiconductor field-effect transistor, Journal of Applied Physics, 2006.

[58] Brett A. Hull, Sei-Hyung Ryu, Husna Fatima, Jim Richmond, John W. Palmour, and James Scofield, Development of a 4H-SiC CMOS Inverter, Materials Research Society, Vol. 911, 2006.

[59] Siddharth Potbhare, Modeling and characterization of 4H-SIC MOSFETS: High field, high temperature, and transient effects, Doctor of Philosophy, Department of Electrical and Computer Engineering, 2008.

[60] www.orcad.com/products/orcad-ee-designer/overview

[61] K. Roy, S. Mukhopadhyay, and H. Mahmoodi-Meimand, Leakage Current Mechanisms and Leakage Reduction Techniques in Deep-Submicrometer CMOS Circuits, Proceedings of the IEEE, vol. 91, 2003.

[62] www.seas.upenn.edu/~jan/spice/spice.MOSparamlist.html

[63] www.ing.unisannio.it/elettronica/didattica/informatica_vo/esd

[64] Dev Alok, Self-Aligned Silicon Carbide LMOSFET, Philips Electronics North America Corporation, New York, NY, United States Patent, Patent No. US 3,323,506 B1, 2001.

[65] www.signatone.com/products/accessories/thermal.asp

[66] www.nikoninstruments.com/Products/Microscope Systems/Stereomicroscopes/SMZ1000

[67] www3.imperial.ac.uk/pls/portallive/docs/1/7290999.PDF

[68] www.thermoscientific.com/en/product/thermochill-ii-recirculating-chillers.html

[69] www.velleman.eu/products/view/?country=be&lang=en&id=381476

[70] www.thorlabs.de/newgrouppage9.cfm?objectgroup_id=3482

[71] www-device.eecs.berkeley.edu/graphics/dcl/dcl%20Cascade%2011861-6%20manual.pdf

[72] http://iopscience.iop.org/0957-4484/23/2/025706/article

[73] http://www.te.astro.it/infoservizi/attivitadivulg/venere.html

[74] http://www.universetoday.com/14131/pictures-of-planet-venus/

[75] C. Cobet, K. Wilmers, T. Wethkamp, N.V. Edwards, N. Esser, W. Richter, Optical properties of SiC investigated by spectroscopic ellipsometry from 3.5 to 10 eV, Thin Solid Films, Volume 364, 2000.

[76] http://www.ioffe.ru/SVA/NSM/Semicond/Si/

[77] V. Kursun, Eby G. Friedman, Multi-voltage Cmos Circuit Design, Wiley, 2006.